
# Characterisation of targeted imaging and theranostic agents for cancer and fibrosis

**By James Andrew Thompson, BSc**

**A thesis for the degree of Doctor of Philosophy**

**The University of Hull and the University of York**

**Hull York Medical School**

**September 2018**

## Abstract

Positron emission tomography (PET) imaging is a non-invasive modality that permits the characterisation of biological processes at the molecular level. Integrin αvβ6 and the chemokine receptor CXCR4 are important receptors in the pathogenesis of various cancers as well other diseases such as idiopathic pulmonary fibrosis (IPF) that may be exploited for the diagnosis, prognosis and assessment of therapeutic response. The gold-standard method for diagnosis of various cancers, such as breast, is immunohistochemistry (IHC), which suffers from a lack of a well-defined and reproducible cut-off value for tumour-positive or benign classification.

The integrin αvβ6 is involved in various signalling pathways and it's expression is generally very low in healthy tissues, and is greatly upregulated in various pathologies such as cancer and IPF, being linked to worse prognosis in pancreatic, head and neck, breast and ovarian cancers. Upregulation of αvβ6 during fibrosis or in tumours makes it an attractive target for a non-invasive imaging agent for the early detection of αvβ6 in cancer or IPF, monitoring of disease progression and the assessment of therapeutic response to existing or novel therapies. This thesis has evaluated αvβ6-targeted peptides for use as non-invasive PET imaging agents. [$^{68}$Ga]Ga-DO3A-JD2-RGD1 was selected as the lead peptide and demonstrated high affinity binding and high specificity for αvβ6 in competitive enzyme-linked immunosorbent assays, surface plasmon resonance and cellular binding assays *in vitro* as well as imaging and biodistribution studies *in vivo* using αvβ6$^{+}$ cancer models, indicating its suitability for the detection of αvβ6 in cancer. Preliminary studies of [$^{nat}$Lu]Lu-DO3A-JD2-RGD1 showed that chelation of lutetium-177 did not affect peptide binding to αvβ6, making it a promising potential peptide-receptor radionuclide therapy (PRRT) agent for αvβ6$^{+}$ cancer.

The chemokine receptor CXCR4 and its cognate ligand CXCL12 play a pivotal role in normal physiological processes. CXCR4 overexpression has been associated with over twenty types of human cancer with aggressive, invasive phenotypes, presenting a requirement for a non-invasive imaging agent for the detection of malignant sites including metastatic lesions. This thesis has evaluated the CXCR4-binding characteristics of novel tetraazamacrocycles [$^{nat}$Cu]CuCB-bicyclam and [$^{nat}$Cu]$Cu_2$CB-bicyclam, synthesised by Archibald and colleagues, by surface plasmon resonance in a comparison study with the clinically used AMD3100. Both novel inhibitors were able to bind to CXCR4 with greater affinity than AMD3100, indicating their suitability for further validation as both PET imaging agents in CXCR4$^{+}$ cancer detection and therapeutic agents in cancer and IPF.

# Contents

## List of Abbreviations

| | |
|---|---|
| **AEC** | Alveolar epithelial cells |
| **ADME** | Adsorption, distribution, metabolism and elimination |
| **ACKR3** | Atypical Chemokine Receptor 3/C-X-C Chemokine Receptor Type 7 |
| **Arg** | Arginine |
| **Asp** | Aspartic Acid |
| **$A_S$** | Specific Activity |
| **ATR** | Attenuated total reflection |
| **BLM** | Bleomycin |
| **Bq** | Becquerels |
| **CDD** | Companion diagnostic device |
| **Chaps** | 3-[(3-Cholamidopropyl)dimethylammonio]-1-propanesulfonate |
| **CHS** | Cholestryl hemisuccinate |
| **CLAD** | Chronic lung allograft dysfunction |
| **CM** | Compartmental Modelling |
| **CSF** | Cerebrospinal fluid |
| **CT** | Computerised tomography |
| **CXCL12** | C-X-C Chemokine ligand 12/stromal cell-derived factor 1 |
| **CXCR4** | C-X-C Chemokine receptor type 4/stromal cell-derived factor 1 receptor |
| **DEPC** | Diethylpyrocarbonate |
| **DLCO** | Diffusing capacity for carbon monoxide |
| **DMSO** | Dimethyl sulfoxide |
| **dNTP** | deoxynucleotide triphosphate |
| **DOM** | *n*-dodecyl-β-D-maltopyranoside |
| **DOTA** | 1,4,7,10-Tetraazacyclododecane-1,4,7,10-tetraacetic acid |
| **dps** | Disintegrations per second |
| **DTPA** | Diethylenetriamine pentaacetic acid |
| **ECM** | Extracellular matrix |
| **EDTA** | Ethylenediamine tetraacetic acid |
| **ELISA** | Enzyme-linked immunosorbant assay |
| **EMT** | Epithelial-mesenchymal transition |
| **ER** | Estrogen Receptor |
| **FBA** | Fluorobenzoic acid |
| **FDG** | 2-Deoxy-2-[18F]fluoroglucose |
| **FLT** | 3-deoxy-3-[18F]fluorothymdine |
| **FMDV** | Foot and mouth disease virus |
| **FPA** | Fluoropropionic acid |
| **FVC** | Forced vital capacity |
| **GLUT-1** | Glucose Transporter 1 |
| **Gly** | Glycine |
| **GPCR** | G-protein coupled receptor |
| **GRP** | Gastrin-releasing peptide |
| **Gy** | Gray |
| **HAX-1** | HS1-associated protein |
| **HER2** | Human epidermal growth factor receptor type 2 |

| | |
|---|---|
| **HRCT** | High-resolution computed tomography |
| **IL-13** | Interleukin-13 |
| **IL-1β** | Interleukin-1-β |
| **IPF** | Idiopathic pulmonary fibrosis |
| **i/t** | Intratracheal |
| **i/v** | Intravenous |
| **ka** | Association constant |
| **kD** | Affinity constant |
| **kd** | Dissociation constant |
| **LAP** | Latency-associated peptide |
| **LB** | Lysogeny broth |
| **LC** | Ligand-competent |
| **LLC** | Large latent complex |
| **LOR** | Line of Response |
| **LPA** | Lysophosphatidic acid |
| **LPAR2** | Lysophosphatidic acid receptor type 2 |
| **LTBP-1** | Latent transforming growth factor binding protein 1 |
| **MAPK** | Mitogen-activated protein kinase |
| **MBq** | Megabecquerels |
| **MRI** | Magnetic resonance imaging |
| **MS** | Mass spectrometry |
| **NAC** | N-Acetylcysteine |
| **NET** | Neuroendocrine tumour |
| **NSCLC** | Non-small cell lung cancer |
| **OSCC** | Oral squamous cell carcinoma |
| **PAR1** | Protease-activated receptor type 1 |
| **PCR** | Polymerase chain reaction |
| **PD** | Pharmacodynamics |
| **PET** | Positron Emission Tomography |
| **PI3K** | Phosphoinositol 3-kinase |
| **PK** | Pharmacokinetics |
| **PLC** | Phospholipase-C |
| **PMT** | Photomultiplier tubes |
| **PRRT** | Peptide receptor radionuclide therapy |
| **PSMA** | Prostate-specific membrane antigen |
| **PVE** | Partial Volume Effect |
| **RCP** | Radiochemical Purity |
| **RCY** | Radiochemical yield |
| **RGD** | Arginine-Glycine-Aspartic Acid |
| **R-HPLC** | Radio-high performance liquid chromatography |
| **ROCK** | Rho kinase |
| **ROI** | Region of interest |
| **RT-PCR** | Reverse-transcription polymerase chain reaction |
| **RU** | Response units |
| **s** | Seconds |

| | |
|---|---|
| **SAAC** | Single amino acid chelate |
| **SC** | Subcutaneous |
| **SDF-1** | Stromal-derived factor 1 |
| **SLB** | Surgical lung biopsy |
| **SLC** | Small latent complex |
| **SPECT** | Single photon emission computerised tomography |
| **SPR** | Surface Plasmon Resonance |
| **SSTR** | Somatostatin receptor |
| **SUV** | Standardised uptake value |
| **TAC** | Time-activity curve |
| **TBR** | Target-to-background ratio |
| **TGF-β** | Transforming growth factor beta |
| **TGF-βR** | Transforming growth factor beta receptor |
| **TMB** | 3,3',5,5'-Teteramethylbenzidine |
| **TNF** | Tumour necrosis factor |
| **UIP** | Usual Interstitial pneumonia |
| **US** | Ultrasound |
| **UV** | Ultraviolet |
| **VEGF** | Vascular endothelial growth factor |
| **WHO** | World Health Organisation |

## List of Figures

## List of Tables

## List of Equations

**Acknowledgements**

Firstly, I would like to thank Hull York Medical School for providing me with the opportunity to study for my PhD in Medical Sciences. I would also like to thank my PhD supervisors, Dr Simon Hart, Dr Christopher Cawthorne and Professor Steve Archibald, as well as my Thesis Advisory Panel Chair, Professor Alyn Morice, all of which have guided me throughout the PhD and given me increased confidence in my ability and for providing me with opportunities from which to expand my skillset. In particular, I would like to thank Dr Chris Cawthorne for supporting me through my undergraduate research project and for introducing me to the world of molecular imaging. Thank you all for your support, both professionally and personally in both good and difficult times.

I wish to thank Dr Juozas Domarkas, the associated postdoctoral associate involved with this project, for his never-ending help with chemistry-related issues, his endless supplies of coffees in the postdoc office, and for his support throughout the entire PhD, without which, this research would not have been possible.

I would like to give a special thanks to all of the friends I have made along the way, in both fellow PhD students as well as technical staff. A special thanks goes to (Dr!) Cecilia Miranda and (Dr!) Rhiannon Lee for their fantastic support, both professionally and personally. Your company made the time spent in the labs and PET centre more enjoyable. To Brittany, Hannah, Ellie, Cordula, Anne, and many others, I thank you all for the countless number of Costa coffees and your company throughout my studies when times have been difficult.

To my family, Mum, Dad, Hayley, Michael and Mamma. You have always been there for me at the drop of a hat and helped me with everything I have needed in any way you can. In particular, I thank my Dad for teaching me the importance of both working hard, and enjoying your work. Your own work ethic was unparalleled and has inspired me to always work harder to achieve my goals, no matter what obstacles may be in the way.

To my wife, Sophie, thank you (and Betsy!) for putting up with me throughout these PhD years and for your endless support and encouragement at home, and for moving half way up the country to an unknown city to be with me while I studied. Without your moral support, this PhD would have been incredibly more difficult, even impossible. I'm sorry it took this long but we can now see the light at the end of the tunnel. Your patience knows no bounds, I will be eternally grateful to you for it.

**Dedication**

This thesis is dedicated to the memory of my father, who died of bowel cancer in May 2016.

**Author's Declaration**

I confirm that this work is original and that if any passage(s) or diagram(s) have been copied from academic papers, books, the internet or any other sources these are clearly identified by the use of quotation marks and the reference(s) is fully cited. I certify that, other than where indicated, this is my own work and does not breach the regulations of HYMS, the University of Hull or the University of York regarding plagiarism or academic conduct in examinations. I have read the HYMS Code of Practice on Academic Misconduct, and state that this piece of work is my own and does not contain any unacknowledged work from any other sources

# Introduction

# 1 Introduction

## 1.1 Molecular Imaging

A wide array of imaging modalities exist that can be used in both clinical and pre-clinical settings for diagnostic and patient management purposes as well as research. With each differing imaging methodology, there are both advantages and disadvantages with regards to their use.

Molecular imaging techniques can be divided into three categories; anatomical, functional and molecular imaging. All imaging modalities can be used to provide information about a patient that could be classified by more than one of these types of imaging. For example, computed tomography (CT) imaging is commonly used for anatomical imaging of broken bones but can also be used as a method to assess gut content movement, which would be classed as functional imaging. Magnetic resonance imaging (MRI) can be used for the anatomical imaging of tumour structures, or functionally as diffusion weighted MRI to determine tumour vessel leakiness. Positron emission tomography, a nuclear imaging technique, is most often used for metabolic imaging of tumours using the commonly used 2-deoxy-2-[$^{18}$F]fluoroglucose (FDG), but PET can also be used for molecular imaging purposes to identify/classify features of a tumour, such as oestrogen receptor (ER) positive tumours in an ER-positive breast cancer patient with metastases. Functional and molecular imaging is defined by the society of nuclear medicine and molecular imaging (SNMMI) as "*the visualization, characterization, and measurements of processes at the molecular and cellular levels in humans and other living systems*." Most anatomical imaging is performed using mainly endogenous information, using methods such as ultrasound, CT or MRI, but are also able to utilise exogenous agents such as contrast agents, for clearer definition of aspects of the anatomy such as the intestines. Functional imaging, on the other hand, requires the administration of exogenous agents such as radioactive molecules, termed radiotracers or radioligands, which are biologically relevant molecules that have been modified to incorporate a radioactive isotope for the purposes of detection. Radiotracers can be used to

report on the rates of biological processes such as glycolysis, with FDG, the most commonly and clinically used PET imaging agent, as an example. Radioligands, however, are analogs or receptor-specific ligands, which are capable of binding to a receptor that may be implicated in various pathologies such as cancer, a good example being the radioligand [$^{68}$Ga]-Prostate-specific membrane antigen ([$^{68}$Ga]-PSMA), which is used for the detection of prostate cancer. The recent advancement of imaging technologies has had a significant impact on the potential of molecular imaging modalities to play a much larger role in not only diagnostic applications in the clinic, but to also allow for improved patient management through accurate characterisation of disease in individual patients, leading to an era of personalised medicine. As well as imaging, genomics techniques have also progressed in recent years towards this goal of personalised medicine, with DNA sequencing and epigenetic processes thought to give valuable information of the diseased state [1]. However, there is a recognised heterogeneity not only between different tumours, but also within the same tumour [2], and a study has revealed that two-thirds of the mutations found in a single biopsy were not detected in all samples taken from different regions of the same tumour [3]. In such a case, imaging has the potential to help non-invasively characterise this intratumour heterogeneity within the entire tumour. Both imaging and genomics technologies should ideally be used in synergy to maximise the amount of information available for clinicians to make effective decisions regarding diagnosis and therapeutic intervention for patients. Not only does imaging have the potential to assist clinicians with diagnosis and management, but it also has applicability in the drug discovery research sector, allowing the evaluation of both pharmacokinetics (PK) and pharmacodynamics (PD) of novel therapeutic agents.

### 1.1.1 Nuclear imaging

As functional imaging techniques, such as SPECT and PET are able to non-invasively provide detailed information with regards to metabolism and receptor expression, this project will focus on the use of nuclear imaging for the

visualisation of receptors that may be exploited as biomarkers for cancer and idiopathic pulmonary fibrosis (IPF).

Within nuclear medicine, the two most widely used techniques are SPECT and PET that both have their advantages, as well as disadvantages, in their use in clinical and preclinical applications, which will be discussed here.

#### 1.1.1.1 SPECT

SPECT imaging uses radiotracers or radioligands that are labelled with a single-photon emitting isotope. These isotopes emit a single gamma-ray photon with each occurring decay event [4]. A collimator is used in order to generate an image, which is produced following the selection of gamma rays that travel within a small angular range within the channels of the collimator (Figure 1). If the gamma rays are outside this angular range, they are either blocked by the collimator or miss the collimator completely. Gamma rays that successfully travel through the collimator will hit a scintillator that utilises the energy from the gamma rays to produce optical wavelength photons that are detected by photomultiplier tubes (PMT). These detections are then organised into histograms that allow reconstruction of an image [4].

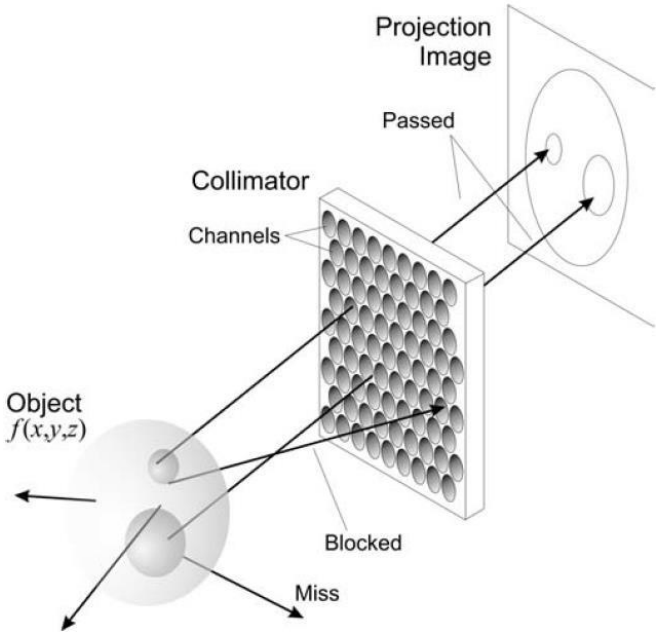


**Figure 1. A collimator forming an image of an object using SPECT. [1]**

#### 1.1.1.2 PET

PET involves the administration of compounds that are labelled with positron-emitting radioisotopes for the visualisation and quantification of biological functions within the body. PET works by the detection of positron emission. As radionuclides are unstable proton-rich atoms, positron decay takes place whereby a proton in the nucleus is converted into a neutron leading to the emission of a positron (β+) with a neutrino (v). This emitted positron traverses a distance dependent upon its positron energy, which may differ between radionuclides, before colliding with an electron (Figure 2). This collision, also known as the annihilation event, produces two equal and opposite gamma rays that radiate 180$^{o}$ from the point of annihilation towards a ring of detectors that surround a subject [5]. This opposite trajectory, known as the line of response (LOR), of two gamma rays allows for electronic collimation, whereby detectors in a PT camera generates a timed pulse when it detects an incident photon. When these pulses are combined, any 2 pulses that fall within a short time wndow are deemed coincident and therefore providing positional information.

Other than PET, many other imaging modalities exist, and are used for various clinical applications, such as magnetic resonance imaging (MRI), ultrasound (US), computed tomography (CT) and x-ray. All of these techniques provide healthcare professionals detailed anatomical images, providing information with regards to the various structures within the body. PET, on the other hand, not only provides detailed anatomical images when paired with CT, but is able to give an insight into the tissue biochemistry as well as the PK distribution of various drug candidates [6, 7]. Information with regards to tissue biochemistry and metabolic function revealed by PET has the potential to identify chemical changes that may occur during disease development before evidence of macroscopic anatomical changes becomes apparent [8, 9]. If a potential, or existing, drug were to be radiolabelled with a positron-emitting isotope, basic PK parameters may be assessed with the caveat that the doses of radioligand administered may differ significantly to the administered dose of therapeutic agent and thus give different results and also the addition of a radionuclide, outside of carbon-11 labelling, may potentially alter the drug properties. A useful application for PET radioligands is in the quantification of receptors and the determination of drug occupancy of these receptors.

**Table 1. Common radionuclides used in PET imaging detailing their half-lives, the nuclear reaction used for their production, decay products and their mean range in water [10].**

| Radionuclide | Half-life (min) | % Positron Emission | Production | Range in Water (mm) | Decay Product |
|---|---|---|---|---|---|
| **$^{15}$O** | 2.04 | 99.9 | Cyclotron: $^{15}$N(d,n)$^{15}$O | 1.5 | $^{15}$N |
| **$^{11}$C** | 20.4 | 99.7 | Cyclotron: $^{14}$N(p,α))$^{11}$C | 3.8 | $^{11}$B |
| **$^{68}$Ga** | 67.7 | 88 | Generator $^{68}$Zn(p,n)$^{68}$Ga | 2.9 | $^{68}$Zn |
| **$^{18}$F** | 109.8 | 97 | Cyclotron: $^{18}$O(p,n)$^{18}$F | 0.6 | $^{18}$O |

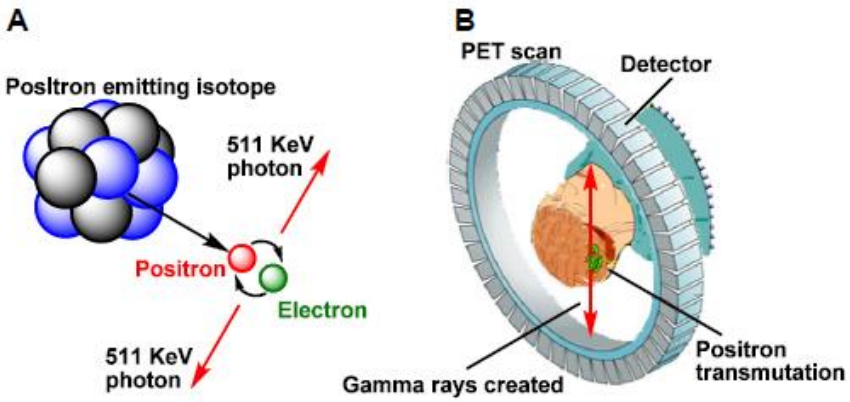


**Figure 2. (A) A positron and an electron annihilate producing two 511 -keV photons travelling in opposite directions. (B) The 511 keV photon was registered by the circular gamma ray detector array in the PET camera. [2]**

This detection of radiation allows the localisation of a radiotracer, such as fluorine-18 ($^{18}$F) carbon-11 ($^{11}$C), gallium-68 ($^{68}$Ga) as well as others, within the

body to be tracked [8]. The tomographic reconstruction of the events detector by the ring of detectors allows the generation of three-dimensional (3D) images that are able to show the radioactivity distribution and the concentration of radiotracer within a specific region of a subject. Various radioisotopes, with different half-lives, percentage positron emission and positron energy, are commonly used in PET, both non-clinical and clinical environments.

#### 1.1.1.3 SPECT vs PET

#### 1.1.1.4 Sensitivity

With regards to the sensitivity of SPECT and PET, that is the ability to detect emitted events, PET is more sensitive than SPECT as a result of the use of collimators in SPECT [11], which reject photons that are not within a small angular range, leading to a large percentage of photon rejections. On the other hand, PET uses a coincidence detection method, which allows a much larger angle of acceptance at each detector position, leading to increased percentages of detected emission events in PET.

This gain in sensitivity in PET allows for improved image quality, the possibility of (1) carrying out shorter scans, (2) multiple field-of-view scanning as a result of shorter scan times as scans in multiple positions can be carried out in reasonable time, and (3) improved temporal resolution as a result of being able to acquire shorter frames in dynamic studies, during which images are acquired continuously for a specified period of time, and therefore more frames, leading to improved capacity to study dynamic biological processes *in vivo*.

#### 1.1.1.5 Spatial Resolution

The spatial resolution in SPECT is generally limited by technological capabilities, such as collimator design, whereas in PET imaging, there are other factors that have an effect on reduced spatial resolution compared to SPECT imaging. These factors include positron range and photon non-collinearity.

Positron range is different dependent upon the radionuclide being used, and their energies (Table 1). Positron range describes the distance to which a positron traverses in the surrounding medium before its annihilation event with an electron. If the positron range is relatively large, then the annihilation event detected by the PET camera will not strictly be identical to the position of the radiotracer or radioligand, which contributes to reduced spatial resolution. Efforts have been made, however, to reduce the positron range of radionuclides in order to improve this spatial resolution, through the application of magnetic fields (58, 59).

The net momentum of an emitted positron is non-zero, which leads to, as a result of the conservation of momentum, slight deviations from the $180^{o}$ trajectories of the gamma rays produced from the annihilation event (Figure 3). This can lead to blurring, and thus reduced spatial resolution, of a PET image and the extent of this blurring is greater with an increased radius of the detector ring as the LOR would be positioned further away from the annihilation event, with regards to absolute distance, as a result of increased ring diameter.

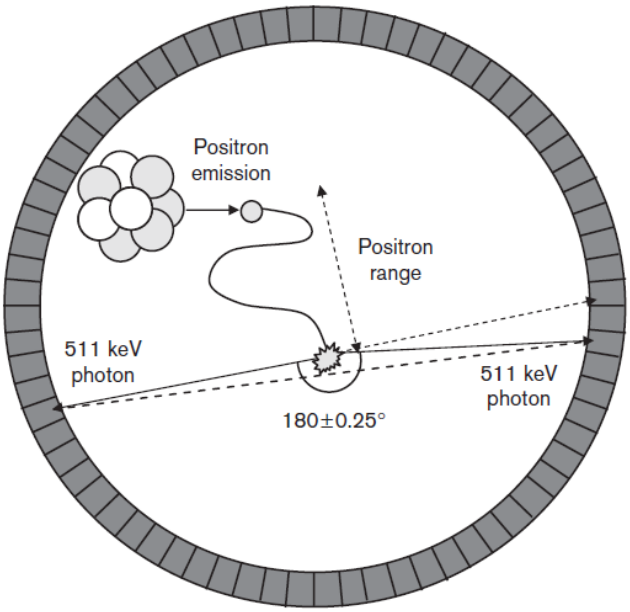


**Figure 3. Depiction of the finite positron range and the non-collinearity of the annihilation photons inherent to the positron-electron annihilation process which give rise to an inherent positional inaccuracy not present in SPECT.**

#### 1.1.1.6 PET Radionuclides

The SI unit that represents radioactivity is the Becquerel (Bq) which represents a single nucleus disintegration per second (dps). The radioactive half-life of a radionuclide is described as the time required for radioactivity present to reduce by 50%. Different radioisotopes have varying half-lives, which may make them useful or unsuitable as clinical PET radionuclides, dependent upon the targeting moiety they are associated with. For example, the use of antibodies as PET imaging agents requires isotopes with longer half-lives such as copper-64 ($^{64}$Cu) or zirconium-89 ($^{89}$Zr) due to the long biological half-life of antibodies, making shorter-lived isotopes unsuitable for antibody imaging unless certain methods, such as click-chemistry [12], are utilised. Alternatively, small molecules and/or small peptides, that may possess faster pharmacokinetics, may be suited to radioisotopes with shorter half-lives such as carbon-11 ($^{11}$C) or gallium-68 ($^{68}$Ga).

## PET Quantification

PET imaging is often used clinically in order to assist diagnosis and monitor response to therapy of various diseases such as cancer. In order to assess the amount of radiotracer accumulation in each area, such as a tumour, and to accurately compare that uptake to the uptake in other patients, or in the same patient following repeated scanning, accurate quantification of PET scans is required.

The uptake of a PET radiotracer is often referred to as the standardised uptake value (SUV), which is dependent upon several factors that may sometimes be difficult to compare across different centres, such as image acquisition and reconstruction as well as the length of time between tracer administration and scan start time [13]. The scintillator size in a preclinical scanner is reduced approximately three-fold, significantly improving spatial resolution, but the 2000 fold size difference between mice and humans makes it challenging to accurately image small structures.

SUV considers the concentration of radioactivity within tissues, whilst normalised against the injected radioactive dose and subject mass in order to express the radioactivity concentrations in the tissue as a percentage of the injected dose (Equation 1). This allows for the comparison of radiotracer uptake between different patients, or differences in the same patient after multiple scans.

**Equation 1. Standardised uptake value (SUV) for calculating PET radiotracer uptake in a region of interest.**

$$SUV = \frac{c(t)}{(injected\ dose\ (t_0)\ /\ body\ mass)}$$

If all the injected radiotracer is retained by the subject, and exhibits a uniform distribution throughout the body, the SUV value for any region of interest would equate to 1, irrespective of subject mass or injected dose. SUVs also assume that 1 ml volume of tissue equates to 1 gm. However, there are limitations of SUV that arise due to factors that make it difficult to compare between different

centres, including the time difference between radiotracer administration and scan, as well as image acquisition settings and image processing. The mean SUV value ($SUV_{mean}$) can be significantly affected by the variable definition of boundaries of the region of interest over which the average uptake is to be measured, with smaller objects being more affected by this than large objects. Another method for the quantification of radiotracer uptake is the use of maximum standardised uptake value ($SUV_{max}$). The use of $SUV_{max}$ has significantly improved reproducibility compared to $SUV_{mean}$, as the maximum value within a region of interest is not as significantly affected by small spatial shifts of the ROI as compared to $SUV_{mean}$. Therefore, the use of $SUV_{max}$ may assist in improving the variability of image quantification across different centres.

#### 1.1.1.7 Issues with PET quantification

##### 1.1.1.7.1 Metabolism

When introduced by intravenous injection, radioligands are subject to a variety of enzymes that may metabolise the radiotracer in different ways, producing radiometabolites. If metabolised, the radiometabolite may not necessarily reach the target of interest. Commonly, products of metabolism are more efficiently eliminated via hepatic or renal excretion. PET technology is unable to distinguish between the parent radiotracer and any potential radio-metabolites may be taken up non-specifically into various tissues such as the liver or spleen, which would lead to changes in overall SUV values, confounding imaging data. Therefore, it is important that the potential for radiotracers to produce radio-metabolites must be thoroughly tested *in vitro* prior to *in vivo* evaluation.

##### 1.1.1.7.2 ROI definition

In oncology, the definition of ROIs, specifically for tumours using $^{18}$F-FDG imaging, determines clinically reported parameters such as tumour size and aggressiveness through expression of SUV values, or the total proliferative volume

(TPF), which is defined as the product of SUV and tumour volume [14]. With radioligands that target a specific receptor, ROIs are used to determine the amount of receptor expression within a tissue or tumour. For consistency in ROI definition across multiple centres, robust approaches for reproducible tumour delineation are required. Currently, various methods for the delineation of tumours are in place, such as manual placement of an ROI across the entire tumour [15], manual placement of an ROI of fixed dimensions capturing the highest intensity signals within a tumour [16] and isocontour methods employing thresholds to allow for delineation from background tissues [17]. After comparison of these methods for ROI definition, it was found that isocontour methods were more reproducible, less user-dependent and more effective at assessing therapy responsiveness [18].

#### 1.1.1.7.3 Partial volume effect

The partial volume effect (PVE) refers to two things. First, is image blurring as a result of the limited spatial resolution of the scanner used, and second, is the fact that any voxel may contain different tissues, due to limited spatial resolution, and the measured signal intensity is expressed as the mean of the tissues within that particular voxel [19]. Typically in oncology, smaller and irregular shaped tumours are affected by PVEs to a greater extent compared to larger more regular sized tumours [19]. Because of this, small tumours may appear larger than they actually are but, more importantly, less aggressive than they actually are, as the intensity of signal within a single tumour will be averaged over a larger area, making the overall average signal in the tumour smaller. This is demonstrated in Figure 4 which shows various radioactive spheres of varying diameter, containing equal radioactivity concentrations. The partial volume effect is evident as the size of the sphere increases and the intensity of the signal decreases, despite the spheres containing the same concentrations of radioactivity. Due to the positron range of gallium-68 (approximately 2.4 mm) it may be difficult to both detect small lesions and resolve two lesions that may be close together, and should be a factor

to consider when performing small animal imaging [20], whereby positron range is the limiting factor in image spatial resolution. In the context of this project, the use of gallium-68, which has larger partial volume effects when compared to the commonly used fluorine-18, requires careful consideration with regards to activity quantification as partial volume effects may result in inaccurate SUV values, particularly in the lung whereby the distance travelled by positrons prior to annihilation will be greater than that of soft tissues due to the reduced density of the lung tissue [21].

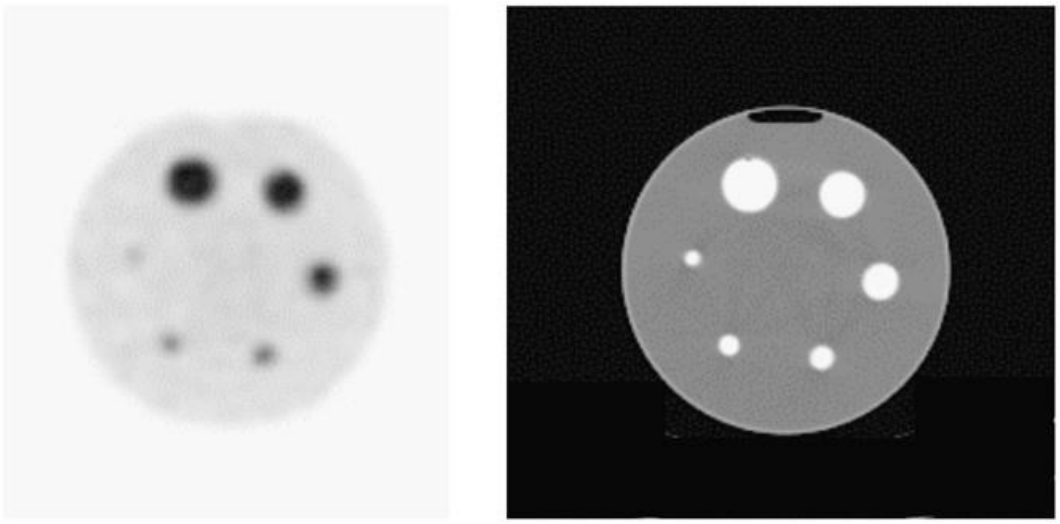

**Figure 4. Transverse PET slice of 6 radioactive spheres with different diameters and filled with same radioactivity concentrations (left) and the corresponding CT slice (right). [25]**

During the development of a radioligand for clinical use, it is important to determine the concentration of radiotracer that resides in tissue over time, in order to calculate the exposure limits. To do this, time-activity curves are plotted following dynamic PET/CT scan acquisition and the amount of radioactivity in various tissues may be determined via the integration of the curve. Several factors may have an effect on the total dose to each tissue, such as target specificity and metabolic stability of the radiotracer [22], as well as suitable pharmacokinetics and radioisotope choice. Radiotracers derivatised from small molecules and peptides

tend to have fast uptake and clearance rates, making them suitable for shorter-lived half-lives to allow for reduced subject exposure to radiation. Other molecules, such as antibodies, have pharmacokinetics that exhibit much slower uptake and clearance rates, making them unsuitable for short half-life isotopes such as fluorine-18 or gallium-68. Antibodies require longer lived isotopes, resulting in increased radiation exposure for the subject.

### 1.1.2 Molecular Imaging in Oncology

Cancer is one of the leading causes of death in the developed world, responsible for 25% of all deaths in the Western world and is also the second leading cause of death in developing countries. Due to advances in healthcare leading to an increasingly aging population, it is thought that the incidence of cancer will increase in the coming years.

Cancer may be defined by a group of cells that grow and divide uncontrollably in disregard of normal cellular division. In the healthy state, cells are constantly subjected to a variety of signals that dictate whether or not a cell should divide, differentiate or die via apoptosis. Cancer cells gain an ability to autonomously divide despite these signalling mechanisms, leading to uncontrolled growth and proliferation. If left unchecked, significant tumour growth may become apparent as well as the spread of these cancer cells to different tissues or organs in a process called metastasis, which is the cause of approximately 90% of cancer-related deaths [23].

Cancer arises from a transformation, or mutation, in the genetic code of a normal, healthy cell. This mutation, likely followed by successive mutations in other genes, leads to the uncontrolled proliferation of progeny [24]. Over time, a tumour can undergo various mutations that may provide the cell with a proliferative advantage, leading to clonal expansion of this cell and the progression of the resultant tumour [25]. This expansion by proliferating tumour cells and tumour progression can result in the eventual invasion through the

basement membrane barrier that surrounds tissues, allowing the tumour to spread to other tissues and organs.

The detection of cancer in patients has relied on the presence of specific biomarkers found in blood, urine, cerebrospinal fluid (CSF) and many others that are elevated with the occurrence of cancer. A biomarker is a "defined characteristic that is measured as an indicator of normal biological processes, pathologenic processes or responses to an exposure or intervention, including therapeutic interventions" [26]. Previous definitions of biomarkers have restricted biomarkers to biological molecules, excluding other potential features, obtained from imaging or other techniques, which could give valuable information and could extend the definition of a (bio)marker. [27]

Imaging techniques can be used to objectively measure various markers in diseases such as cancer. For example, anatomical imaging modalities, such as MRI, CT and ultrasound (US), can be used to detect features such as tumour size and morphology [28], whereas molecular imaging techniques, such as PET, and SPECT, are able to measure tumour features such as metabolic/enzymatic activity [29-33] as well as receptor expression [34-38]. These markers have the potential to be used in the screening, detection, staging, disease monitoring and responsiveness to therapy.

#### 1.1.2.1 Fluorodeoxyglucose (FDG)

Fluorine-18 labelled fluorodeoxyglucose ([$^{18}$F]FDG) is the most widely used PET imaging agent for the molecular imaging of cancer clinically. The use of this imaging agent for the detection of cancer is based on the Warburg effect, whereby tumour cells have abnormally high rates of glycolysis [39]. In instances whereby tumours have inadequate supplies of oxygen, they prefer to generate energy through anaerobic glycolysis and the conversion of pyruvate into lactic acid [40]. Cancer cells also exhibit increased expression levels of glucose transporters, such as glucose transporter 1 (GLUT-1), that allow the transport of glucose across the cell membrane along a concentration gradient.

FDG, an analog of glucose, is able to be transported into cells via GLUT-1 and is phosphorylated by hexokinase, but, due to the lack of a hydroxyl group at position 2, it cannot be metabolised further and is thus trapped within cells as FDG-6-phosphate [41]. When FDG is radiolabelled using fluorine-18, it may be used to clinically assess and quantify glucose metabolism [42]. As cancer cells generally exhibit increased rates of glycolysis, this provides the basis for imaging contrast of cancer cell detection.

Clinically, the use [$^{18}$F]FDG has been widespread due to its rapid blood clearance and efficiency of metabolism by hexokinase, which lead to high target-to-background ratios (TBR) for the detection of metabolically active tumours. There are also very few radiometabolites of [$^{18}$F]FDG, which simplifies the analysis of PET images generated as very little non-specific uptake is observed. Lastly, the half-life of the radioisotope used (~110 mins) allows the production of radioactivity at central facilities, of which there are approximately seven in the UK, and their transport to nearby nuclear medicine departments (ideally with a transportation time of less than one half-life).

#### 1.1.2.2 Role of [$^{18}$F]FDG in monitoring tumour response to therapy

[$^{18}$F]FDG is a useful tool for monitoring treatment efficacy throughout therapy regimens and for assessing treatment response following the end of treatment protocols [40, 43, 44], with various studies showing that early responses to therapy can be detected by FDG-PET, and this can lead to improved clinical outcomes such as extended disease-free survival [45-48]. This has also led to improved patient management with decisions being made to change therapy regimens, as a result of analysis of FDG-PET, with such changes including altered dose or therapy duration, switching to an alternative therapy or a change from therapy to supportive care [49]. The concept of early monitoring of treatment response is to assess therapeutic efficacy at earlier time-points than is possible by other means such as monitoring symptoms, in order to improve the quality of cancer patient management, and FDG-PET has been shown to be able to detect

response to therapy after a single cycle of chemotherapy [50-52] and even a single day after the chemotherapy initiation [53].

#### 1.1.2.3 PET imaging of cell proliferation

Aberrant cellular proliferation is a hallmark of cancer [23] and, as such, the detection in the reduction of aberrant cellular proliferation that occurs in cancer, can be used in order to detect response to cancer therapies . The decline of cell proliferation is one of the earliest changes that can be observed in response to therapy and both radio- and chemotherapy have been shown to reduce proliferation rates in cancer cells before a decline in tumour size has been observed [23, 54, 55], allowing for earlier measurement of therapeutic response compared to anatomical imaging such as CT imaging.

The main radiotracers that have been developed for imaging cellular proliferation have been based on synthetic analogs of thymidine, which is used by proliferating cells for DNA synthesis in the S-phase of the cell cycle. The most widely used radiotracer for imaging cellular proliferation is $^{18}$F-fluorothymidine ([$^{18}$F]FLT). The accumulation of [$^{18}$F]FLT in proliferating cells occurs by facilitated diffusion across nucleoside transporters and phosphorylation leads to trapping of [$^{18}$F]FLT within the cell. Due to the structure of [$^{18}$F]FLT, specifically the absence of a hydroxyl group at the 3’ position, it is not used in DNA synthesis and therefore accumulates in the cytoplasm, leading to increased PET signal in proliferating cells. However, it has been shown that [$^{18}$F]FLT exhibits activity in the bone marrow, liver and reactive lymph nodes, increasing the potential for false-positive cancer diagnoses [56-58].

#### 1.1.2.4 Other PET imaging agents in cancer

Even though radiotracers such as [$^{18}$F]FDG and [$^{18}$F]FLT are useful radiotracers for PET imaging of metabolism and proliferation, respectively, in cancer, they are often deemed to be quite non-specific and less useful for imaging tumours with low growth rates compared to other available imaging agents. There

has been considerable research carried out into the development of radioligands that target various receptors that are specifically expressed, or overexpressed in tumours, providing an alternative basis for providing image contrast in tumour detection.

Of these receptors, prostate-specific membrane antigen (PSMA) is a cell surface protein shown to be highly expressed in prostate carcinoma and multiple PET radioligands have been targeted to this receptor, including N-[N-[(S)-1,3-dicarboxypropyl]carbamoyl]-4-$^{18}$F-fluorobenzyl-Lcysteine ([$^{18}$F]DCFBC) and gallium-68-labelled conjugate (known as [$^{68}$Ga]$^{68}$GaPSMA, although it is a peptidic ligand that is labelled and not the antigen protein) , which have been found to detect prostate carcinoma and metastatic prostate cancer lesions [59, 60]. Another type of receptor, somatostatin (SST) receptors, which are overexpressed in neuroendocrine tumours, has been targeted for detection by PET radioligands. Currently, this receptor is imaged using SPECT, however PET-based radioligands are also in development such as $^{68}$Ga-DOTA-TOC, $^{68}$Ga-DOTA-NOC and $^{68}$Ga-DOTA-TATE, which are all able to bind SST receptor 2 (SSTR2) demonstrate enhanced sensitivity compared to their SPECT counterpart $^{111}$In-DTPA-octreotide [61]. These radioligands do differ, however, as they possess varying affinities for other SST receptors. Fore example, $^{68}$Ga-DOTA-NOC possesses good affinity for SST receptors 3 and 5, and $^{68}$Ga-DOTA-TOC also possesses good affinity, albeit to a lesser degree than $^{68}$DOTA-NOC for SST receptor 5.

By targeting specific cancer-associated antigens, it is not only cancer detection that may be achieved, but also the selection of appropriate therapy for a given patient based on receptor status may be decided upon. Many cancer therapies exist that target specific receptors or enzymes in cancer cells, and therapeutic targets, such as estrogen receptor (ER), HER2 and angiogenesis, may also be targeted using targeted PET imaging agents that can assist in establishing receptor status of tumours which can often be heterogeneous [3, 62], in order to select therapies most likely to be effective. Current examples of this use of PET

include ER, progesterone receptor (PR) androgen receptor (AR) and HER2 receptor imaging [63-66].

#### 1.1.2.4.1 PSMA-PET

An emerging application of PET imaging is the targeting of the prostate-specific membrane antigen (PSMA) using the radioligand [$^{68}$Ga]HBED-CC for the detection of prostate cancer. PSMA is a transmembrane protein that is expressed in prostatic tissues, with increased expression being associated with malignancy [67]. Interestingly, the majority of prostate carcinomas show elevated PSMA levels in both primary and metastatic tumours [68, 69] and the level of expression has been shown to be a good prognostic indicator of disease outcome [70].

### 1.1.3 Peptides as PET Imaging and Radionuclide Therapy Agents

Peptides, generally less than fifty amino acids in length, have become an increasingly popular tool for the development of novel PET imaging agents, partly due to their ease of synthesis, and their generally high affinity and specificity for their target receptor in diseased organs or tissues [71, 72]. Given their size and specificity for their targets, peptides have desirable *in vivo* pharmacokinetics and specific tumour uptake. Not only are they found to be useful candidates in the development of PET imaging agents, there has been growing interest in their use as peptide receptor radionuclide therapy agents, targeted moieties that are coupled to a radionuclide emitting ionising radiation for the treatment of tumours.

Peptide receptor radionuclide therapy (PRRT) is a form of molecular targeted therapy that utilises a peptide labelled with a radionuclide that emits ionising radiation which will be absorbed by cells or neighbouring tissue, such as lutetium-177 ($^{177}$Lu), yttrium-90 ($^{90}$Y) and various others (Table 2). These radionuclides have different energetic emissions such as α particles, $\beta^-$ particles, Auger electrons and conversion electrons [73, 74]. Coupling of these radionuclides

to vectors that are able to target tumour-specific molecules, has given rise to a group of potential targeted cancer therapies that are able to specifically target diseased tissues whilst limiting the ionising effects on healthy tissue, dependent upon the binding efficiency of the targeting vector [75, 76]. The successful ablation or damage targeted towards the diseased tissues, such as tumours, greatly relies on the choice of targeting vector and its ability to bind to its intended target in the diseased state *in vivo*. The use of PRRT has shown encouraging results in the treatment of different cancers including, but not limited to, neuroendocrine tumours (NETs) [77, 78].

**Table 2. List of radionuclides often used for radionuclide therapy [74, 79]**

| Radionuclide | Half-life | Emissions | Mean Energy (MeV) | Production |
|---|---|---|---|---|
| **Actinium-225** | 240.2 h | α (100%) | 5.7 | Generator ($^{229}$Th → $^{225}$Ac) |
| **Yttrium-90** | 64.8 h | $\beta^-$ (100%) | 2.2 | Generator ($^{90}$Sr → $^{90}$Y) |
| **Lutetium-177** | 160.8 h | $\beta^-$ (100%) | 0.5 | Nuclear Reactor |
| **Iodine-131** | 192.0 h | $\beta^-\gamma$ (89%) | 0.7<br>0.4 | Nuclear Reactor |
| **Copper-64** | 12.7 h | $\beta^-$ (61.5%) | 0.65 | Cyclotron |
| **Copper-67** | 61.9 h | $\beta^-$ (100%) | 0.4 | Cyclotron |

There has been a large progression in the development of various radionuclide therapy agents over recent years. The use of peptides as targeting vectors is increasingly popular due to their specificity for a range of receptors that are expressed at high levels in many cancer types and typically have high affinity for their targets. Also, due to their relatively small size, they exhibit rapid pharmacokinetics and are able to penetrate into tumours effectively. Preferably, the targeting peptide moiety would act as an agonist of its cognate receptor, possessing the ability to, after binding to receptor, be internalised to a high degree by receptor-mediated endocytosis, allowing a gradual accumulation of the PRRT agent within the target cell [80, 81]. Peptides that demonstrate antagonistic

behaviour, have minimal to no internalisation, due to the action of receptor-mediated endocytosis being blocked by the peptide antagonist. However, contrary to this, there are studies that have shown that despite this minimal internalisation of peptide antagonists, these antagonists tend to have higher affinity for their cognate receptor relative to peptide agonists, resulting in increased tumour uptake, as demonstrated with somatostatin receptor (SSTR)-targeting peptides [82, 83] and the gastrin-releasing peptide (GRP) hormone receptor [84], potentially due to a higher number of occupied binding sites of the receptor by the antagonist, with prolonged dissociation rates from the receptor.

An important aspect of radionuclide therapy agent development is to establish the absorbed dose a patient receives following administration of a radionuclide therapy agent. Knowing what the absorbed dose to a patient will be is important for several reasons, including the establishments of dose limits and determining treatment schedules. A key aspect of dosimetry of a radionuclide therapy agent is to determine the absorbed dose to individual organs, which depends upon different factors such as radioligand properties, location of the radioligand target, and excretion route of the radioligand, which is typically renal or hepatobiliary. With respect to PRRT, the majority of molecules are excreted renally [85, 86], understanding dosimetry is vital in minimising renal toxicity, ensuring the absorbed dose does not exceed a safe threshold. Molecular imaging is able to play a useful role in the establishment of dosimetry profiles for radionuclide therapy agents.

In addition to its uses for dosimetry purposes, PET imaging can, importantly, be used as a method to select patients that are likely to respond to PRRT, through the use of companion diagnostic devices (CDDs) CDDs are defined, by the FDA as an “an imaging tool that provides information that is essential for the safe and effective use of a corresponding therapeutic product”. Essentially, a targeted peptide coupled with a positron-emitting isotope may be used to select patients who are most likely to respond to radionuclide therapy using an identical targeted moiety couple with a therapeutic isotope such as lutetium-177 or

yttrium-90 [87-89]. A good example of a theranostic approach is the repurposing of somatostatin analogs that are radiolabelled with gallium-68 [90] via a conjugated DOTA chelating molecule for PET imaging. This compound can be switched to act as a therapeutic for treatment of NETs by swapping the gallium-68 for lutetium-177 (DOTA is capable of forming a stable chelate complex with either gallium-68 or lutetium-177[91], making these two isotopes an ideal theranostic pairing).

### 1.1.4 Molecular Imaging in Idiopathic Pulmonary Fibrosis

#### 1.1.4.1 General Background

Idiopathic pulmonary fibrosis (IPF) is described by the American Thoracic Society and the European Respiratory Society as a specific form of chronic, progressive fibrosing interstitial pneumonia of unknown cause, occurring primarily in older adults, limited to the lungs, and associated with the histopathologic and/or radiologic pattern of usual interstitial pneumonia (UIP) [92]. A UIP pattern may be characterised, radiologically, by reticular opacities with little to no ground-glass opacification. There is also pronounced honeycombing shown as subpleural, clustered cystic airspaces surrounded by defined walls, crucial for IPF diagnosis [93]. The histological characterisation of UIP features a heterogeneous appearance with fibrotic airspaces filled with inflammatory cells and alternating areas of lung that appear normal and areas of lung with extensive fibrosis. The presence of fibroblastic foci, found amongst a background a collagen, represents active fibrosis [93].

The prevalence of IPF is increasing in the UK with >5000 cases being diagnosed annually with recent estimates finding the incidence of IPF in the UK to be 7.44 per 100,000 person-years [94]. IPF leads to the irreversible destruction of pulmonary architecture as a result of fibrogenesis, causing gas-exchange disruption, respiratory deficit and eventually respiratory failure and death. Prognosis for IPF patients is poor, with death occurring within 5 years for most patients.

#### 1.1.4.2 Diagnosis

IPF diagnosis is challenging, and achieving a uniform diagnosis among multiple physicians proves difficult [95] as there are a number of conditions, besides IPF, that are associated with a UIP pattern, such as asbestosis, rheumatoid arthritis and Hermansky-Pudlak Syndrome [92]. Therefore, patterns of UIP are not synonymous with IPF, meaning that diagnosis of IPF requires elimination of all other possible diseases, which can be time-consuming. Currently, IPF diagnosis is achieved through collaboration between a multidisciplinary team, which would include chest physicians, radiologists and pathologists, who test against diagnostic criteria required for a definite diagnosis of IPF [96].

IPF diagnosis, according to international guidelines, requires the exclusion of other known causes of interstitial lung disease, the presence of a UIP pattern as shown by high resolution computed tomography (HRCT) in patients that have not undergone surgical biopsy and specific combinations of HRCT and surgical biopsy patterns in patients that have undergone surgical biopsy [97].

A final diagnosis of IPF can be achieved from 6-24 months following the initial onset of symptoms [98]. There is an increasing need for improved and more sensitive diagnostic tests for IPF to aid the earlier detection of the disease and to enable improved patient management.

There is an urgent need for molecular biomarkers that can help clinicians understand disease mechanisms, assist in the development of effective novel therapies and improve clinical management of IPF patients. Currently, the main end-points used to characterise IPF patients are features such as patient history, lung function tests, histopathology and radiology, however these may not accurately relate to potential disease mechanisms, making it difficult to categorise patients into groups, such as those with aggressive, progressive disease, for better patient management. Currently, no molecular biomarkers have been fully validated in the clinical setting for IPF, and the development of such a biomarker would be useful for the identification of patients at risk of developing IPF, effective diagnosis of IPF and evaluating baseline IPF patient prognosis and disease stage and severity.

Despite the current methods used to assist in the diagnosis and management of IPF patients, none of these methods can reliably predict either treatment response or disease behaviour and progression. The use of reliable prognostic and therapeutic molecular biomarkers that would allow for such prediction of disease behaviour would allow clinicians to stratify patients for treatment and also administer aggressive therapeutic regimens in order to prevent or ameliorate acute exacerbations associated with the disease. Potentially, novel imaging methods may be able to address this unmet need.

#### 1.1.4.3 Imaging

It is well known that high-resolution computed tomography (HRCT) is a crucial element for the diagnosis of IPF, however its use in diagnostics is not always easy, due to the heterogeneity of presentation of IPF and also because agreement between radiologists is moderate at best [99].

A typical characteristic of IPF is honeycombing of the lung (Figure 5; [97]), which is described by the Fleischner Society as having "*clustered cystic air spaces, cysts of comparable diameters, and cyst diameters typically <10 mm surrounded by well-defined walls*" [100]. The distribution of honeycombing in UIP, when visualised by HRCT, is predominantly basal and peripheral. Despite various definitions that describe the appearance of honeycombing, interpretations of honeycombing from HRCT scans are often subjective, with some disagreement regarding its features. A study by Watadani *et al.* showed that, with 43 observers studying and rating 80 HRCT mages, in 29% of cases there was disagreement on the identification of honeycombing. One of the factors that may have contributed to this disagreement is the ability to differentiate between honeycombing and traction bronchiectasis. Another example in which honeycombing may be difficult to identify is in patients with emphysema. As stated by the Fleischner Society, honeycombing consists of clustered cystic air spaces surrounded by well-defined or thick-walled, subpleural and parallel to the chest wall, whereas emphysema is considered to be thin-walled with cystic air spaces located larger distances away from the chest wall [101].

Not only has HRCT been used in an attempt for disease prognostication, but it has also been used in order to monitor IPF disease progression to identify temporal changes over the time-course of the disease. It has been shown that for serial scans, taken over the course of two years, significant progression of honeycombing was detected whilst significant reduction in ground-glass opacities was observed [102]. Quantitative analysis of HRCT have also been shown to have potential in identifying probably diagnosis, stratification of prognosis in early disease stages and in the determination of disease progression or response to therapy [103].

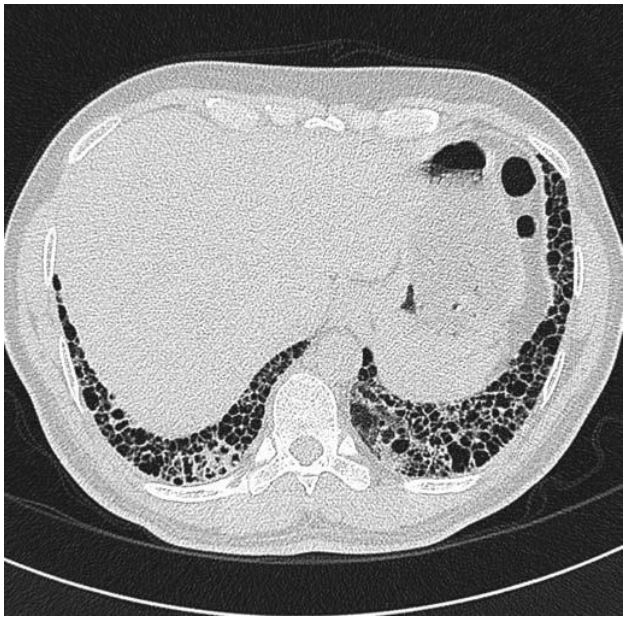

**Figure 5. High resolution computed tomography scan showing typical appearance of usual interstitial pneumonia [144]**

Modalities other than HRCT are being increasingly used in the detection of IPF, such as positron emission tomography (PET). Various different targeted PET imaging agents that target molecules associated with IPF progression, such as the αvβ6-binding peptide A20FMDV2 [104] and a collagen binding peptide [105, 106], are being developed pre-clinically in order to detect the early onset of IPF as well as use imaging as a marker of therapy response in order to improve patient management [105], which will be expanded upon later.

#### 1.1.4.4 Surgical Lung biopsy

When IPF diagnosis cannot be achieved by clinical or radiological studies, which occurs in approximately a third of cases surgical lung biopsy (SLB) is needed [107]. The use of histological data, when collated with clinical and radiologic data, improves agreement between clinicians, radiologists and pathologists [108].

Several drawbacks of SLB exist, however. The procedure of a lung biopsy is incredibly invasive and is itself associated with a risk of mortality 30 days post-surgery [109], usually caused by an exacerbation of IPF, characterised by diffuse alveolar damage superimposed on UIP [110]. Generally, the risk factors of mortality within 30 day days of the surgical lung biopsy were the presence of acute exacerbation at the time of biopsy, which in one study increased mortality from 3% to approximately 29% [111], low diffusion capacity (DLCO), mechanical ventilation and an age over 67 years.

Much like with the interpretation of honeycombing in HRCT images, there is variability between pathologists when observing lung biopsy samples with only some agreement on diagnosis from pathologists who had been given minimal clinical information regarding the patients [112]. Biopsies, as with HRCT, may potentially be used not only for diagnostics, but for prognostic purposes, with the number of fibroblastic foci being shown to correlate with patient survival in some [113-115], but not all [116], studies, but the counting of these foci is yet to be integrated into routine clinical practice due to the variability in evaluation of biopsy samples.

With SLB required in approximately a third of patients, and the associated risk of mortality 30 days post-surgery, the number of patients that may not undergo SLB due to underlying factors that would increase their risk of mortality such as exacerbation of IPF at the time of surgery, fast decline in lung function, or simply the patient's age, present an unmet need for a sensitive, non-invasive technique that may be used in conjunction with radiological and clinical information to assist with IPF diagnosis in a more accurate and uniform way.

#### 1.1.4.5 Pathogenesis of Fibrosis

"Idiopathic" suggests that IPF has no known cause. However, studies have suggested strong associations exist between IPF and smoking and metal or wood dust exposure [117, 118]. Currently there is widespread recognition that IPF results from repeated injury to lung epithelial cells caused by exposure to various potentially harmful agents such as cigarette smoke, dusts, viral infection, environmental toxins, chemotherapy and more. This combined with a genetically predisposed person may induce the activation of abnormal pathways, leading to an out of control wound healing response [119].

Despite the gravity of this disease, the amount of research dedicated to clinical trials and the advancement towards effective treatments has been much less than with other diseases such as cancer. As a result of this, very few treatments have achieved the transition from bench to bedside and there is still an absence in effective treatments that can alter the disease course. For patients who fail to respond to therapy and have progressed to an advanced stage of IPF, lung transplantation represents the only option [120, 121]. However, the 5-year survival rate (47-53%) is still quite poor, with challenges arising due to infections and neoplasms [120, 121], co-morbidities such as heart failure and osteoporosis, which may be exacerbated by lung transplantation [120, 121], chronic lung allograft dysfunction (CLAD) and the recurrence of IPF in the graft, which although rare, has been observed [122].

Generally, treatment with N-Acetylcysteine (NAC), pirfenidone, immunosuppressants or glucocorticoids had been the conventional approach for IPF patients. NAC has anti-oxidant properties and is used in an attempt to treat oxidant/anti-oxidant imbalance that is recognised as a mechanism of alveolar epithelial cell (AEC) injury, however this treatment has had no impact on IPF patients [123].

A clinical trial, named PANTHER (NTC00650091), investigating the effects of a combination therapy (azathioprine, Prednisone, NAC) versus NAC alone versus placebo, in IPF patients was carried out. An interim analysis of this study found

that patients within the combination therapy cohort had increased mortality and hospitalisation rates compared with those of the placebo group, and the combination therapy group was terminated [124]. The NAC group was continued, although no improvements were observed compared with the placebo group [123]. This triggered a change in the routine treatment of IPF, as it was deemed that immunosuppressive regimens that include steroids should not be used.

Pirfenidone, a synthetic molecule, is an oral antifibrotic drug that has been assessed for treatment of IPF in phase 3 clinical trials. Although it has been shown to reduce the rate of decline in FVC and increase progression-free survival [125], it has been unable to change the disease course. Pirfenidone has been shown to regulate the activity of the pro-fibrotic cytokine transforming growth factor (TGF) β and tumour necrosis factor (TNF) α *in vitro* and inhibit the proliferation of fibroblasts as well as collagen synthesis [126-130] , was clinically tested as part of the CAPACITY trial (NCT00287729 and NCT00287716) [131] and shown to reduce the rate of decline in lung function of patients with IPF.

More recently, nintedanib, has been approved for the treatment of IPF [132] and has been shown to reduce the rate of lung function decline in IPF patients, albeit having little effect on symptoms such as breathlessness and cough. Nintedanib works through the inhibition of the receptor tyrosine kinases fibroblast growth factor receptor (FGFR), vascular endothelial growth factor (VEGF) receptor and platelet-derived growth factor (PDGF), which are involved in pathways known to be implicated in fibrosis development [133], such as fibroblast migration, fibroblast transformation and deposition of ECM constituents [133-135]. Through the inhibition of these processes, it is thought that a reduction of lung stiffening, and thus reduction in lung volume decline occurs [133]. Clinically, nintedanib has been tested in three trials; TOMORROW and the INPULSIS trials, which consist of two international phase III trials. These trials revealed that nintedanib reduced the rate of disease progression in IPF patients.

Despite the markedly improved knowledge about the mechanisms involved in the pathogenesis of pulmonary fibrosis, and the large number of anti-

fibrotic drugs being investigated and described pre-clinically, the translation of these compounds from pre-clinical to clinical studies has been lacking, in part due to the difficulties faced with recapitulation of the disease *in vivo*. Various methods exist that try to mimic IPF exist, and will be discussed later, but their ability and suitability to reliably mirror the disease phenotype is highly debated.

#### 1.1.4.6 Management of IPF

The heterogeneous nature of IPF makes it a condition that is difficult to manage due to variability in the disease course. There is a considerable asymptomatic period at the disease onset and patients only seek medical attention once the disease has reached a severity whereby lung fibrosis reaches a point that is enough to induce symptoms. From this point, patients may, most commonly, embark upon a slow clinical and functional decline. Of these patients with slowly progressing IPF a small percentage of them undergo acute exacerbation episodes, described as acute clinical deterioration, in the absence of infection, heart failure or other causes [136, 137], that may induce the terminal phase of the disease course. Patients that do not undergo slow progressive disease may experience either a rapid progression of fibrosis leading to a short illness duration before death or a combined IPF and emphysema diagnosis that may often be seen in heavy smokers. There has been significant effort in researching suitable biomarkers that can be used to monitor the progression of the disease or the response a patient may have to therapy [138, 139]. The validation of such biomarkers, able to both identify both the stage and aggressiveness of IPF at the time of diagnosis would help improve the accuracy of patient prognostication, as well as selection of patients most likely to respond to novel anti-fibrotic drugs and monitor their response to therapy. The most widely used modality for imaging IPF today is high-resolution computed tomography, however this is unable to give enough information with regards to pathogenesis, disease severity, or likely response to therapy. Neither is it able to easily distinguish between IPF patients who are experiencing life-threatening acute fibrosis and those who may be more

stable. An aim of this study is to develop a PET imaging agent that can target the integrin αvβ6, which, as will be discussed later, is upregulated in the fibrotic response, as well as various other pathologies including many cancers.

A reliable biomarker capable of not only identifying IPF but allowing more accurate prognostication and monitoring of disease progression may allow for improved stratification of patients to enable clinicians to identify patients undergoing rapid disease progression, that are in need of more aggressive therapy as well as identifying patients that do not respond to therapy in order for therapy regimens to be changed.

### 1.1.5 PET Imaging in IPF

Currently, the main use of imaging in both the diagnosis and monitoring of IPF has been HRCT, which can be used to characterise lung morphologies such as honeycombing, which is associated with shorter survival, giving HRCT prognostic value [92, 140, 141]. More recently, reports of an increased PET signal in the lungs, in regions of parenchymal changes on HRCT [142-144], of patients with IPF have been recognised. It has also been reported, that PET imaging of IPF patients with $^{18}$F-FDG has highlighted areas with increased tracer uptake that appear normal as determined by HRCT, giving rise to the potential of $^{18}$F-FDG PET scanning to identify crucial early molecular changes occurring within the lungs prior to the establishment of fibrosis [9]. There is potential for this to allow clinicians to select patients with increased $^{18}$F-FDG uptake for close follow-ups using HRCT to determine whether this may indicate early onset IPF. This makes PET imaging a potentially useful tool for the monitoring of disease progression in these patients, allowing for improved patient management by clinicians.

Honeycombing and reticulation changes, detected by HRCT, are linked to fibrotic changes on a microscopic scale [145, 146], however once this stage of the disease has been reached, treatment and reversal of the pathology is unlikely with the treatments available today. Detecting the earliest disease signals, using highly

sensitive PET imaging agents targeting potential biomarkers of IPF, would provide a clearer understanding as to the *in vivo* pathogenesis of IPF, and thus, potentially, upstream targets that may be exploited in order to reduce or halt fibrogenesis in this disease. Of the potential targets that are being increasingly recognised in the pathogenesis of IPF, integrin αvβ6 [147-149] and the GPCR CXCR4 [150, 151] have shown promise as therapeutic targets in preclinical studies, and PET imaging has the potential to be used in order to monitor the responses of IPF patients to both existing and novel therapies.

As well as rising therapeutic targets in IPF, some markers are also being considered as diagnostic targets. Although $^{18}$F-FDG has been reported to be a predictor of lung physiology in patients with IPF, it lacks specificity, which may be found by targeting emerging targets implicated in the pathogenesis of IPF. Of these targets, both integrin αvβ6 [104] and CXCR4 [152] have been investigated as potential PET imaging targets for diagnosis of IPF, with the latter also being investigated as a PET agent to monitor response to therapy using pirfendione in IPF patients. Another imaging agent, gallium-68-labelled collagen binding peptide 8 ($^{68}$Ga-CBP8), was developed by Desogere *et al.* for the noninvasive imaging of type I collagen in a preclinical model of bleomycin-induced fibrosis [105]. Regardless of its location, fibrosis is characterised by the excess deposition of extracellular matrix (ECM) proteins, including collagens, making it an attractive target for a PET imaging agent for the staging of fibrotic diseases. Not only does this probe bind specifically to collagen in a bleomycin model of pulmonary fibrosis in mice, but it is able to be used to both detect and stage pulmonary fibrosis in this model as well as monitor the response to antifibrotic therapy. Importantly, the uptake of this probe was correlated with the extent of fibrosis in resected human lung tissue from IPF patients, indicating the translational potential of the probe from preclinical to clinical studies. In addition to collagen imaging, other studies have focused on imaging elastin with novel probes [153], as elastin is also upregulated in IPF [154].

### 1.1.6 Development of PET Imaging Agents

This project aims at evaluating the use of radioligands in cancer and fibrosis, and, as such, radioligands are required to undergo extensive preclinical validation. This project has focused on the development of peptidic and small molecule PET probes, which will be discussed from here on.

The development of novel PET tracers is a complex process that requires a multidisciplinary research group including expertise in organic chemistry, radiochemistry, pharmacology, cell biology, physics, image analysis and the area of biology the radiotracer is targeting, such as cancer or IPF.

For a PET imaging agent to be used in clinical imaging, it first needs to undergo rigorous validation process that requires a multi-disciplinary team, including medicinal chemists, biologists and radiochemists, to evaluate each stage of the development process. Such a process would include chemical characterisation of a molecular probe, establishment of radiochemistry protocols, evaluation of PET tracer binding *in vitro,* and *in vivo* assessment of tracer suitability, all of which will be discussed here.

**Chemical characterisation of a probe**

The beginning of the PET probe development process involves the synthesis and characterisation of a chemical probe, referred to as the precursor molecule. At this stage, full characterisation of the molecule is required, which would include the product yield, which is the percentage product formed from the primary chemical, chemical purity as determined by radio-high performance liquid chromatography (R-HPLC), mass spectrometry (MS) or composition analysis, and the determination of the number of sites to which a radionuclide may bind to the molecule.

**Characterisation of the radiolabelled probe**

Following initial characterisation of the precursor molecule, the synthesis of the radiolabelled derivative, referred to as the radiotracer, is performed. Here,

properties such as synthesis time, chemical purity, radiochemical yield (RCY), radiochemical purity (RCP), lipophilicity and specific activity ($A_S$) are assessed.

**Synthesis Time**

The time taken between the addition of the precursor to the radiolabelling reaction and the final probe purification step needs to be known as this may dictate whether a specific radioisotope is suited for this molecule. If a radiolabelling reaction were to take considerable time, then radioisotopes with shorter half-lives, such as carbon-11, gallium-68 or fluorine-18 may not be suitable labels for this molecule, which would be more suited to those isotopes with longer half-lives such as copper-64 or zirconium-89.

**Radiochemical Yield and Purity**

It is important to determine the percentage radiochemical yield following a radiolabelling reaction. Radiochemical yield is the percentage of the radiotracer that is formed, based on the total amount of precursor used in the reaction. This can be determined using both R-HPLC and ultraviolet (UV) analysis which are used to detect the amount of radioactive and non-radioactive products, respectively, following the radiolabelling reaction. Ideally, a high RCY is desired whereby the vast majority of precursor is converted into radiotracer, however, a low % RCY, whereby the majority of precursor in the reaction is not converted into radiotracer, may be satisfactory if the non-reacted precursor may be easily separated from the radioactive product to maximise the specific activity of the radiotracer. The choice of radiolabelling procedure is, therefore, crucial in maximising the radiochemical yield of the radioligand. Precursor concentrations are crucial for good RCY and concentrations less than $10^{-5}$ to $10^{-6}$ M are typically ineffective [155] and RCYs of 95% and above are typically desired [156].

Radiochemical purity is described as the percentage of the radioactive radiotracer that is formed, based on the total amount of all radioactive products formed in the radiolabelling reaction. It is important to determine if there are any other radioactive products formed in the reaction and to ascertain as to what these products are before progressing to the biological validation of the

radiotracer, as any other radioactive products may exhibit non-specific uptake that would reduce contrast of radiotracer in regions of interest such as a tumour or fibrotic lung compared to non-target tissues, potentially leading to false-positive cancer diagnoses as a result of non-specific uptake in non-tumour regions.

**Lipophilicity**

When designing a molecular imaging agent, lipophilicity (LogP) of the compound is a crucial aspect to consider when predicting its physiochemical properties as it plays a large role in the tissue absorption, distribution, metabolism and elimination (ADME) of the tracer as well as the potential to cross the blood brain barrier (BBB) and influence non-specific binding [157-159]. Typically, polar compounds, which exhibit low LogP values, are highly soluble in water and have rapid renal clearance. On the other hand, lipophilic molecules, which typically have high LogP values, are associated with increased non-specific binding.

**Specific Activity**

The amount of radioactivity per unit of mass of a radiolabelled compound is referred to as the specific activity ($A_S$) of a radiotracer, and is expressed in the units Becquerel per gram (Bq/g) or gigabequerels per milligram (GBq/mg) etc. [160]. This is an important property of a radiotracer to consider throughout the development of PET imaging agents as the choice of synthesis method can have significant effects on $A_S$ of a radioligand [155]. If a radiotracer was deemed to have a low $A_S$, the non-radioactive molecules within the reaction mixture will compete with the radiolabelled tracer in both *in vitro* and *in vivo* studies, reducing the uptake of the tracer in different cells, tissues or organs. The higher the $A_S$, the lower the amount of non-radiolabelled product, therefore less competition and higher uptake of the radiolabelled probe. Specific activity of a radioligand also has safety implications for both pre-clinical and clinical use. If a potent agonistic radioligand was used to image a specific receptor with a low $A_S$, the required radioactive dose required for imaging, which would be much higher than that of high specific activity radioligands, would lead to the non-radioactive form

potentially pharmacologically activating these receptors, inducing a pharmacological response [156].

**Biological Validation of a radiotracer *in vitro***

Following the validation of the chemical precursor and its radiolabelling methods, the usefulness of the chemical probe is assessed using biological material such as cells, tissues and small animals. In the first instance, if the target of interest has not been imaged before, previously established knowledge of receptor density/concentration is desirable as this can have direct implications for radioligand design. The lower the target density, the higher the affinity of the radioligand is required. This can be determined using radioligand autoradiography experiments.

**Binding characterisation *in vitro***

Radioligand binding is a widely used tool to define the function of receptors at a molecular level. Receptor-mediated endocytosis is the main pathway by which extracellular molecules are taken into cells. Upon the specific binding of a ligand with a membrane receptor, such as a GPCR, if internalisation is induced, the intracellular signalling pathways associated with that receptor are briefly activated, inducing receptor-mediated endocytosis [161]. This internalisation of receptor-radioligand complexes is able to be exploited for the purposes of PET radioligand development, whereby it is advantageous for a radioligand to accumulate in the target tissue of interest [162, 163], through trapping of the radioligand within the cell and for recycling of receptor to the cell surface to occur, in order to attain high imaging contrast or therapeutic efficacy, and internalisation experiments have frequently been used to characterise the novel radioligands [164, 165].

In cases of low target receptor density, the ideal PET radioligand is required to have a high affinity for its target receptor, whereas on the other hand, high receptor density is not as restrictive on radioligand affinity [166]. As mentioned previously, autoradiography experiments using a radioligand that targeted a receptor of interest may be able to characterise receptor concentration/density

within a specific tissue, however this is no guarantee of radioligand suitability *in vivo*, as properties such as metabolism, poor delivery and non-specific binding may not necessarily occur in this setup, therefore *in vivo* characterisation is still required.

In order to characterise the binding of a potential PET imaging agent with its target receptor, various techniques may be employed that give an indication as to the strength of the interaction and even the kinetic properties of the interaction [167-170], such as competitive binding experiments that may involve cell-based assays or competitive enzyme-linked immunosorbent assays, among others, or surface plasmon resonance (SPR) studies, which enable the elucidation of the kinetic properties of an interaction between two molecules. The use of SPR will be discussed in further detail later.

Once a high-affinity interaction between PET tracer and its target has been established, it is also important to evaluate its specificity for the target receptor. Importantly, the tracer should contain no, or very low, affinity for other receptors, so that the signal generated in PET imaging studies can be attributed specifically to the interaction of the PET tracer with its intended target receptor. If a PET tracer does indeed have an affinity to another receptor, this may lead to false positives and images that do not solely reflect the distribution of the intended receptor [171, 172]. Commonly, however, screening of targeted agents is often carried out *in vitro* to determine their selectivity for their intended target, although this may be difficult for some receptors such as the dopamine D2 and D3 receptors, both of which in humans, have high sequence homology within their transmembrane domains, the regions thought responsible for dopamine binding and binding of other small molecules, and no *in vitro* measures of ligand D2/D3 selectivity are currently available, presenting a significant challenge for the development of novel compounds targeting these receptors [173-175]. However, several drawbacks limit the usefulness of these *in vitro* binding characterisation techniques. For example, the binding affinity of a radioligand for its target may differ significantly due to changes in the conditions used in the assay setup, such

as temperature and buffer composition [169], with assays commonly being carried out at 4$^{o}$C, differing significantly from physiological temperatures that would be seen *in vivo* (37$^{o}$C) [176-178].

***In vivo* radiotracer evaluation**

The main essential requirement of an effective PET tracer is that it is able to provide good contrast between the targeted tissue type, such as a tumour, or fibrotic lung, and the background, with background tissues typically consisting of muscles, blood (in order to assist clinicians with making clinical decisions such as diagnoses), assessment of therapy response and disease progression. A key step involved in the development of PET probes is preclinical evaluation.

When injected into an organism intravenously, a radiotracer is exposed to proteases and enzymes that may degrade the radiotracer, producing potentially multiple radiometabolites that may confound PET images [179].

In the context of this project, the targets of interest, integrin αvβ6 and chemokine receptor CXCR4, are both common to IPF as well as cancer, therefore evaluation of radioligands targeted towards these receptors *in vivo* using xenograft models is required. For these models, the use of molecular biology may be exploited to generate cell line models that can differ in expression levels of the target of interest. As these systems often rely on overexpression, the use of various cell lines with different levels of endogenous expression may also be used. Models also exist whereby expression of a target receptor may be induced by treatment with specific agents such as doxycycline [180] or 4-hydroxytamoxifen (4-OHT) [181], allowing for PET imaging of the same animal before and after induction of target expression. Also, the use of knockout models in mice can allow for the determination of binding characteristics of radioligands [182].

Typically, cell lines that are used for xenograft models either possess an endogenous level of target protein/receptor, or they may be transfected to express the protein/receptor of interest at a significantly increased level. Comparison of these xenografts that may display target expression at different

values may be used to correlate tracer uptake with receptor expression levels to give more information with regards to the *in vivo* specificity of a tracer.

A key step in the development of PET radioligands is the assessment of radioligand biodistribution, toxicology and dosimetry, and animal studies are often employed to characterise these properties of radioligands [156]. These assist in ascertaining whether a radioligand is acting specifically or if there is a high level of non-specific binding, which can be a significant factor in the failure of radioligand translation to the clinic. The degree of non-specific binding, and the location of non-specific uptake of a radioligand is also important for dosimetry studies. Initially, using animal models and various timepoints, the radioactivity of organs, tissues, urine and plasma is determined and expressed as a percentage of the injected dose. This allows for the calculation of the predicted effective dose to humans, which can in turn act as a guide for clinical studies, dictating the amount of radioactivity that can be injected into humans, as critical organs such as the liver, kidneys and bladder may be negatively affected by high doses, leading to a reduction in the maximum radioactivity that can be administered and potentially limiting the clinical utility of the radioligand.

**Small Animal PET Imaging**

When it comes to *in vivo* characterisation of a PET radioligand, small animal PET scanners that allow the evaluation of novel radiotracers *in vivo* have been developed. Clinical PET scanners have a typical resolution of approximately 5 mm, whereas pre-clinical small animal PET scanners have an "enhanced" resolution of 2 mm [183]. Despite this increase in absolute resolution, due to the sizes of the subjects to be imaged in either scanner, the resolution achieved by pre-clinical scanners is less than that of clinical PET scanners due to relative subject size. Importantly, small animal PET scanners apply stricter constraints to specific activity requirements of a radioligand targeting a receptor that is expressed at a low density [184].

#### 1.1.6.1 Surface Plasmon Resonance as a useful tool for development of imaging agents

SPR is an analytical microfluidic technique that can directly measure the binding interactions between two molecules in real-time, without the requirement of labels such as fluorescent or radioactive tags, with high precision. As an interaction between two molecules may be observed in real-time the association and dissociation kinetic properties of a molecule, or interaction, may be quantified by utilising the surface plasmon resonance phenomenon, and thus the resultant affinity of an interaction measured with high accuracy.

The determination of the binding kinetics of a biomolecular interaction between a ligand and a receptor may provide extremely useful information that will aid the selection of lead candidate molecules to take forward for PET probe development, based on their association and dissociation kinetic properties, rather than on equilibrium affinity data alone. With regards to the desirable kinetic characteristics of a PET imaging agent, a radioligand ideally has fast association kinetics *in vivo* in order to accumulate at the target of interest, whilst any unbound radioligand may be eliminated. The dissociation rate of the radioligand from its target is also ideally slow, in order to preclude excretion and remain at the target long enough to allow for a patient to be imaged.

Usually, to assess the binding of a molecule for its target receptor, modification of the molecule is required in order to detect the molecule in question, such as radio- or fluorescent labelling. Either molecule in the competition assay may be labelled, however care must be taken when adding labels onto molecules as this may alter the binding characteristics of the molecule for its target. Also, this type of assay does not allow for the determination of association or dissociation constants, only affinity. Whilst affinity of a molecule for its target is important, the kinetic properties of an interaction may differ considerably between two molecules that have been deemed to have similar affinities for a target (Figure 9), therefore meaning that this method does not allow for the selection of lead candidates based on kinetic properties of a molecule. The association and dissociation constants may provide detailed information that can aid *in vivo* imaging studies. For example, the association constant, if known, may

be used to dictate the imaging protocol, including the time left between radioligand injection and scan start times. Interactions with slower association constants may likely result in increased timespans between injection and the scan start, whereas faster association constants will lead to reduced waiting times. Also, the dissociation constant, particularly important for inhibitors that prevent internalisation of the ligand-receptor complex, may be used to select molecules that are more likely to occupy their target receptors long enough in order to avoid washout of the radioligand and enhance the contrast to background activity in PET scans.

SPR works by employing a flow system, which provides continuous flow of buffer over the surface of a gold-coated sensor chip. Experiments typically involve immobilisation of one of the reactants to the sensor surface before injection of the binding partner in solution over the chip surface. The interactions, which cause a shift in the refractive index of a light source aimed at the sensor surface measured by a detector (Figure 7) and are presented in a sensorgram (Figure 6), which plots response units (RU) as a function of time (s) and traces association ($k_a$) and dissociation ($k_d$) of partner binding complexes.

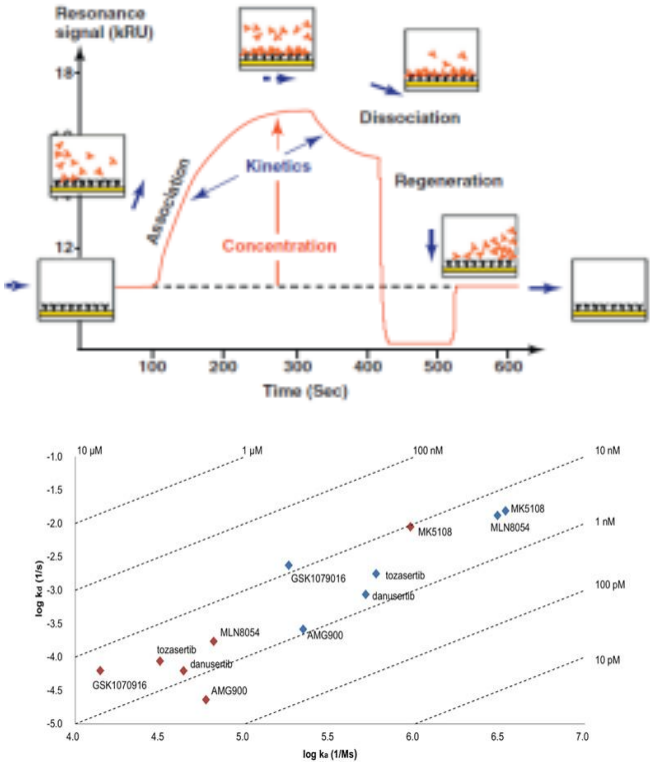


**Figure 6. (A) Typical SPR sensorgram providing real-time information regarding a reaction between two interactants. Binding responses are measured in response units (RU). Report points may be selected at specific periods to give binding responses at any one time. Any unbound sample molecules are removed during a regeneration step, preparing for the injection of the next sample. (B) Plot of association rate and dissociation rate of various inhibitors. Dotted lines refer to equilibrium dissociation constants calculated from on- and off-rates.**

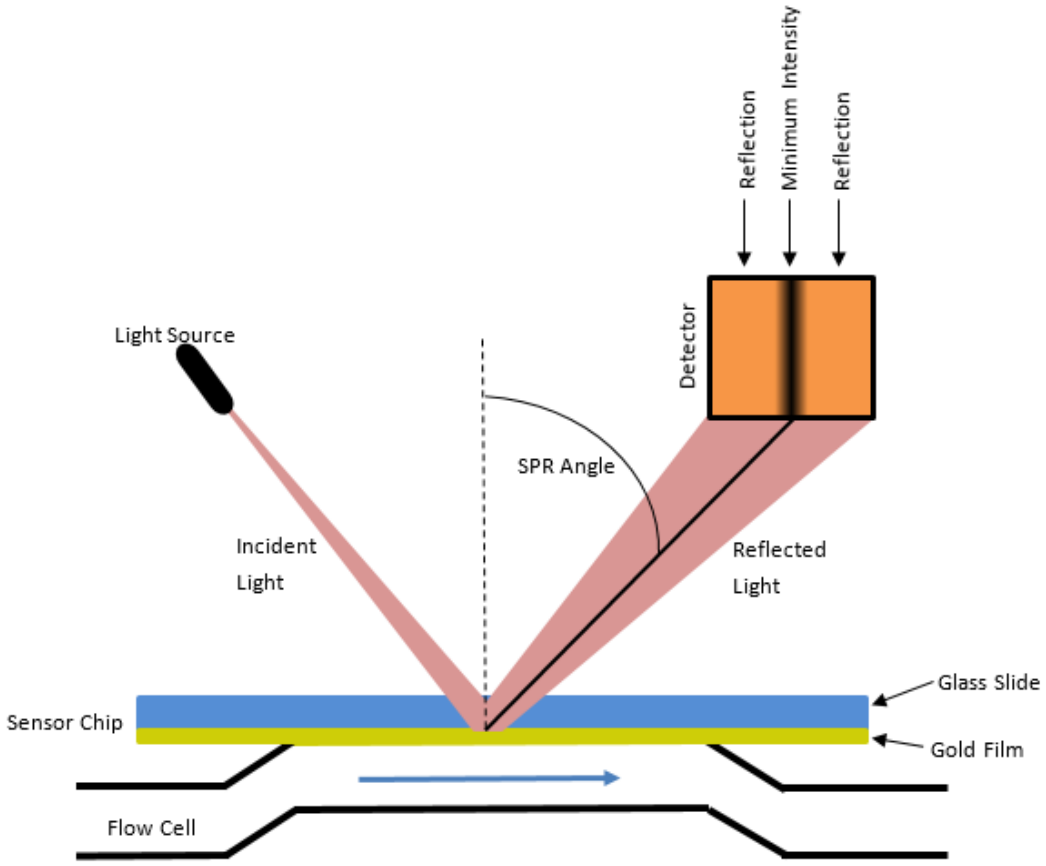


**Figure 7. SPR detection principle.**

The kinetic constants of a bimolecular interaction can be calculated by fitting a mathematical model to the sensorgram generated following an SPR assay. Once the on- ($k_a$) and off-rates ($k_d$) of an interaction have been determined, they can be used together to calculate the affinity ($k_D$) of an interaction by dividing $k_d$ by $k_a$.

$$\text{a)}\ \frac{\Delta[AB]}{\Delta t} = k_a \cdot [A] \cdot [B] \qquad \text{b)}\ \frac{\Delta[AB]}{\Delta t} = -k_d \cdot [AB]$$

SPR could be used as an invaluable tool in the assessment and selection of potential PET imaging agents, through assisting the selection of molecules that

exhibit favourable binding kinetic characteristics for an imaging agent. By elucidating the association and dissociation constants of an interaction, it may also allow distinction between molecules that have similar affinities for a target by other methods.

## 1.2 Integrins

### 1.2.1 Background

Extracellular matrix-cell and cell-cell communication are essential features in all organisms in order to sustain life. These communications allow cells to recognise various factors within their microenvironment to which they can respond and communicate with. The key molecules, with respect to cell adhesion and signalling include the integrin superfamily of receptors.

Integrins are heterodimeric, transmembrane receptors consisting of a single alpha subunit non-covalently associated with a single beta subunit. There are 18 alpha subunits and 8 beta subunits described, which interact in various combinations to give rise to 24 different integrin subtypes [185]. Their primary purpose is to implement regulatory functions during cell adhesion, migration, proliferation and survival as well as apoptosis. They are able to instigate bidirectional signalling across the cell membrane, allowing the exchange of information from the extracellular matrix proteins to intracellular molecules via “outside-in” signalling as well as from the intracellular molecules to the extracellular matrix proteins via “inside-out” signalling. The intracellular portions of integrins are found to be associated with intracellular cytoskeletal components as well as with proteins of the extracellular matrix via the extracellular portion of integrins, which also allows them to function as mechanotransducers (Figure 8; [186].

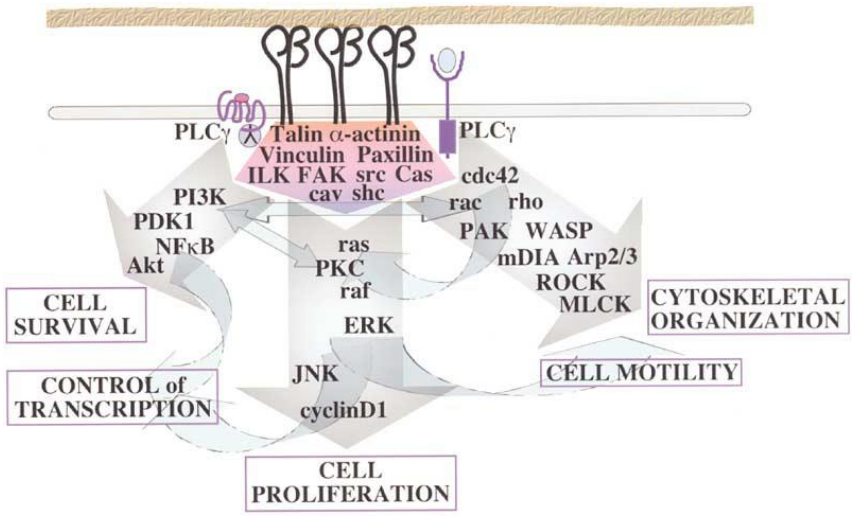


**Figure 8. Integrin signalling pathways showing the downstream effects of receptor stimulation. Reproduced from Hynes, 2002 [186].**

Different types of integrins exhibit different ligand recognition patterns and are also expressed on varying cell types. This has allowed integrins to be categorised into distinct groups based on their ligand specificities; laminin-binding integrins, collagen-binding integrins, leukocyte integrins, and RGD-specific integrins [187]. Upon the extracellular binding of ligand by an integrin, an intracellular signal is generated, that can trigger various pathways within the cell. Integrin function can also, however, be regulated by signals within the cell [186], as they act as links between the extracellular matrix and the actin filaments of the intracellular cytoskeleton via various actin-binding proteins such as talin, vinculin and ERM (ezrin, radixin, moesin) [186].

In the 1980s, a highly conserved integrin recognition motif consisting of three amino acids in the order Arginine (Arg), Glycine (Gly), Aspartic acid (Asp), was discovered and found in fibronectin. This then triggered the discovery of this motif within other extracellular matrix proteins such as vitronectin, laminin and osteopontin. In total, 8 different types of integrin have been shown to possess an affinity for ligands containing this Arg-Gly-Asp (RGD) sequence, these include

αVβ1, αVβ3, αVβ5, αvβ6, αVβ8, α8β1 and αIIβ3 (Figure 9). Ligand specificity for different RGD-recognising integrins is more complex, depending on the conformational and spatial presentation of this motif to an integrin, which may be altered by changing the amino acid residues that flank either side of the RGD motif within the ligand. Targeting integrins in various diseases for both diagnostic and therapeutic purposes has been an expanding field in recent times and has led to the exploitation of the RGD motif in the development of various targeted peptides or peptidomimetics as targeted agents for specific integrins [188-191].

#### 1.2.1.1 Integrin ligand binding

At one point, the mechanisms of integrin activation in response to ligand binding were poorly understood due to lack of structural information. However, studies have since revealed the structure of the integrin αVβ3 in the absence, or presence, of cilengitide, a small cyclic peptide shown to bind integrin αVβ3. Experiments in these studies revealed that the extracellular domain of αVβ3 can be found in a resting state whereby the head groups are bent towards the cell membrane. In response to ligand binding, the hinge region in each of the α and β subunits undergoes structural rearrangement, often referred to as the "switchblade" mechanism (Figure 10).

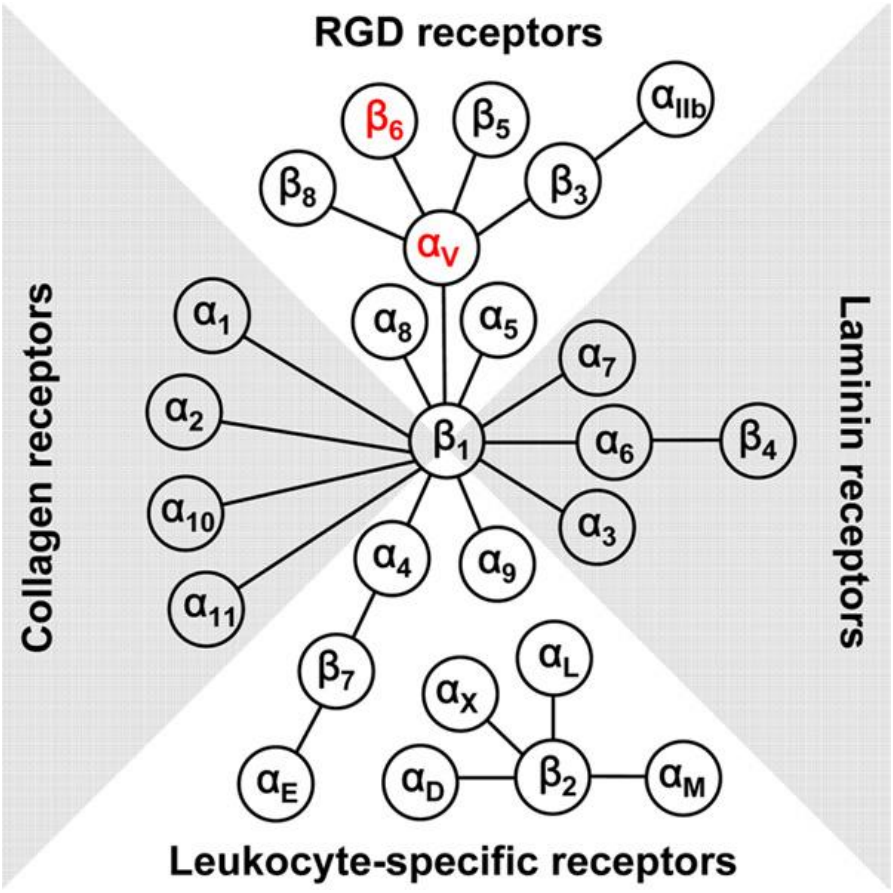


**Figure 9. The integrin family in humans: 18 alpha and 8 beta subunits assemble into 24 different functional heterodimers. [184]**

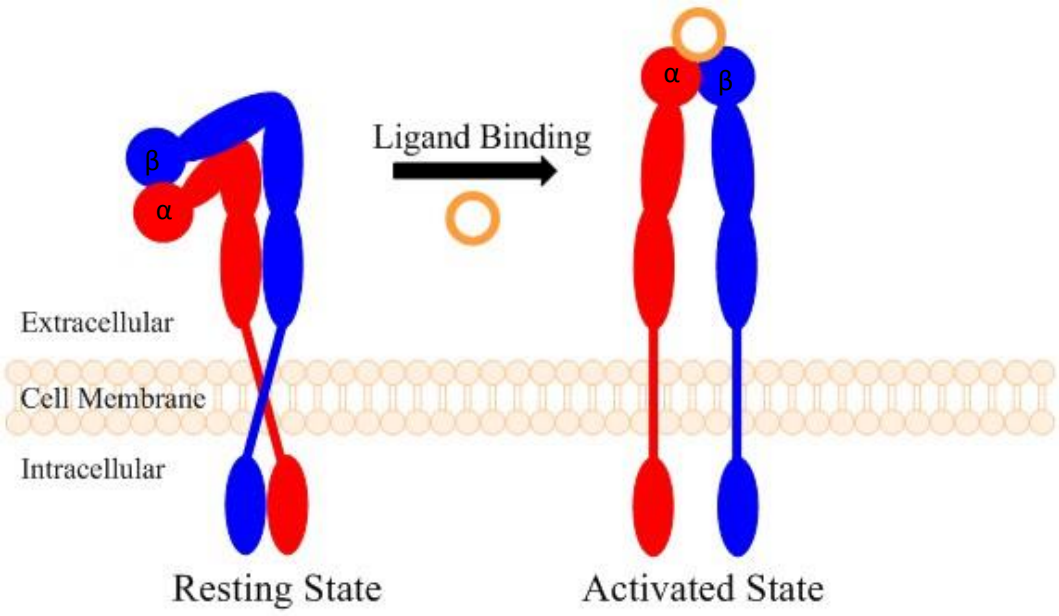


**Figure 10. Diagram of integrin-ligand binding via the "switchblade mechanism.**

#### 1.2.1.1.1 Effects of divalent cations on integrin binding

Integrins contain multiple low affinity divalent cation binding sites within their structure that potentially have significant effects on integrin function and binding. These divalent cations (including $Mg^{2+}$, $Ca^{2+}$ and $Mn^{2+}$) are able to promote or inhibit ligand binding and also change the ligand specificities of an integrin. A "displacement hypothesis" has been theorised, whereby ligands containing an RGD sequence interact with a receptor-bound divalent cation, allowing for an interaction between the ligand and integrin to stabilise before the divalent ion itself is displaced by the RGD ligand. In relation to the promotion and inhibition of ligand binding by divalent ions, it has been shown that the beta3 integrin contains two different types of divalent ion binding sites, termed ligand-competent (LC) and inhibitory sites (I sites), which both regulate ligand binding of integrins.

### 1.2.2 Avβ6 in disease

The αvβ6 integrin is an RGD-dependent receptor, the distribution of which is unlike any other integrin as it is restricted to epithelial cells only. The level of expression at the protein level is relatively low, or undetectable, in healthy tissue, but it has been shown to be vastly upregulated during physiological or pathological processes including wound healing, fibrosis and inflammation and even in some malignancies. This upregulation in itself, makes integrin αvβ6 a very attractive target for both diagnostic and therapeutic applications in various diseases.

### 1.2.3 Avβ6 in Cancer

Under pathologic conditions, integrin signalling may lead the disruption of normal integrin signalling observed in normal physiological conditions, critical for embryogenesis and maintenance of tissue homeostasis, resulting in abnormal cell division, adhesion and migration [192, 193]. The integrin αvβ6 is expressed exclusively on epithelial cells and, generally, the level of expression of integrin αvβ6 is very low to undetectable under conditions of normal physiology. However, this expression is markedly increased in response to physiologic and pathologic events such as wound healing, fibrosis and cancers of the breast, lung, oral

squamous carcinoma, colon and pancreas [194-199]. The enhanced expression of αvβ6 in cancer has been linked to worse prognosis [200, 201] and also shown to be a key mediator, through its interactions with the extracellular matrix via the RGD motif found in fibronectin and collagen, in the promotion of cell invasion and migration in metastasis [194, 201], with high expression of the integrin being shown to be localised at the leading edge of tumours [202]. There is also evidence that suggest the activation of TGF-β by αvβ6 is an important pathway for immunosuppressive signalling in various cancers [203] and that overexpression of this integrin is associated with a change from an epithelial to a mesenchymal-like cell transformation [199, 204]. Further details on the mechanism of TGF-β activation by αvβ6 will be discussed later. There is also evidence that blockade of αvβ6 signalling has the ability to prevent tumour progression *in vivo* in cancers that include pancreatic, ovarian, breast and colon [205]. Another protein, known as HS1 associated protein (HAX-1), has been shown to be an interacting partner for αvβ6 [206] and that this interaction is crucial for the internalisation of the integrin, which is able to increase the invasiveness of oral squamous cell carcinoma (OSCC) and determine the rate of cancer progression [207].

### 1.2.4 Avβ6-associated cancers

#### 1.2.4.1 Avβ6 in oral squamous cell carcinoma

Head and neck-related cancers are one of the most common types of cancer, with OSCC making up 40% of these cases [208]. Currently, the available therapies for this cancer remain standard radiation, chemotherapy and surgical options, with a 5-year survival rate of approximately 50% [209]. Due to the lack in therapeutic options that are able to significantly improve patient survival, new treatment strategies are urgently needed in order to specifically target the cancer and avoid any collateral toxicity caused by radiation and chemotherapy to healthy tissues.

Avβ6 has been shown to be highly expressed in leukoplakia; a premalignant lesion of the oral mucosa and salivary gland neoplasia [210], suggesting a role for αvβ6 in the disease progression in OSCC [211]. A study by Hsaio *et al*. [212]

identified a linear peptide, via a phage display library used to identify peptides that bind to the OSCC cell line, HSC-3, with the amino acid sequence RGDLASL able to bind these cells with a three-fold increase in binding affinity compared to a control phage known to bind to these cells. Bioinformatic analysis revealed that this peptide sequence had similarities to the G-H loop of the viral capsid protein, VP1, found in the foot and mouth disease virus (FMDV) [213], and other peptides with resembling sequences have been shown to bind to αvβ6, specifically [214-216], with little or no cross-reactivity observed with other integrins. A more complete review of the ligands for αvβ6 Is presented in section 3.2.

Importantly for this identified peptide, it was shown to be internalised by HSC-3 cells, expressing αvβ6, in a temperature-dependent manner, with physiological temperature (37$^{o}$C) inducing a large amount of internalisation of this peptide compared to lower temperatures (4$^{o}$C) where peptide accumulation was evident at the cell surface with no internalisation taking place. This RGD ligand-induced, clathrin-dependent [217] internalisation has also been observed for other peptides derived from the foot and mouse disease virus that target αvβ6 [213, 216] and gives rise to the potential of this peptide for use as an effective molecular imaging and/or therapeutic agent targeted towards αvβ6 in cancer.

Hsiao and colleagues tested the ability of their peptide to inhibit tumour cell proliferation in HSC-3 cells and their studies revealed a significant decrease in HSC-3 proliferation. Interestingly, this inhibition was only observed using the cyclised version of their peptide, engineered to contain flanking cysteine residues that could be exploited to circularise the peptide through a single disulphide bond, and not the linear version of the peptide, which may be due to the reduced conformational freedom of cyclic structures resulting in enhanced binding affinities [218]. The ability of this peptide to inhibit proliferation of OSCC cells gives promise to its potential future use as an αvβ6 targeted therapy for OSCC.

### 1.2.4.2 Avβ6 in breast cancer

Breast cancer is the most common cancer in women, with approximately 1.1 million being diagnosed yearly, worldwide [219]. This type of cancer has a variety of subtypes that differ morphologically. Ductal carcinoma *in situ* (DCIS) is the most common subtype of breast cancer, accounting for roughly 80% of invasive breast cancers. The most common classification for describing different types of breast cancers describes 6 distinct subtypes; luminal A, luminal B, HER2, claudin low, basal-like breast cancer (BLBC) and normal [220, 221]. Classification based on receptor expression is also used, classifying breast cancers by their expression of the oestrogen receptor (ER), progesterone receptor (PR), human epidermal growth factor receptors 1 (HER1) and 2 (HER2) and cytokeratins 5 and 6 [222, 223].

Overexpression of HER2 in breast cancer results in a more aggressive and invasive phenotype, and its overexpression is implicated in approximately 20-30% of breast cancer cases [224, 225]. Therapeutic options for these cancers include the use of the HER2-targeting antibody, trastuzumab, which is able to block the downstream signalling of HER2 as well as reduce mortality in $HER2^{+}$ breast cancer [226, 227]. The limitation of trastuzumab, however, is that patients tend to develop a resistance to this therapy, limiting it use in the case of recurrence, or even primary cancers if *de novo* resistance is conferred [228]. Therefore, new therapeutic strategies that can target new pathways implicated in breast cancers may have the potential to aid the treatment of breast cancer patients that may be resistant or develop resistance against existing therapies such as trastuzumab.

With respect to HER2-driven breast cancers, it has been shown that transforming growth factor beta (TGF-B) is implicated in the promotion, migration and metastasis of breast cancer [229-231] and a major mediator of TGF-B activation from its latent form to its active state is integrin αvβ6 [232]. Avβ6 has itself been shown to be involved in the progression of DCIS to invasive breast carcinoma [233] and high expression has been significantly correlated to a worse

prognosis in not only breast cancer [234], but in colon, cervical and non-small cell lung cancer (NSCLC) [199, 200, 235].

Interestingly, a study by Moore *et al.* [234] has shown that αvβ6 drives tumour invasion, and that its blockade, using an αvβ6-targeted antibody, results in its down-regulation, suggesting that αvβ6-targeted therapy may be a potential avenue for breast cancer therapy which was shown to be effective *in vivo* using BT-474 xenograft models. In addition to the promising potential of αvβ6 as a therapeutic target in breast cancer, there may be also an opportunity to exploit αvβ6 as an imaging biomarker for the selection of patients most likely to benefit from this type of therapy.

### 1.2.5 Avβ6 in IPF

In addition to its role in various cancers, there is a marked increase in αvβ6 expression in the alveolar epithelium during fibrosis. This upregulation of expression has been shown to be significant in the promotion of pulmonary fibrosis, which is demonstrated by the prevention of radiation-induced pulmonary fibrosis in murine models in response to the inhibition of αvβ6 by a monoclonal antibody [236].

αvβ6 has also been shown to be important with regards to the promotion of bleomycin-induced pulmonary fibrosis [232]. $\beta6^{-/-}$ mice undergoing bleomycin treatment have shown almost unaltered lung morphology compared to wild type mice that showed significant fibrosis in response to bleomycin instillation. However, the overexpression of αvβ6 is not sufficient alone in order to bring about fibrosis [237].

Another molecule that has been shown to be a crucial mediator of fibrosis is transforming growth factor beta (TGF-βeta). Three mammalian isoforms of this molecule exist (TGF-B1, -B2 and –B3), with TGF-B1 having been the best characterised in the context of pulmonary fibrosis. TGF-B1 is a pleiotropic molecule expressed by all types of cells and tissues within the body and has profound effects upon epithelial cells, promoting apoptosis of epithelial cells

[238], epithelial-mesenchymal transition (EMT), epithelial cell migration and the inhibition of epithelial cell proliferation. The significance of this molecule in the context of pulmonary fibrosis is well described [148, 239, 240], with expression levels being increased in both animal models of pulmonary fibrosis and patients with IPF. Its overexpression has been shown to contribute to persisting pulmonary fibrosis, and its inhibition has the potential to abolish lung fibrosis in small animal models.

Interestingly, TGF-B1 is found constitutively expressed in an inactive, latent form in association with the latency-associated peptide (LAP) which contains an RGD sequence to which αvβ6 can bind to. The molecular mechanism by which αvβ6 can activate TGF-B will be discussed later on. Due to TGF-β's central role in the pathogenesis of IPF, it is a very attractive potential therapeutic target, however due to its pleiotropic nature, global inhibition of TGF-β may be difficult in diseases such as IPF as it is a chronic disease and prolonged inhibition of its function could potentially lead to long-term toxicity [239]. Because of this, identifying different ways of targeting the activation of TGF-β has become a main therapeutic focus for IPF treatment.

**Avβ6-mediated TGF-β activation**

αvβ6-mediated TGF-β activation is dependent on the interaction between the integrin and the actin cytoskeleton [232]. A study by Yang *et al.* [241] showed that substitution of aspartic acid within the RGD domain of LAP with glutamic acid leaves latent-TGF-β unable to bind to the integrins and mice with this mutation exhibit very similar phenotypes to TGF-β1 knockout mice.

TGF-β genes encode a C-terminal TGF-β sequence and an N-terminal latency-associated peptide sequence (LAP). TGF-β1 is synthesised as a small latent complex associated with LAP, however upon cleavage of the bond between them, they remain non-covalently bound, in an inactive form (latent TGF-β) inhibiting the interaction between TGF-β and its activating integrin αvβ6. Latent TGF-β is secreted by the cell in association with the latent TGF-β-binding proteins (LTBP), which bind TGF-β in an isoform-specific manner. The LLC can associate with αvβ6

at the cell surface via recognition of the RGD motif found in LAP, however this alone is insufficient for TGF-β activation [232, 240]. αvβ6 is found constitutively associated with TGF-β, which suggests that the complex is primed to detect any signals that would be associated with injury. Integrins can activate latent TGF-β by two separate mechanisms; cell traction and a protease-dependent mechanism. With regards to αvβ6, the mechanism that is employed to activate the LLC is cell traction [232].

Studies have shown that αvβ6-mediated TGF-β activation can be induced by agonists of G-protein coupled receptors (GPCR), such as PAR1 [242] and LPA2 [149]. The integrin αvβ6 must be able to associate with the actin cytoskeleton in order to activate the latent TGF-β complex. Following damage to the epithelium, platelet-derived mediators such as thrombin or lysophosphatidic acid (LPA) activate their cognate G-protein-coupled receptors (GPCR) in order to induce a signalling cascade that brings about αvβ6 integrin-mediated activation of the LLC [149, 242]. The binding of thrombin and lysophosphatidic acid to their receptors leads to the induction of a signalling cascade involving $G_{\alpha q}$, RhoA and Rho Kinase (ROCK) resulting in actin polymerisation and cellular traction of αvβ6, inducing a conformational change in the integrin, which allows the activation of latent TGF-β. In its active form, TGF-β functions in a paracrine manner, associating with TGF-β receptors (TGF-βR) on neighbouring cells. This association with its receptor induces the phosphorylation of Smad which results in Smad's translocation to the nucleus where it causes increased transcription of the *itgb6* gene and the amount of αvβ6 expression in epithelial cells. The result of disruption to the basement membrane in response to injury gives rise to the potential for interaction between active TGF-β associated with αvβ6 on the epithelial cells and the fibroblasts, inducing the production and deposition of fibroblast-derived matrix proteins, leading to fibrosis (Figure **11**).

The key element in this chain of events is the upregulation of integrin αvβ6 from a low level in the healthy state to a much higher level in the pathologic state. This upregulation makes integrin αvβ6 an attractive target for diagnostic imaging

agents, potentially allowing for the detection early IPF before it becomes evident by other means such as HRCT or biopsy, with the added benefit of being non-invasive. Also, if αvβ6 expression levels are correlated with disease severity, then integrin αvβ6 may serve as a marker of response to therapy with longitudinal PET imaging studies taking place before and after therapy with novel agents.

The development of existing αvβ6 targeted imaging agents will be discussed in Chapter 3.

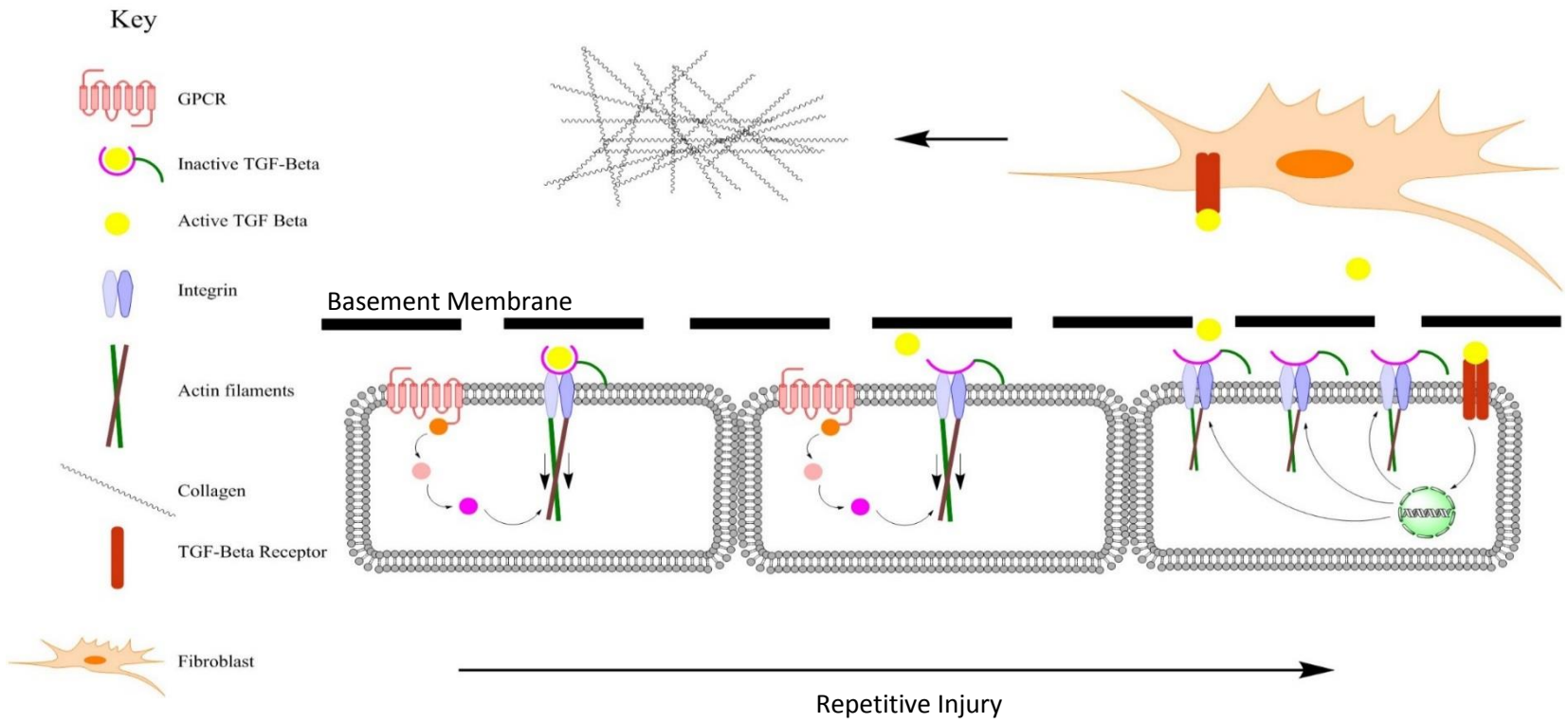


**Figure 11. Diagram of integrin αvβ6-mediated pulmonary fibrosis. Products of injury result in the induction of intracellular pathways via GPCRs leading to contraction of the intracellular cytoskeletal components in association with integrin αvβ6, leading to a conformational change in integrin structure causing activation of TGF-B. TGF-B binds to its cognate receptor on nearby cells, inducing upregulation of integrin subunit beta 6 expression. With increasing injury, damage to the basement membrane takes place, whereby activated TGF-B can translocate to nearby fibroblasts, inducing transformation into myofibroblasts and the deposition of ECM components such as collagens.**

## 1.3 Chemokines and chemokine receptors

### 1.3.1 Background

Chemokine receptors are cell surface receptors that bind chemokines to bring about various biological responses upon stimulation. They consist of seven transmembrane α-helices made up of 20-27 amino acid residues, 3 extracellular domains and 3 intracellular domains. The C-terminus of the receptor is found within the cytoplasm, whereas the N-terminus is extracellular. There are multiple types of GPCR, each of which can have different conformations. They assist in the regulation of a vast array of physiological processes in healthy tissue and also in disease, making them attractive targets for imaging and therapy.

Chemokines derive their name from "chemotactic cytokine" [243] and they act as chemoattractant molecules. They control the trafficking of different cell types, such as immune cells, to an area within the body in a process called chemotaxis, during which various cells are able to direct their movements in response to chemical signals in their surrounding environment. They have the ability to induce a wide range of physiological effects in various types of cells from immune cells to endothelial/epithelial cells. They are able to exert their effects through binding to their cognate GPCR. A selection of chemokines are able to bind to more than one receptor, for example CXCR3 is able to bind CXCL9, CXCL10 or CXCL11. Oppositely, some receptors are capable of binding only one ligand, such as CXCR4, which only has the capacity to bind CXCL12, a chemokine also known as stromal cell-derived factor 1α (SDF1-α). It is worth noting that although CXCR4 is only able to bind to CXCL12, this chemokine is also able to bind to ACKR3, another GPCR [244]. CXCL12 has been shown to act as an attractant for multiple cell types [245-249], providing a chemotactic gradient, along which, CXCR4-expressing cells can migrate.

There are four different families of chemokines, categorised as a result of the highly conserved cysteine residues found on the N-terminus of the molecule; CXC, CC, C and $CX_3C$ [243]. X signifies the number of amino acid residues that separate the 2 cysteine residues. CXC and CC chemokines contain disulphide

bridges between the 1st and 3rd cysteine residues and the 2nd and 4thcysteine residues. The C chemokine family exhibit 2 cysteine residues only, connected by a disulphide bridge.

The signalling mechanisms of GPCRs are complicated, involving a wide range of components [250] ( see an example for CXCR4 in Figure 12). Upon a binding event between a GPCR and its specific ligand, the intracellular domain of the receptor binds to a heterotrimeric G-protein, which is situated on the inner surface of the cell membrane. Gα, Gβ and Gγ are the three subunits that make up the heterotrimeric G-protein, formed through the interaction of Gβ with Gγ before binding to Gα, of which there are four forms that each transmit the signal from the GPCR in a different fashion.

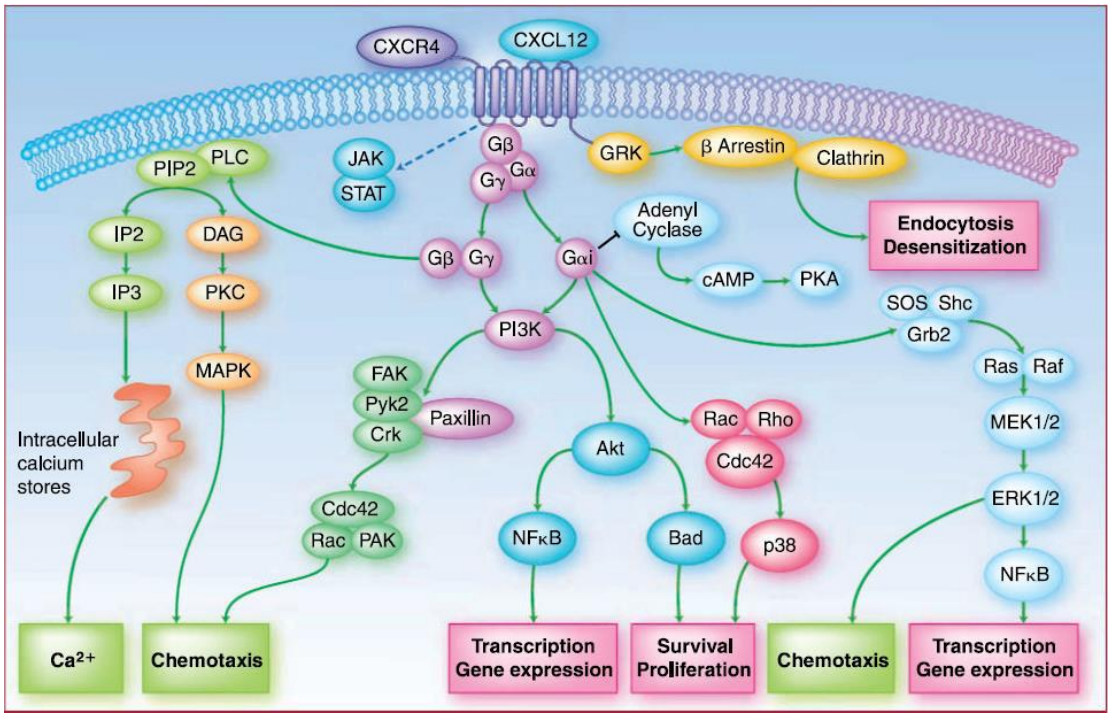


**Figure 12. CXCR4-dependent signalling pathways. Schematic depicting the signalling pathways activated upon CXCR4 binding to its cognate ligand CXCL12. [245]**

Liberated Gβγ subunits have the capability to activate multiple intracellular pathways including phospholipase C (PLC or phosphatidylinositide 3-kinase (PI3K). β-arrestin interaction with CXCR4 is able to influence chemotaxis through the p38 mitogen activated protein kinase (MAPK) pathways. Figure 12 shows a simplified diagram of CXCR4-dependent cell signalling pathways.

### 1.3.2 CXCR4 in Cancer

Chemokine C-X-C motif receptor 4 (CXCR4) is a seven transmembrane G-protein coupled receptor, which interacts with its cognate ligand stromal-cell-derived factor 1α (SDF1-α), also known commonly as CXCL12. This interaction between CXCR4 and CXCL12 is essential throughout development and continues to play a crucial part of normal cell function, such as controlling haematopoietic cells during homeostasis [251, 252].

CXCR4 is overexpressed in over twenty different cancer types, including, but not limited to, breast (16), gastric (17), pancreatic (18,19), ovarian (20,21), cervical (23) and oral squamous cell carcinoma (OSCC) (23), with increased expression being associated with increased tumour cell proliferation, migration and also poor survival rates [253-255]. It has also been shown to play a key role in tumour metastasis, with circulating tumour cells that express CXCR4 metastasising along a chemotactic gradient from the blood to different organs that highly express its cognate ligand CXCL12, such as the liver, lymphatics, bone marrow and lungs [256-258] (Figure 13). The inhibition of the CXCR4-CXCL12 axis by various inhibitors has been shown to reduce the rate of metastasis in various models, including breast cancer, prostate cancer and myeloma [259-261]. Despite the number of cancers that are $CXCR4^+$, not all tumours express CXCR4, and intratumour heterogeneity of CXCR4 expression is often observed [254], with the $CXCR4^+$ subpopulations within a tumour being associated with increased malignancy [262-267].

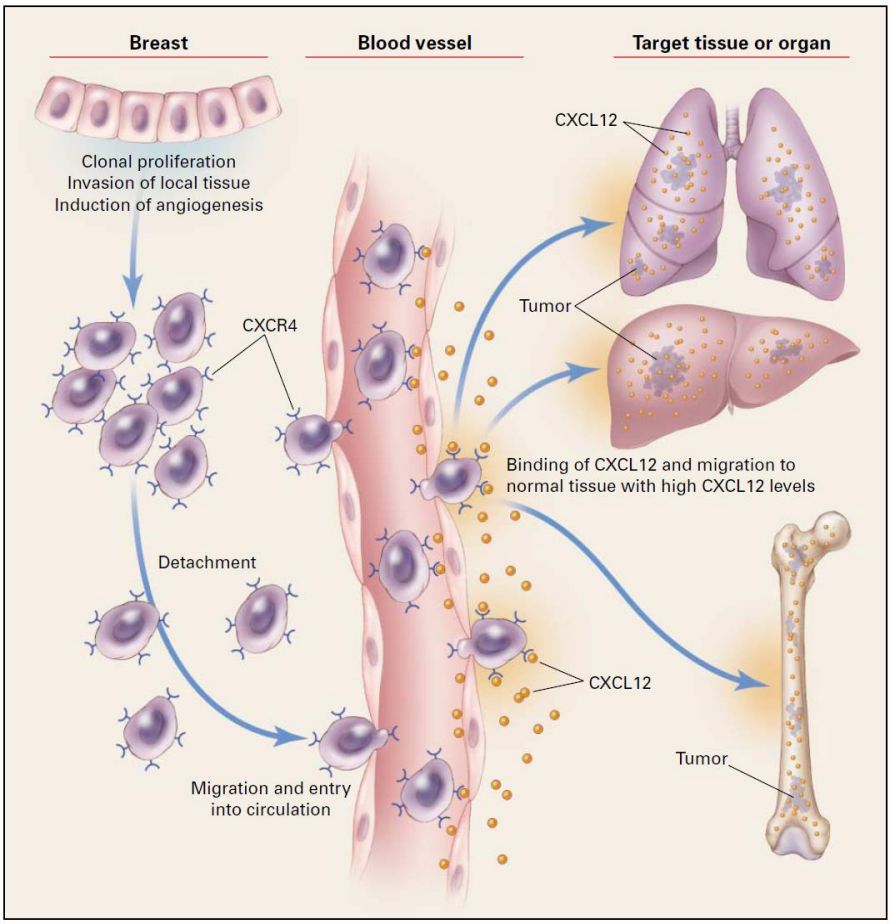


**Figure 13. CXCR4-dependent signalling pathways. Schematic depicting the signalling pathways activated upon CXCR4 binding to its cognate ligand CXCL12. [253]**

The CXCL12/CXCR4 axis impacts on cancer biology by either direct autocrine effects leading to the promotion of cancer cell growth [268], angiogenesis and metastasis and/or by other indirect methods such as the recruitment of $CXCR4^{+}$ cancer cells to organs expressing high levels of CXCL12, along a chemotactic gradient [269]. This axis also has the ability to induce various signal transduction pathways (Figure 14), promote the proliferation and migration of cancer cells, induce angiogenesis and promote the invasion of cancer cells and metastasis [270].

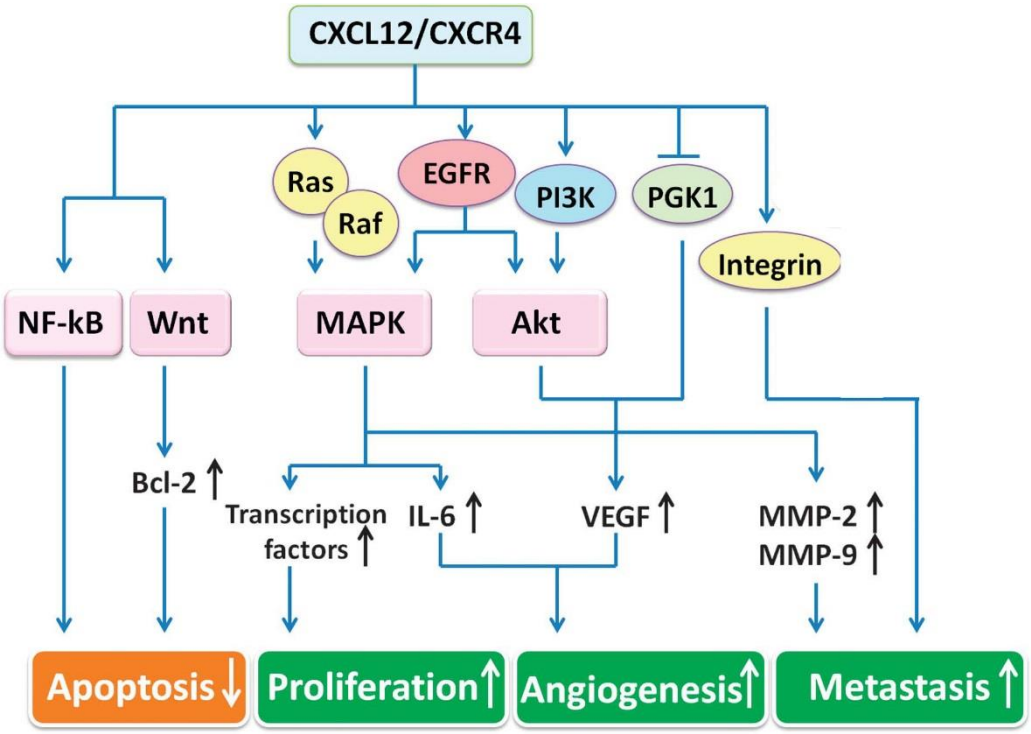


**Figure 14. CXCL12/CXCR4 signalling pathway in epithelial ovarian cancer. CXCL12/CXCR4 suppresses apoptosis and promotes proliferation, angiogenesis and metastasis in tumours by targeting multiple signalling pathways and transcription factors. [269]**

The activation of signalling pathways such as epidermal growth factor receptor (EGFR), mitogen-activated protein kinase (MAPK), Wnt, among others, by CXCL12 leads to increased tumour growth, migration and invasion of tumour cells. Binding of CXCL12 to CXCR4 induces the phosphorylation of EGFR and also the activation of other kinases such as Akt [271, 272], suggesting that an overlap exists between the CXCL12/axis and EGFR pathways that induce tumour cell proliferation in cancer [272]. CXCL12/CXCR4 may also be involved in a potential positive feedback mechanism, whereby Ras and MAPK are activated by CXL12 [273], leading to upregulation of c-myc, and other transcriptions factors, which is able to upregulate CXCR4 expression. This upregulation of CXCR4 positively feeds back into the signalling loop that amplifies further MAPK signalling and thus tumour growth [270].

Due to the role of the CXCR4/CXCL12 axis in cancer biology, the inhibition of this pathway may present a useful opportunity for future cancer therapies. Various CXCR4- or CXCL12-targeted constructs have been developed in preclinical models to inhibit this pathway. They include the CXCR4-targeted, clinically used, AMD3100 [274-277] and AMD3465 [278]. Plerixafor (AMD3100) is currently being clinically investigated as an agent to help the body overcome immune therapy resistance in pancreatic, ovarian and colorectal cancers, which are difficult to treat with immune therapy and chemotherapies (NCT02179970). It is also being trialled as a chemosensitizing agent for relapsed acute leukaemia and myelodysplastic syndromes in paediatric patients (NCT01319864). Copper-64-labeled Plerixafor was currently undergoing clinical trials for imaging CXCR4 expression in cancer patients, however this study has been terminated (NCT02069080).

AMD3100 represents the sole CXCR4 antagonist currently FDA- and EMA-approved for human use under the commercialised trade name of Plerixafor. It is used for haematopoietic stem cell mobilisation in combination with granulocyte colony stimulating factor (GCSF) in patients undergoing autologous stem cell transplantation for Hodgkin's disease, non-Hodgkin's lymphoma and multiple myeloma. AMD3100 has also been shown to inhibit the activation of CXCR4 by CXCL12, abrogating tumourigenesis [274, 277] as well as tumour growth [279] in preclinical models. The CXCR4-targeted monocyclam derivative, AMD3465, induces acute myeloid leukaemia (AML) cell mobilisation into the circulatory system, making it a potentially useful agent for a combination therapy when paired with chemotherapy in AML, which has been shown to increase survival rates in animal models [278]. CTCE-9908 is a small analogue peptide, made up of a dimer of CXCL12, which can competitively inhibit endogenous CXCL12 and reduce secretion of CXCL12. In combination with paclitaxel, it has been shown that it contributes to cytotoxicity involving mitotic catastrophe [280]. See Table 3 for a list of CXCR4-trgeted molecules currently under clinical investigation.

The pathways activated by CXCL12, may also be activated by other stimuli such as chemotherapeutic agents, anti-angiogenic agents and also radiation [281,

282], therefore blocking CXCL12 action alone may not be a sufficient strategy for cancer therapies as it has been suggested that activation of this pathway by therapies may be implicated in the development of therapy resistance [281]. Therefore, it has been proposed that combination of CXCL12-targeted therapies with chemotherapies may have increased efficacy than either therapy alone would have, demonstrated by preclinical studies [283-285]. On the other side of the signalling axis, inhibition of CXCR4 alone may also not be sufficient to block the downstream effects of CXCL12. CXCL12 is a known ligand for another GPCR present on cancer cells, called ACKR3, which has also been shown to have an interesting role in cancer biology [286].

**Table 3. CXCR4-targeted mocules in clinical use/trials**

| | | | |
|---|---|---|---|
| **AMD3100** | Chronic lymphocytic leukaemia; diabetic foot ulcer; glioma; neutropenia; non-hodgkin lymphoma; sickle cell anaemia | Launched | [287] |
| **LY-2510924** | Renal cell carcinoma; small cell lung cancer | Phase 2 | [288] |
| **USL-311** | Glioblastoma; inflammatory disease; solid tumour | Phase 2 | [289] |
| **Ulocuplumab** | Advanced solid tumour | Phase 2 | [290] |
| **BL-8040** | Bone marrow transplantation; metastatic pancreatic cancer; multiple myeloma | Phase 2 | [291] |
| **Burixafor** | Leukaemia; myocardial infarction; stem cell transplantation | Phase 2 | [292] |
| **PTX-9908** | Cancer; lupus nephritis | Phase 2 | [293] |
| **$^{177}$Lu-Pentixather** | Multiple myeloma | Clinical | [294] |

### 1.3.3 CXCR4 in IPF

Not only has CXCR4 been shown to play a crucial role in oncology, but it has also been linked with the pathogenesis of IPF. The recruitment of differentiated fibroblasts to the lung is a key step in the development of pulmonary fibrosis, and CXCL12 is critical to the development of these cells, as embryos lacking CXCl12 or its cognate receptor, CXCR4, exhibit defects such as lymphoid or myeloid haematopoiesis [251, 295]. As mentioned earlier, cells expressing CXCR4 are able to migrate along a CXCL12 gradient from the blood towards different organs. In the context of IPF, this includes bone marrow-derived stem cells (BMDSC), of which a subset of fibroblast progenitor cells, often referred to as "fibrocytes", may be recruited from the bone marrow, into the circulatory system and subsequently to sites of injury, such as the lungs via a CXCL12 concentration gradient [247, 296] where they can contribute to the fibrotic process (Figure 15) [297].

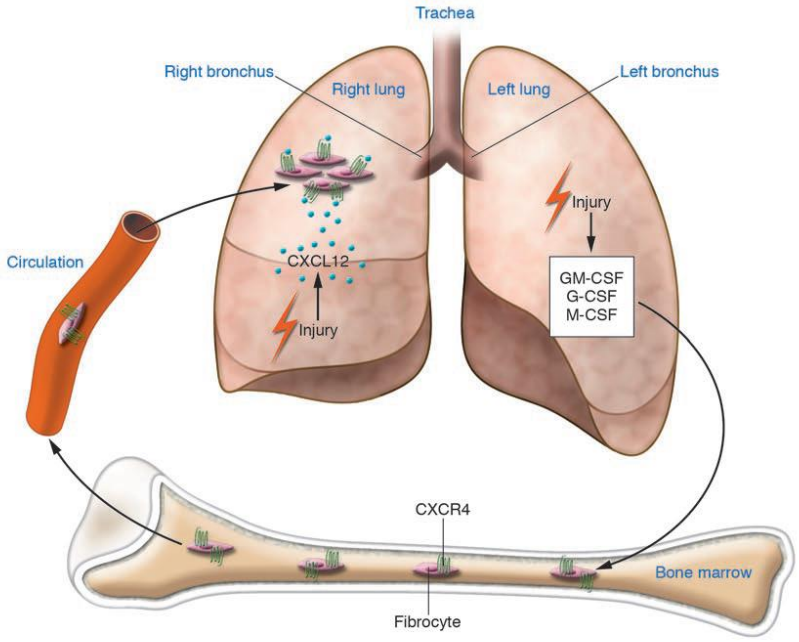


**Figure 15. The role of the CXCL12/SDF1-CXCR4 signalling axis in fibrocyte recruitment in pulmonary fibrosis. Lung derived factors that are expressed under conditions of lung injury (GM-CSF, G-CSF, M-CSF) communicate with the BM and induce expansion of the amount of fibrocytes in the bone marrow as well as recruit CXCR4⁺ cells into the circulation. These CXCR4⁺ fibrocytes traffic through the circulation and extravasate into the lungs in response to a CXCL12 chemotactic gradient established during injury. [291]**

This is in contradiction to earlier hypotheses, whereby fibrosis has been attributed to the activation of resident fibroblasts within the lungs, however studies have shown that these "fibrocyte" populations are source of activated fibroblasts that are able to contribute to fibrosis [297, 298].

Fibrocytes were first described in 1994 [299] as a bone-marrow derived cell in the circulation, able to exhibit traits of a mesenchymal nature and display a fibroblast-like morphology *in vitro*. Although they are rarely found in healthy tissue, they are easily detected in fibrotic tissues, including the lungs [300] of both animals [298, 301] and humans [302] and express various pro-fibrotic cytokines such as interleukin-13 (IL-13), TGF-β, and tumour necrosis factor-α (TNF-α), among others [301, 303, 304]. Upon their recruitment into injured lung, via a CXCL12 chemotactic gradient, transformation into α-smooth muscle actin (α-SMA)-expressing, ECM-producing, myofibroblasts occurs [297, 305, 306] and a loss of expression of various membrane receptors such as CXCR4, CD34, CCR2 and CD45 can be seen [298]. It is thought that this loss of receptor expression may be a mechanism by which activated myofibroblasts are trapped within injured lung tissue, preventing migration away from the lungs.

In patients with IPF, a high number of circulating fibrocytes is associated with worse prognosis, and fibrocyte counts in the blood of IPF patients were found to be significantly higher than that of healthy controls. As often occurs with IPF, acute exacerbations induce a considerable increase (10-fold) in fibrocyte counts compared to those in stable disease [307]. An inverse correlation was found between the numbers of circulating fibrocytes and clinical lung function parameters such as vital capacity (VC) and diffusing capacity of the lung for carbon monoxide (DLCO) [308] and positive correlations have been found between fibrocyte counts and serum levels of the inflammatory biomarker KL-6 [308].

Due to the key role of the CXCR4/CXCL12 axis in the recruitment of fibrocytes to the lungs in idiopathic pulmonary fibrosis, there has been considerable focus on the development of therapies that target fibrocyte differentiation, or target CXCR4, responsible for migration along CXCL12 gradients

to injured lungs. CXCR4-targeted antagonists, such as AMD3100, MSX-122 and TN14003, which will be discussed in more detail later, have been developed and used in an attempt to inhibit the trafficking of fibrocytes to injured lung tissue. Using preclinical models of bleomycin or radiation-induced, these small molecules have been shown to significantly reduce the extent of fibrosis [150, 309-311], although antagonist administration was performed prophylactically, rather than once fibrosis had already established, limiting the clinical relevance of the models as clinical IPF is typically identified at a late stage with established fibrosis potentially already apparent. Despite this, these studies may have some clinical relevance with regards to the prevention of radiation-induced lung injury in patients undergoing radiotherapy treatment [150]. There is, however, a requirement for further development of therapeutics that target fibrocyte differentiation or CXCR4, in order to abrogate the trafficking of $CXCR4^+$ fibrocytes to the injured lung in IPF.

## 1.4 Research Aims

The aim of this project is to develop peptidic or small molecule-based PET imaging or therapeutic agents that target integrin αvβ6 or chemokine receptor, CXCR4, for use in the detection of cancer and/or idiopathic pulmonary fibrosis.

This thesis has the following objectives:

- Evaluation of αvβ6-targeted peptides and derivatives thereof for binding to integrin αvβ6 via surface plasmon resonance and other solid phase assays to assess peptide binding kinetics and selectivity profiles to assist with identification of lead candidates to progress further for radiolabelling.

- Evaluation of radiolabelled peptides via investigation of serum stability, *in vitro* specificity using cell lines that overexpress, endogenously express and do not express integrin αvβ6.

- Evaluation of lead candidate(s) in an $\alpha v\beta 6^{+}$ xenograft model *in vivo* to assess *in vivo* radioligand specificity using blocking studies, as well as the assessment of *in vivo* metabolic probe stability.

- The evaluation of a small library of CXCR4-targeted compounds (configurationally-restricted tetraazamacrocycles) to assess affinity for target using competitive binding flow cytometry assays.

- The development of SPR methodology for the unique characterisation and validation of the binding kinetics of CXCR4-targeted small molecules to aid selection of lead candidates for imaging and chemo/radiotherapy applications, as the off-rate may be a key efficacy parameter.

# Materials and Methods

# 2 Materials and Methods

## 2.1 Materials and Hardware

Protected amino acids, coupling agents and Rink AM resin were supplied by Novabiochem (UK); anhydrous amine free DMF, piperidine, DIPEA, TFA, ammonium formate, Tl(III) trifluoroacetate, $LuCl_3 \times 6H_2O$ were purchased from Alfa Aesar (UK); HEPES, PBS, ethanol, triethylsilane and $Ga(NO_3)_3 \times H_2O$ were bought from Sigma-Aldrich (UK); DOTA-NHS ester was bought from CheMatech (France); spectroscopic grade HPLC solvents were supplied by VWR International (UK). All chemicals were used as supplied. HPLC analysis and semi preparatory purifications were carried out on ACE 5 C18 5A 250×4.6 mm or ACE 5 C18 5A 250×10 mm columns (HiChrom Ltd, UK) on an Agilent 1100/1200 series system equipped with a UV detector (series G1314A) and a NaI radio-HPLC detector (LabLogic). Data was recorded using LabLogic Laura (version 4.1.13.91) software. Mass analysis were carried out on Varian 500-MS IT mass spectrometer.

Primers for cloning were synthesised by Sigma Aldrich Company Ltd, Dorset UK. Restriction enzymes were purchased from New England BioLabs. For every case where buffers were made, water was purified using a Millipore Q-Grade 1 purification system to produce Milli-Q $H_2O$, which is deionised, passed through an activated charcoal filter and a 0.22μm membrane filter. Source and genotypes of *E.coli* strains used are detailed in the table below.

**Table 4. E.coli strains used throughout this project and their genotypes**

| *E.coli Strain* | *Genotype* | *Supplier* |
|---|---|---|
| ***XL10-Gold*** | Tet$^r$delta- (*mcrA)183 delta- (mcrCB-hsdSMR-mrr)173 endA1 supE44 thi-1 recA1 gyrA96 relA1 lac* Hte [F´ *proAB lacI$^q$ZDM15* Tn*10* (Tet$^r$) Amy Cam$^r$]. | *Agilent Technologies* |
| ***DH5α*** | fhuA2Δ(argF-lacZ)U169 phoA glnV44 Φ80 Δ(lacZ)M15 gyrA96 recA1 relA1 endA1 thi-1 hsdR17 | *University of Hull* |

A BIACORE T200 instrument (GE Healthcare, UK) was used for all SPR experiments. The instrument was regularly maintained according to GE Healthcare guidelines, using provided maintenance kits and also received biannual services from a GE Healthcare service engineer. All reagents used for GST-capture (BR-1002-23) and direct amine coupling were purchased from GE Healthcare. Plastic tubes, made from polypropylene to prevent sticking of peptides/small molecules to the tube walls, were purchased from GE Healthcare. Experiments were conducted on CM5 or CM4 Series S sensor chips. Once chips were removed from sealed packaging, chips were stored in running buffer to preserve the dextran matrix that coats the gold film surface. High purity HPLC gradient water was purchased from Fisher Scientific. Stock buffer solutions (10X) were purchased from GE Healthcare. 1X HBS-EP+ (), HBS-N () or HBS-P () solutions were prepared by diluting a stock (10X) with HPLC gradient water. Recombinant human integrins αvβ6 and $\alpha_v\beta_3$ were purchased from R&D Systems. Integrin antibody, 10D5, was purchased from Abcam.

## 2.2 Preparation of peptides, their DO3A conjugates and $^{nat}$Ga complexes.

Peptides, their DO3A conjugates and respective $^{nat}$Ga metallated derivatives were prepared by Dr Juozas Domarkas, University of Hull.

### 2.2.1 General considerations

Linear peptide sequences were synthesised following a Fmoc-based solid phase peptide synthesis (SPPS). The syntheses were carried out in small reactors fashioned from 2 or 5 mL syringes fitted with PTFE frit. All reactions were done on the swollen resin suspended in dry amine free dimethylformamide (DMF), if not indicated otherwise, under gentle swirling provided by an orbital shaker. Protected amino acids and coupling agents (N,N,N',N'-Tetramethyl-O-(1H-benzotriazol-1-yl)uronium hexafluorophosphate (HBTU) or 1-[Bis(dimethylamino)methylene]-1*H*-1,2,3-triazolo[4,5-*b*]pyridinium 3-oxid hexafluorophosphate (HATU)) were weighted in individual eppendorf tubes. The coupling agent was dissolved first and resulting solution was transferred over the amino acid using a pipette with disposable tips to avoid contamination. Dissolution

was facilitated by vortex mixing or sonication. The base (diisopropylethyl amine, DIPEA) was added immediately before the use. Reagents were introduced and removed by action of the syringe reactor plunger and resin was washed 4 times with DMF after every operation except in between of double coupling or deprotection steps.

### 2.2.2 Resin treatment prior and post synthesis

Prior to synthesis, resin was allowed to swell in dry dichloromethane (DCM) for two hours (2 × 1h) under gentle swirling. Dichloromethane was then replaced by dry amine free dimethylformamide (DMF) and the resin was washed 3 times with DMF. At the end of a synthesis or for an over-night interruption, the resin was washed 4 times with DCM, shrunk by washing it twice with methanol and twice with diethyl ether and dried under reduced pressure before storage at 4 $^{o}$C.

### 2.2.3 Fmoc-deprotection

The N terminal Fmoc protecting groups were cleaved using Fmoc cleavage solution containing 50% (v/v) of piperidine in DMF applied twice for 1 min and 5 min.

### 2.2.4 Coupling of the 1$^{st}$ amino acid

The first amino acid (Fmoc-Cys(Acm)-OH, 3 eq. to the load of the resin) was activated with HATU (3 eq.) in presence of DIPEA (4.5 eq.) and coupled to the free amine Rink resin for 3 h (1x1 h and 1 x 2 h).

### 2.2.5 Coupling of the second and consecutive amino acids

Second and consecutive amino acids were coupled in a similar way to the first one using a 4-fold excess of amino acid, coupling agent and DIPEA to free amine. For coupling on a primary N-terminus amine, HBTU was used together with an equimolar amount of DIPEA; 1 x 30 minutes reaction was sufficient. For coupling on a side chain primary amine group or a secondary amine (N-terminus of Pro or N-Me), HATU was used with an 1.5 eq of DIPEA; 1×1h was sufficient for coupling on the primary amine, but double coupling (2 × 1h) was necessary for coupling on a secondary amine.

### 2.2.6 Methylation of $\alpha NH_2$

$\alpha NH_2$ methylation was carried out in N-Me pyrolidinone (NMP) in a three step procedure. The resin washing between the steps was increased to 5 times.

***i. Sulphonylation***

The resin containing a free $\alpha NH_2$ group was treated with NMP solution containing *o*-nitrobenzenesulphonyl chloride(*o*-NBS-Cl, 4 eq.) and collidine (10 eq.) for 30 min (2 × 15 min).

***ii. N-Methylation***

The resin carrying a sulphonylated amine was pre-treated with 1,8-Diazabicyclo[5.4.0]undec-7-ene (DBU, 3 eq.) in NMP for 3 min before addition of dimethylsulfate (10 eq.) in NMP for 2 min. The treatment was repeated three times with a single wash with NMP in between.

***iii. o-NBS Deprotection***

The resin containing $\alpha$N-methylated sulphonylamide was treated with NMP solution containing mercaptoethanol (10 eq) and DBU (5 eq) for 10 min (2 × 5 min).

### 2.2.7 Cyclisation via S-S bond formation

Peptides containing Acm-S protected cysteine residues were cyclised on the resin by treatment with DMF solution of TI(III) trifluoracetate (4 eq.) for 2 hours (2 × 1h).

### 2.2.8 Cleavage from the resin

Cyclised peptides built on a Rink resin were simultaneously side chain deprotected and cleaved from the resin by treatment with a cleavage cocktail containing trifluoroacetic acid (TFA, 95%), triethylsilane (2.5%) and water (2.5%) for 2h. The mixture was then concentrated under reduced pressure and crude peptides precipitated as trifluoroacetate salt by addition of diethyl ether.

Peptide sequence built on a 2-Cl-trytyl resin was cleaved from the resin by treatment with 1,1,1,3,3,3-hexafluoro isopropanol (HIP) (20% v/v) in DCM for 2h (2 × 1h). Volatile HIP and DCM were removed under reduced pressure leaving

crude side chain protected peptide used for cyclisation without additional purification.

### 2.2.9 Cyclisation via peptide bond formation between αCOOH(first AA)-αNH$_2$(last AA)

To the side chain protected peptide dissolved in dry DCM was added diphenylphosphoryl azide (DPPA, 1.5 eq.) and solid sodium bicarbonate (3 eq.) and solution was stirred under inert gas overnight. At completion, confirmed by HPLC and/or MS analysis, the insoluble salts were removed by filtration and solvent evaporated under reduced pressure leaving a crude cyclised peptide as an oil. To remove the side chain protecting groups, the oil residue was treated with cleavage cocktail containing TFA (95%), triethylsilane (2.5%) and water (2.5%) v/v/v for 2 hours, volatiles were evaporated under reduced pressure and peptide precipitated as TFA salt by addition of diethyl ether.

## 2.3 Cell Culture

Adherent cell lines were maintained in appropriate media (Table 5. Details of cell lines used, their morphology and culture medium used.) and incubated at 37$^{o}$C in a humidified atmosphere of 95% air and 5% $CO_2$. To maintain cells in exponential growth phase, they were sub-cultured 2-3 times weekly dependent on growth rate. Culture media was aspirated from the culture flask and cells were washed with PBS to remove all traces of media. Cells were then incubated with TrypLE, trypsin enzyme replacement, at 37$^{o}$C until all cells had detached from the flask as visualised on a microscope. An equal volume of fresh culture media was added. Cells were either sub-cultured as per supplier recommendations, or, if required for seeding, transferred to a falcon tube before centrifugation at 200 x g for 5 minutes, re-suspending in fresh media and viable cells counted to allow seeding of a constant number of cells. For counting cells, trypan blue (4%) was mixed with cell suspension at a 1:1 ratio and cells were counted using a Neubauer haemocytometer. Testing was performed to ensure all cell cultures were mycoplasma-free. Frozen stocks of each cell line were continuously made to ensure constant stocks. At approximately 70-80% confluency, cells were harvested as detailed above, pelleted by centrifugation and re-suspended in fresh media

before counting. Cells were centrifuged again and the media removed. Cells were re-suspended in 1 mL of freeze media, 10% Dimethyl sulfoxide (DMSO) in FBS, before aliquoting into cryovials (Nunc/Thermo Scientific, UK), which were placed in a freezing container containing isopropanol in order to control a steady reduction in temperature, and incubated at -80$^{o}$C for 24 hours. After 24 hours, cells were transferred to liquid nitrogen Dewars for long-term storage. When required, a vial of cells was rapidly warmed to allow thawing and cells were transferred slowly into pre-warmed, appropriate, media before centrifugation and the supernatant discarded to remove traces of DMSO. Cells were re-suspended in appropriate media and transferred into a 25 cm$^2$ or 75 cm$^2$ flask and grown for at least 2 passages before being used in experiments. For transfected cell lines, selection antibiotic was added at least 24 hours post revival.

**Table 5. Details of cell lines used, their morphology and culture medium used.**

| Cell Line | Tissue/Morphology | Culture Media | Subculture Ratio |
|---|---|---|---|
| **MEFwt** | Murine embryonic fibroblast, adherent | DMEM (high glucose), 10% (v/v) FBS | 1:3 to 1:10 |
| **MEFβ6** | Transfected murine embryonic fibroblast expressing integrin β6 subunit, adherent | DMEM (high glucose), 10% (v/v) FBS, 5 µg/ml blasticidin | 1:3 to 1:10 |
| **BxPC3** | Pancreatic ductal adenocarcinoma, epithelial, adherent | RPMI-1640, 10% (v/v) FBS | 1: 3 to 1:6 |
| **MDA-MB-468** | Human mammary gland, epithelial, adherent | RPMI-1640, 10% (v/v) FBS | 1:2 to 1:4 |
| **HT-29** | Human colorectal adenocarcinoma, epithelial, adherent | DMEM (high glucose), 10% (v/v) FBS | 1:3 to 1:8 |
| **U87** | Glioblastoma, epithelial, adherent | DMEM (high glucose), 10% (v/v) FBS | 1:2 to 1:5 |
| **Jurkat** | Leukaemia, lymphoblast, suspension | RPMI-1640, 10% (v/v) FBS | Maintain between $1x10^5$ and $1x10^6$ cells/ml |
| **Cf2Th** | Dog thymocyte, adherent | DMEM (high glucose), 10% (v/v) FBS | 1:2 to 1:6 |
| **Cf2Th-CXCR4-GST** | Transfected dog thymocyte expressing GST-tagged CXCR4, adherent | DMEM (high glucose), 10% (v/v) FBS, 2 µg/ml puromycin | 1:2 to 1:6 |
| **Cf2Th-CXCR4-C9** | Transfected dog thymocyte expressing C9-tagged (TETSQVAPA) CXCR4, adherent | DMEM (high glucose), 10% (v/v) FBS, 0.4 mg/ml G418 | 1:2 to 1:6 |

## 2.4 Characterisation of receptor expression by flow cytometry

Cells were grown to approximately 60-80% confluency in a 75 $cm^2$ culture flask before removal of medium and washing twice with ice-cold phosphate-buffered saline (PBS). Flasks were placed on ice at all times to prevent receptor internalisation. Cells were removed from the flask using a cell scraper, centrifuged at 200 x g for 5 min before re-suspending in 50 µL at a density of $4x10^6$ cells/ml.

For evaluation of integrin αvβ6 expression, anti-integrin αvβ6 antibody (clone 10D5; Abcam, UK) or mouse $IgG_{2A}$ isotype control antibody was added to

the cells at a final concentration of 10 µg/mL and incubated on ice for one hour. Cells were washed three times in ice-cold PBS before the addition of Alexa Fluor 568nm (ThermoFisher #A-11004; Final conc. 10 µg/mL) or phycoerythrin (PE)-conjugated anti-mouse secondary antibody (Biolegend #405307) for 45 minutes on ice in darkness. Cells were washed a further three times in ice-cold PBS and re-suspended in ice-cold FACS flow buffer (BD Biosciences) prior to analysis using a FACSCalibur (Becton Dickinson USA).

For evaluation of CXCR4 expression, 10 µL of either PE conjugated anti-human CXCR4 monoclonal antibody (clone 12G5) or PE-conjugated mouse $IgG_{2A}$ isotype control antibody (0.25 µg/$10^6$ cells) for 60 minutes on ice in the dark. Cells were washed three times in ice-cold PBS and re-suspended in ice-cold FACS flow buffer prior to analysis.

Ten thousand events were acquired per sample and data were analysed using Cellquest software (BD Biosciences, USA), with the geometric mean fluorescence detected used to quantify relative receptor expression.

## 2.5 Evaluation of peptide binding to integrin αvβ6 by competitive enzyme-linked immunosorbant assay (ELISA)

### 2.5.1 Determination of $ED_{50}$ 10D5 mAb concentration for competitive ELISA experiments

The wells of a 96-well plate were coated with 100 ng (100 µl of 1 µg/mL stock) of αvβ6 in ELISA coating buffer (50 mM sodium bicarbonate, pH 9.6) and incubated overnight at 4°C. The following morning, the wells of the plate were washed 3 times with wash buffer (50 mM Tris, 0.15 M NaCl, 5 mM $MgCl_2$, 1 mM $CaCl_2$, 0.05% Tween 20, pH 8.0) using an automated plate washer, before being blocked for 1 hour at room temperature with blocking solution (50 mM Tris, 0.15 M NaCl, 5 mM $MgCl_2$, 1 mM $CaCl_2$, 1% BSA, pH 8.0). Varying concentrations (10 µg/mL to 100 pg/mL) of αvβ6-specific 10D5 mAb were incubated with αvβ6 for 1 hour at room temperature. After 3 further washes, Horseradish peroxidase (HRP) conjugated anti-mouse secondary antibody was diluted 1 in 1000 in 100 µl and added to wells for 45 minutes at room temperature. Any unbound secondary

antibody was removed with 3 washes and 100 µl 3,3',5,5'-Tetramethylbenzidine (TMB) substrate was added and allowed to react with HRP for 10-15 minutes, resulting in a colour change to blue. To stop the reaction, 100 µl of 2 N $H_2SO_4$ was added, which resulted in a colour change from blue to yellow. The absorbance of the wells was detected at 450 nm on a plate reader.

### 2.5.2 Competitive Binding ELISA

Competitive ELISA experiments were conducted in the same way as in 2.5.1, except for an added incubation step. Following blocking with blocking solution, peptides and/or their cold-flourine labelled derivatives were serially diluted (1:10) from 1 µM to 10 pM in PBS (100 µl) before being incubated with integrin at room temperature for 1 hour. Plates were washed with washing buffer 3 times before incubation with 50 ng/mL 10D5 mAb (100 µl). Further washes and incubations with HRP-conjugted antibody and subsequent addition of TMB and $H_2SO_4$ were performed as described in 2.5.1.

Controls consisted of empty wells (negative control) and integrin-coated wells incubated only with 10D5 mAb (positive control) and HRP-conjugated secondary antibody.

All results were normalised to antibody binding to αvβ6

## 2.6 Evaluation of integrin selectivity of peptides by surface plasmon resonance

### 2.6.1 pH Scouting

Before amine-coupling of JD2-RGD1 to a CM5 series S sensor chip, the optimum pH of the ligand-containing solution to be used for immobilisation was determined. JD2-RGD1 was diluted in 10 mM Sodium Acetate at pH 5.5, 5.0, 4.5 and 4.0. Each solution was injected over a sensor chip surface, which had not been activated, at 5 µl/min for 1-2 minutes and the response gained due to electrostatic

interaction between sample and sensor chip was observed. A subsequent wash using a low pH wash solution such as NaOH removed any remaining traces of peptide from the sensor surface.

The optimum pH of the buffer used in the ligand solution was determined from the generated sensorgrams. The sensorgram trace exhibiting the largest response indicated which pH buffer should be used in immobilisation experiments for a particular ligand.

### 2.6.2 Immobilisation via amine coupling chemistry

Amine coupling of JD2-RGD1 to a CM5 series S sensor chip using an amine coupling kit (GE Healthcare, UK) as per manufacturer instructions. Amine coupling kit reagents, 0.4 M 1-ethyl-3-(3-dimethylaminopropyl)-carbodiimide (EDC) and 0.1 M N-hydroxysuccinimide (NHS) in water, were made prior to use and frozen at -20$^{o}$C until required.

Amine coupling was carried out at 25$^{o}$C at a flow rate of 5 µl/min Carboxylic acid groups present on the carboxyl-derivatised CM5 sensor chip were activated by injecting a 1:1 mixture of 0.4 M EDC and 0.1 M NHS for 7 minutes. JD2-RGD1 was made up in a pre-optimised immobilisation buffer (2.6.1) at 20-50 µg/mL and injected for 7 minutes. Any excess reactive groups were deactivated with an injection of 1 M ethanolamine, pH 8.5 for 7 minutes. The amount of ligand immobilised was represented by the difference in response level between the initial baseline and the new baseline following ethanolamine injection.

### 2.6.3 Binding Kinetic Screening by SPR

The binding of αvβ6 or αvβ6 dissolved in running buffer (HBS-N) containing 5 mM $MgCl_2$ and 1 M $CaCl_2$ was shown by injection of analyte at 30 µL/min for 3 minutes, before allowing dissociation to occur for a further 10 minutes. All data were processed and analysed using BIACORE evaluation software (version 1.0) and the dissociation constant of the generated sensorgrams determined using a 1:1 Langmuir model fit.

## 2.7 Radiochemistry

All radiochemistry was performed by Juozas Domarkas, University of Hull.

[$^{68}$Ga]$GaCl_3$ was obtained either from an Eckert & Ziegler iGG100 $^{68}$Ge/$^{68}$Ga or an iThemba $^{68}$Ge/$^{68}$Ga generator eluted with 4 mL of aqueous 0.6 M HCl solution. The generator elution was diluted 6-10 times with deionised water and produced $^{68}$Ga was trapped on Strata$^{TM}$-X-C 33 m Polymeric Strong cation cartridge (Phenomenex). [$^{68}$Ga]$GaCl_3$ was eluted from the cartridge by 1.0-1.5 mL of acetone containing 2% of 0.1M $HCl_{aq.}$ and dried in a 1.1 mL conical HPLC vial (Kinesis) by a stream of inert gas while heating at 90$^{o}$C. A lyophilised aliquot of 25 µg of DO3A-JD2-RGD1 was dissolved in 200 µL of 10% methanol / 0.1M HEPES pH 4.5 buffer. The precursor solution was transferred onto dried $^{68}GaCl_3$ and reaction was shaken while heated at 90$^{o}$C for 10 min. Radiolabelled tracer was purified by a semi preparatory HPLC eluted with a mixture of MeOH (solvent A) and 0.1M ammonium formate pH 6.5 (solvent B) (4.7 mL/min, gradient from 40% A to 60% A in 20 min.) giving a decay corrected preparative radiochemical yield of 13 ± 8 % (n=6). The tracer containing fraction ($R_t$ = 13 min) was diluted 3-folds with deionised water and passed through a home-made Waters cartridge containing 80 mg of Oasis HLB LP (Waters) sorbent. Cartridge was washed with 0.05 M $HCl_{aq}$ and water, dried by a current of inert gas and eluted with 0.5 mL of ethanol. Ethanol was evaporated by a stream of inert gas under heating and a radiotracer formulated in PBS solution, filtered through a 0.22 µm filter for sterility and used for *in vitro* and *in vivo* evaluation.

### 2.7.1 Assessment of Specific Activity (SA)

Specific activity measurements were performed by Juozas Domarkas, University of Hull.

3-8 MBq of [$^{68}$Ga]Ga-DO3A-JD2-RGD1 was injected into analytical HPLC eluted with a mixture of MeOH (solvent A) and 0.1M ammonium formate pH 6.5 (solvent B)(1.0 mL/min, gradient from 40% A to 60% A in 20 min). Product containing fraction was collected and activity measured in Capintec dose

calibrator. The area under the curve (AUC) of UV trace was measured and SA calculated using a calibration curve.

To generate the calibration curve, [$^{nat}$Ga]Ga-DO3A-JD2-RGD1 was dissolved in MeOH and diluted in deionised water to a final concentration of 100 µg/ml. This was diluted 1:2 and 1:50 to create stock solutions for calibration. Various masses (5 µg – 0.06 µg) were analysed by HPLC and the AUC for trace peaks determined and plotted against peptide mass.

### 2.8 Receptor binding assay

Cells were seeded into the wells of a 6-well plate ($5x10^5$/well) and left to adhere to the plates overnight (16h) at 37°C, 5% $CO_2$. Cells were incubated with 37 kBq/ml (1 µCi/ml) of radiotracer (<50 µL) in 2 mL PBS for 60 minutes at 4°C. Following incubation, cells were washed quickly three times with ice-cold PBS and cells were harvested in PBS by scraping. The radioactivity associated with the harvested cells was measured using an Automatic γ Counter (Wizard 3" Wallac). The cell-associated radioactivity represented both the cell surface-bound radioactivity and internalised radioactivity. Data are expressed as percentage of ID (%ID) per million cells.

### 2.9 Receptor internalisation assay

Cells were seeded into the wells of a 6-well plate ($5x10^5$/well) and left to adhere to the plates overnight at 37°C, 5% $CO_2$. Cells were incubated with 37 kBq/ml of radiotracer in serum-free media for 60 minutes at 37°C, 5% $CO_2$. Following incubation, cells were washed quickly three times with ice-cold PBS to remove unbound radiotracer prior to a 10-minute acid wash (50 mM glycine-HCl in PBS, pH 2.8) at room temperature to remove surface bound activity. Cells were solubilised in NaOH. The supernatant, representing surface bound radioactivity and cells, representing internalised radioactivity, were collected for γ counting [312]. The percentage of internalised radiotracer was quantified as the percentage of total bound radioactivity, which was defined as the sum of the surface bound radioactivity and internalised radioactivity.

**Equation 2. Formula for the determination of internalised radioactivity**

$$\%\ Internalised\ Radioactivity = \frac{Internalised\ Radioactivity}{(Internalised + Surface\ bound\ Radioactivity)} \times 100$$

## 2.10 Serum Stability Studies

2 MBq of dried [$^{68}$Ga]Ga-DO3A-JD1-RGD1 or [$^{68}$Ga]Ga-DO3A-JD2-RGD1 was incubated at 37$^{o}$C in human serum up to 3 h. At various time points (30 min, 1h, 2h, 3h), an aliquot was sampled out, proteins were precipitate by addition of a double volume of ice cold acetonitrile and removed by centrifugation (14.5k rpm, 5 min). The supernatant was analysed by analytical HPLC eluted with a mixture of MeOH (solvent A) and 0.1M ammonium formate pH 6.5 (solvent B)(1.0 mL/min, gradient from 40% A to 60% A in 20 min).

## 2.11 LogD$_{7.4}$ Analysis

Following elution from a C18 cartridge 0.5 – 1 MBq of radiotracer was dried with a stream of inert gas whilst heating. Radiotracer was recovered in 600 µl PBS and 500 µL of radiotracer solution was mixed with 500 µl octanol in a 1.5 ml microcentrifuge tube. The mixture was vigorously mixed by vortexing for 5 minutes before separation by centrifugation (14,000 RPM, 3 min). 100 µl octanol and 20 µl PBS were added to 900 µl and 980 µl PBS, respectively, in γ counting tubes and the activities determined by an Automatic γ counter. LogD$_{7.4}$ was calculated by applying a log function to the ratio of average activities of triplicate measurements of octanol and PBS.

## 2.12 *In vivo* xenograft model

Animal studies were performed in accordance with the United Kingdom's Guidance on the Operation of Animals (Scientific Procedures) Act 1986 and within guidelines set out by the United Kingdom National Cancer Research Institute Committee on the Welfare of Animals in Cancer Research. Tumour implantations and biodistribution studies were carried out by Dr Christopher Cawthorne. (PPL licence number: 60/4549).

Female NSG (NOD.*Cg-Prkdc*$^{SCID}$*Il2rg*$^{tm1Wjl}$*/SzJ*) mice (age 21-27 days), weight 20-25g) were purchased from Charles River Laboratories. Mice were subcutaneously (s.c) implanted with 5x10$^6$ BxPC3 cells in 100 µl of 1:1 serum-free media:Geltrex basement membrane (Thermo Fisher, UK) in the upper flank under anaesthesia. Tumour sizes were measured every 2 days using callipers, and tumour volume was determined by using the equation diameter(1) *diameter(2) at 90° *height to give volume in mm$^3$.

## 2.13 PET Imaging Studies

Whole body PET and CT images were acquired on the Sedecal SuperArgus 2R PET scanner (Sedecal, Spain). For imaging studies, mice were induced with 1L/min 5% isoflurane/oxygen (v/v) anaesthesia and maintained at 2% before cannulation in the tail vein using a bespoke catheter. Either naïve mice or BxPC3 tumour-bearing mice were scanned as detailed in Table 6. Scanning protocols for αvβ6 imaging in naive and tumour-bearing mice.

**Table 6. Scanning protocols for αvβ6 imaging in naive and tumour-bearing mice**

| | Naïve animals | | | Tumour-bearing animals | |
|---|---|---|---|---|---|
| **Tracer** | [$^{68}$Ga]Ga-JD1 | [$^{68}$Ga]Ga-JD2 | [$^{68}$Ga]Ga-JD2 | [$^{68}$Ga]Ga-JD2 | [$^{68}$Ga]Ga-JD2 |
| **Injected Dose (MBq)** | 9.32 ± 0.23 | 4.79 ± 0.04 | 2.88 ± 0.84 | 5.83 ± 1.34 | 8.99 ± 0.08 |
| **Blocking agent** | None | None | anti-αvβ6 | None | anti-αvβ6 |
| **Blocking dose (mg/kg)** | N/A | N/A | 2.5 | N/A | 2.5 |
| **Imaging Protocol** | 90 minutes dynamic scan | | | 60 minutes static scan | |

Upon placement into an imaging cell (Minerve, France), temperature and respiration of the mice was continuously monitored for the duration of the scan. Mice were maintained at 1% isoflurane/oxygen (v/v) anaesthesia during scanning. Following PET scans, a CT image was acquired for anatomic co-registration (40kV, 140µA, 360 projections, 8 shots). For specificity studies, mice were injected with a blocking dose of 2.5 mg/kg 10D5 antibody administered intraperitoneally 24 hours prior to injection of radiotracer. PET emission data were reconstructed using a 3D

ordered subset expectation maximisation (OSEM3D) algorithm [313] with corrections for randoms, scatter and attenuation applied. Data were analysed using AMIDE and Vivoquant (InVicro, Boston, USA) softwares [314], with regions of interests (ROI) drawn over tumours and various tissues to generate time activity curves. Standardised uptake values (SUV) were obtained after correction for injected dose and animal weight.

### 2.14 *Ex vivo* Biodistribution Studies

Biodistribution studies were performed by Dr Christopher Cawthorne. Mice were induced with 1L/min 5% isoflurane/oxygen (v/v) anaesthesia and maintained at 2% isoflurane for radiotracer injections. 68Ga-JD2 (activity range) was directly injected into the tail vein using a positive displacement syringe in a volume of 100 µl. Exact injected volume was determined by weighing the loaded syringe both before and after injection. After approximately 1 hour 45 minutes, animals were sacrificed under anaesthesia and tissues of interest such as heart, lung, liver, spleen, kidneys, tumour etc. were collected in pre-weighed γ counting tubes. Tissues were transferred to pre-weighed γ counting tubes to determine the mass of the tissue, and the radioactivity contained within was counted in a γ spectrometer (Automatic γ counter, Wizard 3" Wallac). Counts per minute (cpm) for each tissue was normalised to the total injected dose of radioactivity to give the percentage of injected dose per gram of tissue (%ID/g). To determine the total injected dose, 10 µl volumes of radiotracer were added to 990 µl PBS and counted. The cpm recorded by counting was used as a reference to determine the amount of radioactivity injected into each mouse based on the volume of radiotracer injected.

For blocking studies, biodistribution analysis was carried out as described above, however animals undergoing blocking received an intraperitoneal injection of 10D5 mAb (2.5 mg/kg) 24 hours prior to radiotracer injection.

### 2.15 Radiometabolite Analysis

Following urine retrieval of urine, radio-HPLC analyses were performed by Dr Juozas Domarkas. Immediately following imaging studies, urine was obtained

from mice (n=3) and urine proteins were precipitated by addition of a double volume of ice-cold acetonitrile and removed by centrifugation (14,500 RPM, 5 min). The supernatant was analysed by an analytical HPLC eluted with a mixture of MeOH (solvent A) and 0.1 M ammonium formate pH 6.5 (solvent B) (1.0 ml/min, gradient from 10% A/90% B to 100% A/0% B in 30 min).

### 2.16 Immunohistochemistry

For immunohistochemistry, animals were sacrificed following PET imaging studies and various tissues excised prior to fixation in formalin for 24 hours and transferred to 70% ethanol until processing. Tissues were dehydrated glass bottles containing 50% ethanol (2 hours), 75% ethanol (1.5 hours), 95% ethanol (1.5 hours), 100% ethanol (1 hour) twice, 100% ethanol:histoclear (1:1 (v/v)) (1.5 hours), histoclear (overnight), prior to embedding in paraffin. Histoclear was removed from the tissue-containing bottle and the tissue was placed in a bottle containing molten paraffin wax and incubated at 58$^{o}$C for 3 hours. The paraffin was replaced with fresh molten paraffine and incubate at 58$^{o}$C for a further 3 hours. This was repeated so that tissues were incubated in fresh paraffin three times prior to mounting on a tissue cassette and leaving on ice to set. Once set, paraffin-embedded tissue sections were sectioned to a thickness of 4 µm.

For paraffin embedding and paraffin embedding. Immunohistochemistry was carried out using a HRP-AEC tissue staining kit (R&D Systems; CTS006) as per manufacturer protocols. 4 µm sections were stained for integrin β6 subunit expression using an anti-mouse rabbit polyclonal integrin β6 antibody (GeneTex; GTX118323). Tissue sections were dewaxed in histoclear prior to hydration in decreasing concentrations of ethanol, rinsing in deionised water and rehydrated in PBS for 10 minutes. Antigen retrieval using Digest-All-3 (ThermoFisher Scientific, UK) was performed at 37$^{o}$C for 10 minutes before blocking of non-specific peroxidase activity and protein binding with peroxidase blocking reagent and rabbit serum, respectively. Slides were washed and incubated with avidin-blocking reagent prior to incubation with either an anti-β6 antibody or an IgG isotype antibody overnight at 4$^{o}$C in a humidified chamber. All slides were washed before

incubation with a biotinylated anti-rabbit secondary antibody for an hour. After further washes, HSS-HRP was added to the slides for 30 minutes, followed by addition of AEC chromagen-containing buffer for 5-10 minutes. Slides were rinsed in deionised water and counterstained with haematoxylin before they were mounted and examined under the microscope.

### 2.17 Evaluation of small molecule binding to CXCR4 by flow cytometry

To demonstrate the ability of small molecule inhibitors to inhibit CXCR4, Jurkat cells were re-suspended to $4x10^6$ cells/ml in 50 µl ice-cold PBS (5 mM $MgCl_2$, 1 mM $MgCl_2$) prior to addition of small molecule antagonists at a final concentration of 20 µM for 60 minutes on ice. Cells were washed three times in ice-cold PBS to remove excess antagonist and 10 µl of PE-conjugated human CXCR4 mAb (clone 12G5) was added to the cells and incubated for a further 60 minutes on ice and in darkness. Following incubation, cells were washed a further three times prior to re-suspending cells in ice-cold FACS flow buffer and analysing using a FACSCalibur (FL-2 channel). Samples containing only anti-CXCR4 mAb or $IgG_{2A}$ isotype control antibodies were used as positive and negative controls, respectively.

To demonstrate binding of CXCR4 small molecule antagonists, competitive binding experiments were performed as above using a range of antagonist concentrations. The potency of small molecule binding to CXCR4 was reported as the concentration required to inhibit 50% ($IC_{50}$) of anti-CXCR4 antibody binding. The mean fluorescent intensity (MFI) detected for each sample by the FACSCalibur, representing fluorescence of anti-CXCR4 antibody, was used as a measure of antibody binding and for calculating the percentage inhibition by CXCR4 antagonists in the following equation:

**Equation 3. Formula for the determination of the percentage antibody inhibition**

$$\%\ mAb\ inhibition = 100 - \frac{(MFI\ cells\ with\ antagonist - MFI\ negative\ control)}{(MFI\ positive\ control - MFI\ negative\ control)} \times 100$$

## 2.18 Molecular Cloning of GST-tagged CXCR4

### 2.18.1 RNA Extraction

Extraction of RNA was performed using the E.Z.N.A® Total RNA Kit (VWR). Jurkat cells were used as they express CXCR4. Cells were trypsinised and collected as a cell pellet prior to lysis. The cells were lysed by adding 350 µl (for < $5x10^6$ cells) or 750 µl (for > $5x10^6$ cells) TRK Lysis buffer before mixing thoroughly using a vortex. The lysate was passed through a 19-gauge needle 5-10 times to shear high molecular-weight DNA. An equal volume of 70% ethanol was added to the cell lysate before mixing thoroughly using a vortex. The lysate was applied to a HiBind RNA mini column inserted into a 2 ml collection tube and centrifuged at 20,000 x g for 1 minute at room temperature. Further wash steps were performed using RNA Wash buffer I and RNA wash buffer II as per manufacturer's instructions. The column was then centrifuged at maximum speed for 2 minutes to dry and remove any residual ethanol that may inhibit downstream applications. All RNA samples were then eluted into clean nuclease-free sample tubes using 40-70 µl DEPC water and centrifuging at maximum speed for 1 minute.

### 2.18.2 Quantification of nucleic acids

The quantification of RNA/DNA was achieved using a NanoDrop Lite Spectrophotometer. The purity of the sample was measured by calculating the ratio $A_{260nm}/A_{280nm}$ which shows contaminant protein content in relation to DNA. An efficient maxiprep or miniprep yielding DNA or RNA has a ratio of 1.8 or 2.0, respectively. The NanoDrop Lite Spectrophotometer was used to calculate the concentration of RNA and DNA prior to setting up RT-PCR and ligation reactions, respectively.

### 2.18.3 Reverse-Transcriptase Polymerase Chain Reaction (RT-PCR)

RT-PCR of RNA extractions was achieved using qScript™ Flex cDNA kit (Quanta). The reaction was achieved by mixing up to 1µg RNA with 2 µl OligodT in a volume of 15 µl. The mixture was incubated for 5 minutes at $65^0$C and snap chilled on ice. To the mixture, 4 µl qScript Flex Reaction Mix (5X) and 1 µl qScript

Reverse Transcriptase was added to achieve a final volume of 20 µl. The mixture was incubated as follows:

**Table 7. Incubation protocol for RT-PCR**

| Step | Temperature | Duration |
|---|---|---|
| **1** | 42°C | 60-90 mins |
| **2** | 85°C | 5 mins |
| **3** | Hold at 4°C | |

Following cDNA synthesis, 1/5$^{th}$ to 1/10$^{th}$ of the first-strand reaction (2-4 µl) was used for PCR amplification.

### 2.18.4 Agarose Gel Electrophoresis

Agarose gel electrophoresis as used to separate linear fragments of DNA relative to their size. 1-2% agarose gels were constructed by adding the appropriate mass of agarose to 1 X TAE buffer (0.04 M Tris-acetate, 1 mM ethylene-diaminetetra-acetic acid (EDTA) pH 8.0) and heating in a microwave oven. After cooling, Sybr Safe (13000X) was added to a final concentration of 1X and the gel was poured into a casting tank and allowed to set with a lane comb inserted. DNA samples were mixed with loading buffer (0.25 % bromophenol blue, 40% Milli-Q $H_2O$) before being loaded and subjected to 100V until the loading buffer dye had migrated towards the end of the gel. The bands were visualised and imaged using either a UV transilluminator or a ChemiDoc™ XRS+ System.

### 2.18.5 Polymerase Chain Reaction

#### 2.18.5.1 Gradient Polymerase Chain Reaction

To determine the optimum practical annealing temperature for PCR amplification, a temperature gradient PCR assay was set up. Multiple reactions were set up as in 1.2.4.2 and using the gradient scheme in the BioRAD thermal cycler, each tube underwent the annealing step at varying temperatures. All PCR products were then run out on a 1-2% agarose gel (1X Sybr Safe) and analysed by a ChemiDoc™ XRS+ System. The annealing temperature for future PCR amplification was chosen by selecting the brightest band as determined by the ChemiDoc™ XRS+ System.

#### 2.18.5.2 Amplification of DNA using the Polymerase Chain Reaction

The amplification of DNA fragments for the purpose of cloning was carried out using the Polymerase Chain Reaction. The PCR reaction first uses a high temperature (95$^{o}$C) to melt the bonds between the bases of dsDNA. The exposed bases are allowed to anneal to matching sequences in oligomeric primers of varying length, depending on the project, by lowering the reaction temperature below the specific melting temperature of the primers. Finally, the reaction is held at 72$^{o}$C to allow polymerase binding and synthesis of dsDNA fragments.

First, a PCR mastermix was assembled as listed below:

**Table 8. Composition of PCR mixtures for PCR product amplification**

| Reagent | Volume/sample (µl) | Volume (µl) for Mastermix (x10) |
|---|---|---|
| **10X Key Buffer** | 2.5 | 25 |
| **25 mM $MgCl_2$** | 1.5 | 15 |
| **dNTP mix (10 mM each)** | 0.4 | 4 |
| **Forward Primer (10 µm)** | 0.5 | 5 |
| **Reverse Primer (10 µm)** | 0.5 | 5 |
| **AccuPOL DNA Polymerase** | 0.5 | 5 |
| **cDNA** | 2 | - |
| **PCR-grade H2O** | 17.1 | 171 |
| **Total** | **25** | **230** |

The mastermix was divided into 10x 0.2 ml PCR tubes in 23 µl volumes before adding 2 µl cDNA to relevant samples. A negative DNA-free control was used to check for contamination. The samples were subjected to thermal cycling as follows:

**Table 9. Thermal cycling protocol for PCR reactions**

| Step | Temperature | Duration | Step Purpose |
|---|---|---|---|
| **1** | 95°C | 2 mins | Initial denaturation step |
| **2** | 95°C | 30 secs | Denaturation step |
| **3** | 58-68°C | 30 secs | Annealing step |
| **4** | 72°C | 1-2 mins (1 kb/min) | Elongation step |
| **Repeat steps 2-4 for 25-35 cycles** | | | |
| **5** | 72°C | 10 minutes | Extension step |
| **6** | Hold at 4°C | | |

The annealing temperature is dictated by the specific primers used and their melting temperatures. Annealing temperature is calculated by using the following equation:

**Equation 4. Formula for determination of optimal annealing temperature of cloning primers**

$$T_m = 4 \times (*G + C) + 2 \times (*A + T)$$

Elongation time was adjusted according to the extension speed of the polymerase used, which was typically between 1 and 2 kb per minute.

### 2.18.6 Polymerase Chain Reaction Product Purification

A fraction (5 µl) of PCR product from PCR amplification experiments was analysed by gel electrophoresis (1.2.4). Remaining PCR product was purified using the E.Z.N.A® Cycle-Pure Kit (Omega Bio-Tek®). 4-5 volumes of CP buffer was added to the PCR product before loading onto a HiBind® DNA Mini Column and spinning at 13,000 x g for 1 minute. Filtrate was discarded before repeating using DNA wash buffer. Filtrate was discarded and the empty column was dried by spinning for 2 minutes to remove traces of ethanol that may inhibit downstream enzymatic reactions. The DNA was eluted using 30-50 µl elution buffer.

### 2.18.7 Restriction Endonuclease Digestion of DNA

DNA constructs were digested for diagnostic purposes and vector ligation. The digest solution should contain no more than 12.5% glycerol (present in enzyme storage buffer) and to be buffered by a $10^{th}$ (v/v) of appropriate 10X buffer. For diagnostic tests, approximately 300ng of plasmid DNA was used. For ligation reactions, 3-5 µg of plasmid DNA was cut with a total of 2 µl restriction enzyme in a total volume of 20 µl. Fragments that were produced from a restriction digest were separated by agarose gel electrophoresis 2.18.4) and bands were excised using disposable SafeXtractors (5Prime) and purified using the GeneJET Gel Extraction Kit (Thermo Scientific). All steps were carried out at room temperature. The gel slice was dissolved in a 1:1 volume (w/v) of binding buffer at 50-60$^{o}$C for 10 minutes. A yellow solution indicated optimal pH. If the solution was purple, 10 µl of 3 M sodium acetate (pH 5.2) was added. The solution was then applied to a GeneJET purification column and centrifuged at 12,000 x g for one minute before discarding the flow-through. 700 µl wash buffer was applied to the purification column and centrifuged as before. Flow-through was discarded and the empty column was centrifuged for 2 minutes to remove any residual ethanol from the wash buffer. Any residual ethanol in the DNA sample may inhibit downstream enzymatic reactions. The DNA was eluted from the column using 30-50 µl elution buffer before being quantified using the NanoDrop Lite spectrophotometer.

### 2.18.8 Ligation of Restriction Endonuclease digested Plasmid DNA

Prior to DNA ligation, a restriction digest of both plasmid and insert DNA was carried out. After addition of T4 Ligase, the reaction was left at room temperature for 15-20 minutes or 16$^{o}$C overnight. A fraction (5 µl) of the ligation mixture was run on a 1-2% agarose gel, using cut, unligated vector as a control to analyse the outcome of the ligation reaction.

### 2.18.9 Preparation of ultra-competent *E.coli*

Ultra-competent DH5α *E. coli* cells were generated using the following protocol. A single *E. coli* colony was picked from a previously streaked plate that

had been incubated at 37°C for 16-20 hours. The colony was transferred to 25ml LB broth in a 250 ml conical flask and incubated for 6-8 hours at 37°C with vigorous shaking (250 rpm). The starter culture was used to inoculate 3 x 2 L conical flasks containing 250 ml LB broth with 10, 4 and 2 ml of starter culture. All flasks were incubated overnight at 18-23°C with shaking (200rpm). The $OD_{600}$ of all three cultures was measured using a spectrophotometer and was monitored every 45 minutes until one of the cultures reached an $OD_{600}$ of 0.55. This culture was transferred to an ice water bath for 10 minutes, whilst the others were discarded. Cells were harvested by centrifuging the culture at 2500 x g for 10 minutes at 4°C. Medium was removed and cells were re-suspended in ice-cold ITB buffer (55 mM $MnCl_2.4H_2O$, 15 mM $CaCl_2.2H_2O$, 250 mM KCl, 10 mM PIPES pH 6.7). Cells were harvest by centrifugation before the supernatant discarded. Cells were re-suspended in 20 ml ITB buffer before 1.5 ml DMSO was added. Cell suspension was mixed by swirling before being stored on ice for 10 minutes. Cells were aliquotted into sterile 1.5 ml tubes and snap-frozen in liquid nitrogen. Cells were stored at -80°C until required for transformations.

#### 2.18.10 Transformation of Chemically Competent Cells

Competent *E. coli* (DH5α or XL10-Gold) were thawed on ice and 1 µl of ligation mixture was added to 50 µl of cells. A negative control, containing no DNA, was set up as well as a positive control tube that contained 50 µl competent cells and 10ng of pUC18 plasmid DNA. DNA was added in a volume <10% of the final volume. Cells were stored on ice for 30 minutes before being heat shocked at 42°C for exactly 45 seconds. Tubes were snap-chilled on ice and LB broth was added. LB broth did not contain antibiotic at this stage in order to allow the cells to recover and for the transformed cells to begin expressing their antibiotic resistance marker. Tubes were incubated in a shaking incubator at 220 rpm, 37°C for 1 hour before 150 µl of cells were plated out on LB agar containing the appropriate antibiotic. Plates were inverted and incubated for 12-16 hours at 37°C.

### 2.18.11 Colony PCR Screening for positive clones

To ensure that colonies of transformed *E. coli* possess the insert of interest, a colony PCR screen was set up to test clones for the presence of the insert.

Colonies were stabbed using a pipette tip which was used to inoculate 5 µl $H_2O$. 1 µl of this was then transferred to a 0.2 ml PCR reaction tube, whilst the other 4 µl was transferred to 100 µl LB broth so that the cells could be expanded if the PCR screen was positive. PCR tubes were set up with the following:

**Table 10. Composition of PCR mixture for colony PCR screening.**

| Reagent | Volume/sample (µl) | Volume (µl) for Mastermix (x10) |
|---|---|---|
| **10X Key Buffer** | 2.5 | 25 |
| **25 mM $MgCl_2$** | 1.5 | 15 |
| **dNTP mix (10 mM each)** | 0.4 | 4 |
| **Forward Primer (10 µm)** | 0.5 | 5 |
| **Reverse Primer (10 µm)** | 0.5 | 5 |
| **AccuPOL DNA Polymerase** | 0.5 | 5 |
| ***E.coli*** | 1 | - |
| **PCR-grade $H_2O$** | 18.1 | 181 |
| **Total** | **25** | **230** |

24 µl samples of Mastermix was added to 1 µl *E.coli* samples to give a final reaction volume of 25 µl and the thermal cycling protocol used is outlined below:

**Table 11. Thermal cycling protocol used for colony PCR screening. *The initial denaturation step allows release of DNA by E.coli.**

| Step | Temperature | Duration | Step Purpose |
|---|---|---|---|
| **1** | 95°C | 2 mins | Initial denaturation step* |
| **2** | 95°C | 30 secs | Denaturation step |
| **3** | 58-68°C | 30 secs | Annealing step |
| **4** | 72°C | 1-2 mins (1 kb/min) | Elongation step |
| **Repeat steps 2-4 for 25-35 cycles** | | | |
| **5** | 72°C | 10 minutes | Extension step |
| **6** | Hold at 4°C | | |

Amplified DNA was run by agarose gel electrophoresis and insert-positive colonies were then identified and corresponding 50 µl of 100 µl inoculated LB broth samples were transferred into 5ml B broth in 50 ml Falcon tubes. Tubes were incubated at 37$^{o}$C for 12-16 hours in a shaking incubator at 200 rpm. Cultures were used in miniprep experiments to isolate plasmid DNA. The remaining 50 µl of inoculated LB broth was spread on LB agar plates before glycerol stocks of positive clones were made.

**2.18.12 Miniprep DNA preparation**

Following confirmation of the insert DNA sequence, a small scale plasmid preparation as performed using E.Z.N.A Mini kit. Following *E.coli* transformation, bacterial colonies were picked and used to inoculate 5ml of starter culture that was incubated at 37$^{o}$C with vigorous shaking (300 rpm) to allow adequate aeration for 12-16 hours. Starter culture was centrifuged at 4,000 x g for 10 minutes at room temperature before the culture medium was aspirated. Solution I/RNase A was added to the cell pellet and vortexed to completely re-suspend the cells, before transferring the culture to a 50ml falcon tube. Solution II was added before inverting the tube at least 10 times to obtain a clear lysate. Solution III was added and the tube rotated until flocculent white precipitates had formed. The tube was centrifuged at 15,000 x g for 10 minutes at room temperature before clear supernatant was processed using a HiBind® DNA Mini Column as per manufacturer instructions to obtain purified plasmid DNA.

**2.18.13 DNA Sequencing**

Following plasmid construct purification, sequencing of the insert and the fusion protein DNA sequence was performed using commercially available primers at Macrogen. Due to the length of the inserted DNA, custom internal primers were designed to allow internal sequencing. A typical read gave ~ 600-800 bp. Sequence fidelity was confirmed through global alignments using Chromas Lite™ software. For the vector map, see Appendix Figure 11.

**2.18.14 Maxiprep DNA preparation**

Following confirmation of the insert DNA sequence, a largescale plasmid preparation as performed using E.Z.N.A Maxi kit. Following *E.coli* transformation, bacterial colonies were picked and used to inoculate 200ml of starter culture that was incubated at 37$^{o}$C with vigorous shaking (300 rpm) to allow adequate aeration for 12-16 hours. 200ml of starter culture was centrifuged at 4,000 x g for 10 minutes at room temperature before the culture medium was aspirated. Solution I/RNase A (12ml) was added to the cell pellet and vortexed to completely re-suspend the cells, before transferring the culture to a 50ml falcon tube. Another 12ml of Solution II was added before inverting the tube at least 10 times to obtain a clear lysate. Solution III (16ml) was added and the tube rotated until flocculent white precipitates had formed. The tube was centrifuged at 15,000 x g for 10 minutes at room temperature before clear supernatant was processed using a HiBind® DNA Maxi Column as per manufacturer instructions to obtain purified plasmid DNA.

**2.18.15 Transfection**

*Wild type* Cf2Th cells were transfected with the CXCR4-GST vector using Lipofectamine 3000™. Cells were seeded in a 10 cm dish so that they were at approximately 70% confluency at the time of transfection. 7.5 µl Lipofectamine 3000™ reagent was diluted with 125 µl Opti-MEM™ medium before vortexing to mix. 5 µg DNA was diluted in 250 µl Opti-MEM™ medium prior to addition of 10 µl P3000™ reagent and vortexing to mix. The diluted DNA (125 µl) was mixed 1:1 with the diluted Lipofectamine™ 3000 reagent and incubated for 15 minutes at room temperature before adding to cells in culture. Cells were incubated at 37$^{o}$C, 5% $CO_2$ for 48 hours prior to selection.

**2.18.16 Selection of positive clones**

Following transfection, cells were incubated for 48 hours before the addition of the selection antibiotic puromycin at a final concentration of 2 µg/ml. This selection was maintained for a further 7 days prior to harvesting the cells by trypsinisation. In order to isolate positively transfected clones, a dilution series in a 96-well plate was performed in order to obtain wells that contained a single cell

from which a stably-transfected colony can be grown. After harvesting, cells were re-suspended to a density of $2x10^4$ cells/ml in suitable culture medium before 200 µl of the cell suspension was added to position A1 in a 96 well plate. All wells, except A1, were previously filled with 100 µl culture medium containing selection antibiotic. A 2-fold dilution series was carried out along the first column in the plate using a single pipettor, as indicated in Figure 16 by the blue arrow. A volume of 100 µl was removed from position H1 following the dilution series to maintain equal volumes across these wells. Using an 8-channel pipettor, the wells in column 1 were diluted 2-fold across the plate to column 12 and 100 µl was removed from column 12 to maintain equal volumes in all of the wells across the plate. The plate was placed in an incubator at 37°C, 5% $CO_2$ and left undisturbed to allow the cells to settle and adhere to the bottom of the wells. The 96-well plate was visualised under a light microscope and wells containing a single cell were identified and monitored until they established colonies and each colony was given a unique identification number. When cells reached approximately 70-80% confluency, they were transferred into 24-well, followed by 12-well plates. When cells reached a confluency of approximately 70% in the 12-well plate, each well was divided into two wells of a 6-well plate. One of these wells was used to maintain the transfected cell line, whilst the other was harvested by scraping and used in flow cytometry studies to assess expression of the receptor encoded by the insert DNA using specific monoclonal antibodies.

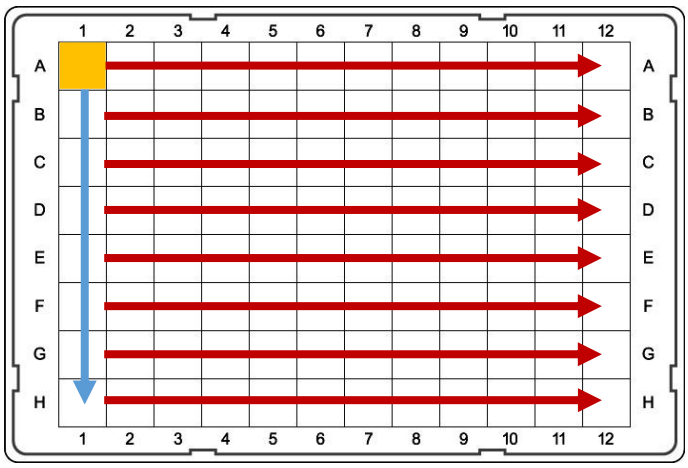


**Figure 16. 96 well plate layout showing a two-way dilution series for single cell colony selection.**

## 2.19 Evaluation of small molecule binding to CXCR4 by surface plasmon resonance

### 2.19.1 Lipid/detergent micelle preparation

Aliquots of DOPC in chloroform (final concentration 5 mM) were transferred into glass test tubes and a thin lipid film was formed on the glass wall by evaporating the chloroform with a stream of nitrogen gas (99%) whilst rotating the tube. The tube was placed under vacuum for at least 1 hour to eliminate any last trace of chloroform. After vacuum, a millilitre of running buffer (50 mM Hepes, 150 mM NaCl, pH 7.0; GE Healthcare, UK) was added to the dried lipid, which was then frozen, thawed and vortexed 4 times before subsequently extruding through a 100 nm polycarbonate filter using the Avanti Mini-extruder kit as per manufacturer instructions. A pre-made detergent solution (2% Cholestyrl hemisuccinate tris salt (CHS)/10% n-Dodecyl-β-D-Maltopyranoside (DOM)/10% 3-[(3-Cholamidopropyl)-Dimethylammonio]-1-Propane Sulfonate] • N,N-Dimethyl-3-Sulfo-N-[3-[[3α,5β,7α,12α)-3,7,12-Trihydroxy-24-Oxocholan-24-yl]Amino]propyl]-1-Propanaminium Hydroxide (Chaps)) was added to the extruded lipids at a lipid:detergent ratio of 5:1 (v/v) and vortexed.

### 2.19.2 Immobilisation of capturing antibody

Polyclonal anti-GST antibody surfaces were prepared using instructions provided by GE Healthcare in the GST-capture kit. Immobilisation of anti-GST was performed at 25$^{o}$C using a flow rate of 5-10 µl/min. Anti-GST antibody was diluted in immobilisation buffer to yield a 30 µg/ml solution and immobilised onto CM4 series S sensor chips as previously described (2.6.2). Polyclonal anti-GST antibody contains a minor fraction of high-affinity sites. These are potentially difficult to regenerate, and were therefore blocked to avoid capture of GST-tagged ligand by these sites. Recombinant-GST was diluted in running buffer at 5 µg/ml and injected over the ant-GST surface for 3 minutes. This was followed by a regeneration injection using 10 mM glycine-HCl, pH 2.0 for 2 minutes. The recombinant-GST and regeneration injections were carried out 3 times to block high affinity sites of anti-GST.

The monoclonal antibody 1D4 was immobilised so a series S CM4 sensor chip using standard amine-coupling chemistry, with HBS-N (10 mM Hepes, 150 mM NaCl, pH 7.4; GE Healthcare, UK) used as the running buffer. The sensor chip surface was activated by a 7-minute injection of a 1:1 ratio of 0.4 M 1-ethyl-3-(3-dimethylaminoporpyl)carbodiimide hydrochloride (EDC) and 0.1 M *N*-Hydroxysuccinimide (NHS). The antibody (30µg/mL in 10 mM sodium acetate pH 4.0) was injected for a further 7 minutes. Any remaining activated groups on the chip surface were blocked with a 7-minute injection of 1 M ethanolamine (pH 8.5).

### 2.19.3 Receptor Solubilisation

#### 2.19.3.1 Automated Solubilisation

Cf2Th-CXCR4-GST or Cf2Th-CXCR4-C9 cells were solubilised and captured on a GST or 1D4 antibody-coated surface, respectively, as previously described by Navratilova *et al.* (2005). Briefly, 4x10$^{6}$ cells were re-suspended in solubilisation buffer (20 mM Tris pH 7.0, 0.1 M $(NH_4)_2SO_4$, 10% glycerol, 1 protease inhibitor tablet per 50 ml buffer) that did not contain detergent and transferred to a sample vial in the BIACORE T200 sample compartment. The BIACORE T200 autosampler was programmed to mix the cells within the vial before transferring 180 µl of cell

suspension to a tube containing 20 µl of lipid/detergent mixture. The components in this vial were mixed twice and allowed to incubate for 10 minutes prior to injection over antibody-coated surfaces at 20 µl/min for 10 minutes. The sample loop was washed with buffer prior to injection of analyte. The sample compartment and flow cell temperatures were maintained at 4$^{o}$C and 25$^{o}$C, respectively.

#### 2.19.3.2 Manual Solubilisation

Cf2Th-CXCR4-C9 cells were solubilised as described by Navratilova et al (2006) with minor alterations. Briefly, cells were solubilised in 20 mM Tris (pH 7.0), 0.1 M $(NH_4)SO_4$, 10% glycerol, 0.07% CHS, 0.33% DOM, 0.33% Chaps, 0.33 mM DOPC and 1 protease inhibitor tablet per 50 ml buffer. Approximately $4x10^6$ cells were solubilised in 0.5 ml buffer and were sonicated for 1 second, 6 times over. Cell preparations were placed on a rocker for 2 hours at 4$^{o}$C before centrifugation for 20 minutes at 14,000 RPM. The supernatants, containing solubilised receptor, were transferred to new tubes and frozen at -80$^{o}$C until required.

### 2.19.4 Receptor binding assay

Solubilised CXCR4 was injected of 1D4-coated surfaces for 10 minutes at 20 ul/min. To assess the activity of the CXCR4-coated surface, conformational-dependent antibodies, diluted in running buffer, were injected over the surface.

Small molecules, SJA05, SJA324 and AMD3100 were dissolved in running buffer (50 mM Hepes (pH 7.0) 150 mM NaCl, 0.02% CHS, 0.1% DOM, 0.1% Chaps, 50 nM DOPC, 5 mM $MgCl_2$, 1 mM $CaCl_2$) serially diluted 3-fold and injected over receptor surfaces for 3 minutes at 30 ul/min and the dissociation rate monitored for a further 10 minutes. All molecules were tested in a concentration series of 22.2, 7.5, 2.5 and 0.8 nM, with injections beginning from the lowest concentration and progressing through increasing concentrations. Each analyte injection was followed by a blank buffer injection to correct for drift caused by the decaying receptor surface. Replenishment of receptor surfaces was carried out following injection of all analyte concentrations, prior to analysis of the next small molecule. Data were normalised for maximum binding capacity and analysed using BIACORE

evaluation software (version 1.0) and the kinetic constants of each small molecule determined using a 1:1 Langmuir model fit.

## 2.20 Data Analysis

The software Prism (Graphpad, USA) was used for all statistical analyses. Each experiment was repeated three times, unless stated otherwise. Any significance in observable differences was assessed using appropriate statistical analyses. The standard error means (SEM) were calculated and reported on graphs as error bars. Statistical significance was reported as p-values.

# Evaluation of αvβ6-targeted peptides as targeted imaging and therapy agents

# 3 Evaluation of αvβ6-targeted peptides as targeted imaging and therapy agents

## 3.1 Chapter Aim

The aim of this chapter was to develop an αvβ6-targeting peptide into an agent suitable for both PET imaging of αvβ6 in cancer and fibrosis and for αvβ6-targeted PRRT in cancer. Herein reports the validation of an αvβ6-binding cyclic peptide which has potential application as a PET imaging agent and/or a therapeutic peptide receptor radionuclide therapy (PRRT) agent. A range of experiments were used in order to validate αvβ6-binding and integrin selectivity prior to αvβ6 imaging studies *in vivo* using an αvβ6-positive xenograft model both with and without αvβ6 blocking.

## 3.2 Previous Studies

As αvβ6 has been shown to be upregulated in patients with IPF, and its expression has been shown to be linked, both temporally and spatially to fibrosis development. Its upregulation in the epithelium of the lungs has been shown to be detectable before fibrosis is established, and also continue within fibrotic lesions [236]. Due to the increased expression of αvβ6 in fibrosis of the lung, liver and kidneys, as well as in other diseases such as cancer, it has become an attractive and promising target for both diagnostics and therapy. Multiple αvβ6-specific antibodies have been developed, by Weinreb *et al.* [315], which are capable of blocking the integrin, preventing it binding to the LAP and thus thwarting integrin-mediated TGF-β activation. Avβ6-targeting peptides have also been developed, preclinically, for both diagnostic and therapeutic purposes, such as A20FMDV2, H2009.1, HBP-1 and various other peptides (Table 12).

**Table 12. List of different αvβ6-targeted imaging agents used in different disease models**

| Imaging Agent | Disease Model | Reference |
|---|---|---|
| [$^{18}$F]FBA-**A20FMDV2** | Melanoma | [316] |
| [$^{18}$F]FBA-PEG$_{28}$-**A20FMDV2** | Pancreatic Cancer | [317] |
| [$^{64}$Cu]Cu-PEG$_{28}$-**A20FMDV2** | Melanoma | [318, 319] |
| [$^{18}$F]FBA-C$_6$-ADIBON$_3$-PEG$_7$-**A20FMDV2** | Melanoma | [320] |
| [$^{64}$Cu]Cu-DOTA-**R$_0$1** | Pancreatic Cancer | [321] |
| [$^{64}$Cu]Cu-DOTA-**S$_o$2** | Pancreatic Cancer | [321] |
| [$^{18}$F]-Fluorobenzoate-**R$_0$1** | Pancreatic Cancer | [322] |
| [$^{18}$F]-Fluorobenzoate-**S$_0$2** | Pancreatic Cancer | [322] |
| [$^{64}$Cu]Cu-**AcD10** | NSCLC | [323] |
| [$^{68}$Ga]Ga-TRAP-**Avebehexin** | Lung Cancer | [324] |
| [$^{68}$Ga]Ga-DOTA-SFITGv6 | HNSCC | [312] |
| [$^{111}$In]In-DTPA-**A20FMDV2** | Pulmonary Fibrosis | [325] |
| [$^{99m}$Tc]Tc-SAAC-**S$_0$2** | Lung Cancer | [326] |
| [$^{99m}$Tc]Tc-HYNIC-**HK** | Pancreatic Cancer | [327] |

#### 3.2.1.1 A20FMDV2

A20FMDV2 is a 20 amino acid peptide derived from the VP1 coat protein of the foot-and-mouth disease virus and also contains the RGD sequence recognised by integrin αvβ6. This peptide has been shown to have high specificity for the αvβ6 integrin with minimal interaction with other RGD-recognising integrins such as αVβ5 and a αVβ3. This peptide has been radiolabelled for PET imaging of the αvβ6 integrin in animal models, using $^{18}$F and $^{64}$Cu.

Modification of A20FMDV2 with fluorobenzoyl acid (FBA) allowed the radiolabelling of the molecule with $^{18}$F [316]. This imaging agent displayed high specificity for αvβ6 over other integrins and *in vivo* studies demonstrated that this tracer was able to selectively image αvβ6$^+$ tumours in mice. However, the stability of this tracer was questionable as it was broken down into multiple metabolites, raising concerns over translational potential. This tracer was compared with the

same peptide conjugated to 2 different radiolabelled prosthetic groups, [$^{18}$F]-fluoropropionic acid ([$^{18}$F]-FPA) and a 1,4 disubstituted 1,2,3-triazole ([$^{18}$F]-FC5) [320], however instability issues were still present. A20FMDV2 was further modified with polyethylene glycol (PEG) to produce [$^{18}$F]FBA-PEG$_{28}$-A20FMDV2 and [$^{18}$F]FBA-(PEG$_{28}$)$_2$-A20FMDV2 [317]. Inclusion of a PEG unit demonstrated both increased αvβ6-specific binding and improved pharmacokinetic properties and slightly improved metabolic stability when compared with the parent tracer [$^{18}$F]FBA-A20FMDV2.

The PEGylated A20FMDV2 peptide was labelled with $^{64}$Cu, a radioisotope with a longer half-life, and conjugated with DOTA and CB-TE2A chelators [318]. Both $^{64}$Cu-labelled tracers were shown to highly accumulate in the kidneys and the liver. Accumulation in the later may suggest poor stability of the tracer. Hu *et al.,* [319] conjugated the peptide with 4 different chelators; CB-TE1A1P, DOTA, NOTA and BaBaSar but stability of the tracers was not greatly improved.

A20FMDV2 has also been used as a SPECT imaging agent via Indium-111 labelling through DTPA ([$^{111}$In]-DTPA-A20FMDV2) [325]. Much like the PET tracer counterparts, this tracer was shown to distinguish between αvβ6$^+$ and αvβ6$^-$ tumours in mice. Much like the PET tracer equivalents, however, this tracer demonstrated poor stability *in vivo*.

John *et al*. [104] utilised $^{111}$In-DTPA-A20FMDV2 and a scrambled control peptide in a murine bleomycin-induced model of IPF. It was shown that as well as detecting increased αvβ6 expression in the lungs of diseased mice, αvβ6 can be used to predict the progression of fibrosis. This supports the targeting of αvβ6 as a biomarker of IPF.

### 3.2.1.2 Cysteine-knot peptides

Knottins, or cysteine-knot peptides, have appeared to be a significant class of molecules with both diagnostic and therapeutic potential. They are all structurally similar, sharing a common fold in which a disulphide bond is threaded through a macrocycle that is create by two other disulphide bonds and the backbone of the peptide. This gives the knottin its knot-like structure, providing it with moderate protection against chemical, proteolytic and/or thermal damage. Within these knottins are loop regions, which can give rise to a knottin's specificity for particular molecular sequences. Due to the high stability of knottins, they are able to withstand mutations in their amino acid sequence without denaturing their structures, providing an advantage over the use of linear peptides which have poor *in vivo* stability. This characteristic makes them attractive tools for use in both diagnostic and drug discovery applications.

Engineered knottin peptides have been developed as imaging agents to target αvβ6 and labelled with [$^{64}$Cu] by Kimura *et al*. [321] in studies involving a murine pancreatic adenocarcinoma xenograft model. These cysteine knot peptides display high affinity for the αvβ6 integrin. In their studies, they conjugated the cysteine knot peptides $R_0$1, $R_0$2, $S_0$2, $E_0$2 and a positive control peptide A20 with DOTA-NHS and radiolabelled them with [$^{64}$Cu]. Of these, [$^{64}$Cu]DOTA-$S_0$2 demonstrated the most favourable imaging properties *in vivo*, showing good tumour-to-background ratio. This radiotracer also proved to be more stable in serum (>95%) when incubated over 24 hours. Although most knottin peptides exhibit high resistance to degradation or denaturing, alterations made to their loops may make them more vulnerable to degradation such as [$^{64}$Cu]DOTA-$R_0$2.

Hackel *et al.,* [322], labelled knottin peptides $R_0$1 and $S_0$2 with [$^{18}$F] via fluorobenzoate to produce [$^{18}$F]Fluorobenzoate-$R_0$1 or [$^{18}$F]Fluorobenzoate-$S_0$2 and used them in the same model as Kimura *et al.,* [321]. When compared to the $^{64}$Cu-labelled equivalents, [$^{18}$F]-labelled $R_0$1 and $S_0$2 showed slightly reduced

uptake in the kidneys and liver, however they showed slightly lower tumour uptake. The fluorine-labelled knottins showed more desirable pharmacokinetics than their copper-labelled counterparts, exhibiting rapid renal clearance of the peptides. More recently, modification of $S_0$2 with a single amino acid chelator (SAAC) and subsequent radiolabelling with the SPECT isotope technetium-99m ($^{99m}$Tc), reproduced high metabolic stability as with other cysteine knot peptide derivatives, however biodistribution studies showed that tumour:organ ratios, excluding tumour:muscle, were approximately one or less, with very high kidney uptake observed once again, despite using a serine-rich peptide derivative, which theoretically should result in reduced kidney uptake.

More recently, as attempts were made to improve the metabolic stability of linear peptides, such as A20FMDV2, a cyclic peptide consisting of 9 amino acids (cyclo(FRGDLAFp(*N*Me)K) was discovered to have, as well as high integrin αvβ6 selectivity, high integrin αvβ6 binding affinity. The peptide was also found to be completely stable in human plasma past three hours, by which time, any imaging protocol should have been completed. This peptide, designed by Maltsev, *et al..,* [191] and further functionalised via the lysine side chain by Notni *et al.,* [324] was found to be unaffected by modifications that would allow its use as a radiolabelled peptide targeting integrin αvβ6. The peptide was functionalised with a 1,4,7-triazacyclononane-1,4,7-tris[methylene(2-carboxyethyl)]phosphonic acid (TRAP) chelator, capable of incorporation gallium-68 into its structure. This chelator, interestingly allowed the conjugation of up to three targeting moieties, therefore, in addition to the monomeric radiolabelled peptide, a dimer and trimeric radiolabelled peptide was synthesised in an attempt to increase the affinity of the radiotracer for integrin αvβ6, as other studies had shown this may positively influence increased tumour uptake [328-332]. Despite multimerisation having a profound effect on increasing affinity for integrin αvβ6 (monomer $IC_{50}$ = 260 pM ± 17; trimer $IC_{50}$ = 23 pM ± 4), the pharmacokinetics were poor, with poor tumour:organ ratios compared to the monomer, likely a result of increased lipophilicity.

An alternative peptide, identified by Altmann *et al.,* [312] from a phage-display library, demonstrated high αvβ6 affinity and specificity in blocking studies as well as impressive tumour contrast. Substitution of gallium-68 in this radiotracer for therapy radionuclide lutetium-177 led to an increasing internalisation in the $\alpha v\beta 6^{+}$ HNO97 cell line, making it a promising candidate as a PRRT agent. Despite promising internalisation of the lutetium-177 labelled peptide, there are issues with high renal uptake, as with many other peptides, which may limit its potential as an endoradiotherapy agent due to potential nephrotoxicity. Importantly, this peptide has been studied in first-in-man studies in two patients with hypopharynx carcinoma, or non-small cell lung cancer (NSCLC), whereby $^{68}$Ga-DOTA-SFITGv6 demonstrated tumour-specific, but not inflammation-associated, accumulation of radiotracer. When compared to the equivalent $^{18}$F-FDG PET scans in the same patients, which displayed inflammation-associated uptake, $^{68}$Ga-DOTA-SFITGv6 has encouraging potential to detect these tumours without exhibiting uptake in the lymph nodes in response to inflammation.

Various efforts have been made in the research community to develop an αvβ6-specific agent with high affinity, specificity and selectivity over other integrins, whilst demonstrating high tumour uptake and high tumour:organ ratios. Targeting αvβ6 has relied on the exploitation of the established RXDLXXL amino acid motif, discovered by Kraft et al. [190] to give peptides an extraordinary specificity for αvβ6 over other RGD-specific peptides. whereby X represents any amino acid. From this motif, many derivatives and novel imaging agents, targeting αvβ6 have been developed, as outlined in

Table 13.

**Table 13. Avβ6-targeted peptides and their respective affinities**

| Avβ6-targeted peptide | Amino Acid Sequence | Avβ6 Affinity (nM) | Reference |
|---|---|---|---|
| A20FMDV2 | NAVPNLRGDLQVLAQKVART | 3 | [316] |
| HBP-1 | SPRGDLAVLGHKY | 38.9 | [333] |
| $R_0$1 | GCILNMRTDLGTLLFRCRRDSDCPGACICRGNGYCG | 4.1 | [321] |
| $S_o$2 | GCRSLARTDLDHLRGRCSSDSDCLAECICLENGFCG | 2.7 | [321] |
| AcD10 | GDLATLRQL | 1.3 | [323] |
| Peptide 29 | CRGDLASLC | < 1 | [212] |
| Avebehexin | FRGDLAFp(*N*Me)K | 0.26 | [324] |
| SFITGv6 | GRCTFRGDLMQLCYPD | 14.8 | [312] |

Most of these targeted peptides, which have been used in PET or SPECT applications, have demonstrated excellent tissue penetration, minimal immunogenicity and good tumour uptake *in vivo*. However, most peptides tested have been reported to have poor metabolic stability, especially linear peptides such as A20FMDV2, and high uptake in critical organs such as the kidneys [317, 318, 320] and the intestinal tract [312] Efforts have been made to improve upon the metabolic stability of peptides through cyclisation and amino acid substitutions, however there still remains high uptake of αvβ6-targeted probes in normal organs and tissues. However, a recent first in man study of $^{18}$F-FB-A20FMDV2 [334] revealed that uptake of this probe in healthy organs including the kidneys, small intestine, stomach wall, liver, spleen, thyroid and gallbladder was quickly cleared to the bladder by the kidneys, resulting in an effective dose of 0.0217 mSv/MBq [335], close to the effective dose seen with the most widely used PET agent $^{18}$F-FDG (0.019 mSv/MBq), indicating that this probe is an encouraging prospect for clinical PET imaging of αvβ6. The relatively high liver uptake, however, may be an indicator of PET probe metabolism, although this was not confirmed by the study. At the time when the work reported in this thesis commenced there was a clear requirement to improve these properties and to further investigate

the applications of cyclic peptides. This was an area where a number of groups worldwide were working simultaneously.

Even though the main applications of αvβ6-targeted imaging agents are focused towards oncology, there is increasing use of these agents to provide useful information regarding pathophysiology of other diseases such as pulmonary fibrosis [104] (Clinical trial: NCT03183570).

Therefore, this project aims to develop an αvβ6-specific targeted agent that may be used for both diagnostic imaging in cancer and pulmonary fibrosis as well as a peptide-receptor radionuclide therapy agent for the treatment of $\alpha v\beta 6^{+}$ cancers.

## 3.3 Results

### 3.3.1 Solid Phase Peptide Synthesis

All peptides (Figure 17) were synthesised successfully by Dr Juozas Domarkas as confirmed by mass spectrometry (Appendix Figure 1-4). Amino acid sequences of peptides are referred to in Table 14.

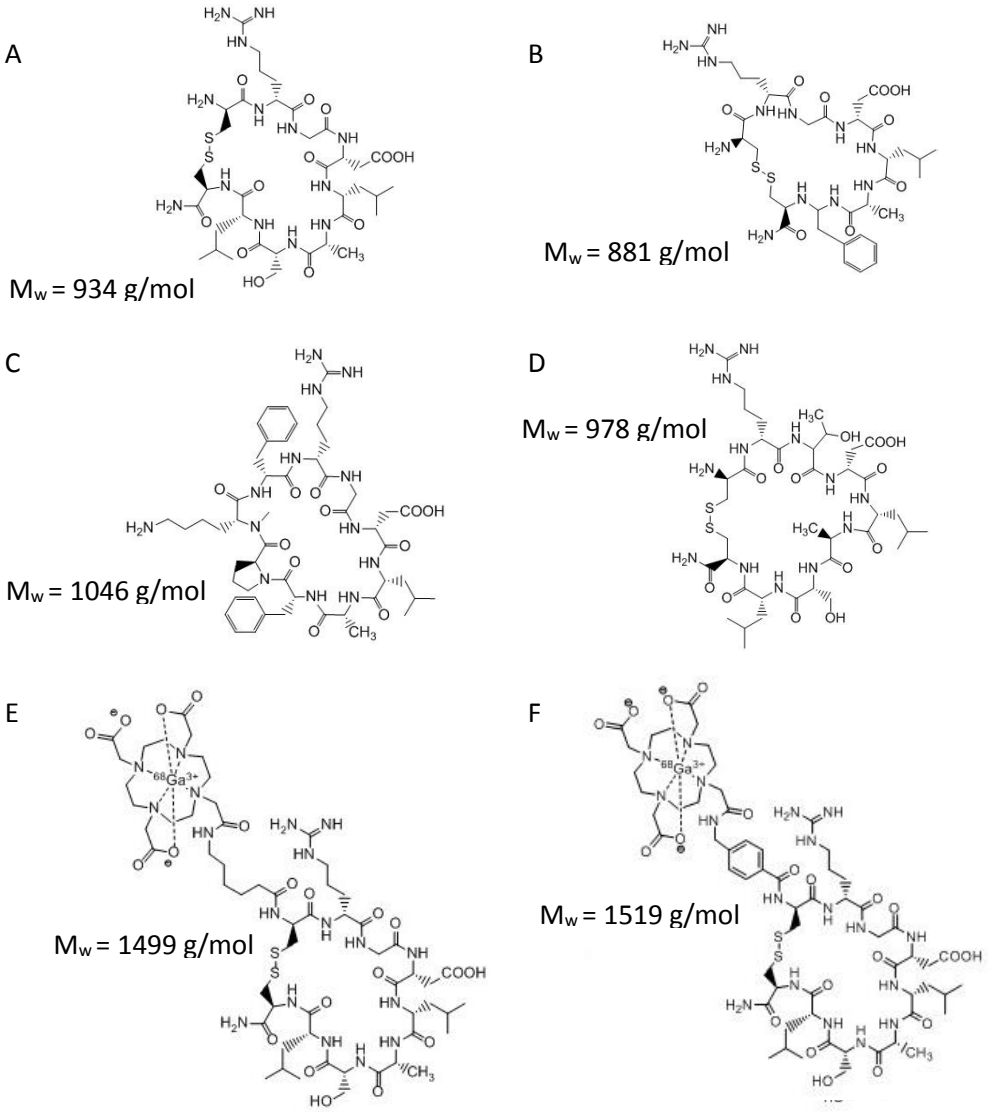


**Figure 17. Structures of cyclic peptides synthesised by Fmoc-based solid phase peptide synthesis and their labelled derivatives. (A) RGD1, (B) RGD2, (C) RGD3, (D) RGD4, (E) [$^{68}$Ga]Ga-DO3A-JD1-RGD1, (F) [$^{68}$Ga]Ga-DO3A-JD2-RGD1**

**Table 14. Amino acid sequences of cyclic peptides synthesised by Fmoc-based solid phase peptide synthesis.**

| | Peptide | Sequence |
|---|---|---|
| **A** | RGD1 | CRGDLASLC |
| **B** | RGD2 | CRGDLAFC |
| **C** | RGD3 | FRGDLAFp(*N*Me)K |
| **D** | RTD1 | CRTDLASLC |
| **E** | DO3A-JD1-RGD1 | DO3A-JD1-CRGDLASLC |
| **F** | DO3A-JD2-RGD1 | DO3A-JD1-CRGDLASLC |
| **G** | [$^{nat}$Ga]Ga-DO3A-JD1-RGD1 | [$^{nat}$Ga]Ga-DO3A-JD1-CRGDLASLC |
| **H** | [$^{nat}$Ga]Ga-DO3A-JD2-RGD1 | [$^{nat}$Ga]Ga-DO3A-JD2-CRGDLASLC |

### 3.3.2 Assessment of αvβ6-binding by cyclic peptide panel

#### 3.3.2.1 ELISA validation

In order to assess the ability of peptides to inhibit binding of the well-characterised anti-αvβ6 antibody, 10D5, to αvβ6, the concentration of competing antibody must be kept constant. In order to determine the half-maximal effective dose ($ED_{50}$), a ten-fold concentration of 10D5 mAb was incubated with 100 ng recombinant human αvβ6 previously coated into the wells of 96 well plates. The amount of antibody present was quantified using a HRP-conjugated secondary antibody which was reacted with TMB substrate to induce a colour change that is proportional to the concentration of primary mAb present. This reaction was quenched with the addition of acid so that the absorbance at 450 nm may be quantified by a plate reader. A non-linear regression curve was fitted to the data (log(ligand) vs response) and data were normalised based on the maximum absorbance detected, so that the concentration of 10D5 mAb at 50% maximal effective dose could be calculated.

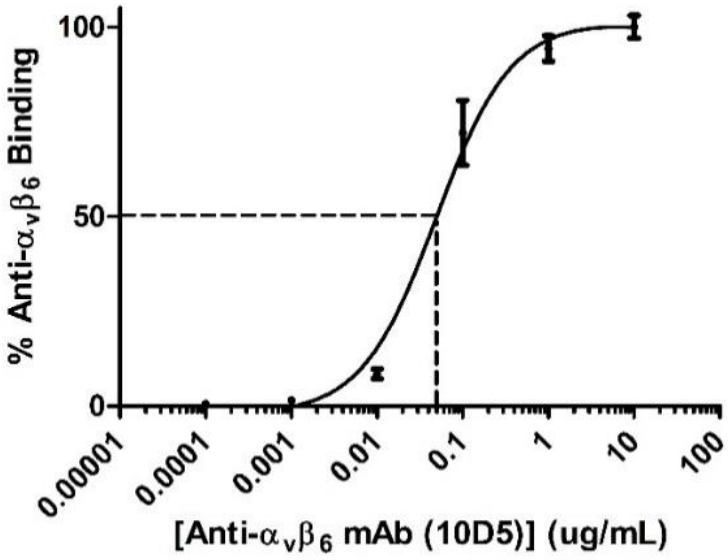


**Figure 18. Optimisation of antibody concentration for competitive binding ELISA. Binding of anti-αvβ6 (clone 10D5) to recombinant human αvβ6 normalised to maximal antibody binding in the absence of peptide, n=3.**

It was shown that the $ED_{50}$ of the αvβ6-specific antibody, 10D5, was 49.1 ± 12.7 ng/mL, therefore an antibody concentration of 50 ng/mL was used as the concentration of competitor in further experiments to determine the αvβ6-binding affinity of various peptides (Figure 18).

### 3.3.2.2 Assessment of peptide-αvβ6 binding by competitive ELISA

Each peptide was tested for its ability to inhibit binding of anti-αvβ6 to αvβ6 previously coated on the wells of a 96 well plate. Each peptide was incubated with αvβ6 prior to washing to remove any excess peptide and incubation with the 10D5 mAb. The amount of 10D5 bound to αvβ6 was assessed as in 3.3.2.1 and the percentage of antibody binding, normalised to antibody binding in the absence of peptide, was determined. The half-maximal inhibitory concentration of each peptide was then calculated to give an indication as to the strength of the interaction between peptide and αvβ6.

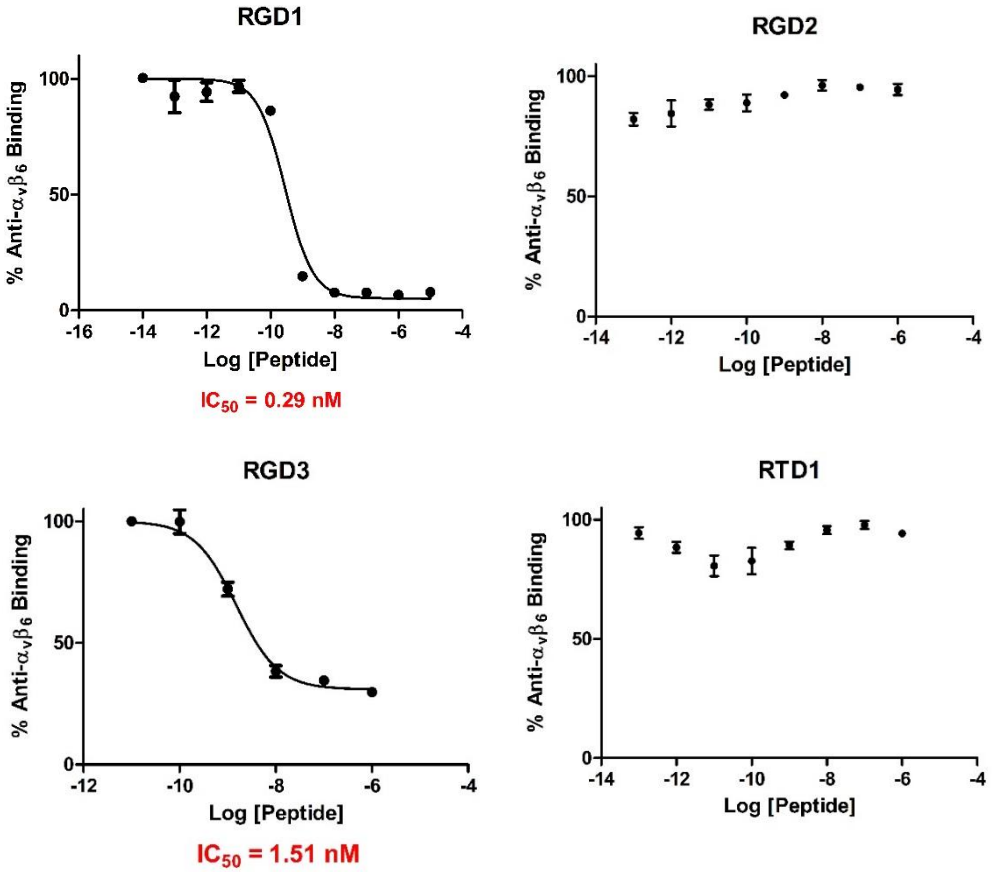


**Figure 19. Competitive binding ELISA between cyclic peptide panel and anti-αvβ6 antibody. Data were normalised against antibody-binding in the absence of peptide.**

Out of the four peptides tested, only two were able to inhibit antibody binding to αvβ6 at the tested concentrations (Figure 19). RGD1 was able to inhibit antibody binding with an $IC_{50}$ of 0.29 nM, suggesting a strong interaction between the peptide and integrin. RGD2 was shown not to have the ability to inhibit anti-αvβ6 at the tested concentrations. In contrast to RGD1, RGD2 does not possess a second leucine residue in its amino acid sequence. The absence of this amino acid may suggest that this is critical for the αvβ6-binding ability, which is in accordance with findings in the literature [190, 191]. RGD3 was able to inhibit anti-αvβ6 binding at 1.51 nM, indicating a strong peptide-integrin interaction. This affinity is reflective of the reported affinity of the peptide in the literature. There are reports of αvβ6-targeting peptides that contain a threonine residue in place of a glycine residue within the RGD motif [322], therefore a peptide that contained R-T-D,

RTD1, was tested for binding affinity to αvβ6. It was shown that RTD1, which is identical to RGD1, except for the substitution of threonine for glycine was unable to inhibit anti-αvβ6 binding at the concentrations tested, suggesting that in this case, the glycine residue is critical for this peptide to be able to bind to αvβ6.

If RGD2 and RTD1 were tested at much higher concentrations, there is a possibility that they may display some αvβ6 binding ability, however they would be deemed unsuitable as potential PET imaging agents as PET radioligands are required to display high receptor affinity in cases of low receptor density. A limitation of this study is that receptor density was not determined, however it was clear from the results that there was significant expression. Therefore, RTD1 and RGD2 were not taken forward to further evaluation as potential αvβ6-targeted imaging agents.

The competitive ELISA experiment established that RGD1 and RGD3 were able to find to αvβ6 with high affinity and these were therefore taken forward for further validation as potential αvβ6-targeted imaging agents.

### 3.3.3 Re-assessment of αvβ6-binding of peptide derivatives by ELISA

In order for the cyclic peptides RGD1 and RGD3 to be developed into molecular imaging agents, specifically PET probes, modification of their structures was required to be able to incorporate a positron-emitting radioisotope such as gallium-68. After modification of RGD1 and RGD3, it was important for the binding of the peptide derivatives to αvβ6 be retested to determine if the modification itself had an effect on target binding. Therefore, the competitive ELISA, as performed in 3.3.2.2, was repeated for all peptide derivatives both with and without complexed metal ions.

Compared to the parent peptide, RGD1, the derivative DO3A-JD1-RGD1, which did not contain $[^{68}Ga]Ga^{3+}$, inhibited antibody binding with an $IC_{50}$ of 0.51 ± 1.19 nM. Complexation of $[^{nat}Ga]Ga^{3+}$ into DO3A, producing the derivative $[^{nat}Ga]Ga^{3+}$-DO3A-JD1-RGD1, resulted in an $IC_{50}$ value of 0.48 nM (Figure **20**A). Conjugation of RGD1 to DO3A via an AMBA spacer to produce DO3A-JD2-RGD1

and subsequent complexation with gallium to produce [$^{nat}$Ga]Ga$^{3+}$-JD2, resulted in $IC_{50}$ values of 0.11 nM and 0.13 nM, respectively (Figure **20**B). The lutetium-labelled JD2 derivative was shown to inhibit antibody binding with an $IC_{50}$ value of 0.16 nM. Derivatisation of RGD3 with the chelator DO3A (DO3A-RGD3), resulted in an $IC_{50}$ value of 3.63 nM, and complexation of [$^{nat}$Ga]Ga ([$^{nat}$Ga]Ga-DO3A-RGD3) resulted in an $IC_{50}$ value of 2.81 nM (Figure **20**C).

Importantly, the chelation of [$^{nat}$Ga]Ga$^{3+}$ by DO3A in all molecules, and of [$^{nat}$Lu]Lu$^{3+}$ in the JD2 derivative, giving a more representative net charge of the radiolabelled version of all molecules, did not hinder any binding that was observed with the parent peptide alone.

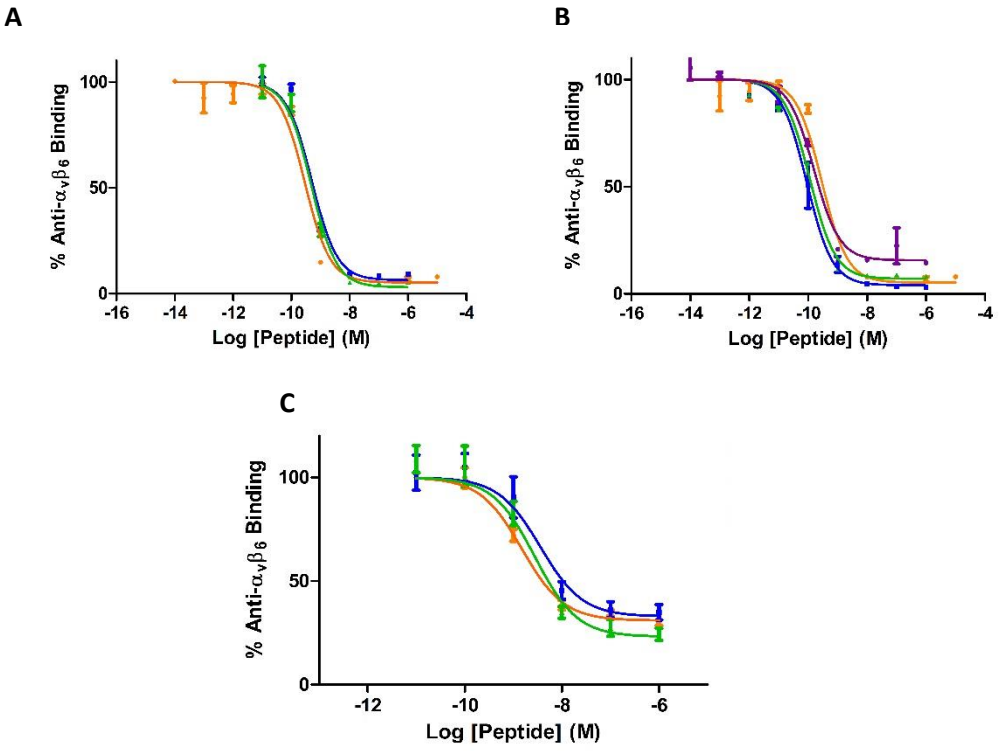


**Figure 20. Competitive binding ELISA between cyclic peptide derivatives and anti-αvβ6 antibody. Data were normalised against antibody-binding in the absence of peptide. (A) Orange line = RGD1; Green line = DO3A-JD1-RGD1; Blue line = [$^{nat}$Ga]Ga$^{3+}$-DO3A-JD1-RGD1. (B) Orange line = RGD1; Green line = DO3A-JD2-RGD1; Blue line = [$^{nat}$Ga]Ga$^{3+}$-DO3A-JD2-RGD1. (C) Orange line = RGD3; Green line = DO3A-RGD3; Blue line = [$^{nat}$Ga]Ga$^{3+}$-DO3A-RGD3; Purple line = [$^{nat}$Lu]Lu$^{3+}$-DO3A-JD2-RGD1.**

### 3.3.4 Assessment of peptide-integrin selectivity by SPR

As it was shown that RGD1 and RGD3 were able to specifically bind to αvβ6, it was necessary to determine if there was any potential cross-reactivity of these peptides with other integrins that recognise the RGD motif in their ligands.

Further validation of RGD1 was needed in order to determine peptide selectivity for αvβ6 over other integrins, such as αVβ3. Despite there being eight known integrins that recognise the RGD motif in their ligands, integrin αVβ3 has the greatest amount of overlap with integrin αvβ6 with regards to their natural ligands, and is able to bind to the αvβ6 ligands LAP-TGF-B, fibronectin and osteopontin [336], therefore this integrin serves as a good counter-screen to give an indication as to the selectivity of targeted peptides for integrin αvβ6 over other integrins [187], especially given other reports of RGD-containing peptides that are able to bind, albeit weakly, to αVβ3 [191, 312]. Any potential cross-reactivity with non-target integrins would lead to off-target binding, potentially giving false positive signals in any prospective PET scan.

Surface plasmon resonance was used to monitor the interaction of peptide with different integrins to establish how strongly, or if, they interact. In these experiments, only RGD1 was tested for integrin selectivity as RGD3 selectivity for αvβ6 over other integrins had already been established in another study.

Prior to immobilisation of RGD1 to a CM5 sensor chip surface, modification of the peptide with a 6-aminomethylbenzoic acid spacer via the N-terminal cysteine residue amine group was performed to provide the peptide with a moiety from which it may be extended away from the sensor chip surface to increase the likelihood of binding with analyte (Figure 21). The resulting peptide, JD2-RGD1, was then injected over a sensor surface that had not been activated, whilst diluted in 10 mM sodium acetate of varying pH in order to establish a condition that resulted in maximal attraction of the peptide with the sensor surface. This would increase the amount of contact between the peptide and the sensor surface that would then result in increased immobilisation yields.

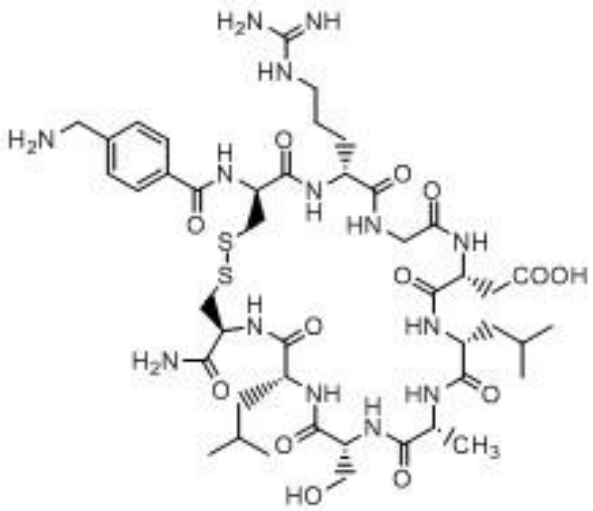


**Figure 21. Structure of RGD1-JD2-NH2 following conjugation of 6-aminomethylbenzoic acid spacer via N-terminal cysteine residue amine group.**

It was revealed that the solution of 10 mM sodium acetate (pH 4.0) provided the greatest response from JD2-RGD1 injection, compared to other solutions tested, and was, therefore, used in future immobilisation procedures involving this peptide derivative. Immobilisation of JD2-RGD1 by amine coupling resulted in a response of approximately 140 RU, resulting in theoretical maximum response ($R_{max}$) values of ~25,000 for both integrins αvβ6 and αVβ3 (Equation 5).

**Equation 5. Maximum response values for αvβ6 and αVβ3 binding to immobilised RGD1-JD2-$NH_2$.**

$$R_{max} = \frac{189100}{1067} \times 140 \; = \; 24{,}811 \; RU \; for \; \alpha v\beta 6$$

$$R_{max} = \frac{191300}{1067} \times 140 \; = \; 25{,}100 \; RU \; for \; \alpha V\beta 3$$

To establish integrin selectivity of the immobilised peptide, either αvβ6 or αVβ3 were injected over the peptide-coated surface. αVβ3 was used as this tends to be the most promiscuous RGD-binding integrin that recognises multiple RGD-containing ligands.

Integrins αvβ6 or αVβ3 were injected over the peptide surface at various concentrations for 3 minutes and any binding to the immobilised peptide was observed. Integrins were then allowed to dissociate from the peptide for 10 minutes before surfaces were regenerated prior to injection of the next concentration. Each concentration was repeated 3 times to assess reproducibility of the assay.

The integrin selectivity studies (Figure 22) revealed that JD2-RGD1 is able to specifically bind to αvβ6 with an association constant of 7.88 ± 2.39 $M^{-1}s^{-1}$, a dissociation constant of $1.07x10^{-3}$ ± $1.70x10^{-4}$ $M^{-1}$, and a resulting affinity of 15.3 ± 2.73 nM. It was also shown that injection of αVβ3 did not show any increases in response, at any concentration, indicating no binding was taking place. Because of this, kinetic data was unable to be determined. Therefore, due to no cross-reactivity of RGD1 with αVβ3, this peptide is a selective, as well as specific, targeted peptide for αvβ6.

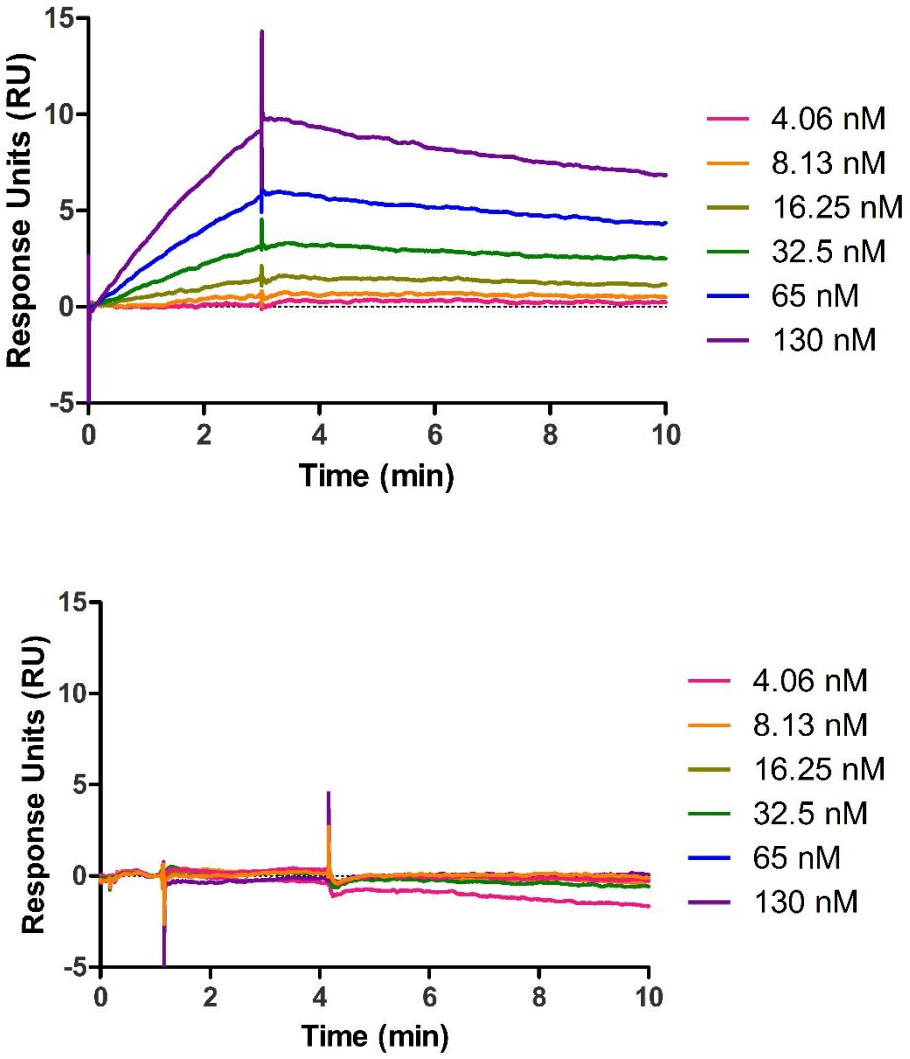


**Figure 22. SPR sensorgrams of multi-cycle kinetics experiments between RGD1 and (top) αvβ6 or (bottom) avb3**

### 3.3.5 Characterisation of αvβ6 expression

To assess the potential of αvβ6-targeted PET imaging agents, it was necessary to determine the most appropriate cell lines to use for characterisation of integrin αvβ6 specificity *in vitro* prior to *in vivo* studies. As discussed in the introduction, *in vitro* validation using cell lines that do, or do not, express the target of interest, is an important step in the development of a PET radioligand and allows for the determination, at an early stage, of radioligand affinity and specificity. The relative expression levels of αvβ6 were tested using flow cytometry and the αvβ6-specific monoclonal antibody, 10D5, which, importantly, only binds in the presence of both the αV and β6 subunits, and not either subunit individually, therefore is unable to cross-react with other αV-containing integrins. The cell lines tested for αvβ6 expression included murine embryonic fibroblasts ($MEF_{wt}$), β6-transfected MEFs (MEFβ6), pancreatic ductal adenocarcinoma (BxPC3) cells, human breast cancer cell line MDA-MB-468, human glioblastoma cell line (U87) and human colorectal adenocarcinoma (HT-29) cells. Flow cytometry studies (Figure 23), carried out at 4$^{o}$C to prevent receptor internalisation, of these cell lines revealed that the transfected cell line, MEFB6 had the highest relative expression of αvβ6. HT-29, MDA-MB-468 and BxPC3 cell lines also had endogenous expression of αvβ6, however at a lower relative amount compared to MEFβ6. The wild type MEF cell line, as well as U87 cells showed no αvβ6 expression, proving their usefulness as negative controls in future cell-based uptake assays. It should be stated that the wild-type MEF cell line expresses endogenous αV, therefore by transfecting β6 into this cell line, the heterodimeric αvβ6 can be expressed at the cell membrane. Importantly, it has been shown that the human glioblastoma cell line, U87, expresses the integrin αVβ3 [337], which would allow the assessment of integrin selectivity in future cell-based uptake assays.

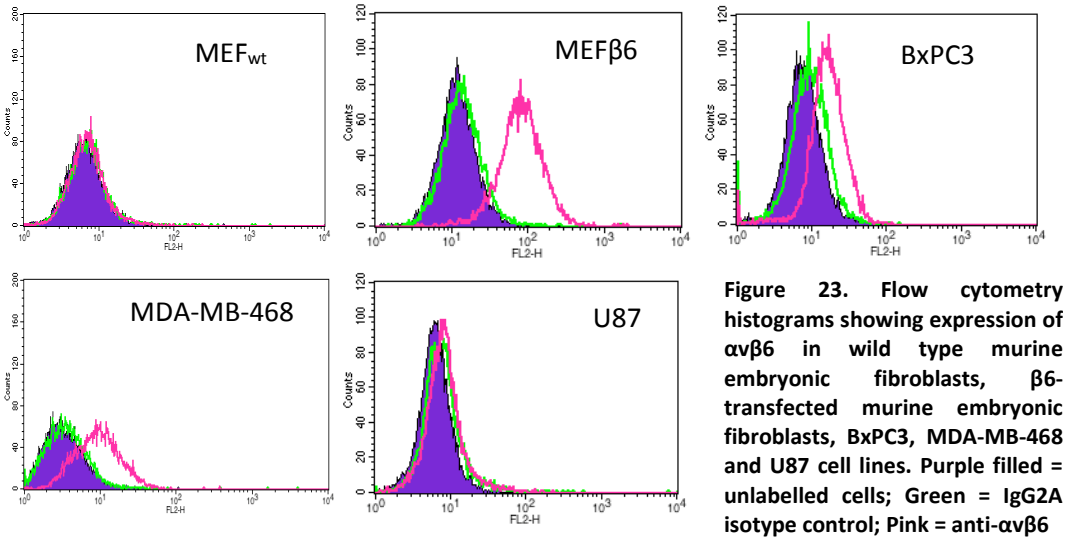


**Figure 23. Flow cytometry histograms showing expression of αvβ6 in wild type murine embryonic fibroblasts, β6-transfected murine embryonic fibroblasts, BxPC3, MDA-MB-468 and U87 cell lines. Purple filled = unlabelled cells; Green = IgG2A isotype control; Pink = anti-αvβ6**

### 3.3.6 Serum stability studies

A key property of a radiotracer that requires assessment is stability of the radiolabelled compound. Following radiolabelling of JD1-RGD1, JD2-RGD1 and DO3A-RGD3 to produce [$^{68}$Ga]Ga-DO3A-JD1-RGD1, [$^{68}$Ga]Ga-DO3A-JD2-RGD1 and [$^{68}$Ga]Ga-DO3A-RGD3, respectively, each radioligand was incubated in human serum for up to 3 hours prior to radio-HPLC analysis by Dr Juozas Domarkas. Radio-HPLC analysis showed that both [$^{68}$Ga]Ga-DO3A-JD1-RGD1 and [$^{68}$Ga]Ga-DO3A-JD2-RGD1 were completely stable in human serum for up to 3 hours (Figure 24). [$^{68}$Ga]Ga-DO3A-RGD3 was shown to be less stable with a stability of 94.24% ± 5.76 (Appendix Figure 5).

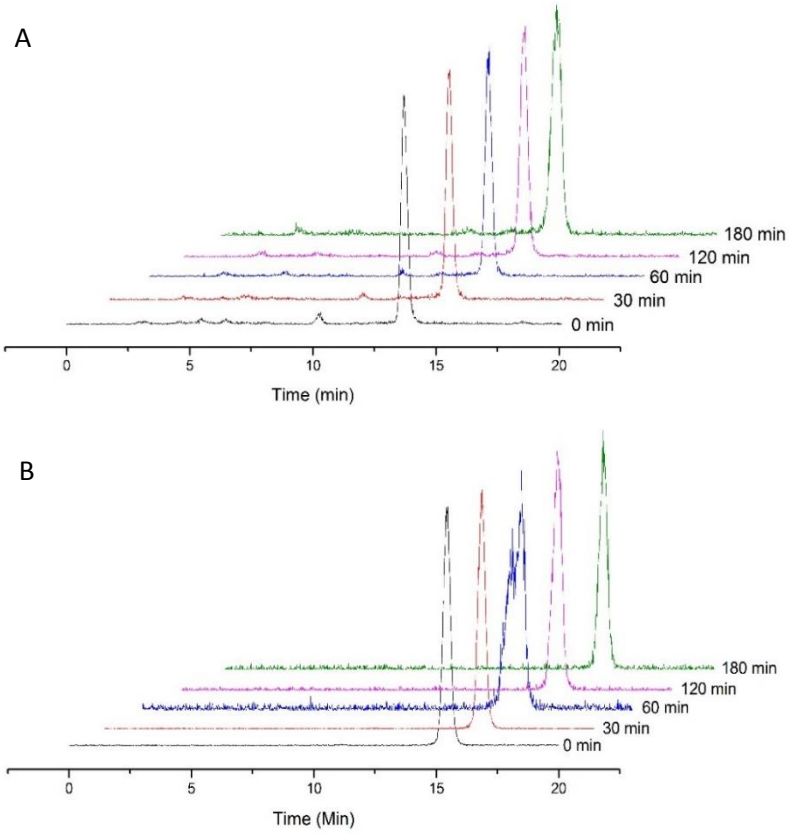


**Figure 24. Radio-HPLC chromatograms of $^{68}$Ga-JD1 (A) and $^{68}$Ga-JD2 (B) following incubation in human serum at 37°C for up to 3 hours. NOTE: The unusual trace in the 60 minute sample of trace B is an artefact.**

### 3.3.7 Lipophilicity studies

Lipophilicity studies were performed by Dr Juozas Domarkas. To determine the lipophilicity of radioligands, they were dissolved in PBS and added to an equal volume of octanol before being vigorously shaken to mix both phases. After separation of the phases, samples from each phase were taken to allow the measurement of radioactivity in each phase. In this case, PBS (pH 7.4) was used instead of water, therefore $LogD_{7.4}$ of each molecule was calculated using the following equation:

**Equation 6. Formula for the determination of radioligand lipophicility**

$$LogD_{7.4} = Log_{10}\left(\frac{Radioactivity\ of\ Octanol\ phase}{Radioactivity\ of\ PBS\ (pH\ 7.4)\ phase}\right)$$

[$^{68}$Ga]Ga-DO3A-JD1-RGD1, [$^{68}$Ga]Ga-DO3A-JD2-RGD1 and [$^{68}$Ga]Ga-DO3A-RGD3 exhibited $LogD_{7.4}$ values of -2.98 ± 0.03, -3.04 ± 0.01 and -3.54 ± 0.09, respectively, making them hydrophilic and likely to be excreted via the renal pathway *in vivo*.

### 3.3.8 Specific Activity

Due to the low UV signal generated by [$^{68}$Ga]Ga-DO3A-JD2-RGD1 (Appendix Figure 6) it was difficult to ascertain the $A_S$ of the radioligand, therefore a calibration curve was constructed using different amounts of peptide and the detected UV for each mass was determined. The calibration curve was generated (Appendix Figure 7) and the equation of the line of best fit was used to determine the $A_S$ of [$^{68}$Ga]Ga-DO3A-JD2-RGD1. It was deemed that the $A_S$ of [$^{68}$Ga]Ga-DO3A-JD2-RGD1 was approximately 7 MBq/µg.

### 3.3.9 Radioligand cell binding assay

#### 3.3.9.1 Cell binding

Following the characterisation of cell lines that do or do not express integrin αvβ6, validation of the radiolabelled peptide derivatives was carried out in radioligand cell binding assays to investigate their affinity and specificity for integrin αvβ6. For this, initial studies involved the incubation of [$^{68}$Ga]Ga-DO3A-JD1-RGD1, [$^{68}$Ga]Ga-DO3A-JD2-RGD1 or [$^{68}$Ga]Ga-DO3A-RGD3 with $MEF_{wt}$, MEFβ6, or MDA-MB-468 cells. Importantly, the experiments were carried out at 4$^{o}$C, which has been shown to prevent receptor internalisation [164].

Figure 25 shows the mean percentage of incubated dose ± SEM, with numerical values outline in Table 15, normalised per million cells present, of (A) [$^{68}$Ga]Ga-DO3A-JD1-RGD1, (B) [$^{68}$Ga]Ga-DO3A-JD2-RGD1 or (C) [$^{68}$Ga]-DO3A-RGD3 with $MEF_{wt}$, MEFβ6 or MDA-MB-468 cells. As shown by flow cytometry, both MEFβ6 and MDA-MB-468 have been shown to express integrin αvβ6, whereas $MEF_{wt}$ has been shown to lack integrin αvβ6.

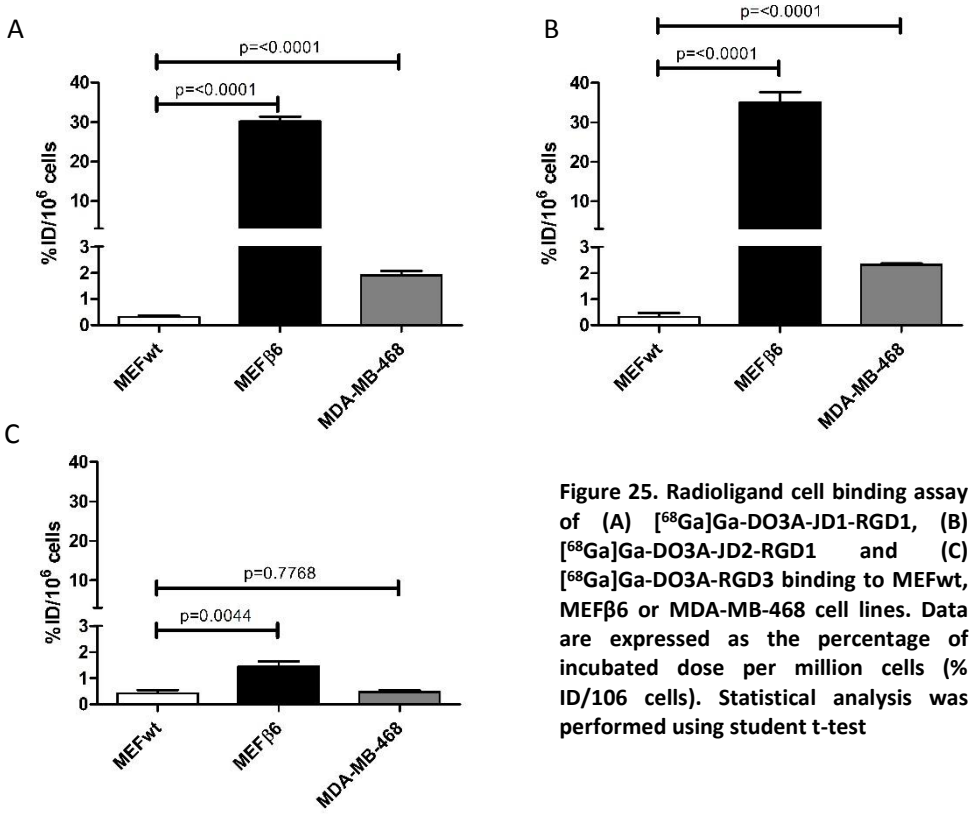


**Figure 25. Radioligand cell binding assay of (A) [$^{68}$Ga]Ga-DO3A-JD1-RGD1, (B) [$^{68}$Ga]Ga-DO3A-JD2-RGD1 and (C) [$^{68}$Ga]Ga-DO3A-RGD3 binding to MEFwt, MEFβ6 or MDA-MB-468 cell lines. Data are expressed as the percentage of incubated dose per million cells (% ID/106 cells). Statistical analysis was performed using student t-test**

**Table 15. Percentage incubated dose per million cells of radioligands with MEFwt,** MEFβ6 **and MDA-MB-468 cell lines**

| | 68Ga-JD1 | 68Ga-JD2 | 68Ga-RGD3 |
|---|---|---|---|
| **$MEF_{wt}$** | 0.31 ± 0.05 | 0.33 ± 0.14 | 0.42 ± 0.13 |
| **MEFβ6** | 30.15 ± 1.21 | 34.65 ± 4.10 | 1.46 ± 0.12 |
| **MDA-MB-468** | 2.33 ± 0.04 | 2.72 ± 0.11 | 0.47 ± 0.08 |

As shown is Figure 25A, [$^{68}$Ga]Ga-DO3A-JD1-RGD1 showed uptake in MEFβ6 ($p<0.0001$) and MDA-MB-468 ($p<0.0001$) cells displayed significantly increased uptake than in the αvβ6$^{-}$ MEF$_{wt}$ cell line, which displayed negligible uptake. The uptake of [$^{68}$Ga]Ga-DO3A-JD2-RGD1 showed a similar uptake profile to [$^{68}$Ga]Ga-DO3A-JD1-RGD1 (Figure 25B), with uptake in MEFβ6 ($p<0.0001$) and MDA-MB-468 ($p<0.0001$) cells displaying significantly superior uptake in comparison to MEF$_{wt}$ cells.

It was shown that the percentage of incubated dose of [$^{68}$Ga]Ga-DO3A-RGD3 associated with MEF$_{wt}$, MEFβ6 and MDA-MB-436 cells was much lower than with [$^{68}$Ga]Ga-DO3A-JD1-RGD1 or [$^{68}$Ga]Ga-DO3A-JD2-RGD1, and uptake in MEFβ6 ($p=0.004$) but not in MDA-MB-468 ($p=0.777$) cells displaying significantly increased uptake than in MEF$_{wt}$ cells. Interestingly, the uptake values for [$^{68}$Ga]Ga-DO3A-RGD3 were significantly lower than the uptake values of both [$^{68}$Ga]Ga-DO3A-JD1-RGD1 ($p<0.0001$) and [$^{68}$Ga]Ga-DO3A-JD2-RGD1 ($p<0.0001$) (Figure 25C). At this point, due to the very low levels of uptake of $^{68}$Ga-RGD3 in αvβ6-positive cell lines, it was not taken forward for further evaluation.

Due to the higher affinity for αvβ6 and increased cellular uptake of [$^{68}$Ga]Ga-DO3A-JD2-RGD1 in both competitive ELISA and radioligand cell binding assays, respectively, it was taken forward for further cell binding assays using the αvβ6$^{+}$ pancreatic adenocarcinoma cell line, BxPC3 and the human glioblastoma cell line, U87, which has been shown to be negative for αvβ6, but is well known to express integrin αVβ3 [337] to a high level, providing an effective selectivity control. The uptake of [$^{68}$Ga]Ga-DO3A-JD2-RGD1 in BxPC3 or U87 cell lines, was compared with that of MEFB6 and MEF$_{wt}$ from Figure 25B. As shown by Figure 26, with numerical values detailed in Table 16, significantly higher uptake was observed in BxPC3 cells, as compared to U87 cells ($p<0.0001$) and MEF$_{wt}$ cells ($p<0.0001$). As expected, no significant difference was observed for the uptake of [$^{68}$Ga]Ga-DO3A-JD2-RGD1 in U87 cells or MEF$_{wt}$ cells ($p=0.742$), with negligible uptake being observed in these lines.

**Table 16. Percentage incubated dose per million cells of radioligands with MEFwt, MEFβ6, U87 and BxPC3 cell lines**

| | [$^{68}$Ga]Ga-DO3A-JD2-RGD1 |
|---|---|
| **MEF$_{wt}$** | 0.31 ± 0.05 |
| **MEFβ6** | 30.15 ± 1.21 |
| **U87** | 0.23 ± 0.11 |
| **BxPC3** | 5.03 ± 0.40 |

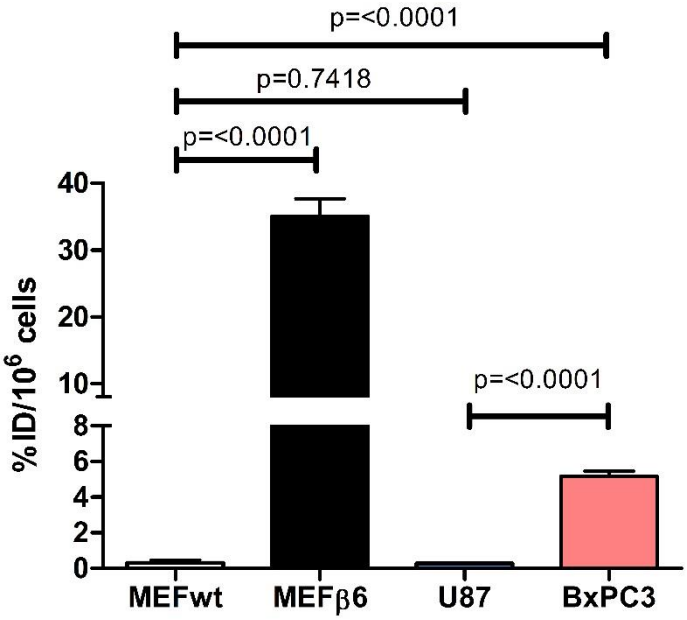


**Figure 26. Radioligand cell binding assay of [$^{68}$Ga]Ga-DO3A-JD2-RGD1 binding to MEFwt, MEFβ6, U87, BxPC3 or MDA-MB-468 cell lines. Data are expressed as the percentage of incubated dose per million cells (% ID/106 cells). Statistical analysis was performed using student t-test**

### 3.3.9.2 Internalisation of [$^{68}$Ga]Ga-DO3A-JD2-RGD1

Following validation of [$^{68}$Ga]Ga-DO3A-JD2-RGD1 binding to αvβ6 in cell line models, the next step involved the assessment of radioligand internalisation by the both the αvβ6-positive BxPC3 cell line and the αvβ6-negative U87 cell line.

The internalisation of a radioligand that binds to a membrane-associated receptor, such as αvβ6, would lead to increased tumour:background ratios and enhanced tumour contrast, therefore an ideal radiotracer would be internalised by the cells to allow accumulation within the cell in order to enhance this contrast.

BxPC3 cells were used as a positive control, as they express αvβ6, whereas U87 cell lines, which do not express αvβ6 were used as a negative control, to which any internalisation that may be observed could be considered as non-specific uptake of the radioligand, as there was negligible uptake of [$^{68}$Ga]Ga-DO3A-JD2-RGD1 in U87 cells at 4$^{o}$C, whereby receptor internalisation was prevented.

To determine the amount of radioligand internalisation, all experiments were performed at 37$^{o}$C to allow for receptor internalisation. Radioligand [$^{68}$Ga]Ga-DO3A-JD2-RGD1 was incubated with cells for 1 hour prior to washing away any unbound radioligand. An ice-cold acid wash was performed to remove any surface bound radioactivity, which was harvested, and the remaining cell pellet was solubilised using NaOH and harvested along with any associated radioactivity. The amount of internalised radioactivity was expressed as the percentage of cell-associated activity and can be characterised as:

**Equation 7.** Calculation for determining radioligand internalisation as a percentage of cell-associated radioactivity.

$$\%\, Internalisation = \frac{(Cell\ associated\ activity)}{(Surface\ bound\ activity + Cell\ Associated\ Activity)} \times 100$$

A missed opportunity in this study was to evaluate whether or not receptor recycling was taking place, and also, if externalisation of the radioligand was taking place following internalisation. This experiment would include an extra washing step following the acid wash to remove surface-bound radioactivity, with the radioactivity of the last wash being taken at various timepoints to observe whether the radioactivity of the supernatant increases, as would be expected if the radioligand was being externalised.

The percentage internalisation of [$^{68}$Ga]Ga-DO3A-JD2-RGD1 was 64.86% ± 1.98 in BxPC3 cells, compared to 11.38% ± 1.32 of radioactivity in U87 cells (Figure 27). The amount of internalisation was found to be significantly greater in BxPC3

cells than in U87 cells ($p<0.0001$), as determined by student's t-test, although the internalisation in U87 cells may be considered negligible as this represents the percentage of total bound radioactivity to these cells, which was extremely low in the experiments involving incubation with radioligand at 4°C.

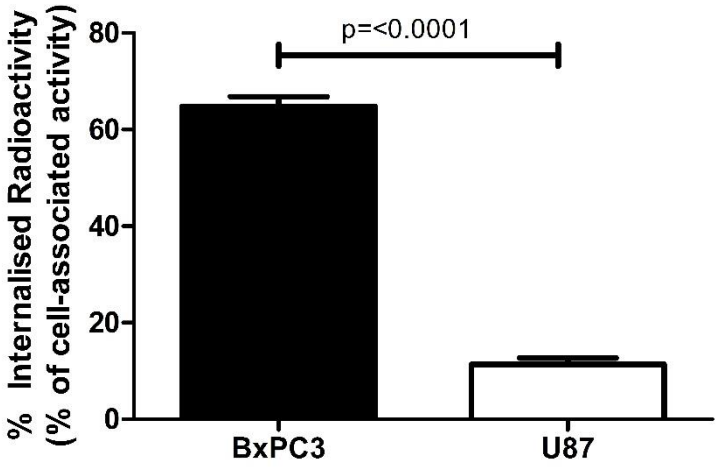


**Figure 27. Radioligand internalisation assay of 68Ga-JD2-RGD1 in BxPC3 and U87 cell lines. Data are expressed as the percentage of cell-associated activity. Statistical analysis was performed using student t-test**

### 3.3.10 PET imaging studies in non-tumour bearing mice using [$^{68}$Ga]Ga-DO3A-JD1-RGD1 and [$^{68}$Ga]Ga-DO3A-JD2-RGD1

To assess the pharmacokinetics and tissue localisation of both [$^{68}$Ga]Ga-DO3A-JD1-RGD1 and [$^{68}$Ga]Ga-DO3A-JD2-RGD1 *in vivo*, dynamic PET/CT studies were undertaken in non-tumour bearing CD1-nude mice.

[$^{68}$Ga]Ga-DO3A-JD1-RGD1 (9.32 ± 0.23 MBq) or [$^{68}$Ga]Ga-DO3A-JD2-RGD1 (4.79 ± 0.04 MBq) was injected intravenously via the tail vein of anaesthetised mice and images acquired over a 90 minute window.

Following administration of [$^{68}$Ga]Ga-DO3A-JD1-RGD1 , uptake of the radioligand was observed in the gastrointestinal tract ($SUV_{mean}$ = 0.78 ± 0.07) and

submandibular gland area ($SUV_{mean}$ = 0.63 ± 0.01) (Figure 28). As with other αvβ6-targeted molecules in the literature, the uptake, in the 90 minute imaging window, in muscle was significantly lower in the muscle ($SUV_{mean}$ = 0.17 ± 0.08) than the GI tract (p=0.026) and SMG (p=0.027), as assessed by student's t-test, indicating potential specific binding of [$^{68}$Ga]Ga-DO3A-JD1-RGD1 to integrin αvβ6.

Administration of [$^{68}$Ga]Ga-DO3A-JD2-RGD1 produced very similar results to [$^{68}$Ga]Ga-DO3A-JD1-RGD1. Uptake was observed in the GI tract ($SUV_{mean}$ = 0.92 ± 0.11) and SMG ($SUV_{mean}$ = 0.91 ± 0.14), with high uptake also being observed in the kidneys. Hind leg muscle uptake of [$^{68}$Ga]Ga-DO3A-JD2-RGD1 ($SUV_{mean}$ = 0.29 ± 0.01) was found to be significantly lower than that of the GI tract (p=0.005) and SMG (p=0.012), indicating potential specificity of [$^{68}$Ga]Ga-DO3A-JD2-RGD1 binding to integrin αvβ6.

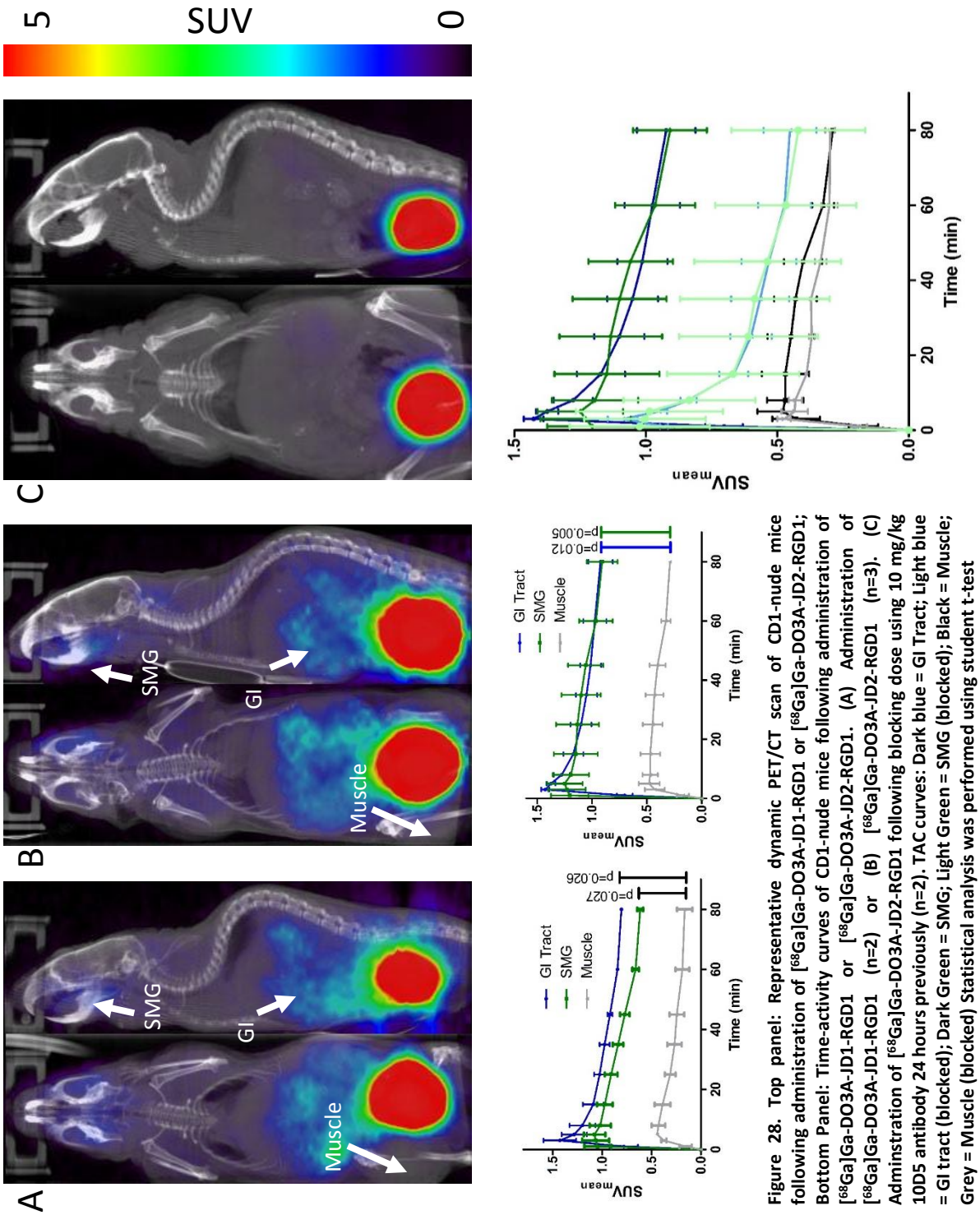


**Figure 28. Top panel: Representative dynamic PET/CT scan of CD1-nude mice following administration of [$^{68}$Ga]Ga-DO3A-JD1-RGD1 or [$^{68}$Ga]Ga-DO3A-JD2-RGD1; Bottom Panel: Time-activity curves of CD1-nude mice following administration of [$^{68}$Ga]Ga-DO3A-JD1-RGD1 or [$^{68}$Ga]Ga-DO3A-JD2-RGD1. (A) Administration of [$^{68}$Ga]Ga-DO3A-JD1-RGD1 (n=2) or (B) [$^{68}$Ga]Ga-DO3A-JD2-RGD1 (n=3). (C) Adminstration of [$^{68}$Ga]Ga-DO3A-JD2-RGD1 following blocking dose using 10 mg/kg 10D5 antibody 24 hours previously (n=2). TAC curves: Dark blue = GI Tract; Light blue = GI tract (blocked); Dark Green = SMG; Light Green = SMG (blocked); Black = Muscle; Grey = Muscle (blocked) Statistical analysis was performed using student t-test**

To confirm the *in vivo* specificity of [$^{68}$Ga]Ga-DO3A-JD2-RGD1 for integrin αvβ6, a blocking study using the anti-integrin αvβ6 monoclonal antibody, 10D5, was performed. Mice were injected by intraperitoneal injection 24 hours prior to radioligand administration.

Following blocking, and subsequent injection of [$^{68}$Ga]Ga-DO3A-JD2-RGD1 (2.88 ± 0.84 MBq), there was a notable decrease in the uptake seen in the GI tract and SMG compared the non-blocked state (Figure 28). The GI tract, following blocking, ($SUV_{mean}$ = 0.33 ± 0.26) exhibited a 64.1% decrease compared to GI tract uptake in absence of blocking, although this was not deemed to be statistically significant (p=0.062). The submandibular glands also exhibited a decrease of 60.4% compared to uptake of SMG in the absence of antibody blockade. This difference was also not found to be significant (p=0.160), however it is indicative of the specificity of [$^{68}$Ga]Ga-DO3A-JD2-RGD1 for integrin αvβ6.

### 3.3.11 *Ex vivo* metabolite analysis of [$^{68}$Ga]Ga-DO3A-JD1-RGD1 and [$^{68}$Ga]Ga-DO3A-JD2-RGD1

To increase understanding of the *in vivo* metabolic stability of [$^{68}$Ga]Ga-DO3A-JD1-RGD1 and [$^{68}$Ga]Ga-DO3A-JD2-RGD1, urine was obtained from all animals imaged and processed by Dr Juozas Domarkas for radio-HPLC analysis to observe whether or not any radiometabolites had been produced during the imaging procedure. Image quality and quantitative analysis of images rely significantly on radiotracer stability. The production of metabolites may give rise to off target effects, and potential non-specific uptake in various tissues, giving false signals that may confound PET images.

Following administration of [$^{68}$Ga]Ga-DO3A-JD1-RGD1 or [$^{68}$Ga]Ga-DO3A-JD2-RGD1, urine was harvested after 90 minutes prior to analysis by radio-HPLC. Any radioactive peaks observed in the resulting chromatogram were highlighted (Figure 29), compared to a non-metabolised control chromatogram for either radioligand.

Figure 29 shows that 54.19% ± 3.47 of [$^{68}$Ga]Ga-DO3A-JD1-RGD1 was excreted in the urine intact, with a radiometabolite peak appearing upstream of the intact radioligand. On the other hand, [$^{68}$Ga]Ga-DO3A-JD2-RGD1 was 40.99% ± 0.10 stable, with a radiometabolite peak eluting at the same timepoint as with [$^{68}$Ga]Ga-DO3A-JD1-RGD1, indicating that the radiometabolite may be the same in both radioligands. Samples were analysed from three different administrations into different animals.

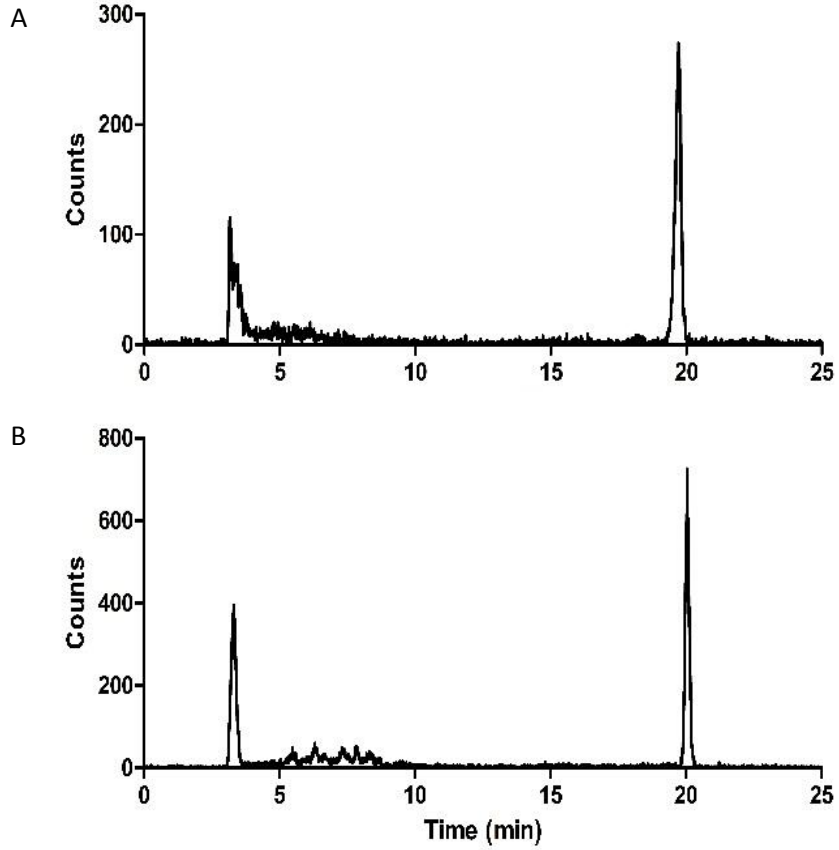


**Figure 29. Stability analysis of [$^{68}$Ga]Ga-DO3A-JD1-RGD1 and [$^{68}$Ga]Ga-DO3A-JD2-JD2 in the urine. (A) Radio-HPLC chromatogram of [$^{68}$Ga]Ga-DO3A-JD1-RGD1 after 90 minute administration in CD1-nude mice. (B) Radio-HPLC chromatogram of [$^{68}$Ga]Ga-DO3A-JD2-RGD1 after 90 minute administration in CD1-nude mice (n=3).**

### 3.3.12 PET imaging studies in BxPC3 tumour-bearing mice using [$^{68}$Ga]Ga-DO3A-JD2-RGD1

Following previous imaging studies with the purpose of evaluating the tissue distribution and pharmacokinetics of [$^{68}$Ga]Ga-DO3A-JD1-RGD1 and [$^{68}$Ga]Ga-DO3A-JD2-RGD1, it was necessary to validate the *in vivo* specificity of RGD1 further. Following confirmation of integrin αvβ6 expression in the PDAC cell line, BxPC3, in 3.3.5, a xenograft model was established using this cell line to validate the uptake of [$^{68}$Ga]Ga-DO3A-JD2-RGD1 in this tumour model. This radiopeptide was chosen due to its higher affinity and rigid linker.

Female NSG (NOD.*Cg-Prkdc$^{SCID}$//2rg$^{tm1Wjl}$/SzJ)* mice were implanted with 5x10$^6$ BxPC3 cells subcutaneously on the right flank and tumours growth was monitored (Figure 30) until they reached approximately 100 mm$^3$, at which point imaging studies with [$^{68}$Ga]Ga-DO3A-JD2-RGD1.

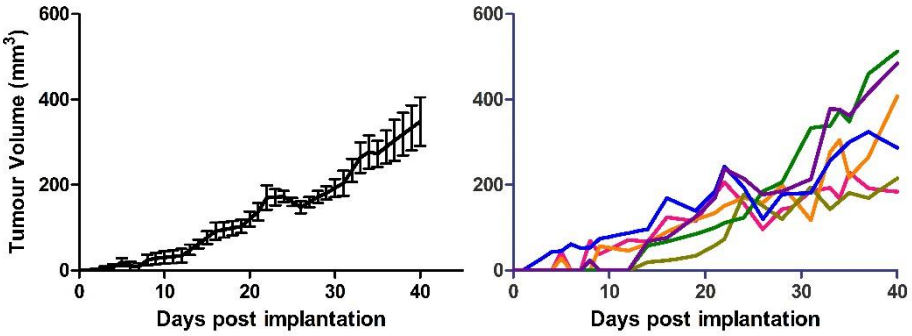


**Figure 30. BxPC3 xenograft growth curves. Left: Average tumour growth of cohort of 6 mice with SEM. Right: Individual xenograft growth curves for 6 mice within cohort.**

PET imaging studies of [$^{68}$Ga]Ga-DO3A-JD2-RGD1 in BxPC3 tumour-bearing mice (Figure 31A-B) revealed that there was significantly higher uptake of radioligand in the tumour (0.90 ± 0.03; p<0.0001), gastrointestinal tract (1.57 ±

0.05; p<0.0001) and submandibular glands (0.94 ± 0.04; p<0.0001) compared to that of the muscle (0.24 ± 0.03).

To confirm specificity of [$^{68}$Ga]Ga-DO3A-JD2-RGD1 *in vivo*, another blocking study was performed to confirm that the uptake seen with [$^{68}$Ga]Ga-DO3A-JD2-RGD1 was due to radioligand binding to integrin αvβ6.

Following blocking studies (Figure 31C-D), it was shown that antibody blockade led to tumour uptake ($SUV_{max}$ = 0.90 ± 0.03) being significantly reduced (p=0.0039) by 54.1% in the blocked tumour ($SUV_{max}$ = 0.57 ± 0.15), indicating specific uptake of $^{68}$Ga-JD2 in the αvβ6$^{+}$ BxPC3 xenograft. The uptake of $^{68}$Ga-JD2 in the GI tract ($SUV_{max}$ 1.57 ± 0.78) and SMG ($SUV_{max}$ = 0.94 ± 0.04) was also found to be significantly reduced by 50.2% and 31.7%, respectvely (GI tract $SUV_{max}$ = 0.78 ± 0.15, p<0.0001; SMG $SUV_{max}$ = 0.64 ± 0.15, p=0.0027). Importantly, there was no difference between the uptake of $^{68}$Ga-JD2 in the muscle before ($SUV_{max}$ = 0.24 ± 0.03) or after ($SUV_{max}$ = 0.19 ± 0.02) blockade of integrin αvβ6 (p=0.4618).

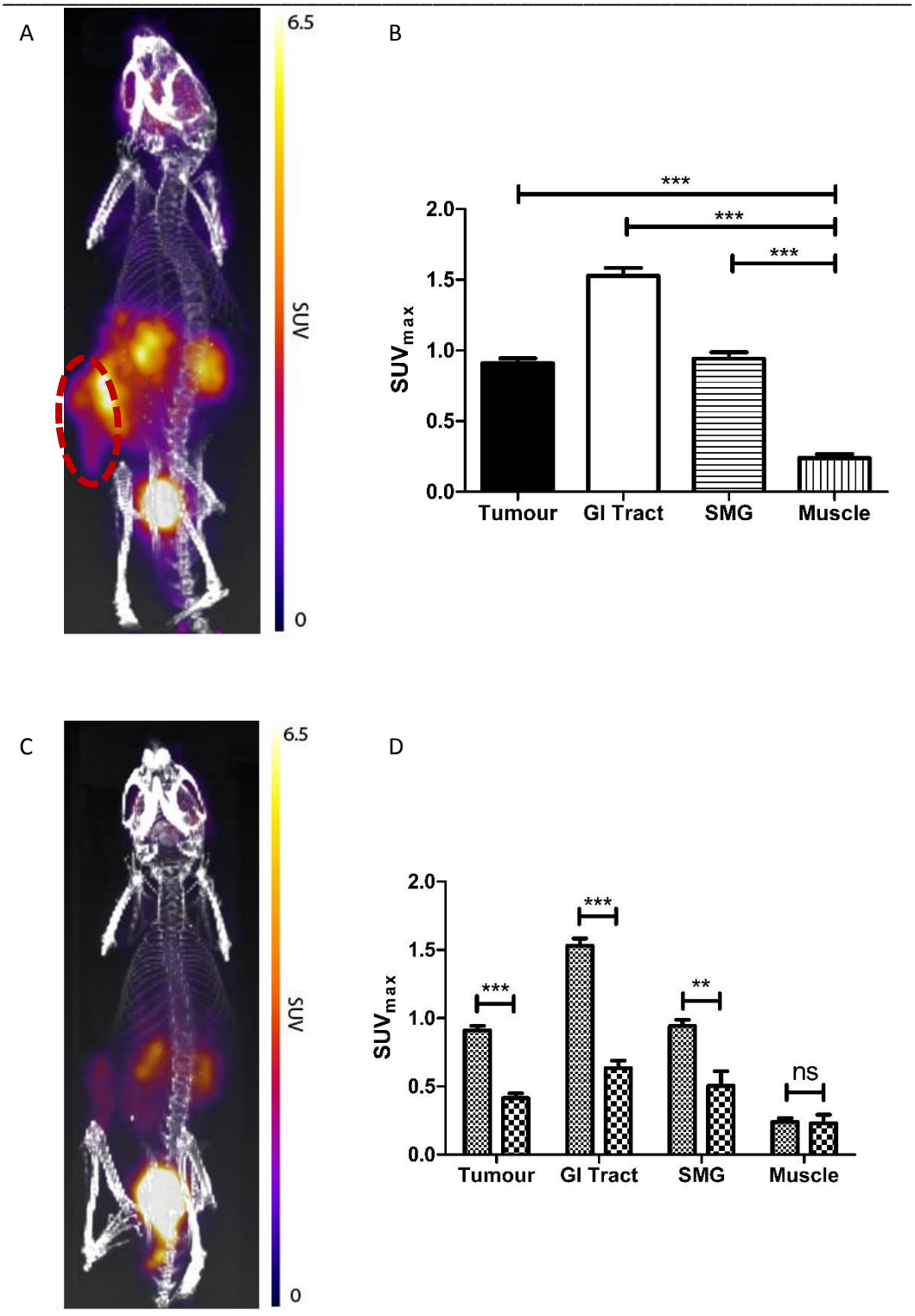


**Figure 31. PET/CT images of BxPC3 tumour-bearing NSG mice. (A) Representative maximum intensity projection PET/CT image of BxPC3 tumour-bearing mouse after 60 minute injection of [$^{68}$Ga]Ga-DO3A-JD2-RGD1. (B) Maximum standard uptake values of [$^{68}$Ga]Ga-DO3A-JD2-RGD1 in the tumour, GI tract, SMG and muscle, (n=9). (C) 60 minute injection of [$^{68}$Ga]Ga-DO3A-JD2-RGD1 following antibody blockade 24 hours previously (n=2). (D) Maximum standard uptake values of [$^{68}$Ga]Ga-DO3A-JD2-RGD1, following blockade, in the tumour, GI tract, SMG and muscle. *** = p<0.0005, ** = p<0.005, * = p<0.05. Statistical analysis was performed using student t-test**

### 3.3.13 Biodistribution analysis of [$^{68}$Ga]Ga-DO3A-JD2-RGD1 in BxPC3 xenograft-bearing mice

Biodistribution experiments were performed by Dr Christopher Cawthorne. With imaging small animals, it is difficult to obtain truly quantitative data due to partial volume effects and difficulty with ROI definition for delineating various tissues or organs within the anatomy of a small animal. ROI definition relies on effective contrast, by CT imaging, between different tissues of a subject, which is achieved through differential attenuation between different tissues. The greatest CT contrast that can be observed in small animals is between bone and soft tissues, however contrast between different types of soft tissues, such as the gastrointestinal tract, submandibular glands and others, is limited due to the reduced sensitivity of CT by several orders of magnitude compared to PET, and is the reason why contrast agents are often used to enhance contrast between soft tissues. This limited contrast between soft tissues makes accurate ROI definition difficult, potentially leading to skewed uptake values as a result. Therefore, biodistribution studies, whereby animals are injected with radiotracer for specific timepoints prior to sacrifice and dissection of all major organs and the activity contained within counted, can be a useful tool in determining the absolute activity within a tissue, without the issues of partial volume effects or inaccurate ROI definition. However, problems with biodistribution analyses do exist, such as the requirement for animal sacrifice and the loss of blood flow, although biodistribution studies can be compared against imaging results [338].

[$^{68}$Ga]Ga-DO3A-JD2-RGD1 ($1.5x10^7$ CPM ± $8.67x10^5$) was injected intravenously via the tail vein in 0.2 ± 0.01 mL either following 24 hour blockade with anti-integrin αvβ6 mAb or no blocking and animals were sacrificed after approximately 1 hour 45 minutes. Animals were dissected and organs weighed and counted for radioactivity.

Figure 32 shows the biodistribution of [$^{68}$Ga]Ga-DO3A-JD2-RGD1 in BxPC3 tumour-bearing NSG mice, and numerical values for each tissue can be found in

Table 17. The uptake of [$^{68}$Ga]Ga-DO3A-JD2-RGD1 in the tumour (4.51% ID/g ± 0.47) was greater than in any other tissues, except for the small intestine (SI) (5.63% ID/g ± 1.04), large intestine (4.52% ID/g ± 0.73) and kidneys (10.62% ID/g ± 0.78). Other areas of interest that had elevated levels of [$^{68}$Ga]Ga-DO3A-JD2-RGD1 uptake were the lungs (3.00% ID/g ± 0.34) and cecum (4.04% ID/g ± 0.83).

Comparing tracer uptake in animals that did not undergo blocking to those that did, there were significant reductions in [$^{68}$Ga]Ga-DO3A-JD2-RGD1 uptake in tumour (p=0.0036), lung (p=0.0053), pancreas (p=0.0016), small intestine (p=0.0278), submandibular glands (p=0.0139) and, curiously, muscle (p=0.0004), There was also noticeable reduction in radioligand uptake in the large intestine (p=0.0547) and cecum (p=0.0766), but these were not found to be statistically significant.

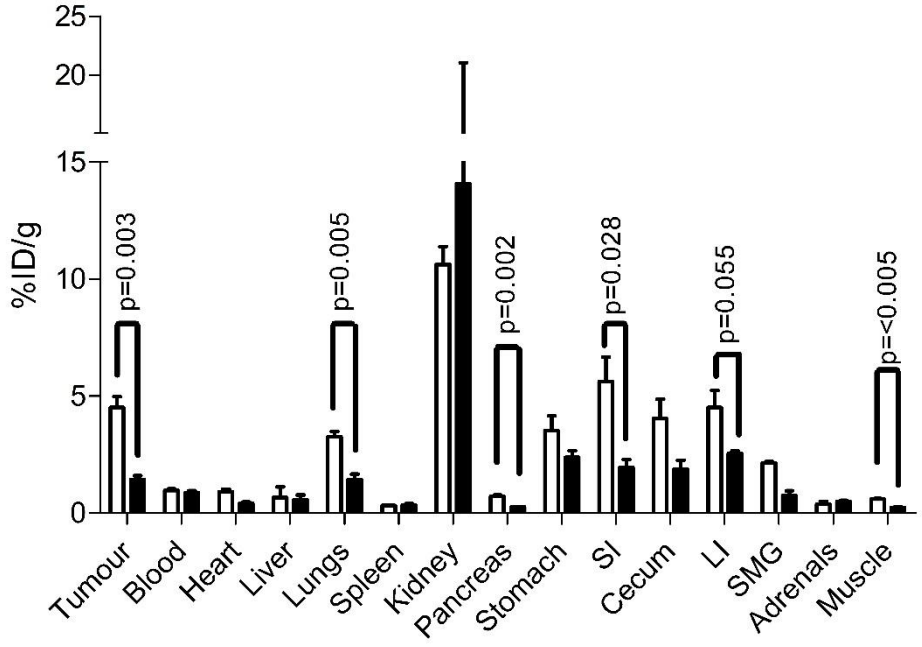


**Figure 32. Biodistribution of [$^{68}$Ga]Ga-DO3A-JD2-RGD1 in BxPC3 tumour-bearing NSG mice**

**Table 17. Biodistribution data for [$^{68}$Ga]Ga-DO3A-JD2-RGD1**

| Organ/Tissue | $^{68}$Ga-JD2 | | Blockade |
|---|---|---|---|
| | %ID/g | Tumour/Organ Ratio | %ID/g |
| Tumour | 4.51 ± 0.47 | | 1.44 ± 0.16 |
| Blood | 0.97 ± 0.07 | 4.74 ± 0.77 | 0.87 ± 0.09 |
| Heart | 0.91 ± 0.12 | 5.05 ± 0.70 | 0.42 ± 0.05 |
| Liver | 0.83 ± 0.35 | 7.24 ± 2.41 | 0.56 ± 0.22 |
| Lungs | 3.00 ± 0.34 | 1.51 ± 0.14 | 1.43 ± 0.24 |
| Spleen | 0.32 ± 0.02 | 14.15 ± 1.94 | 0.36 ± 0.05 |
| Kidney | 10.62 ± 0.78 | 0.43 ± 0.04 | 6.65 ± 0.56 |
| Pancreas | 0.71 ± 0.06 | 6.35 ± 0.75 | 0.27 ± 0.02 |
| Stomach | 3.52 ± 0.64 | 1.33 ± 0.13 | 2.39 ± 0.29 |
| SI | 5.63 ± 1.04 | 0.83 ± 0.12 | 1.96 ± 0.32 |
| Cecum | 4.04 ± 0.83 | 1.22 ± 0.31 | 1.89 ± 0.37 |
| LI | 4.52 ± 0.73 | 1.03 ± 0.13 | 2.54 ± 0.11 |
| SMG | 2.15 ± 0.04† | 1.97 ± 0.35 | 0.75 ± 0.21 |
| Adrenals | 1.33 ± 0.95† | 8.21 ± 3.47 | 0.50 ± 0.03 |
| Muscle | 0.60 ± 0.02 | 7.57 ± 0.95 | 0.24 ± 0.02 |

### 3.3.14 *Ex vivo* immunohistochemical analysis of tissues for αvβ6 expression

In order to reinforce imaging and biodistribution data for [$^{68}$Ga]Ga-DO3A-JD2-RGD1, it was necessary to show, using a different technique, that integrin αvβ6 was expressed in areas of radioligand uptake, in order to prove the specificity of [$^{68}$Ga]Ga-DO3A-JD2-RGD1 for integrin αvβ6.

Following fixation and paraffin embedding, BxPC3 tumour, submandibular glands, small intestine, lungs, kidneys (Figure 33) and U87 tumours (Figure 34) were processed and stained for the integrin β6 subunit, which is only able to dimerise with the integrin αV subunit, therefore staining reflected αvβ6 distribution. As shown in Figure 33, BxPC3 tumours expressed integrin αvβ6 to a high level throughout the tumour. It was also shown to be highly expressed in the submandibular glands and the small intestine. Importantly, the localisation of staining in the small intestine was at the epithelium, whereby αvβ6 is exclusively expressed.

There was also a small amount of αvβ6 expression in the alveolar epithelium of the lungs. Interestingly, despite the high uptake of [$^{68}$Ga]Ga-DO3A-JD2-RGD1 in the kidneys, there was no detectable kidney αvβ6 expression by IHC. A U87 xenograft tumour was used as a negative and selectivity control, as U87 cells have been shown to not express αvβ6, but express a high degree of the related integrin αVβ3.

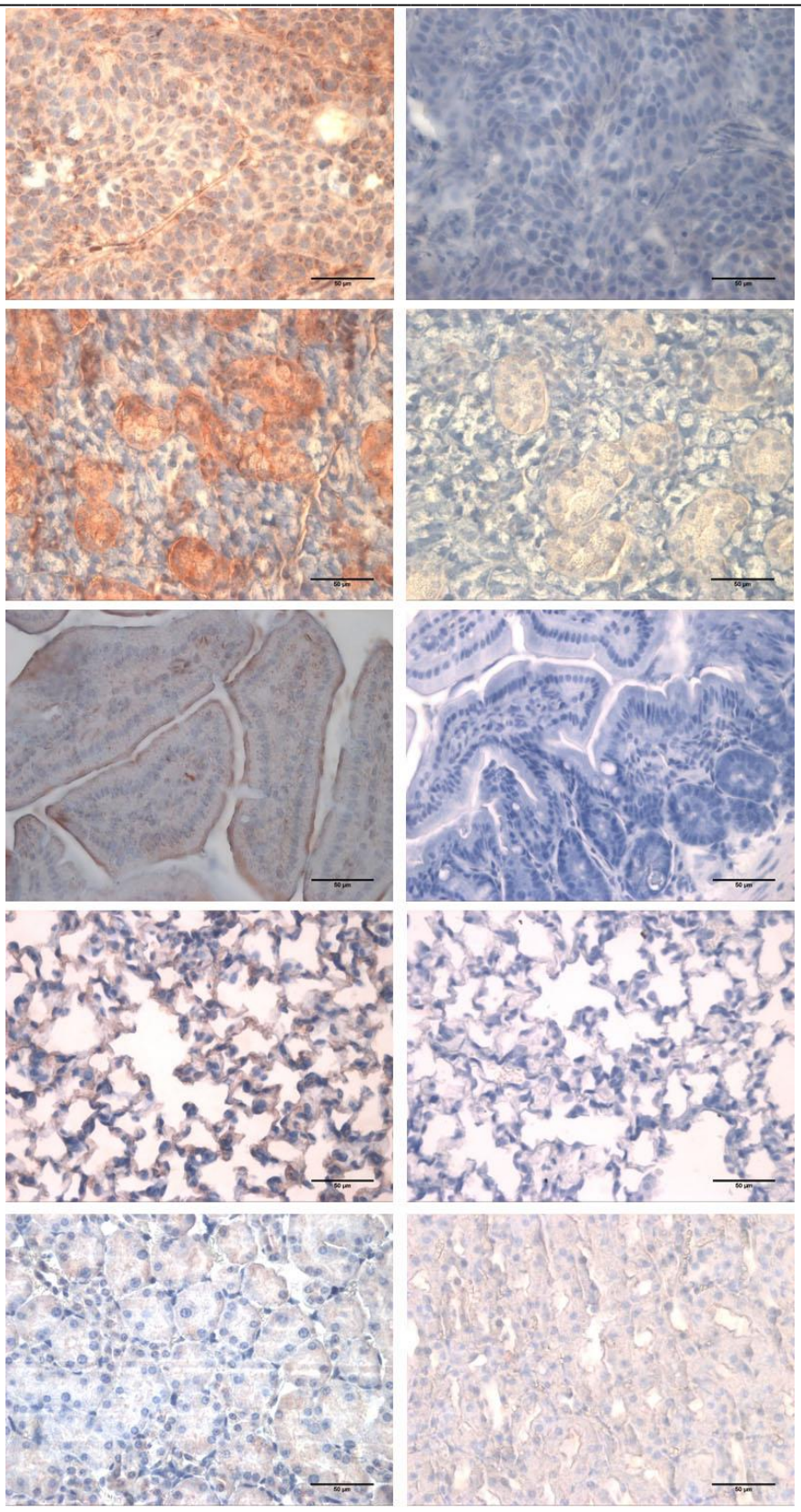

**Figure 33. Immunohistochemical analysis of (left panel) integrin β6 and (right panel) IgG isotype control. (Top) BxPC3 tumour, (Second row) submandibular glands, (Middle) small intestine (duodenum), (Fourth row) lung, and (Bottom) kidney. Bars indicate 50 µm.**

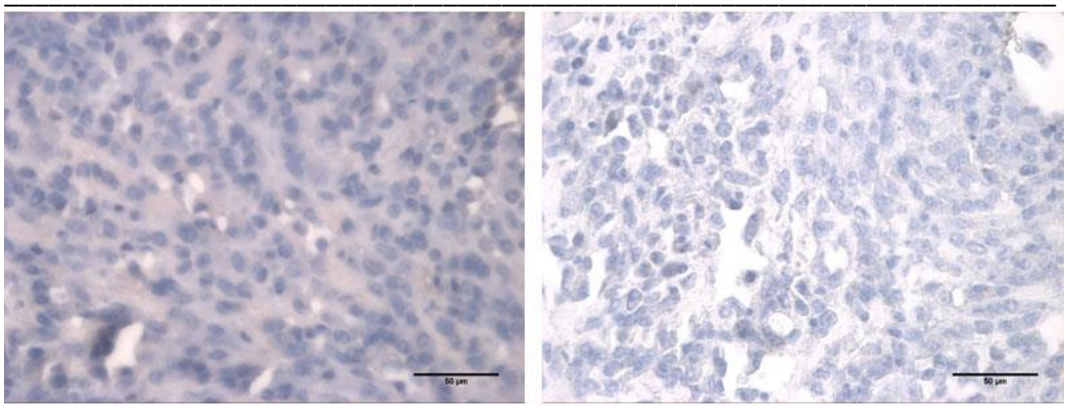

**Figure 34. Immunohistochemical analysis of (left panel) integrin β6 and (right panel) IgG isotype control in U87MG xenografts. Bars indicate 50 µm.**

These images were compared to equivalent images that involved an isotype antibody in place of the integrin β6 antibody. It was shown that using the isotype antibody did not result in any staining in any of the tissues used, indicating that non-specific binding of the antibody was not taking place.

## 3.4 Discussion

This study has evaluated an integrin αvβ6-targeted cyclic peptide, RGD1, which can selectively, and specifically bind to αvβ6 with high affinity. This thesis has shown that in addition to RGD1 having potential as a clinical diagnostic PET imaging agent for oncology and respiratory medicine, there is potential to evaluate this radioligand for use as a peptide-receptor radionuclide therapy agent.

Competitive binding ELISA experiments, using the αvβ6-specific antibody, 10D5, as a competitor molecule allowed the assessment of αvβ6-binding of various peptides. Of the four peptides tested, only RGD1 and RGD3 were shown to be able to bind to integrin αvβ6. RGD1, with the amino acid sequence CRGDLASLC, is a literature-described peptide, originally derived from a phage display library aimed at identifying cancer-identifying peptides, which is reported to have subnanomolar affinity for αvβ6. Following synthesis of CRGDLASLC, competition binding experiments of the peptide against an αvβ6-specific antibody

were performed showing binding of the peptide to integrin αvβ6. The results were in accordance with another report in the literature, showing RGD1 to possess a subnanomolar affinity for αvβ6. Importantly for RGD1, the cyclisation of the peptide by flanking cysteine amino acid residues on N- and C-termini allows for the conjugation of additional groups via the sole free amine group on the N-terminal cysteine in order to allow modifications essential for radiolabelling. A slightly modified version of RGD1, RGD2, had an altered sequence in which the serine residue was removed and the second leucine residue was replaced with phenylalanine, as it was reported this amino acid could typically be substituted with a bulky amino acid in order to provide increased affinity [191]. As shown by the ELISA results, RGD2 was unable to inhibit integrin αvβ6 antibody binding within the concentration range tested, indicating a very low, or no affinity for the receptor. The inability of RGD2 to bind to integrin αvβ6 can be explained by an altered peptide amino acid sequence from RGD1. The serine residue has been substituted for a phenylalanine, whilst the second leucine residue has been removed. This loss of affinity for αvβ6 by RGD2 shows that the second leucine residue is crucial in the binding of peptides to αvβ6. RGD3 is another literature-described peptide, which was derived from a small library of cyclic peptides with single amino acid alterations in order to identify a selective, specific and high affinity peptide that targets integrin αvβ6 [191]. This cyclic peptide was also deemed a suitable candidate for development into an imaging agent, despite the N- to C-termini coupling by amine chemistry, due to the side chain amine group found on the lysine amino acid side chain to which additional groups for radiolabelling could be attached. There have been reports of not only peptides containing RGD binding to integrin αvβ6 with high affinity, but of peptides containing R-T-D sequences, whereby the glycine residue is replaced by a threonine residue (see Table 13) [322]. Therefore, RTD1 was synthesised, which possessed an identical structure to RGD1, except for the substitution of the glycine residue for threonine. This peptide, however, much like RGD2, was unable to bind to integrin αvβ6 at the tested concentration range, suggesting that for αvβ6

binding the glycine residue is critical for maintaining a strong affinity for αvβ6. Other peptides that have contained R-T-D sequences have typically been longer in length and have incorporated the recognition sequence into exposed loops that may allow the peptide more conformational freedom [321, 322, 339, 340], potentially allowing for binding of peptides containing RTD sequences. Following ELISA experiments, RGD1 and RGD3 were identified as two peptides able to bind to αvβ6 with high affinities, and were taken forward for further development.

To develop RGD1 and RGD3 into radioligands for imaging αvβ6 in cancer and IPF, the peptides required chemical modification in order to incorporate radioisotopes. Given the emerging interest in theranostic agents, the chelating moiety DOTA, which is the most widely used chelator for complexation of radiometals [341, 342], was chosen as a suitable vector for the incorporation of the positron-emitting [$^{68}$Ga]Ga$^{3+}$ and β$^{-}$ emitting [$^{177}$Lu]Lu$^{3+}$ radioisotopes, both of which are easily incorporated into DO3A [91, 312]. This would allow the peptide(s) to be evaluated as a potential tool for selecting for αvβ6$^{+}$ tumours for PRRT using the [$^{177}$Lu]Lu-labelled derivative as the therapeutic agent, although the therapeutic derivative would require validation in preclinical models. Despite [$^{18}$F]F possessing a lower linear positron range than gallium-68, which would allow enhanced image resolution, favourable half-life, decay profile and positron energy (27), gallium-68 was chosen as the imaging radioisotope as it is conveniently available from $^{68}$Ge/$^{68}$Ga generators that do not require as extensive training as for fluorine-18 production, which requires cyclotrons that are accompanied by much greater costs than benchtop generators.

For RGD1, either a simple, flexible, 6-aminohexanoic acid (Ahx) spacer, or a rigid 4-aminomethylbenzoic acid (AMBA) spacer, both of which are commonly used in the conjugation of targeting vectors with moieties for radioisotope incorporation [343, 344], were conjugated to the N-terminal amine group on the cysteine residue. Each of these spacers acted as extensions, to which the chelator moiety, DO3A was conjugated. A spacer molecule was not attached to RGD3, due

to the presence of a lysine residue within its structure, exposing a free amine group on its variable side chain to which DO3A could be conjugated. RGD3, previously reported as Avebehexin [324], has been shown to retain its ability to bind to αvβ6 following conjugation to chelators via its lysine residue, so it was not expected that DO3A would affect the binding of RGD3 to αvβ6 significantly, however it had done so. This is because in this study, DO3A was conjugated directly to the lysine residue within the peptide, whereas avebehexin was conjugated to a chelator moiety indirectly via a spacer molecule. Also, the chelator used in avebehexin was NODAGA, rather than DO3A, which may contribute to the differences observed in binding of the conjugate to αvβ6.

Following modification of the cyclic peptides RGD1 and RGD3, it was necessary to re-assess their ability to bind to integrin αvβ6, in order to see if the chemical modifications had led to the hindrance or enhancement of integrin binding, as structural changes such as PEGylation [345], metal chelation [346] and even incorporation of different radiometals into the same structure have been known to have effects on pharmacokinetics of radioligands [347]. Repetition of the competitive ELISA experiment using the modified peptide deriatives showed that conjugation to DO3A and subsequent chelation with $[^{nat}Ga]Ga^{3+}$ or $[^{nat}Lu]Lu^{3+}$ did not abrogate binding of the peptide derivatives to αvβ6. The competitive ELISA experiment only allows indirect assessment of binding, whereas another technique, SPR, allows the direct assessment of binding between two interactants. In addition, SPR is able to monitor, in real-time, the binding of one interactant to another and determine the association and dissociation constants of an interaction, allowing for the calculation of affinity. Ideally, the assessment of binding kinetics between peptides and integrin αvβ6 by SPR would have provided detailed information as to how structural modifications impacted the binding properties of the peptides, however this would require the immobilisation of αvβ6 to the sensor chip by amine coupling, and this led to a largely inactive surface to which responses from peptide binding were unable to be detected (Appendix Figure 8). This inactivation of αvβ6 during the immobilisation process, as seen in another

study [312], meant that it was not possible to investigate the effects of chemical modifications on peptide binding kinetics, which would be useful in determining how structural changes in the radioligand may affect the binding kinetic and affinity properties of the radioligand, allowing for the selection of the most promising candidates for further investigation as imaging/therapeutic agents. Therefore, surface plasmon resonance was utilised to demonstrate both direct binding of RGD1 to αvβ6 and peptide selectivity for αvβ6 over integrin αvβ3 using a similar setup as reported previously [312].

By immobilising JD2-RGD1 to the sensor surface, the injection of different integrins over the immobilised surface provided insight into the cross-reactivity of JD2-RGD1. Avβ6 was shown to bind to JD2-RGD1 in a concentration-dependent manner, with a slow dissociation constant that indicates high affinity, whereas the injection of αVβ3 induced no such response, from which no kinetic data could be obtained, suggesting no cross-reactivity of JD2-RGD1 to αVβ3. This is an improvement upon another peptide, SFITGv6 [312], reported to bind to αvβ6 selectively over αVβ3, as this peptide was still shown to bind to αVβ3 with an affinity of 185 nM in the same experimental setup, making RGD1 a more selective peptide for integrin αvβ6 than SFITGv6. This slight affinity of SFITGv6 for αVβ3 raises questions over its *in vivo* suitability for αvβ6 imaging, as cross-reactivity may lead to radioligand uptake in regions of αVβ3 expression rather than αvβ6 expression alone.

Binding kinetics can have differing effects on the *in vivo* properties of agonists or antagonists, with reports of highly effective antagonistic effects arising as a result of slow binding kinetics, whilst agonistic effects being related to faster binding kinetics [348, 349], and differences in binding properties have been shown to have consistent effects on *in vivo* pharmacodynamics [350]. With this in mind, it was deemed that in addition to competition ELISA experiments, which allow indirect assessment of peptide binding, SPR spectroscopy could be a useful tool

for the characterisation of the direct interaction between αvβ6 and designed radioligands.

Radioligand binding experiments using [$^{68}$Ga]Ga-DO3A-JD1-RGD1, [$^{68}$Ga]Ga-DO3A-JD2-RGD1, and [$^{68}$Ga]Ga-DO3A-RGD3 with $MEF_{wt}$, MEFβ6, BxPC3, MDA-MB-468 and U87 cell lines demonstrated that RGD1 is able to bind specifically to integrin αvβ6 to levels that with the relative integrin αvβ6 expression levels, in the order of MEFβ6 >> BxPC3 >> MDA-MB-468 >> $MEF_{wt}$/U87. Importantly, no uptake of [$^{68}$Ga]Ga-DO3A-JD1-RGD1 or [$^{68}$Ga]Ga-DO3A-JD2-RGD1 was seen in U87 cells, which are well known to express high levels of αVβ3, but no αvβ6, reinforcing the selectivity of RGD1 for αvβ6 over other integrins [339, 351-353]. [$^{68}$Ga]Ga-DO3A-RGD3 was also able to specifically bind to MEFβ6 cells, however, the levels were very low compared to [$^{68}$Ga]Ga-DO3A-JD1-RGD1 and [$^{68}$Ga]Ga-DO3A-JD2-RGD1 and there was no significant difference between MDA-MB-468 ($\alpha v\beta 6^{low}$) and negative control $MEF_{wt}$ cell lines. Perhaps this may be due to the close proximity of the macrocycle moiety to the RGD recognition sequence, as this differs from Notni *et al.*'s work that used a spacer molecule to protrude the chelating moiety away from the same peptide sequence, following which they were able to see binding of the peptide to αvβ6 both *in vitro* and *in vivo*. However, the binding of [$^{nat}$Ga]Ga-DO3A-RGD3 to integrin αvβ6 was still observed in ELISA experiments, albeit with a 10-fold weaker affinity than reported in another ELISA study using the same peptide [191]. This assay setup involved the use of purified, recombinant protein, with no other constituents of the cellular membrane that may interact with or interfere with integrin αvβ6 binding in cellular models.

As mentioned previously, the internalisation of an imaging agent into the cytoplasm of cells ideally leads to the accumulation of tracer specifically in those tissues, allowing enhancement of the contrast between $\alpha v\beta 6^{+}$ tissues and tissues that are negative for αvβ6 expression. It was therefore a requirement to determine if the radioligand [$^{68}$Ga]Ga-DO3A-JD2-RGD1, which had displayed higher uptake in $\alpha v\beta 6^{+}$ cell lines, as well as a higher affinity for αvβ6 as determined

by competitive ELISA experiments, was internalised by integrin αvβ6, and specifically, how much was internalised. Consequently, a radioligand internalisation assay was performed using an assay setup already optimised for integrin αvβ6-specific peptides as described previously [312]. [$^{68}$Ga]Ga-DO3A-JD2-RGD1 was shown to bind to αvβ6 in a relevant cancer cell line, BxPC3, and approximately 70% of the total bound radioactivity in this cell line was internalised, higher than that seen in Altmann *et al.* [312], which showed approximately 37% internalisation of [$^{177}$Lu]Lu-DOTA-SFITGv6 for up to 4 hours, suggesting that this radioligand has promising potential as not only a high contrast PET agent in future imaging studies looking into the identification of αvβ6$^{+}$ tissues, but also as a PRRT agent due to its agonistic behaviour inducing a high amount of internalisation in αvβ6$^{+}$ cancer cells, which is deemed desirable for a radionuclide therapy. However, [$^{68}$Ga]Ga-DO3A-JD2-RGD1 internalisation was only evaluated a single time-point (60 minutes) and further studies to address the retention of the radioligand by αvβ6-positive cells should be undertaken to further assess its suitability as a potential PRRT agent. The results of the internalisation experiments were reinforced by another report that looked into the internalisation of this peptide in immunofluorescent confocal microscopy experiments [212], whereby the peptide displayed consistency with regards to the addition of a labelling moiety, albeit not DO3A, not altering the internalisation properties of the peptide.

Serum stability analysis of the three radioligands tested revealed that [$^{68}$Ga]Ga-DO3A-JD1-RGD1 and [$^{68}$Ga]Ga-DO3A-JD2-RGD1 were completely stable, with no loss of radioactive metal. It was therefore appropriate to assume that these radioligands had been sufficiently evaluated *in vitro* to warrant further investigation into their potential use as imaging agents *in vivo.* On the other hand $^{68}$Ga-RGD3 was not advanced to the next stage of preclinical evaluation because (1) the uptake in cellular models was much lower than the other radioligands tested, (2) of the three radioligands tested, it had the lowest affinity for integrin αvβ6 and (3) it would likely exhibit non-specific uptake due to the instability with regards to chelation of the radioisotope.

The lipophilicity of both [$^{68}$Ga]Ga-DO3A-JD1-RGD1 and [$^{68}$Ga]Ga-DO3A-JD2-RGD1 was also determined and both tracers were revealed to be highly hydrophilic. This may be the reason for the fast clearance of radioligand from the blood via renal excretion [354], as radiolabelled peptides with enhanced lipophilicity have been shown to delay blood clearance as a result of increased plasma protein binding [355] and a shift from renal to hepatic excretion [347].

Following successful *in vitro* evaluation of [$^{68}$Ga]Ga-DO3A-JD1-RGD1 and [$^{68}$Ga]Ga-DO3A-JD2-RGD1, *in vivo* evaluation in both non tumour-bearing and BxPC3 tumour-bearing mice. Non tumour-bearing mice were used to assess the radioligand biodistribution as well as the *in vivo* stability of the radioligand, whilst BxPC3 tumour-bearing mice were used to validate the *in vivo* specificity of [$^{68}$Ga]Ga-DO3A-JD2-RGD1.

In non-tumour bearing models, both [$^{68}$Ga]Ga-DO3A-JD1-RGD1 and [$^{68}$Ga]Ga-DO3A-JD2-RGD1 exhibited similar tissue uptake patterns. There was significant uptake in the gastrointestinal tract and the submandibular glands, in accordance with other literature findings [104, 317, 320-322], and this was significantly reduced by approximately 60-65% following blocking of integrin αvβ6 with a monoclonal specific blocking antibody, further reinforcing the specificity of the [$^{68}$Ga]Ga-DO3A-JD2-RGD1 for integrin αvβ6 *in vivo*. In further support of the *in vivo* specificity of [$^{68}$Ga]Ga-DO3A-JD2-RGD1, immunohistochemical analysis showed that areas of uptake of the radioligand, such as the GI tract, submandibular glands and also the lungs, positively expressed integrin αvβ6, in accordance with similar findings in the literature [324, 356].

Analysis of the urine for any radiometabolites produced *in* vivo following radioligand injection revealed that for both peptides, one major metabolite was produced. It should be noted that the radiometabolite analysis performed here was limited to the assessment of the proportion of intact radioligand excreted in the urine, as opposed to full metabolite analysis that would usually be performed using LC-MS. It is has been established that the macrocycle itself is stable, and

therefore it is unlikely that any free gallium is being transchelated. If this were to be occurring, significant uptake of gallium-68 in organs such as the liver and heart would take place, as shown by Burke *et al.* [357]. It is probable that the macrocycle is being rapidly excreted renally, contributing to the high kidney uptake seen in the PET images, however, further analysis, such as mass spectrometry analysis, is required in order to prove that this is the radiometabolite being produced. If this theory is correct, the production of this radiometabolite, although it is likely being excreted renally, may pose problems with regards to αvβ6 imaging, as there would be increased, non-labelled peptide in circulation, as a result of cleavage of the macrocycle from the peptide, which is then free to block integrin binding sites, potentially reducing the uptake of the radioligand in $\alpha v\beta 6^{+}$ tissues. Therefore, further modifications of $^{68}$Ga-JD2 in order to enhance the *in vivo* stability of the radioligand are warranted.

Further validation of the *in vivo* specificity of [$^{68}$Ga]Ga-DO3A-JD2-RGD1 was performed using an $\alpha v\beta 6^{+}$ murine xenograft model. The accumulation of [$^{68}$Ga]Ga-DO3A-JD2-RGD1 was shown to be higher in the tumour than in any other tissue, except for the kidneys and GI tract. Visible uptake was also observed in the lungs, which have been known to express integrin αvβ6 to a low level in healthy alveolar epithelium [104], and the SMG. Imaging studies revealed a significant reduction, as determined by student t-test, although not abolishment, of radioligand uptake was observed in these areas following antibody blockade of integrin αvβ6. It is likely that internalisation of the antibody over the 24 hour blocking time occurred, and integrin αvβ6 was recycled back to the cell surface, providing fresh, available binding sites for the radioligand, which would make 100% blockade of [$^{68}$Ga]Ga-DO3A-JD2-RGD1 impossible. This is supported by studies of αvβ6-targeted ligand-mimetic antibodies, of which 10D5 is one, whereby these antibodies were shown to be internalised in an $\alpha v\beta 6^{+}$ cell line [315]. The characterisation of integrin αvβ6 expression in all of these areas by immunohistochemical analysis of the tissues from the same animals imaged, confirmed presence of αvβ6 expression in the tumour, SMG, lungs and GI tract.

The kidneys, however, did not exhibit any expression of αvβ6 by IHC, which raises questions with regards to their high uptake of the radioligand. The high kidney uptake does, however, support the prediction derived from the lipophilicity studies performed on [$^{68}$Ga]Ga-DO3A-JD2-RGD1 that the radioligand is likely to be renally excreted due to the hydrophilic nature of the tracer. Of concern, the high kidney uptake may be a limiting factor for any future PRRT treatment regimen, as this would lead to high radiation dose to the kidneys, which is highly undesirable and thorough dosimetry profiles are required to determine the actual dose to kidneys.

Biodistribution experiments were successful in supporting the imaging and immunohistochemical analysis data, showing specific uptake of [$^{68}$Ga]Ga-DO3A-JD2-RGD1 in tumours, GI tract and SMG in accordance with imaging studies. Statistically significant (student t-test) reductions of radioligand accumulation was observed in the tumour (65%), GI tract (65%), SMG (65%), lungs (52%), pancreas (62%). also seen in these tissues, providing a strong case for the high specificity of [$^{68}$Ga]Ga-DO3A-JD2-RGD1 for integrin αvβ6 *in vivo.* Very similar levels of blockade was observed by Notni and colleagues investigating [$^{68}$Ga]Ga-Avebehexin for imaging αvβ6 expression (Tumour: 66%; Lungs: 59%; GI tract: 66%) although pancreas uptake reduction was only 26% in their study, despite confirming integrin expression in the pancreas by IHC [324].

There is promising potential for $^{68}$Ga-JD2 to be modified for use as a PRRT agent, through the substitution of [$^{68}$Ga]Ga$^{3+}$ for [$^{177}$Lu]Lu$^{3+}$. Competitive ELISA experiments showed that this substitution of gallium-68 for lutetium-177 did not change the binding properties of RGD1 for integrin αvβ6, as has been seen in other studies that have looked at internalisation of [$^{177}$Lu]Lu-labelled peptides by αvβ6$^{+}$ cell lines, although this requires further validation for [$^{177}$Lu]Lu-DO3A-JD2-RGD1. In light of ELISA data presented here, it may be said that a similar uptake pattern to [$^{68}$Ga]Ga-DO3A-JD2-RGD1 *in vivo* may be predicted for [$^{177}$Lu]Lu-DO3A-JD2-RGD1, although this requires further investigation. Therefore, modification of the

peptide in order to try and reduce kidney uptake such as multimerisation or addition of polyethylene glycol (PEG) units in an attempt to alter the lipophilicity of the peptide, and thus tissue absorption, may be needed to limit the radiation dose received by the kidneys. However, attempts have been made to improve the pharmacokinetics of αvβ6-specific peptides through multimerisation [324] and inclusion of PEG linkers [317], which, although have prolonged circulation time allowing for imaging at later timepoints, poor clearance of both multimerised and PEGylated peptides has resulted in inferior tumour:organ ratios than monomeric or non-PEGylated peptide imaging agents. The same efforts have been made in the optimisation of radionuclide therapy agent pharmacokinetics [324]. Alternatively, without modification of the PRRT agent, pre-injections of different agents, such as lysine, poly-glutamic acid (PGA) or gelofusine (GF), in order to inhibit renal accumulation of radiolabelled peptides and help reduce the dose delivered to the kidneys in order to avoid nephrotoxicity. This has been performed in other preclinical studies focused on the reduction of radiolabelled peptide uptake by the kidneys [85], however it was concluded that the conditions that lead successful kidney uptake reduction must be optimised for each individual peptide, as different agents may have different effects on the kidney uptake of different peptides.

## 3.5 Conclusions

This study successfully characterised the binding of αvβ6-targeted radiolabelled peptides to αvβ6. This was achieved *in vitro* through competitive ELISA experiments, which included re-assessment of target receptor binding following peptide modification, as well as determination of integrin selectivity by surface plasmon resonance, serum stability and lipophilicity studies and cell binding and internalisation experiments, but not receptor recycling studies. RGD1 was identified as a lead candidate peptide to take forward for *in vivo* imaging studies in the form of [$^{68}$Ga]Ga-DO3A-JD1-RGD1 or [$^{68}$Ga]Ga-DO3A-JD2-RGD1. *In vivo* imaging studies using both naïve and tumour-bearing mice showed uptake of both radioligands in tissues shown to express αvβ6 by immunohistochemistry, and [$^{68}$Ga]Ga-DO3A-JD2-RGD1 in αvβ6-positive tumours. Both of these findings were reinforced by blocking studies, demonstrating *in vivo* specificity of these agents. Furthermore, the *in vivo* stability of these radioligands was shown to be greater than that of previously validated linear αvβ6-targeted peptides. An early competitive ELISA experiment using a non-radioactive lutetium-177-labelled derivate of RGD1 showed that affinity for target was not altered significantly, therefore giving rise to the potential of this agent to be used as a therapeutic agent in αvβ6-positive cancers, however this requires thorough preclinical validation and should be planned for future work.

# Evaluation of CXCR4 antagonists as targeted imaging and therapy agents

# 4 Evaluation of CXCR4 antagonists as targeted imaging and therapy agents

## 4.1 Aim

The aim of this chapter is to characterise the receptor binding interactions of novel azamacrocyclic compounds as CXCR4 chemokine receptor antagonists. The binding properties of the compounds, SJA05 and SJA324, were compared against the clinically used azamacrocyclic CXCR4 antagonist AMD3100 (FDA approved in 2008 as Plerixafor for haematopoietic stem cell mobilisation) and the related compound AMD3465 in flow cytometry and surface plasmon resonance experiments to determine the binding and kinetic profiles of the molecules. This type of data can be used for lead candidate selection for diagnostic imaging or therapeutic development using *in vivo* studies.

## 4.2 Previous Studies

As a result of its role in cancer and pulmonary fibrosis, the CXCR4 chemokine receptor has become an attractive candidate target for both diagnostic and therapeutic purposes, and as a result, various CXCR4-targeted inhibitors have been developed.

### 4.2.1 AMD3100 (Mozobil)

Since its discovery, various research groups have investigated azamacrocycle containing compounds as CXCR4-targeted antagonists as therapeutics for cancer, HIV and other diseases such as IPF.

An antagonist is described as a molecule that is able to bind to a receptor, blocking the binding site, whilst not provoking a biological response, thus inhibiting its action. Alternatively, an agonist does the opposite, binding to its cognate receptor in order to induce a biological response within the cell via the receptor. Although there was some debate, and contradictory reports, as to the properties of AMD3100 it is now accepted to be an antagonist of CXCR4 [358, 359].

#### 4.2.1.1 Discovery of AMD3100 and related azamacrocyclic antagonists

Research into anti-HIV therapy led to the discovery of AMD3100 [360]. A batch of cyclam (JM1498) was tested that contained an impurity which showed a high amount of CXCR4-binding potential. It was identified (JM1567) and synthesised, and was then taken forward for further testing and derivatisation in order to develop an optimised small molecule that specifically targets CXCR4 with high affinity. This small molecule was a bis-cyclam, which is two cyclam moieties connected directly by a carbon-carbon (C-C) link. Further derivatisation of JM1657, using different connecting moieties between the two cyclams, such as aliphatic or aromatic linkers, led to the synthesis of a variety of small molecules. From this library of small molecules (Figure 35), JM2987/ JM3100 was shown to be a more potent inhibitor of CXCR4 than JM1657 [360]. JM3100 later underwent a name change to AMD3100, following acquisition of the technology by AnorMED, a company that took over the development of the small molecule drug compound.

AMD3100 is effective at inhibiting the entry of HIV, and thus its replication, in cell based assays, however this result was not reproduced in simian immunodeficiency virus (SIV) strains. This was due to a different mechanism of cell entry for SIV, which involves CCR5 rather than CXCR4. Some strains of the human virus (e.g. X4 strains) use the CXCR4 receptor, relying on an interaction with the viral gp120, an interaction which has been shown to be inhibited by AMD3100. Furthermore it has been shown that AMD3100 is an effective inhibitor of HIV-1 replication (in X4 viral strains, CXCL12-induced $Ca^{2+}$ flux and anti-CXCR4 mAb-binding [361].

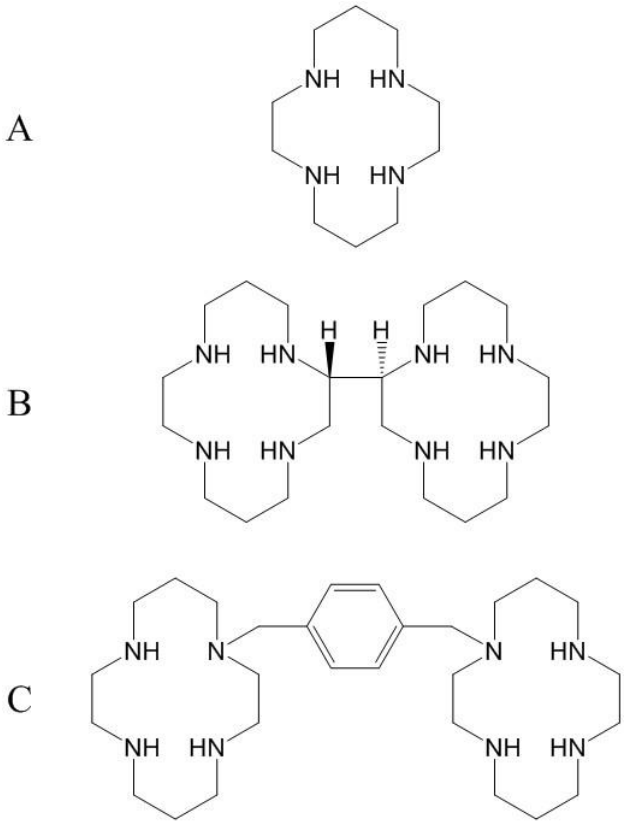


**Figure 35. Key structures involved in the development of AMD3100. (A) JM1498, (B) JM1657, (C) JM2987/ JM3100.**

Following progression of AMD3100 into clinical trials against HIV, a side effect of AMD3100 administration were elevated white blood cell counts, which was shown to be dose-dependent. This unexpected side effect was seen to have potential application in autologous stem cell transplantation in sufferers of Hodgkin's disease, non-Hodgkin's lymphoma and also multiple myeloma [362]. Patients with these diseases are unable to produce sufficient amounts of white blood cells, therefore by using AMD3100 as a mobilisation agent it would be possible to collect white blood cells from these patients at an early stage, retaining them for when needed at a later disease stage. This discovery showed promise for overcoming the challenge in using the variably effective standard stem cell mobilisation agent, granulocyte-colony stimulation factor (G-CSF) on its own.

Under the trade name, Plerixafor, AMD3100 is now used clinically for the haematopoietic stem cell collection in the diseases mentioned above in combination with G-CSF, in the form of an injection, referred to as Mozobil [360] (injection of Plerixafor), and is now licensed by the FDA in both the USA and Europe for routine clinical use.

### 4.2.2 Development of CXCR4-targeted imaging/therapeutic agents

AMD3100 has been shown to bind to CXCR4 via the glutamate and aspartate amino acid residues of the receptor [363] through electrostatic interactions that occur between the charged (protonated) nitrogen atoms of the cyclam ring and the negatively charged carboxyl groups of the glutamate (Glu) and aspartate (Asp) residues in the receptor. This was further supported by site-directed mutagenesis experiments, which showed that $Asp^{171}$ and $Asp^{262}$ crucial for binding between AMD3100 and CXCR4 to occur [364-366].

Since it is already used clinically as a haematopoietic stem cell mobilising agent, AMD3100, with the two azamacrocyclic binding components has provided a useful framework for the design of other CXCR4-targeted antagonists. The structure of this small molecule has been modified in several different ways to better understand the pharmacological properties of the compound, such as binding affinity [367]. AMD3100 possesses two flexible cyclam rings with nitrogen donor atoms which have the potential to incorporate various metal ions, such as copper(II), nickel(II) or zinc(II), generally resulting in significantly enhanced binding affinity of the drug for CXCR4 [368], due to the potential for formation of a coordinate bond between the metal ion and the carboxylate group of the aspartate residues in CXCR4.

As a result of these findings, AMD3100 is an excellent starting point for the development of a radiometal-containing PET imaging agent. Previous work has led to the radiolabelling of AMD3100 by incorporation of the radiometal copper-64 into the macrocyclic ring to produce [$^{64}$Cu]CuAMD3100 [369]. The incorporation of copper-64, as with non-radioactive copper(II) has been shown in some assays o

result in a reduced affinity of AMD3100 for CXCR4, whereas incorporation of zinc(II) or nickel(II) was shown to enhance the binding affinity of AMD3100 for CXCR4.

The Nimmagadda group have reported on the use of [$^{64}$Cu]CuAMD3100 in various preclinical models [164, 370]. The key aspect of these studies was the presence of radioisotope in non-target tissues such as the liver, spleen and kidneys. In an effort to determine if this uptake was due to non-specific uptake (which could be due to the loss of radiolabel), they performed blocking experiments using non-radioactive AMD3100, which would be expected to abrogate the PET signals observed previously, as it was administered at a much higher dose than the radioligand. Subsequent PET images revealed that the high liver uptake was maintained, despite uptake in CXCR4$^+$ xenografts being largely eliminated. Based on [$^{64}$Cu]$CuCl_2$ scans within the same study, it was proposed that the [$^{64}$Cu]CuAMD3100 complex is kinetically unstable, and this is reinforced by other reports that imply that the radiometal may be transchelating from the cyclam moiety in the blood or other organs to the copper transport protein, ceruloplasmin. This ultimately leads to accumulation in the liver as a result of normal metabolic pathways whereby it may be incorporated into superoxide dismutase (SOD) to give high levels of liver uptake [371-373], which cannot be blocked with high doses of a CXCR4 antagonist. This instability of the [$^{64}$Cu]Cu-cyclam complex has been the focus of further development of a library of configurationally restricted tetraazamacrocycles. Archibald and colleagues synthesised a novel tetraazamacrocycle, $Cu_2$CB-bicyclam, based on the structure of AMD3100, however containing ethylene cross bridges between non-adjacent nitrogen atoms in both macrocycles. This modification led to an increased affinity, when compared to AMD3100, for the metal complexes of copper(II) and zinc(II) for CXCR4, leading to increased receptor residence time as a result of both coordinate bond formation between the metal ion and the aspartate residue carboxylate group of CXCR4 and also the rigidity of the structure provided by the

cross bridge that contributes to the kinetic stability of the metal-chelator complex (Figure 36E).

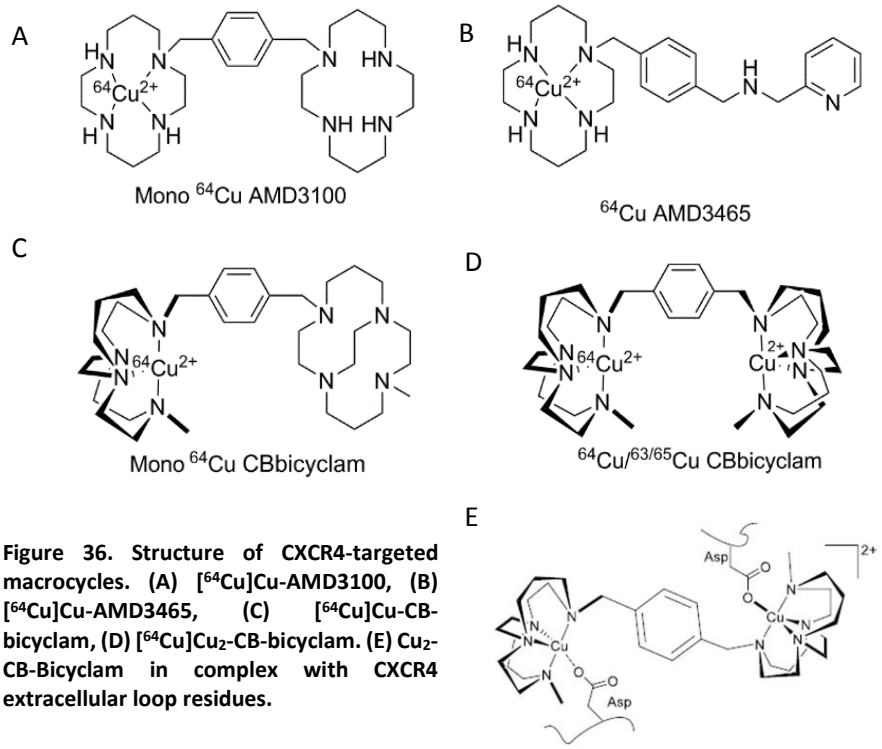


**Figure 36. Structure of CXCR4-targeted macrocycles. (A) [$^{64}$Cu]Cu-AMD3100, (B) [$^{64}$Cu]Cu-AMD3465, (C) [$^{64}$Cu]Cu-CB-bicyclam, (D) [$^{64}$Cu]$Cu_2$-CB-bicyclam. (E) $Cu_2$-CB-Bicyclam in complex with CXCR4 extracellular loop residues.**

### 4.2.3 The analysis of GPCR ligands by surface plasmon resonance

Different methods have been formulated when trying to generate SPR biosensor data, but there is limited literature demonstrating SPR work involving GPCRs. Works that have involved the analysis of GPCRs, and specifically CXCR4, by SPR have come across numerous problems. Methods have been developed and used extensively and successfully by Stenlund *et al.* and Navratilova *et al.* to model CXCR4 binding to natural ligands and small molecules [374-376]. The main problem that arises is the challenge of maintaining a natural conformation. Being a transmembrane helix receptor, CXCR4 requires a lipophilic environment to maintain its natural conformation and ligand-binding capability, and it is an environment that can be difficult to re-create in SPR experiments, which are primarily solid-phase assays. Detergents have been used to assist in solubility of

the receptor, however this has the potential to alter the receptor conformation, and thus, how it binds to ligands. Another issue that rises is that the reconstitution of membrane proteins can be complex.

Stenlund *et al.* [376] formulated a protocol for the immobilisation of GPCRs on an L1 sensor chip and subsequent reconstitution of a lipid bilayer to aid the maintenance of GPCR conformation. Briefly, they immobilised an anti-rhodopsin (1D4) antibody and captured CXCR4 and CCR5 receptors engineered to encode a nine amino acid sequence (TETSQVAPA) on their C-terminus, recognised by the 1D4 antibody. This method provided an improved orientation of the receptor on the chip surface and they were able to detect binding of CXCR4 to its natural ligand, SDF-1/CXCL12. Navratilova *et al.* [375] further developed this methodology, testing a large number of conditions such as types of detergents, lipids and the best lipid:detergent ratios to use when solubilising the receptor for use in SPR experiments. With regards to CXCR4, they found that using a 5:1 lipid to detergent ratio of a DOPC/DOPS blend (7:3; final concentration 5 mM) and 2% CHS/10% DOM/10% Chaps (w/v) and a standard solubilisation time of 10 minutes gave the best receptor activity. These conditions may be used in order to screen a library of potential imaging or therapeutic agents against GPCRs such as CXCR4, or other membrane bound proteins that are implicated in pulmonary fibrosis.

## 4.3 Results

### 4.3.1 Characterisation of CXCR4 antagonists

Non-radioactive analogues [$^{nat}$Cu]$Cu_2$CB-bicyclam and [$^{nat}$Cu]CuCB-bicyclam and were synthesised by Professor Steve Archibald's research group, based on the structure of the macrocyclic CXCR4 antagonist AMD3100 (Figure 36).

### 4.3.2 Characterisation of CXCR4-expressing cell lines

To assess the binding of CXCR4-targeted antagonists to CXCR4, it was first necessary to validate the expression of CXCR4 in a cell model that can be used to evaluate the specificity of novel CXCR4-targeted small molecules. The expression levels of CXCR4 was tested in a human T lymphocyte cell line, Jurkat cells.

Flow cytometry studies of this cell line revealed that the Jurkat cells express high levels of CXCR4 on the cell surface, with minimal to undetectable binding being observed for the isotype control antibody (Figure 37).

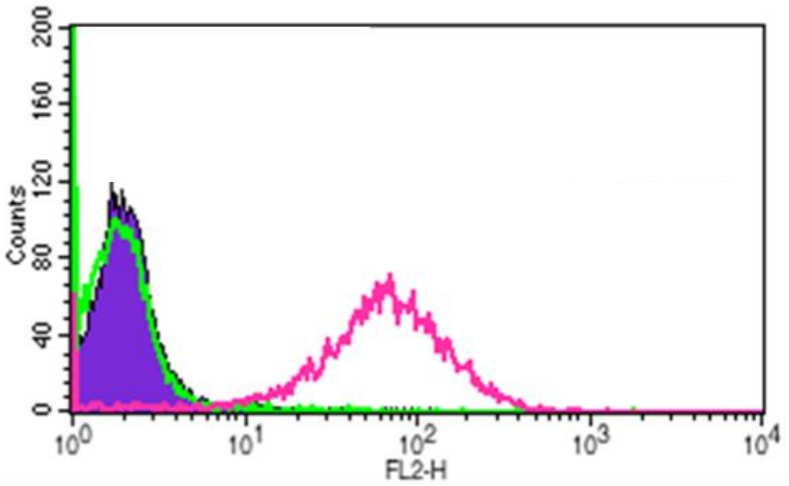


**Figure 37. Flow cytometry histogram showing CXCR4 expression in Jurkat cells. Pink line = anti-CXCR4 mAb (12G5); green line = IgG2A isotype control Ab, purple, filled = unlabelled cells.**

### 4.3.3 Evaluation of antagonists binding to CXCR4 by flow cytometry

Following confirmation of Jurkat CXCR4 expression, assessment of CXCR4 antagonist binding to CXCR4 using this cell line was investigated in an antibody displacement assay, using the CXCR4-specific, phycoerythrin-conjugated, monoclonal antibody, 12G5-PE in competition against [$^{nat}$Cu]$Cu_2$CB-bicyclam, [$^{nat}$Cu]CuCB-Bicyclam, [$^{nat}$Cu]CuAMD3100 and [$^{nat}$Cu]CuAMD4465 (Figure 38).

In the first instance, ligands were incubated with Jurkat cells in excess (20 µM). Importantly, to maintain receptor presence at the surface, this assay was performed at 4°C, with all washes being performed with ice-cold wash buffer, to prevent receptor internalisation and recycling.

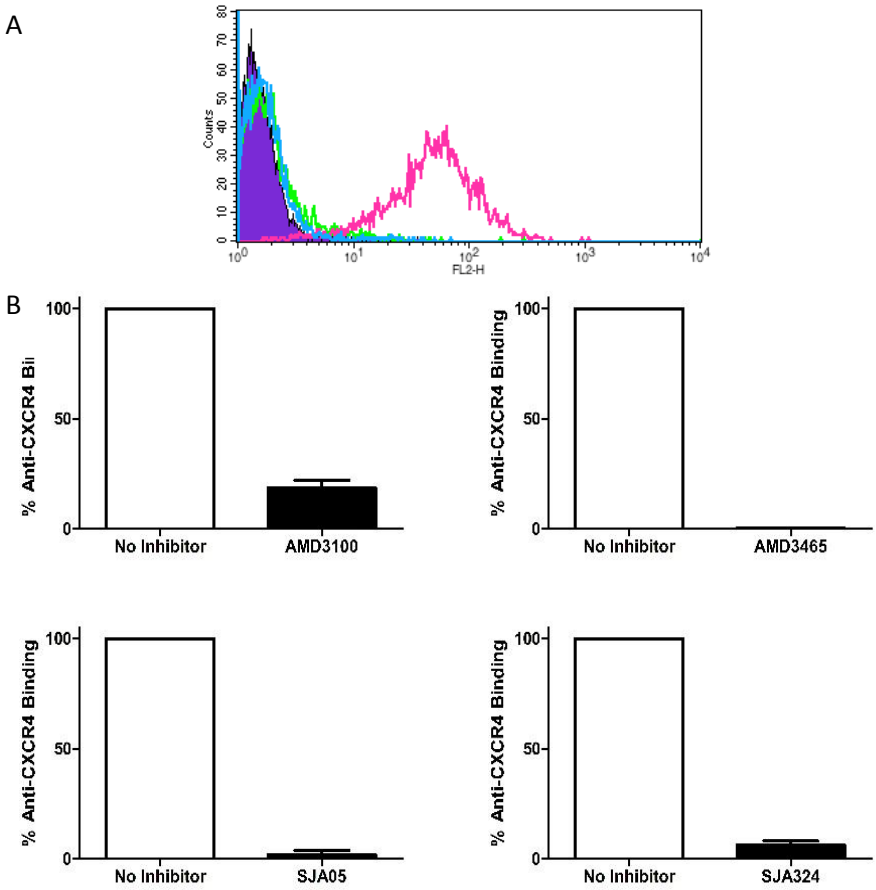


**Figure 38. (A) Representative flow cytometry histograms showing binding of anti-CXCR4 to Jurkat cells and inhibition of antibody binding by addition of 20 µM ligand. Figure shows binding of $Cu_2$CB-bicyclam. Purple, filled = unlabelled cells; pink line = 12G5-PE; green line = isotype Ab; blue line = 20 µM $Cu_2$CB-bicyclam. (B) Bar graphs showing inhibition of anti-CXCR4 mAb (12G5-PE) by macrocyclic CXCR4-targeted inhibitors, normalising for antibody binding in the absence of ligand. AMD3100 (n=3), AMD3465 (n=3), [$^{nat}$Cu]CuCB-bicyclam (n=4) and $Cu_2$CB-bicyclam (n=4).**

In competition against mAb binding, at excess concentration (20 μM), the ligands were shown to inhibit antibody binding at levels of 81.2% ± 4.1, 99.8% ± 0.2, 93.6% ± 1.8 and 98.0% ± 1.9, respectively, demonstrating that all four ligands are able to specifically target CXCR4.

Once binding of all four macrocyclic complexes was established, competition experiments were repeated using a titration (200 pM - 20 μM) of each compound to provide an indication as to the affinity of binding of each compound for CXCR4. The normalised geometric mean fluorescence for each concentration corresponding to the percentage of antibody binding in the absence of ligand was then used to calculate the percentage inhibition for each concentration, which was plotted against the concentration of compound (Figure 39).

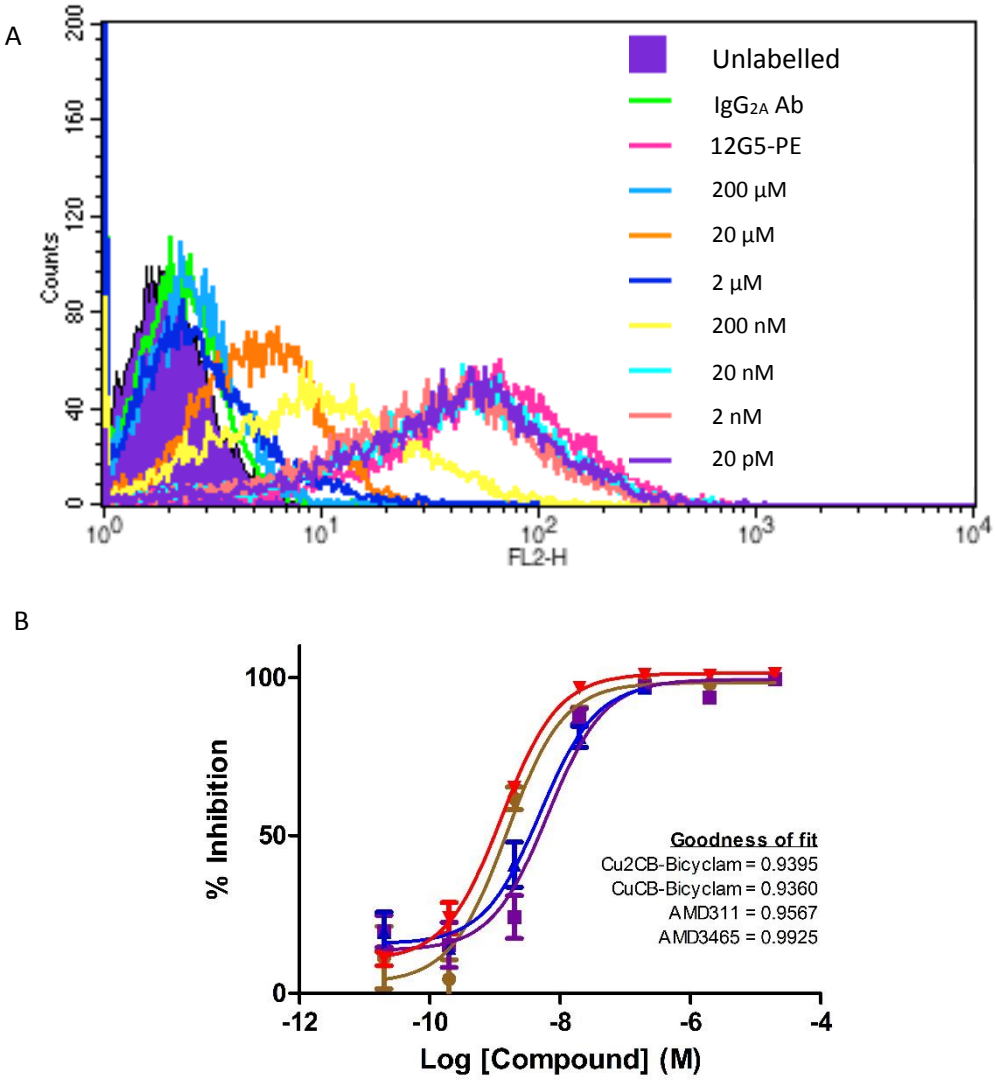


**Figure 39. (A) Representative flow cytometry histograms showing inhibition of anti-CXCR4 mAb, 12G5-PE, binding to CXCR4 on Jurkat cells by [$^{nat}$Cu]Cu-CB-bicyclam. Compound concentrations for each histogram are outlined. (B) Inhibition curves of AMD3100 (blue), AMD3465 (red), $Cu_2$CB-bicyclam (brown) and [$^{nat}$Cu]Cu-CB-bicyclam (red) inhibiting anti-CXCR4 mAb binding to CXCR4 on Jurkat cells for comparison.**

Figure 39 shows that all compounds were able to effectively inhibit 12G5-PE binding, with $IC_{50}$ values of 4.96 nM ± 1.35, 1.28 nM ± 2.85, 16.0 nM ± 1.34, and 3.90 nM ± 1.29, for [$^{nat}$Cu]CuAMD3100, [$^{nat}$Cu]CuAMD3465, [$^{nat}$Cu]CuCB-bicyclam

and [$^{nat}$Cu]Cu$_2$CB-bicyclam, respectively, shows an overlay of all four inhibition curves for all compounds for comparison.

### 4.3.4 Evaluation of CXCR4 antagonist binding by surface plasmon resonance

Evaluation of all four macrocyclic compounds revealed that all four molecules bind to CXCR4 with high affinity, however, it does not give any indication as to the kinetic properties of the binding interactions with CXCR4. As affinity can be derived from the association and dissociation constants of an interaction (Equation 8), it is possible for two molecules, which have similar affinities for the same receptor, to have very different kinetic binding profiles.

**Equation 8. Calculation for determining the affinity ($K_D$) of an interaction using the dissociation ($k_d$) and association ($k_a$) constants.**

$$K_D = \frac{k_d}{k_a}$$

In order to understand the binding kinetics of an interaction, SPR may be used to track the association and dissociation constants, and thus the affinity constant, of an interaction between binding partners. Therefore, SPR assays were performed to assess the binding kinetics of [$^{nat}$Cu]Cu$_2$CB-bicyclam and [$^{nat}$Cu]CuCB-bicyclam and compared against the clinically used AMD3100. However, as already discussed in the introduction to this chapter, GPCRs rely on a membrane-like environment for their correct protein folding [374-379] and a key challenge is ensuring that expression and purification of membrane proteins is carried out to promote receptor stability and ligand-binding functionality when not within the cell membrane.

#### 4.3.4.1 Molecular cloning of glutathione-S transferase onto the C-terminus of CXCR4

As GE Healthcare have a commercial kit designed for the capture of glutathione-S transferase (GST) tagged proteins, molecular cloning of CXCR4, using

cloning primers outlined inTable 18, was carried out with the addition of a GST tag on the C-terminus of the receptor using a C-terminal GST mammalian expression vector (Oxford Genetics). Due to receptor solubilisation conditions already being established in the Cf2Th cell line, these cells were used as the expression vector for this CXCR4-GST construct (Figure 40), and CXCR4 expression of clones was confirmed by flow cytometry prior to use in SPR experiments.

**Table 18. Cloning primers used for molecular cloning of GST-tagged CXCR4**

| Primer | Base Sequence |
|---|---|
| **CXCR4 Forward** | ATATTGAATTCGCCACCATGGAGGGGATCAGTAT |
| **CXCR4 Reverse** | ATAGCTCGAGGCTGGAGTGAAAACTTGAAGACT |

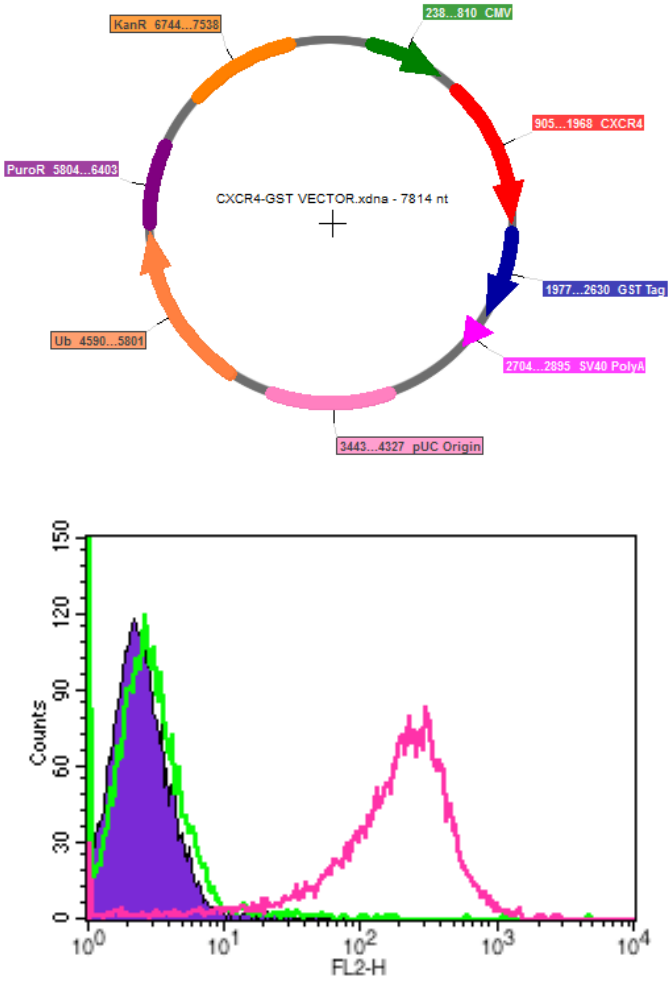


**Figure 40. (A) Flow cytometry histogram of Cf2Th-CXCR4-GST clone showing CXCR4 expression. Purple, filled = unlabelled cells; green line = isotype control Ab; pink line = anti-CXCR4 mAb, 12G5-PE. (B) CXCR4-GST-C vector used for mammalian expression of CXCR4-GST fusion protein under a cytomegalovirus (CMV) promoter.**

### 4.3.4.2 Immobilisation of anti-GST polyclonal antibody on a CM4 sensor chip

In order to be able to capture CXCR4-GST onto a sensor surface, a capturing antibody, capable of binding to the exogenous GST tag, needs to be immobilised onto the dextran matrix of the sensor surface. Using a commercial amine coupling

kit, an anti-GST polyclonal antibody (pAb) was immobilised on flow cells 1 and 2 to a level of approximately 6500 RU, respectively (Appendix Figure 9).

#### 4.3.4.3 Automated solubilisation, capture and assessment of CXCR4-GST activity

As the CXCR4-GST protein is expressed in Cf2Th cells, it requires purification from the cell membrane so that it is able to be captured by the immobilised anti-GST antibody. Navratilova *et al.,* [375] had previously optimised a set of solubilisation conditions using a specific mixture of different lipids and detergents in order to solubilise Cf2Th cells and maintain CXCR4 in an active conformation for maximal ligand-binding by SPR. Using the same method, Cf2Th-CXCR4-GST cells were solubilised automatically by the BIACORE T200 instrument. This ensures reproducible solubilisation time periods that may vary if performed manually, prior to injection over the antibody-coated sensor surface.

Injection of the crude Cf2Th-CXCR4-GST lysate did not result in a significant levels of CXCR4-GST capture (Figure 41A), and subsequent injection of the CXCR4-specific antibody, 12G5, which is only able to bind to CXCR4 when it is correctly folded, resulted in no response (Figure 41B), indicating that either (1) CXCR4-GST was not present on the sensor surface, or (2) any receptor present on the receptor surface is not conformationally active and is unable to bind to analyte. Therefore, this method, which sought to emulate the experimental work of Navratilova and colleagues using a different variant of CXCR4 containing a nine amino acid C9 tag (TETSQVAPA), did not give useful results when utilising a GST-tagged variant of CXCR4. It was reasoned that a shorter tag may improve the solubility of the receptor and allow for it to be captured with higher levels of binding activity.

Work performed by Navratilova and colleagues has indicated that the receptors are highly sensitive to solubilisation protocols to give correct receptor folding, and thus, give the expected binding to their ligands. In this project, despite the ability of GST to increase solubility of fusion proteins [380], the solubilisation

conditions used did not allow capture of CXCR4 and the conditions used require modification.

As the C9-tagged variant of CXCR4, used by Navratilova and colleagues, is significantly smaller in mass compared to a GST tag, the solubilisation conditions may need to be changed in order to retain full activity of the receptor in fusion with GST. In order to screen CXCR4-targeted compounds, Cf2Th-CXCR4-C9 cells were obtained from the NIH AIDS Reagent Program to exactly reproduce the method that had previously been established.

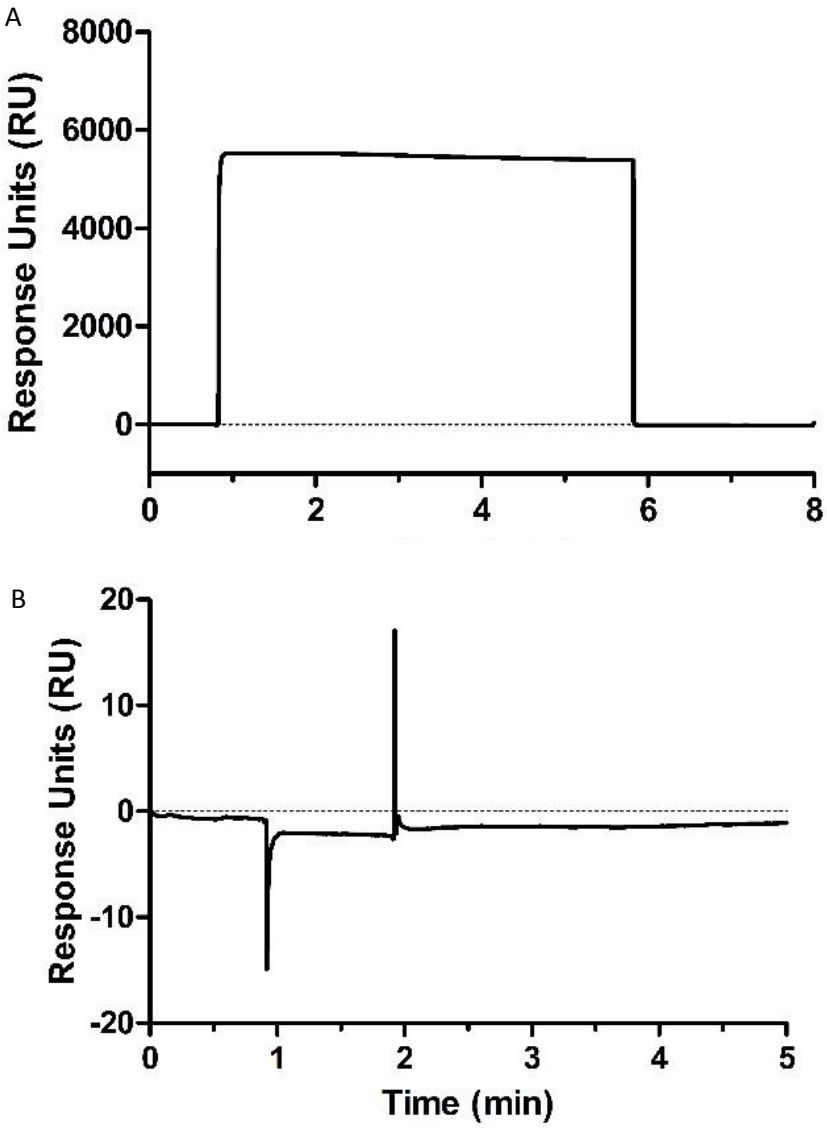


**Figure 41. Assessment of CXCR4-GST activity by surface plasmon resosnance. (A) Injection of solubilised Cf2Th-CXCR4-GST cells over an anti-GST antibody coated surface and (B) assessment of CXCR4-GST activity by the conformation-dependent antibody, 12G5.**

#### 4.3.4.4 Automated solubilisation, capture and assessment of CXCR4-C9 by SPR

Prior to solubilisation in SPR experiments, the expression of CXCR4-C9 by Cf2Th-CXCR4-C9 cells was confirmed by flow cytometry. Following confirmation of CXCR4 expression by flow cytometry in Cf2Th-CXCR4-C9 cells, an SPR experiment as in 4.3.4.3 was repeated using this cell line and the solubilisation conditions outlined by Navratilova *et al.* [375].

First, the C9-specific capturing antibody, 1D4, was immobilised on a sensor surface to approximately 3800 RU. Figure 42 shows that CXCR4-C9 was captured to a level of approximately 200 RU, as dictated by the difference between the baseline prior to injection, and the baseline following injection of the crude Cf2Th-CXCR4-C9 lysate. It was also shown, after injection of anti-CXCR4 mAb that the captured receptor was in an active conformation able to bind to analyte (Figure 42), indicating that the receptor is active and suitable for screening. However, the response generated by the antibody was lower than expected, reaching a maximum response of approximately 100 RU. As the antibody is approximately 100-fold larger than the small molecules to be investigated, the responses that would be generated from analyte 100-fold smaller would be in the single-digit range.

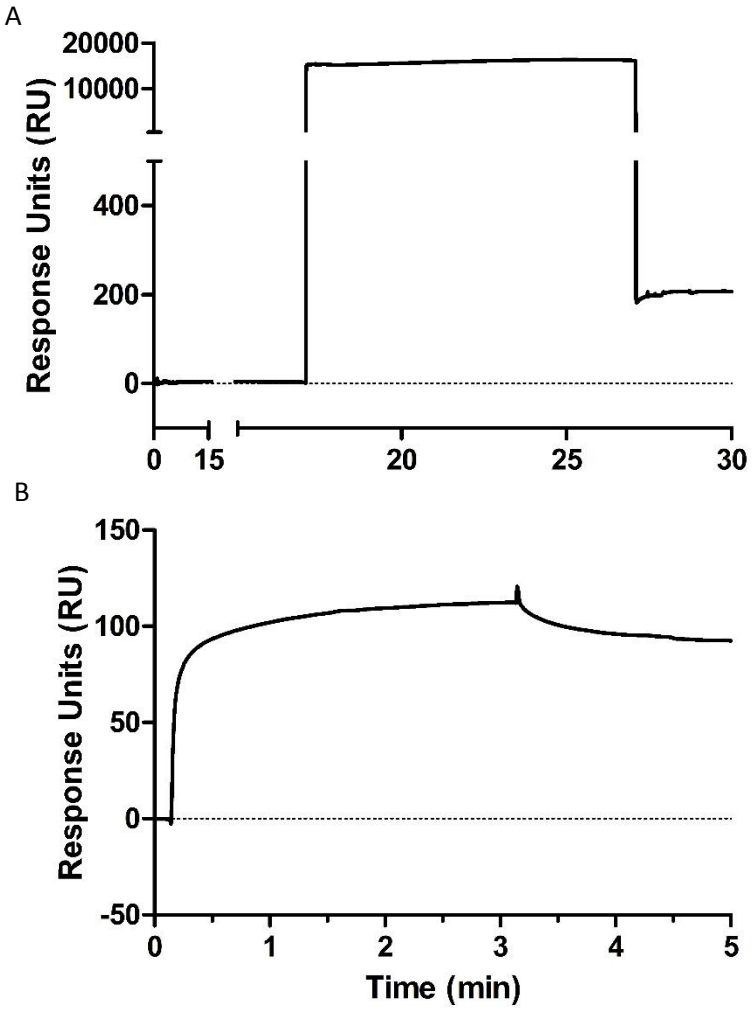


**Figure 42. SPR sensorgrams showing (A) injection and capture of solubilised Cf2Th-CXCR4-GST cells over an anti-GST antibody coated surface and (B) injection of the CXCR4-specific 12G5 mAb over CXCR4-captured surfaces**

Therefore, in order to increase the capture yield of CXCR4-C9, a new approach was taken, also developed by Navratilova and colleagues [374], using a manual solubilisation approach, involving a higher cell density for solubilisation, that is claimed to yield higher capture levels required for small molecule screening.

#### 4.3.4.5 Batch preparations of manually solubilised receptor resulted in higher receptor capture levels

Cf2Th-CXCR4-C9 cells were manually solubilised in a specific mixture of lipid and detergent, as outlined in 2.19.1, prior to either freezing for long term

storage or injection over 1D4 antibody-coated sensor surfaces. Using a higher cell density, of $8x10^6$ cells/ml of solubilisation buffer, resulted in capture levels of ~2000 RU (Figure 43), 10-fold higher capture levels than with the automated solubilisation method. The increased capture levels meant that screening CXCR4 with small molecules could be attempted.

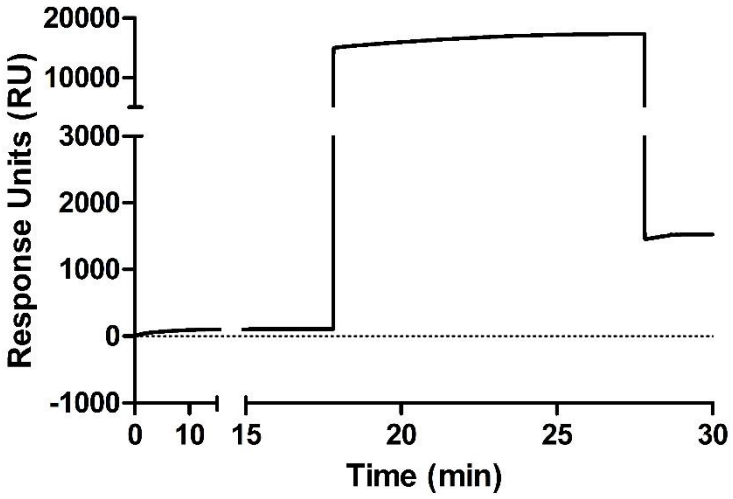


**Figure 43. SPR sensorgram showing injection of manually solubilised Cf2Th-CXCR4-C9 cells over a 1D4 antibody sensor surface**

#### 4.3.4.6 Novel tetraazamacrocyclic compounds have significantly increased affinity for CXCR4 compared to AMD3100

Following increased capture yields of CXCR4-C9 by manual-based solubilisation and capture, receptor surfaces were screened for binding against the novel macrocyclic compounds $Cu_2$CB-bicyclam, CuCB-bicyclam and also the already established AMD3100 small molecule for comparison, with the intention of elucidating the effects of structural changes on binding kinetic profiles of these

agents to aid the selection of lead candidates for PET probe or therapeutic agent development.

Following CXCR4-C9 capture, AMD3100, CuCB-bicyclam and $Cu_2$CB-bicyclam were injected over receptor containing surfaces at 30 µl/min and allowed to associate with receptor for three minutes, following by a 10 minute dissociation phase whereby analyte injection had ceased. All analytes were injected at 0.82 nM, 2.47 nM, 7.41 nM and 22.22 nM. All SPR curves were double referenced, whereby the responses observed on reference flow cells, responsible for non-specific binding and bulk-response, were subtracted from responses observed on active flow cells. A blank injection, containing only running buffer was also subtracted from the responses observed on the receptor-coated flow cell.

Figure 44-54 shows the sensorgrams generated by the binding of AMD3100, CuCB-bicyclam and $Cu_2$CB-bicyclam to CXCR4 by SPR and Table 19 outlines the kinetic constants of each molecule for association, dissociation and resultant affinity. Following kinetic analysis using a 1:1 binding model (Langmuir model), AMD3100 was revealed to bind to CXCR4 (Figure 44) with an association constant of $8.27 \times 10^4 \pm 3.34 \times 10^4$ $M^{-1}s^{-1}$, a dissociation constant of $3.86 \times 10^{-4} \pm 1.6 \times 10^{-4}$ $s^{-1}$, and a resultant affinity of 4.61 ± 0.15 nM (n=3), with this affinity value similar to data from a previous study by Navratilova and colleagues with an AMD3100-CXCR4 affinity of 4 nM [360, 374].

**Table 19. Binding kinetic and affinity constants for small molecules binding to immobilised CXCR4 by SPR**

| Compound | AMD3100 | Cu-CB-bicyclam | $Cu_2$-CB-bicyclam |
|---|---|---|---|
| Association ($M^{-1}s^{-1}$) | **8.27**±3.34x$10^4$ | **3.89**±0.37x$10^5$ | **5.85**±0.13x$10^5$ |
| Dissociation ($s^{-1}$) | **3.86**±1.66x$10^{-4}$ | **6.82**±1.21x$10^{-4}$ | **4.80**±1.18x$10^{-4}$ |
| Affinity (M) | **4.61**±0.15x$10^{-9}$ | **1.18**±0.23x$10^{-9}$ | **1.23**±0.28x$10^{-9}$ |

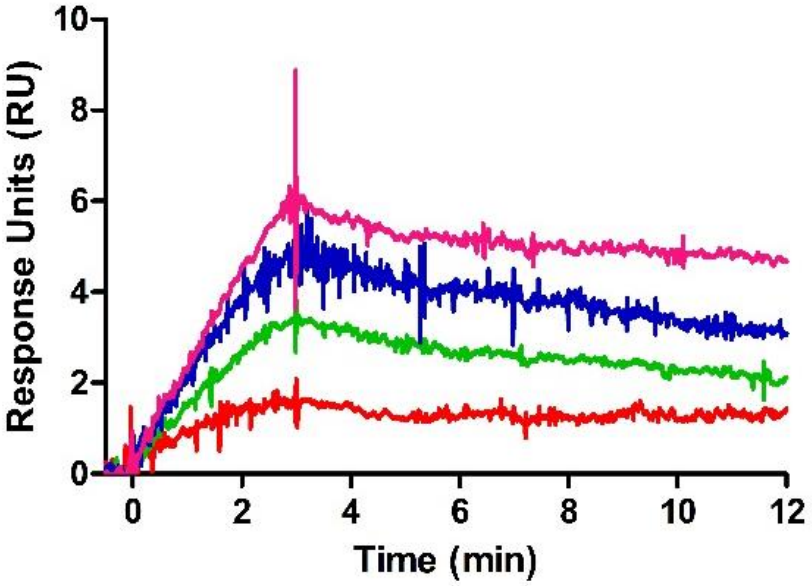


**Figure 44. Multi-cycle kinetics sensorgram of AMD3100 binding to immobilised CXCR4. Pink = 22.2 nM; Blue = 7.4 nM = Green = 2.5 nM; Red = 0.8 nM**

Figure 46 shows the binding of CuCB-bicyclam to CXCR4, with an association constant significantly faster than that of AMD3100 (3.89x$10^5$ ± 3.7x$10^4$ $M^{-1}s^{-1}$; p=0.0005). Interestingly, there was no significant difference in the dissociation constants between CuCB-bicyclam and AMD3100. Despite this, the resultant affinity of CuCB-bicyclam (1.18 ± 0.23 nM) was significantly greater than that of AMD3100 (p=0.0017).

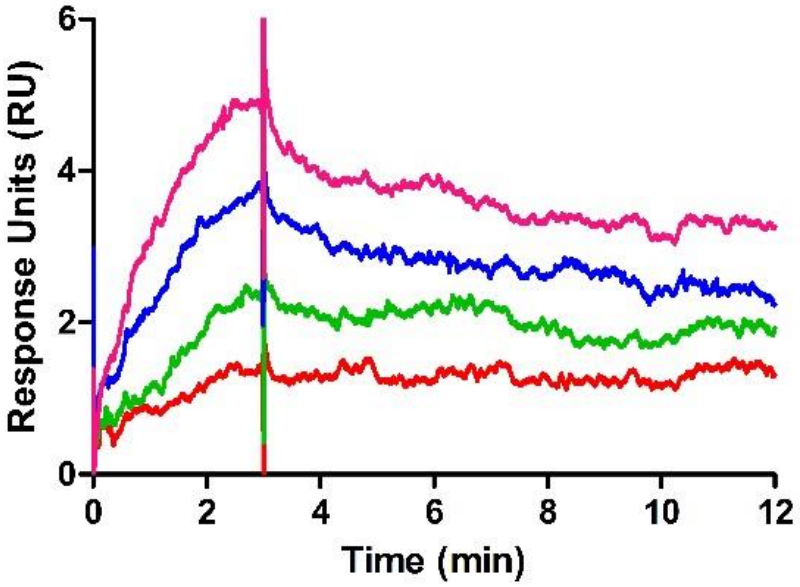


**Figure 46. Multi-cycle kinetics sensorgram of CuCB-bicyclam binding to immobilised CXCR4. Pink = 22.2 nM; Blue = 7.4 nM = Green = 2.5 nM; Red = 0.8 nM**

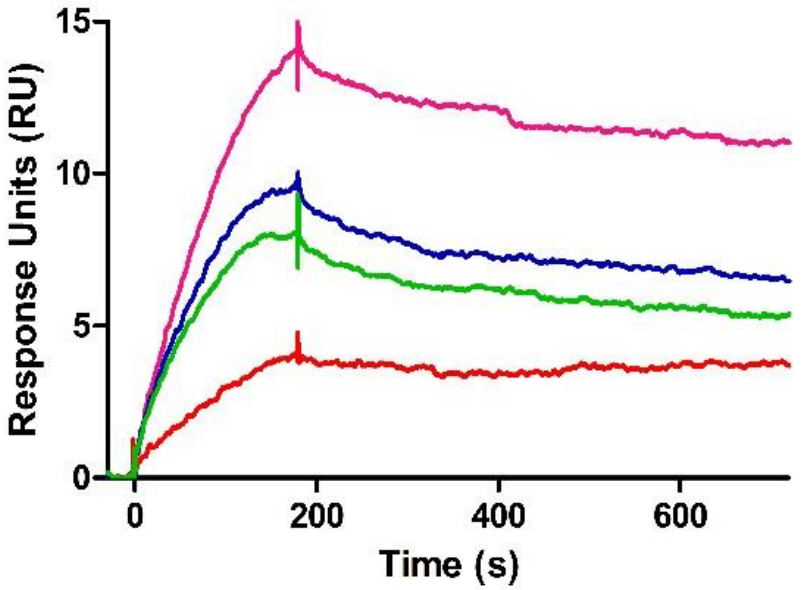


**Figure 45. Multi-cycle kinetics sensorgram of $Cu_2$CB-Bicyclam binding to CXCR4. Pink = 22.2 nM; Blue = 7.4 nM = Green = 2.5 nM; Red = 0.8 nM**

$Cu_2$CB-bicyclam was also able to bind to immobilised CXCR4 with high affinity (Figure 45). Similarly to the CuCB-bicyclam molecule, $Cu_2$CB-bicyclam was

shown to associate with CXCR4 with a binding constant of $5.85 \times 10^5 \pm 1.3 \times 10^4$ $M^{-1}s^{-1}$, which is significantly higher than both AMD3100 ($p=0.011$) and CuCB-bicyclam ($p=0.0079$). The dissociation constant of $Cu_2$CB-bicyclam ($4.80 \times 10^{-4} \pm 1.18 \times 10^{-4}$ $s^{-1}$), on the other hand, was not found to be significantly different from that of AMD3100 ($p=0.6613$) or CuCB-bicyclam ($p=0.2976$). Due to the significantly higher affinity of $Cu_2$CB-bicyclam (1.23 nM), the affinity, derived from the association and dissociation constants, for CXCR4 was shown to be significantly greater than that of AMD3100 ($p=0.0028$), but not CuCB-bicyclam ($p=0.8953$). Measurements for each concentration (for each compound) was performed three times.

From the SPR screening analysis, affinity for CXCR4, from highest to lowest found to be in the order of $Cu_2$CB-bicyclam $\approx$ CuCB-bicyclam > AMD3100, reflecting results observed a different experimental setup utilising competitive binding experiments to show binding of novel macrocycles, and AMD3100 to CXCR4 [381].

## 4.4 Discussion

The chemokine receptor CXCR4 has been associated with both cancer progression and IPF pathogenesis, and may be a potential marker of prognosis in both scenarios. The work presented here details approaches made to characterise the binding properties, affinity and binding kinetics, of novel configurationally-restricted tetraazamacrocycles in a comparative study against the clinically-used AMD3100. The main aim of this project was to characterise the binding profiles of novel configurationally-restricted tetraazamacrocycles to assess their suitability as CXCR4-targeted PET imaging agents and targeted therapeutic agents applied to cancer and IPF.

The structure of AMD3100 allows for transition metal complexation and direct labelling with copper-64 has been carried out to allow PET imaging of $CXCR4^+$ tumours. These imaging studies revealed high non-specific accumulation in the liver, likely due to complex instability and transchelation of the transition metal from the structure, preventing further development of these compounds [382] As these compounds lack the stability to retain their radiolabel [371, 383-385], this project aims to evaluate the binding characteristics of configurationally-restricted tetraazamacrocyclic CXCR4-targeted antagonists, with specific focus on binding kinetics. As the molecules to be evaluated have potential to act as both a drug and imaging agent, as they are able to contain the radioactive isotope copper-64, this could present opportunities for both patient stratification and therapy response monitoring in patients with $CXCR4^+$ cancer or IPF.

This study has evaluated the binding profiles of high-affinity CXCR4-specific antagonists [$^{nat}$Cu]CuCB-bicyclam and [$^{nat}$Cu]$Cu_2$-CB-bicyclam that are able to bind to CXCR4 with high specificity and favourable binding kinetics giving them potential as clinical diagnostic PET imaging or therapeutic agents in oncology and/or IPF.

Through cross-bridging tetraazamacrocycles between non-adjacent nitrogen atoms via an ethyl linker there is formation of a single *cis*-V configuration following

complexation of a transition metal ion [383]. With unbridged small molecule macrocycles, such as [$^{nat}$Cu]Cu-AMD3100, there is an equilibrium between up to six different configurations leading to variable affinities that reflect a specific configuration it is in. Cross-bridging these macrocycles gives a locked, single configuration and shorter coordination bonds with aspartate residues of CXCR4 and, thus, an improved CXCR4 affinity [381, 386].

In accordance with the characterisation of both [$^{nat}$Cu]Cu-CB-bicyclam and [$^{nat}$Cu]$Cu_2$-CB-bicyclam by Archibald and co-workers in collaboration with Schols and co-workers, both molecules were deemed to have high affinity for CXCR4 *in vitro* using competition binding experiments by flow cytometry in this work. Furthermore, the affinities of these molecules for CXCR4 were significantly greater for both novel compounds compared to the well-established, and clinical used, AMD3100. There were, however, differences in the amount of antibody inhibition of the compounds between competition experiments involving saturating concentrations of antagonists and titrated concentrations of the antagonists. In the titration experiment, the percentage of antibody-inhibition was lower than that of the initial experiment using only a single concentration. This may be a potential source of variability in the purity between different batches of compound as fresh compound was solubilised for each experiment. If any impurities were indeed present in successive batches, the practical concentration of the compounds may not have accurately reflected the theoretical concentrations.

As flow cytometry competition binding experiments only give an indirect indication as to the strength of an interaction, and do not reflect kinetic parameters such as association and dissociation constants, SPR experiments were utilised to obtain accurate, quantitative kinetic data regarding these molecules in an attempt to decipher how structural changes affect the binding kinetic properties of this new class of small molecule. An important aspect to consider for the use SPR is that there is no requirement for labelling either binding partner, therefore “true” binding profiles of the molecules tested directly without the

potential of labels interfering or altering binding of a molecule to its target. The capability to assess the direct interaction of molecules to a target receptor is a useful tool in the development of an imaging/therapeutic agent. The use of other binding techniques such as competitive ELISA or flow cytometry allows the determination of equilibrium affinity alone, whereas SPR is able to resolve equilibrium affinity into on- and off-rates. The use of SPR in the development of imaging or therapeutic molecules can allow for the quantification of association and dissociation constants of an interaction, and the binding kinetic profiles can be used to predict *in vivo* behaviour. For example, if a molecule was deemed to have a slow association constant, it may struggle to reach equilibrium *in vivo*, which will result in lower receptor binding. On the other hand, quickly associating molecules may achieve equilibrium *in vivo* faster and, therefore, demonstrate higher receptor occupancy than molecules with slower binding kinetics.

The use of SPR is suitable for this project, as the sensitivity of BIACORE T200 instrument, used throughout this study, is ideal for the analysis of small molecule binding. The SPR results showed that all small molecules tested bound to CXCR4 with high affinity in the order [$^{nat}$Cu]Cu$_2$-CB-bicyclam $\approx$ [$^{nat}$Cu]Cu-CB-bicyclam > AMD3100. This order of affinities for CXCR4 is likely due to structural differences in these molecules. The restriction of the configuration of both of [$^{nat}$Cu]Cu$_2$-CB-bicyclam and [$^{nat}$Cu]Cu-CB-bicyclam through cross-bridging has led to an increase in affinity for CXCR4 compared to AMD3100. This is in line with the shorter coordination bonds with aspartate residues of CXCR4 leading to an increased CXCR4 affinity [381, 386]. As discussed before, AMD3100 is in equilibrium between multiple different configurations, up to six possible configurations which will have varying affinities for CXCR4 (nuclear magnetic resonance (NMR) studies have shown that Zn$_2$AMD3100 is in equilibrium between three configurations when in solution [387]).

With shorter coordination bonds leading to increased affinity for CXCR4, it could be postulated that the dissociation of both [$^{nat}$Cu]Cu$_2$-CB-bicyclam and [$^{nat}$Cu]Cu-CB-bicyclam would be slower than AMD3100. However, there was no

significant differences in the dissociation constants observed between any of the three small molecules tested. A potential reason for this may be mass transport limitation (MTL) within the fluidic system of the BIACORE instrument. Due to the captured receptor and the analytes tested being in physically distinct locations, one immobilised on the sensor surface and one located in solution, there is a necessity for the analyte in solution to be transported from the bulk solution being injected over the sensor surface to the immobilised ligand on the sensor surface during the association phase. Equally, it is necessary for the transport of dissociating analyte from the sensor surface to the bulk solution to take place during the dissociation phase. Under conditions of MTL during the association phase there is insufficient supply of analyte to the surface that becomes rate-limiting [388] and there is formation of a depletion zone (Figure 47A) that is created, whereby the concentration of analyte at the sensor surface is less than in the bulk solution, whereas within the dissociation phase there is a retention zone close to the sensor surface (Figure 47B) whereby the concentration of the analyte is greater at the sensor surface than the bulk solution. This retention zone allows for the re-binding of dissociated analyte to other “free” receptors on the sensor surface, which may prolong the dissociation phase observed on any resultant sensorgrams, which would reflect more the rate of mass transport limitation rather than the true binding kinetics [389].

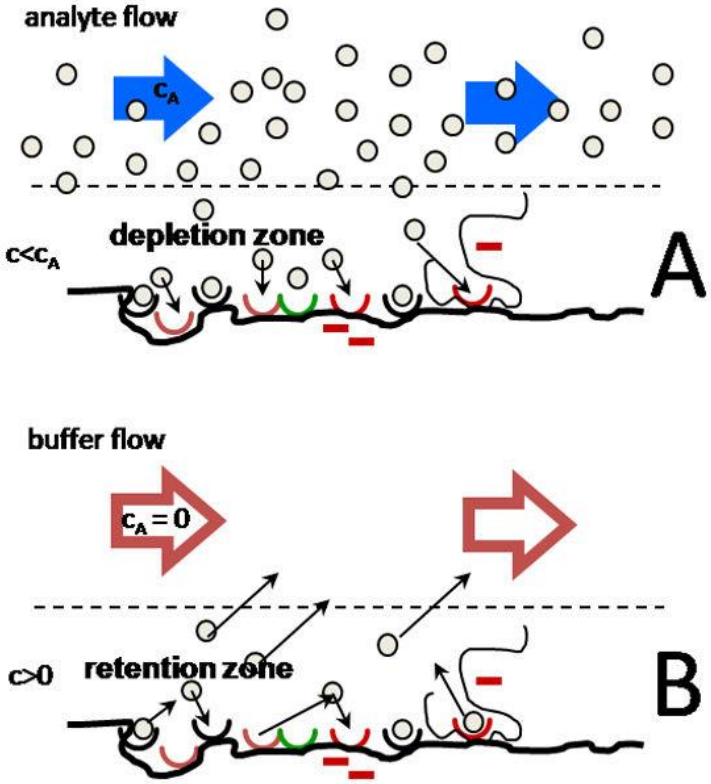


**Figure 47. Cartoon depicting the effect of mass transport limitation on analyte concentration. (A) During association, limited mass transport causes the analyte close to the surface to be bound more quickly than it can be resupplied by the bulk analyte flow. (B) During dissociation, limited mass transport leads to the retention of analyte close to the surface, whereby analyte rebinding to empty surface sites occurs before it can diffuse to the bulk flow. [381]**

Despite the increase in surface receptor density, the number of different concentrations of analyte that were able to be tested were limited. At concentrations of 66.7 nM and 200 nM, the responses observed were lower than that of 22 nM (Appendix Figure 10). This is most likely due to the receptor surface not being regenerated between each cycle, reducing the number of "free" receptors with subsequent cycles. As the concentrations were injected from lowest to highest, this saturation of the receptor surface was occurring at the higher concentrations, resulting in lower responses observed as the number of available binding sites diminished. Therefore, these concentrations were excluded from the kinetic analysis. This reduction in response that was observed with higher

concentrations was surprising due to the capture yields of approximately 2000 RU resulting in a theoretical $R_{max}$ of ~50 RU. The highest response observed in this setup was approximately 15 RU, much lower than the theoretical $R_{max}$.

Calculating the theoretical $R_{max}$ in this setup is difficult, due to the variety of components that are present on the sensor surface, including captured receptor as well as lipids. It is difficult to delineate how much of the response increase observed during the capture phase is attributed to by the receptor only, which may explain the discrepancies between the calculated $R_{max}$ value and the responses seen throughout the study. This information would allow for a more accurate quantification of a theoretical $R_{max}$ for any small molecule that is to be injected as analyte.

A potential method to eliminate, or minimise, MTL is to increase the flow rate of the fluidic system. With regards to association, the increased flow rate will supply a greater amount of analyte to the sensor surface, reducing the shortage of analyte at the surface that would happen under MTL conditions due to fast association of the analyte. With regards to dissociation, increased flow rates will assist in the removal of the analyte from the sensor surface before it has the opportunity to re-bind to free ligand. Alternatively, immobilisation of less ligand on the sensor surface is another method to reduce MTL, which would both reduce the demand of analyte to the surface from the bulk solution, and also reduce the number of free binding sites for dissociating analyte to bind to during the dissociation phase. However, in the context of this work with small molecules, reducing the density of CXCR4 captured on the sensor surface would be detrimental to the observation of small molecule binding as, due to their size, they require higher amounts of immobilised ligand in order to produce enough of a response for binding to be observed. Therefore, further experiments involving increased analyte flow rates should be performed to see if the system is under MTL. If the system, as currently is, is under MTL conditions, then removal of MTL by increasing the flow rate should reveal the true binding kinetic profiles for AMD3100, [$^{nat}$Cu]$Cu_2$-CB-bicyclam and [$^{nat}$Cu]Cu-CB-bicyclam.

In light of these SPR studies, both [$^{nat}$Cu]Cu-CB-bicyclam and [$^{nat}$Cu]$Cu_2$-CB-bicyclam both have desirable binding characteristics for use as novel PET imaging and therapeutic agents. This is reinforced by studies undertaken by Cecilia Miranda (University of Hull) and colleagues that radiolabelled both compounds with the radioisotope copper-64 for imaging tumour CXCR4 expression *in vivo* [390]. Miranda and colleagues showed, using CXCR4-transfected and wild-type (CXCR4$^{-ve}$) U87 xenografts, specific uptake of [$^{nat}$Cu]Cu-CB-bicyclam in CXCR4$^{+ve}$ tumours. Despite high liver uptake in this mouse model, a blocking experiment, using the [$^{nat}$Cu]$Cu_2$-CB-bicyclam derivative reduced liver uptake by over 90%, and *ex vivo* immunohistochemistry, FACS and mRNA analysis demonstrated that the mouse liver expressed high levels of the murine isoform of CXCR4. Metabolite analysis confirmed that a high percentage [$^{64}$Cu]CuCB-Bicyclam was excreted intact in the urine (stability values of 92 ± 3%), whereas most urine radioactivity from [$^{64}$Cu]CuAMD3100 injected animals was in the form of free copper-64 ions (stability values of 9 ± 5%). *In vitro* acid stability assays (6 M HClO4) yielded comparable results.

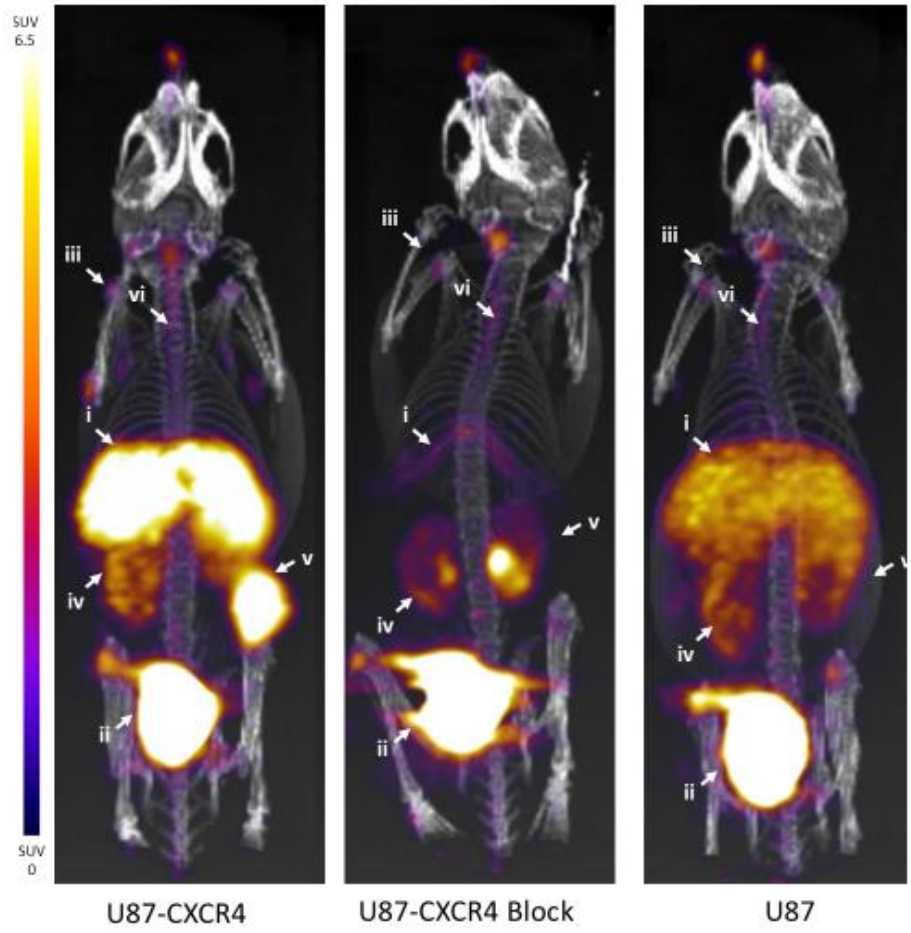


**Figure 48. Evaluation of [$^{64}$Cu]Cu-CB-bicyclam *in vivo*. PET/CT images at 80-90 minutes post-injection with 9.6 ± 0.7 MBq [$^{64}$Cu]Cu-CB-bicyclam. Left panel: U87-CXCR4 tumour-bearing animal. Middle panel: U87-CXCR4 tumour-bearing animal pre-administered with 5 mg/kg of $Cu_2$CB-Bicyclam. Right panel: U87 tumour-bearing animal. Tracer uptake in (i) liver, (ii) bladder, (iii) bony growth plates, (iv) kidneys, (v) tumour and (vi) bone marrow. [382]**

## 4.5 Conclusion

This study has evaluated a new class of CXCR4-targeted antagonists as potential diagnostic imaging and therapeutic agents using SPR as a technique to assess the binding properties of these molecules to CXCR4. Both [$^{nat}$Cu]Cu-CB-bicyclam and [$^{nat}$Cu]$Cu_2$-CB-bicyclam were shown to bind to CXCR4 with enhanced affinity compared to the clinically-used AMD3100. Although this method was able to characterise the high binding affinity of these molecules to CXCR4, more work is warranted in order to ascertain whether or not mass transport limitation is having an effect on the dissociation constant of these molecules in this experimental setup, and, if so, further experiments are required to minimise this in order to optimise the experimental setup and correct the measured dissociation rates and resultant affinities. These results, however, coalesce with imaging studies of these novel tetraazamacrocycles labelled with copper-64, undertaken by Miranda and colleagues, which show useful image timepoints and blockable liver uptake. These findings encourage further investigation of these compounds as potential CXCR4-targeted PET imaging or therapeutic agents in both preclinical cancer and IPF models prior to translation to the clinic.

# Further discussion and Conclusions

# 5 Further discussion and conclusions

## 5.1 Summary

The chemokine receptor CXCR4 belongs to the family of G-protein coupled receptors and, along with its cognate ligand, CXCL12, plays a pivotal role in normal physiological processes. The overexpression of CXCR4 has been associated with at least twenty-three types of human cancers including, but not limited to, breast, prostate, haematopoietic, ovarian cancers as well as multiple myeloma and leukaemia. Due to its involvement in an array of processes in carcinogenesis, such as tumour cell invasion, cellular transformation and trafficking of malignant cells to organs expressing high levels of CXCL12, efforts have been made in the development of molecular agents that can both inhibit this signalling axis in cancer, as well as image CXCR4 expression for the stratification of patients that may be deemed at a higher risk of developing metastatic lesions for therapeutic intervention.

Positron emission tomography is a molecular imaging technique that permits the investigation of the function and expression of clinically relevant targets *in vivo*, rather than solely anatomical features that would be achieved through other imaging modalities such as X-ray or computerised tomography. The work presented in this thesis has focused mainly on the development of PET imaging agents, as well as therapeutic agents, that target either integrin αvβ6 or CXCR4 in xenograft models, to evaluate their suitability as imaging or therapeutic agents in cancer or idiopathic pulmonary fibrosis. This thesis does not include preclinical models of IPF due to the complexities that are associated with the development of the model, such as long latency periods and increased mortality rates, however the use of xenograft models that express the target of interest, which are relatively easy to generate and quicker to establish, it was possible to assess the ability of targeted agents to detect the target receptor *in vivo*. Radioligands or non-radiolabelled antagonists were synthesised by either Dr Juozas Domarkas (αvβ6-targeted peptides) or other members of the Archibald group (CXCR4-targeted agents).

The first chapter of this thesis introduces molecular imaging and examples of its use in the diagnosis, stratification and assessment of therapeutic responses of different cancers, as well as its current use in idiopathic pulmonary fibrosis. Also outlined are the biology of both CXCR4/αvβ6-associated cancers and their roles in the pathogenesis of IPF, as well as the requirement for novel agents for the diagnosis and therapy of these pathologies. An overview of other αvβ6- or CXCR4-targeted imaging agents that have been developed elsewhere is also presented.

The second chapter outlines the methodologies used throughout the project in order to evaluate these targeted agents as theranostic molecules.

Chapter 3 evaluates the development of peptide-based agents for PET imaging of αvβ6 *in vivo*. This study characterised the binding of various peptides based on the well-known RXDLXXL binding motif that gives peptides selectivity for αvβ6 over other integrins, to integrin αvβ6, one of which was previously described but had not been evaluated as a potential imaging agent, using *in vitro* techniques such as competitive ELISA, SPR and radioligand cell binding assays. ELISA and SPR studies demonstrated the high affinity of various peptides for αvβ6 and, in particular, SPR and radioligand cell binding studies showed the high specificity of RGD1 for αvβ6 over other integrins. In particular, cellular uptake of [$^{68}$Ga]Ga-DO3A-JD1-RGD1 and [$^{68}$Ga]Ga-DO3A-JD2-RGD1 showed uptake relative to the expression level of αvβ6 in various cell lines (MEFβ6 > BxPC3 > MDA-MB-468 > $MEF_{wt}$/U87). Internalisation experiments showed that [$^{68}$Ga]Ga-DO3A-JD2-RGD1 was able to induce integrin internalisation in BxPC3 cells, with approximately 70% of the total bound radioactivity being internalised, indicating the promising translational potential of [$^{68}$Ga]Ga-DO3A-JD2-RGD1, or a modified PRRT derivative [$^{177}$Lu]Lu-JD2-RGD1, to be used as an imaging or therapeutic agent in αvβ6$^{+}$ cancer, respectively. Based on *in vitro* data, derivatives of the peptide RGD1 were taken forward to *in vivo* imaging studies in naïve nude mice, using the incorporation of [$^{68}$Ga]$Ga^{3+}$ into the chelator DO3A, which had been conjugated to the peptide to image the radioligand biodistribution. DO3A had specifically been used due to its clinical use and ability to chelate other radionuclides, including therapeutic

nuclides such as lutetium-177, giving rise to the potential to develop a radionuclide therapy agent. Results showed that both derivatives of RGD1 were distributed mainly across the intestines and submandibular glands, with a low uptake in the healthy lungs of these mice, in accordance with other αvβ6-targeted PET imaging agents in the literature and these tissues were also shown, in this study, to express αvβ6. Interestingly, the uptake seen in the lungs, which express αvβ6 to a low level, as confirmed by IHC, shows [$^{68}$Ga]Ga-DO3A-JD2-RGD1 has promising potential in the detection of elevated levels of αvβ6 that occurs in the lungs during fibrosis, although this still requires evaluation pre-clinically. Importantly, the specificity of [$^{68}$Ga]Ga-DO3A-JD2-RGD1 was demonstrated in blocking experiments with a previously validated anti-αvβ6 blocking antibody, resulting in significant reductions in radioligand uptake in the previously mentioned tissues. In light of this, BxPC3 tumour-bearing NSG mice were used in tumour imaging studies. BxPC3 had been shown to express high levels of endogenous αvβ6 and [$^{68}$Ga]Ga-DO3A-JD2-RGD1 was selected as the lead candidate for this studies. [$^{68}$Ga]Ga-DO3A-JD2-RGD1 was shown to accumulate, as previously, in the gastrointestinal tract and submandibular glands, as well as in in the tumour, which was shown by IHC to express high levels of endogenous αvβ6. A further blocking experiment in tumour-bearing mice, as with the naïve animals, resulted in significant reductions in uptake in the tumour, GI tract and submandibular glands, validating the specificity of [$^{68}$Ga]Ga-DO3A-JD2-RGD1 for αvβ6 *in vivo*. To validate the imaging findings, a biodistribution experiment was performed using [$^{68}$Ga]Ga-DO3A-JD2-RGD1. The results of the biodistribution experiment reflected the uptake seen in imaging studies, with high uptake observed in the gastrointestinal tract, tumour, submandibular glands and kidneys, and significant reductions in radioligand uptake in the small intestine, lungs, tumour and submandibular glands following blocking with anti-αvβ6. *Ex vivo* urine analysis of [$^{68}$Ga]Ga-DO3A-JD2-RGD1 showed that approximately half of the radioligand was metabolised. The metabolism of [$^{68}$Ga]Ga-DO3A-JD2-RGD1 did not result in any confounding effects during *in vivo* imaging studies, and was most likely cleared from circulation rapidly via the kidneys. The substitution of

[$^{nat}$Ga]Ga$^{3+}$ for [$^{nat}$Lu]Lu$^{3+}$ to produce [$^{nat}$Lu]Lu-DO3A-JD2-RGD1 did not result in any significant changes in binding affinity for αvβ6 in competitive binding ELISA experiments. This indicates that the $^{177}$Lu radiolabelled derivative may have a similar binding and pharmacokinetic profile to [$^{nat}$Ga]Ga-DO 3A-JD2-RGD1 *in vivo*.

Chapter 4 reports the assessment of the binding kinetic profiles of [$^{nat}$Cu]CuCB-bicyclam and [$^{nat}$Cu]Cu$_2$CB-bicyclam, two novel tetraazamacrocycle CXCR4-targeted inhibitors, in a comparison study with the clinically used AMD3100 to evaluate their suitability as CXCR4-targeted PET imaging or therapeutic agents. Affinity of novel tetraazamacrocycles, and existing molecules AMD3100 and AMD3465 was assessed in competitive binding experiments using CXCR4$^+$ Jurkat cells in flow cytometry studies, which showed that all four antagonists possess high affinity for CXCR4. However, these results do not reflect the binding kinetic profiles that is association and dissociation, of these molecules, which may differ significantly between different compounds that have reportedly similar affinities by equilibrium binding assays. SPR experiments were utilised to evaluate the binding kinetic properties of [$^{nat}$Cu]CuCB-bicyclam and [$^{nat}$Cu]Cu$_2$CB-bicyclam compared to AMD3100. Capture and reconstitution of a CXCR4-GST fusion receptor to a sensor chip did not yield active receptor surfaces, therefore a smaller fusion tag, C9 (TETSQVAPA) was used, as optimised previously by Navratilova *et al.* [374, 375] and Stenlund *et al.* [376], enabling capture of functional receptor. Both novel antagonists were shown to have enhanced affinity for CXCR4 compared to AMD3100, however the dissociation constants were not significantly different between any of the agents tested, potentially as a result of limited mass transport away from the receptor surface due to fast re-binding to other nearby unoccupied receptors, therefore further work is required in order to eliminate, or at least minimise as much as possible the mass transport effects that may be observed.

## 5.2 Clinical Translation

The results from this thesis indicate the translational potential of [$^{68}$Ga]Ga-DO3A-JD2-RGD1 to detect endogenous levels of αvβ6 *in vivo*, which may be used

for the diagnosis of αvβ6$^{+}$ tumours and the stratification of patients that may benefit from αvβ6-targeted therapy. Although it was shown that approximately half of [$^{68}$Ga]Ga-DO3A-JD2-RGD1 was metabolised *in vivo*, it is an improvement upon the more well-known αvβ6-targeted peptide, A20FMDV2 (NCT03069989), which has been shown to be completely degraded after 1 hour, post-injection, whereas both [$^{68}$Ga]Ga-DO3A-JD1-RGD1 and [$^{68}$Ga]Ga-DO3A-JD1-RGD1 were shown in this study to be at least 50% stable up to at least 90 minutes post-injection. Despite this, it has progressed into the clinical trial stages of tracer validation, most likely due to the rapid clearance of radiometabolites preventing any non-specific uptake in tissues *in vivo*. It is likely that, in light of the high renal uptake of [$^{68}$Ga]Ga-DO3A-JD2-RGD1 and the significant reduction in uptake in response to blocking αvβ6, that any radiometabolites are rapidly excreted via the kidneys. In light of the high kidney uptake of [$^{68}$Ga]Ga-DO3A-JD2-RGD1, the translational potential of a therapeutic derivative of this radiopharmaceutical may be limited, as the critical organs when characterising the dosimetry of radiopharmaceuticals that are excreted renally are the kidneys and bladder. If the effective dose to these organs is high, the risk of nephrotoxicity is increased. However, when comparing pre-clinical dosimetry data of [$^{18}$F]F-FB-A20FMDV2 in rats to that in a first time in human study, the effective dose in the human (0.0217 mSv/MBq) was found to be less than the equivalent effective dose in rats (0.0355 mSv/MBq), therefore high uptake in a pre-clinical setting does not necessarily make a radiopharmaceutical unsuitable for clinical translation.

Following the preclinical evaluation of radiopharmaceuticals, there are various pathways that can be taken to facilitate the transition of a radiopharmaceutical from pre-clinical to a clinical setting [391] (Figure 49).

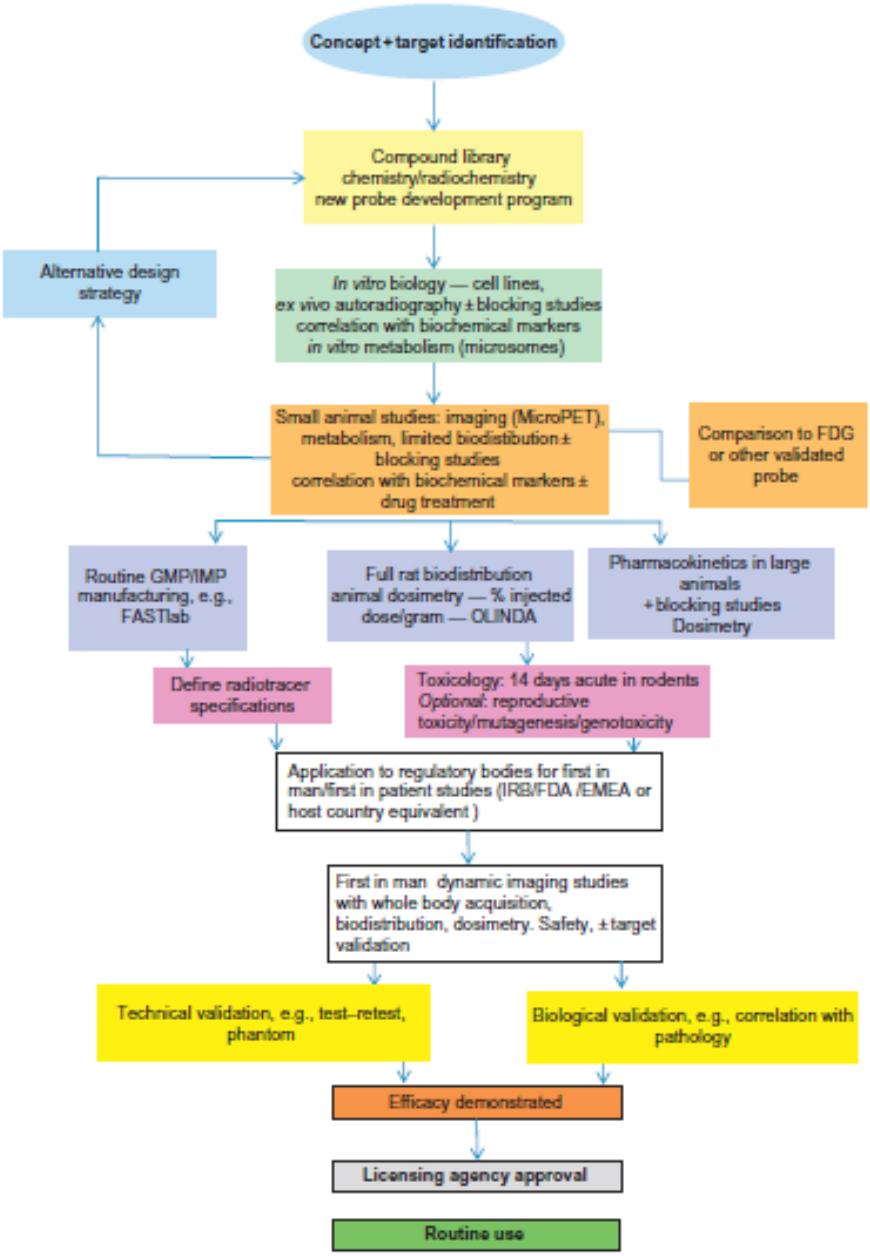


**Figure 49. Pathway to develop new radiotracers [383]**

In order to translate the work presented here to the clinical environment, various parameters require investigation such as animal dosimetry using OLINDA (**O**rgan **L**evel **IN**ternal **D**ose **A**ssessment) software [392] or the more recently developed RADAR (**RA**diation **D**ose **A**ssessment **R**esource) software [393]. For the translation of radiopharmaceuticals into the clinic, an estimation of absorbed doses to critical organs is required for the prediction of biological effects of these

radiopharmaceuticals. Typically, for diagnostic radionuclides, biokinetics of the imaging agent may be determined in a small number of representative, often healthy, volunteers. However, for therapeutic radiopharmaceuticals, the determination of the biokinetics must be understood for each individual in order to calculate the absorbed doses to critical healthy organs and tissues as well as target tissues, such as a tumour, with high accuracy. With regards to the use of therapeutic radionuclides, the aim is to deliver the highest possible absorbed dose to the tumour as possible, whilst limiting, as much as possible, the dose delivered to healthy organs. As the population is highly variant, models intended to be representative of the general population are unable to be used to estimate the dose delivered to organs of an individual. Because of this, it can be difficult to gain accurate dosimetry profiles of therapeutic radiopharmaceuticals.

In the context of this work, which has shown in preliminary studies that the incorporation of either $Ga^{3+}$ or $Lu^{3+}$ does not lead to changes in αvβ6 binding of DO3A-JD2-RGD1. If, in following further *in vivo* investigations of the radioactive derivatives, it was deemed that the *in vivo* pharmacokinetics of [$^{68}$Ga]Ga-DO3A-JD2-RGD1 and [$^{177}$Lu]Lu-DO3A-JD2-RGD1 are similar, it may be possible to use the imaging derivative, [$^{68}$Ga]Ga-DO3A-JD2-RGD1, to obtain a dosimetry profile that can be used to estimate the absorbed dose to critical organs and tissues for [$^{177}$Lu]Lu-DO3A-JD2-RGD1. This would be extremely important, and necessary, to determine if renal toxicity occurs and to observe whether the effective/ablative dose is reached within the targeted tumour. If the received kidney dose is too high, or the effective dose in the tumour is not reached, then a lutetium-177 derivative would not be suitable for clinical translation and this agent would only be potentially useful as a PET imaging agent.

Following pre-clinical validation of [$^{68}$Ga]Ga-DO3A-JD2-RGD1 and [$^{177}$Lu]Lu-DO3A-JD2-RGD1 dosimetry profiles, and development of routine good manufacturing practice, applications for progression into a first-in-man dynamic imaging study with whole-body acquisition to assess human biodistribution and dosimetry over time for these radiopharmaceuticals can take place prior to

mechanistic studies that focus on parameters such as metabolism, distribution and other information regarding human physiology, pathophysiology, and biochemistry of the radiopharmaceuticals.

This thesis has also characterised the binding kinetics of configurationally-restricted tetraazamacrocycles for the chemokine receptor CXCR4 by surface plasmon resonance to aid the selection of lead candidate molecules for CXCR4-targeted imaging and/or therapy in cancer or IPF.

The use of SPR to quantify the binding kinetic parameters of molecules for a target receptor is being increasingly used in drug development. In the context of this work, SPR is a valuable tool for the characterisation of potential imaging and therapeutic agent binding kinetics, which have significant implications for imaging/therapeutic agents. The actions of $Cu_2$CB-bicyclam and CuCB-bicyclam have been previously shown to be antagonistic, preventing receptor-induced internalisation of either molecule. If an imaging agent or radionuclide drug was to be internalised by target cells, it would allow for the accumulation of the agent within target cells whereby it could elicit its detection or therapeutic function. The same is not true for antagonists that are not internalised. Antagonists are more likely to wash out from the target tissue if receptor-ligand dissociation is fast. In order to allow antagonists to evoke their inhibitory effects, maximum residence time is desired so as to prevent this washout, therefore a slow dissociation constant is desired, and is a parameter that can be accurately quantified using SPR technology. In the context of using these antagonists as imaging agents however, a long receptor residence time is desired in order to preclude early tracer washout from the circulation in order to enhance properties such as tumour-to-background ratio and enhance tumour contrast. The SPR data presented here demonstrated both $Cu_2$CB-bicyclam and CuCB-bicyclam to possess high affinity and slow dissociation constants for CXCR4 binding. The slow dissociation constants of the radiolabelled equivalents, incorporating $[^{64}Cu]Cu^{2+}$, which has a half-life of 12.7 hours, will allow for CXCR4 imaging at longer timepoints, giving potential to greatly enhanced tumour-to-background ratios following elimination of unbound

radioligand. However, this increased receptor residence time in combination with a relatively long half-life may be problematic in downstream dosimetry studies in both preclinical and clinical studies. Therefore, functionalisation of $Cu_2$CB-bicyclam and CuCB-bicyclam with DOTA may be used to allow for radiolabelling with the shorter-lived radioisotope [$^{68}$Ga]$Ga^{3+}$, which would result in reduced effective radiation doses to critical organs. If this were to be achieved, incorporation of radionuclide therapy isotopes such as lutetium-177 could be investigated, potentially allowing for targeted endoradiotherapy of CXCR4-expressing tumours.

Recently, a [$^{68}$Ga]Ga-labelled CXCR4-targeted cyclic pentapeptide, Pentixafor, has been described and further developed into [$^{177}$Lu]Lu-Pentixather, a lutetium-177 derivative of the Pentixafor scaffold for use as a PET or PRRT agent, respectively, and is under investigation both pre-clinically and clinically. Preliminary studies have indicated that [$^{177}$Lu]Lu-Pentixather possess good CXCR4 binding properties however it is important to note that the preclinical validation of this molecule is limited due to its low affinity for the murine isoform of CXCR4. [$^{64}$Cu]CuCB-bicyclam and [$^{64}$Cu]$Cu_2$CB-bicyclam are able to bind to both human and murine isoforms of CXCR4 with high affinity, allowing for broader pre-clinical assessment of CXCR4 expression in syngeneic tumour models as well as the investigation of CXCR4 imaging in other preclinical models of disease that may require the detection of endogenous murine CXCR4, such as in radiation-induced pulmonary fibrosis. Another advantage of using [$^{64}$Cu]CuCB-bicyclam and [$^{64}$Cu]$Cu_2$CB-bicyclam as CXCR4-targeted PET agents over [$^{177}$Lu]LuPentixather or [$^{68}$Ga]GaPentixafor is that the free ligand starting material, containing no radiometal, possesses no affinity for CXCR4, therefore any unreacted starting material following the radiolabelled process will not compete with the high affinity radiolabelled product. The Pentixafor precursor peptide still possesses an affinity for human CXCR4, therefore any traces of unreacted precursor that may be present in the administered dose may compete with the radioligand and reduce effects such as tumour contrast.

Similarly to earlier discussion, regarding theranostic pairing, $Cu_2$CB-bicyclam and CuCB-bicyclam may also be radiolabelled with the radionuclide [$^{67}$Cu]$Cu^{2+}$, allowing for their use as a theranostic radionuclide pair alongside the [$^{64}$Cu]Cu-labelled derivative.

## 5.3 Final conclusions

This thesis has evaluated various peptides and small molecules that specifically target integrin αvβ6 or the chemokine receptor CXCR4.

*In vitro* and *in vivo* evaluation of [$^{68}$Ga]Ga-labelled αvβ6-targeted peptides led to the selection of [$^{68}$Ga]Ga-DO3A-JD2-RGD1 as the lead candidate for an αvβ6-targeted PET or PRRT agent. *In vivo* studies showed the ability of [$^{68}$Ga]Ga-DO3A-JD2-RGD1 to specifically and selectively detect endogenous αvβ6 expression in a pancreatic adenocarcinoma xenograft model. Further work is required to validate this imaging/PRRT agent for the detection of αvβ6$^+$ cancer or IPF and therapeutic intervention of αvβ6$^+$ cancers. The work presented here warrants further investigation of these radioligands for use as clinical PET imaging and radionuclide therapy agents in order to ascertain dosimetry profiles to facilitate clinical translation.

[$^{nat}$Cu]CuCB-bicyclam and [$^{nat}$Cu]$Cu_2$-CB-Bicyclam were both shown in SPR experiments to bind to reconstituted CXCR4 with enhanced affinity compared to the clinically used small molecule AMD3100, however further optimisation of the technique is required to first establish whether the system is mass transport limited and, if so, to implement a strategy to minimise this effect in order to assess the dissociation rate of these antagonists from CXCR4. These findings suggest that both [$^{64}$Cu]CuCB-bicyclam and [$^{64}$Cu]$Cu_2$CB-bicyclam possess desirable receptor binding kinetic profiles to warrant further investigation further as PET imaging agents.

In particular, PET imaging studies using [$^{64}$Cu]CuCB-bicyclam, performed by this research group, suggest [$^{64}$Cu]CuCB-bicyclam would be a suitable PET probe for the *in vivo* monitoring of CXCR4 expression levels. In addition to their use as

imaging agents, the binding kinetic properties and *in vivo* characteristics of both $Cu_2$CB-bicyclam and CuCB-bicyclam may warrant their investigation as radionuclide theranostic agents as a [$^{64}$Cu]Cu/[$^{67}$Cu]Cu pair.

# 6 References


1. Varmus, H., *Ten years on--the human genome and medicine.* N Engl J Med, 2010. **362**(21): p. 2028-9.
2. Longo, D.L., *Tumor heterogeneity and personalized medicine.* N Engl J Med, 2012. **366**(10): p. 956-7.
3. Gerlinger, M., et al., *Intratumor heterogeneity and branched evolution revealed by multiregion sequencing.* N Engl J Med, 2012. **366**(10): p. 883-892.
4. Wernick, M.N. and D.S. Lalush, *Emission Tomography: The fundamentals of PET and SPECT.* Elsevier Academic Press: London, 2004.
5. Li, Z. and P.S. Conti, *Radiopharmaceutical chemistry for positron emission tomography.* Adv Drug Deliv Rev, 2010. **62**(11): p. 1031-51.
6. Liu, R.S., et al., *Biodistribution, pharmacokinetics and PET imaging of [(18)F]FMISO, [(18)F]FDG and [(18)F]FAc in a sarcoma- and inflammation-bearing mouse model.* Nucl Med Biol, 2009. **36**(3): p. 305-12.
7. Lovqvist, A., et al., *Pharmacokinetics and experimental PET imaging of a bromine-76-labeled monoclonal anti-CEA antibody.* J Nucl Med, 1997. **38**(3): p. 395-401.
8. Miller, P.W., et al., *Synthesis of 11C, 18F, 15O, and 13N radiolabels for positron emission tomography.* Angew Chem Int Ed Engl, 2008. **47**(47): p. 8998-9033.
9. Win, T., et al., *Areas of normal pulmonary parenchyma on HRCT exhibit increased FDG PET signal in IPF patients.* Eur J Nucl Med Mol Imaging, 2014. **41**(2): p. 337-42.
10. Saha, G.B., *Basics of PET Imaging: Physics, Chemistry and Regulations*, ed. Springer. 2005.
11. Rahmim, A. and H. Zaidi, *PET versus SPECT: strengths, limitations and challenges.* Nucl Med Commun, 2008. **29**(3): p. 193-207.
12. Meyer, J.P., et al., *(18)F-Based Pretargeted PET Imaging Based on Bioorthogonal Diels-Alder Click Chemistry.* Bioconjug Chem, 2016. **27**(2): p. 298-301.
13. Tomasi, G., F. Turkheimer, and E. Aboagye, *Importance of quantification for the analysis of PET data in oncology: review of current methods and trends for the future.* Mol Imaging Biol, 2012. **14**(2): p. 131-46.
14. Hatt, M., et al., *Reproducibility of 18F-FDG and 3'-deoxy-3'-18F-fluorothymidine PET tumor volume measurements.* J Nucl Med, 2010. **51**(9): p. 1368-76.
15. Avril, N., et al., *Breast imaging with fluorine-18-FDG PET: quantitative image analysis.* J Nucl Med, 1997. **38**(8): p. 1186-91.
16. Schelling, M., et al., *Positron emission tomography using [(18)F]Fluorodeoxyglucose for monitoring primary chemotherapy in breast cancer.* J Clin Oncol, 2000. **18**(8): p. 1689-95.
17. Lee, J.R., et al., *A threshold method to improve standardized uptake value reproducibility.* Nucl Med Commun, 2000. **21**(7): p. 685-90.
18. Krak, N.C., et al., *Effects of ROI definition and reconstruction method on quantitative outcome and applicability in a response monitoring trial.* Eur J Nucl Med Mol Imaging, 2005. **32**(3): p. 294-301.
19. Soret, M., S.L. Bacharach, and I. Buvat, *Partial-volume effect in PET tumor imaging.* J Nucl Med, 2007. **48**(6): p. 932-45.
20. van Dalen, J., et al., *Effect of the positron range on the spatial resolution of a new generation pre-clinical PETscanner using F-18, Ga-68, Zr-89 and I-124. .* J Nucl Med, 2008(49): p. 404.

21. Sanchez-Crespo, A., *Comparison of Gallium-68 and Fluorine-18 imaging characteristics in positron emission tomography.* Appl Radiat Isot, 2013. **76**: p. 55-62.
22. Horwitz, K.B., Y. Koseki, and W.L. McGuire, *Estrogen control of progesterone receptor in human breast cancer: role of estradiol and antiestrogen.* Endocrinology, 1978. **103**(5): p. 1742-51.
23. Hanahan, D. and R.A. Weinberg, *Hallmarks of cancer: the next generation.* Cell, 2011. **144**(5): p. 646-74.
24. Renan, M.J., *How many mutations are required for tumorigenesis? Implications from human cancer data.* Mol Carcinog, 1993. **7**(3): p. 139-46.
25. Nowell, P.C., *The clonal evolution of tumor cell populations.* Science, 1976. **194**(4260): p. 23-8.
26. Biomarkers Definitions Working, G., *Biomarkers and surrogate endpoints: preferred definitions and conceptual framework.* Clin Pharmacol Ther, 2001. **69**(3): p. 89-95.
27. O'Connor, J.P., et al., *Imaging biomarker roadmap for cancer studies.* Nat Rev Clin Oncol, 2017. **14**(3): p. 169-186.
28. Jaffe, C.C., *Measures of response: RECIST, WHO, and new alternatives.* J Clin Oncol, 2006. **24**(20): p. 3245-51.
29. Challapalli, A., et al., *18F-ICMT-11, a caspase-3-specific PET tracer for apoptosis: biodistribution and radiation dosimetry.* J Nucl Med, 2013. **54**(9): p. 1551-6.
30. Scabini, M., et al., *In vivo imaging of early stage apoptosis by measuring real-time caspase-3/7 activation.* Apoptosis, 2011. **16**(2): p. 198-207.
31. Zhang, Z., et al., *Activatable molecular systems using homologous near-infrared fluorescent probes for monitoring enzyme activities in vitro, in cellulo, and in vivo.* Mol Pharm, 2009. **6**(2): p. 416-27.
32. McIntyre, D.J., et al., *Magnetic resonance spectroscopy of cancer metabolism and response to therapy.* Radiat Res, 2012. **177**(4): p. 398-435.
33. Buerkle, A. and W.A. Weber, *Imaging of tumor glucose utilization with positron emission tomography.* Cancer Metastasis Rev, 2008. **27**(4): p. 545-54.
34. Afshar-Oromieh, A., et al., *Comparison of PET/CT and PET/MRI hybrid systems using a 68Ga-labelled PSMA ligand for the diagnosis of recurrent prostate cancer: initial experience.* Eur J Nucl Med Mol Imaging, 2014. **41**(5): p. 887-97.
35. Eder, M., et al., *Preclinical evaluation of a bispecific low-molecular heterodimer targeting both PSMA and GRPR for improved PET imaging and therapy of prostate cancer.* Prostate, 2014. **74**(6): p. 659-68.
36. Niu, G., W. Cai, and X. Chen, *Molecular imaging of human epidermal growth factor receptor 2 (HER-2) expression.* Front Biosci, 2008. **13**: p. 790-805.
37. de Herder, W.W., et al., *Neuroendocrine tumors and somatostatin: imaging techniques.* J Endocrinol Invest, 2005. **28**(11 Suppl International): p. 132-6.
38. Deshpande, N., A. Needles, and J.K. Willmann, *Molecular ultrasound imaging: current status and future directions.* Clin Radiol, 2010. **65**(7): p. 567-81.
39. Warburg, O., F. Wind, and E. Negelein, *The Metabolism of Tumors in the Body.* J Gen Physiol, 1927. **8**(6): p. 519-30.
40. Mathupala, S.P., A. Rempel, and P.L. Pedersen, *Aberrant glycolytic metabolism of cancer cells: a remarkable coordination of genetic, transcriptional, post-translational, and mutational events that lead to a critical role for type II hexokinase.* J Bioenerg Biomembr, 1997. **29**(4): p. 339-43.
41. Smith, T.A., *Mammalian hexokinases and their abnormal expression in cancer.* Br J Biomed Sci, 2000. **57**(2): p. 170-8.

42. Shankar, L.K., et al., *Consensus recommendations for the use of 18F-FDG PET as an indicator of therapeutic response in patients in National Cancer Institute Trials.* J Nucl Med, 2006. **47**(6): p. 1059-66.
43. Phelps, M.E., et al., *Tomographic measurement of local cerebral glucose metabolic rate in humans with (F-18)2-fluoro-2-deoxy-D-glucose: validation of method.* Ann Neurol, 1979. **6**(5): p. 371-88.
44. Minn, H. and I. Soini, *[18F]fluorodeoxyglucose scintigraphy in diagnosis and follow up of treatment in advanced breast cancer.* Eur J Nucl Med, 1989. **15**(2): p. 61-6.
45. Mankoff, D.A., et al., *Changes in blood flow and metabolism in locally advanced breast cancer treated with neoadjuvant chemotherapy.* J Nucl Med, 2003. **44**(11): p. 1806-14.
46. Hutchings, M., et al., *FDG-PET after two cycles of chemotherapy predicts treatment failure and progression-free survival in Hodgkin lymphoma.* Blood, 2006. **107**(1): p. 52-9.
47. Krause, B.J., et al., *18F-FDG PET and 18F-FDG PET/CT for assessing response to therapy in esophageal cancer.* J Nucl Med, 2009. **50 Suppl 1**: p. 89S-96S.
48. Cuaron, J., M. Dunphy, and A. Rimner, *Role of FDG-PET scans in staging, response assessment, and follow-up care for non-small cell lung cancer.* Front Oncol, 2012. **2**: p. 208.
49. Hillner, B.E., et al., *The impact of positron emission tomography (PET) on expected management during cancer treatment: findings of the National Oncologic PET Registry.* Cancer, 2009. **115**(2): p. 410-8.
50. Smith, I.C., et al., *Positron emission tomography using [(18)F]-fluorodeoxy-D-glucose to predict the pathologic response of breast cancer to primary chemotherapy.* J Clin Oncol, 2000. **18**(8): p. 1676-88.
51. Romer, W., et al., *Positron emission tomography in non-Hodgkin's lymphoma: assessment of chemotherapy with fluorodeoxyglucose.* Blood, 1998. **91**(12): p. 4464-71.
52. Ott, K., et al., *Metabolic imaging predicts response, survival, and recurrence in adenocarcinomas of the esophagogastric junction.* J Clin Oncol, 2006. **24**(29): p. 4692-8.
53. Yamane, T., et al., *Decreased 18F-FDG uptake 1 day after initiation of chemotherapy for malignant lymphomas.* J Nucl Med, 2004. **45**(11): p. 1838-42.
54. Troost, E.G., et al., *18F-FLT PET/CT for early response monitoring and dose escalation in oropharyngeal tumors.* J Nucl Med, 2010. **51**(6): p. 866-74.
55. Weber, W.A., *Monitoring tumor response to therapy with 18F-FLT PET.* J Nucl Med, 2010. **51**(6): p. 841-4.
56. Barwick, T., et al., *Molecular PET and PET/CT imaging of tumour cell proliferation using F-18 fluoro-L-thymidine: a comprehensive evaluation.* Nucl Med Commun, 2009. **30**(12): p. 908-17.
57. Troost, E.G., et al., *18F-FLT PET does not discriminate between reactive and metastatic lymph nodes in primary head and neck cancer patients.* J Nucl Med, 2007. **48**(5): p. 726-35.
58. Troost, E.G., et al., *18F-FDG and 18F-FLT do not discriminate between reactive and metastatic lymph nodes in oral cancer.* J Nucl Med, 2009. **50**(3): p. 490-1.
59. Cho, S.Y., et al., *Biodistribution, tumor detection, and radiation dosimetry of 18F-DCFBC, a low-molecular-weight inhibitor of prostate-specific membrane antigen, in patients with metastatic prostate cancer.* J Nucl Med, 2012. **53**(12): p. 1883-91.

60. Afshar-Oromieh, A., et al., *PET imaging with a [68Ga]gallium-labelled PSMA ligand for the diagnosis of prostate cancer: biodistribution in humans and first evaluation of tumour lesions.* Eur J Nucl Med Mol Imaging, 2013. **40**(4): p. 486-95.
61. Ambrosini, V., et al., *(6)(8)Ga-labelled peptides for diagnosis of gastroenteropancreatic NET.* Eur J Nucl Med Mol Imaging, 2012. **39 Suppl 1**: p. S52-60.
62. Yap, T.A., et al., *Intratumor heterogeneity: seeing the wood for the trees.* Sci Transl Med, 2012. **4**(127): p. 127ps10.
63. Dehdashti, F., et al., *Assessment of progesterone receptors in breast carcinoma by PET with 21-18F-fluoro-16alpha,17alpha-[(R)-(1'-alpha-furylmethylidene)dioxy]-19-norpregn- 4-ene-3,20-dione.* J Nucl Med, 2012. **53**(3): p. 363-70.
64. Chan, S.R., et al., *Longitudinal noninvasive imaging of progesterone receptor as a predictive biomarker of tumor responsiveness to estrogen deprivation therapy.* Clin Cancer Res, 2015. **21**(5): p. 1063-70.
65. Fowler, A.M., et al., *Imaging Diagnostic and Therapeutic Targets: Steroid Receptors in Breast Cancer.* J Nucl Med, 2016. **57 Suppl 1**: p. 75S-80S.
66. Allott, L., et al., *PET Imaging of Steroid Hormone Receptor Expression.* Mol Imaging, 2015. **14**(10): p. 534-50.
67. Silver, D.A., et al., *Prostate-specific membrane antigen expression in normal and malignant human tissues.* Clin Cancer Res, 1997. **3**(1): p. 81-5.
68. Mannweiler, S., et al., *Heterogeneity of prostate-specific membrane antigen (PSMA) expression in prostate carcinoma with distant metastasis.* Pathol Oncol Res, 2009. **15**(2): p. 167-72.
69. Bostwick, D.G., et al., *Prostate specific membrane antigen expression in prostatic intraepithelial neoplasia and adenocarcinoma: a study of 184 cases.* Cancer, 1998. **82**(11): p. 2256-61.
70. Ross, J.S., et al., *Correlation of primary tumor prostate-specific membrane antigen expression with disease recurrence in prostate cancer.* Clin Cancer Res, 2003. **9**(17): p. 6357-62.
71. Schottelius, M. and H.J. Wester, *Molecular imaging targeting peptide receptors.* Methods, 2009. **48**(2): p. 161-77.
72. Lee, S., J. Xie, and X. Chen, *Peptide-based probes for targeted molecular imaging.* Biochemistry, 2010. **49**(7): p. 1364-76.
73. Britton, K.E., *Towards the goal of cancer-specific imaging and therapy.* Nucl Med Commun, 1997. **18**(11): p. 992-1007.
74. Volkert, W.A. and T.J. Hoffman, *Therapeutic radiopharmaceuticals.* Chem Rev, 1999. **99**(9): p. 2269-92.
75. Joensuu, H. and M. Tenhunen, *Physical and biological targeting of radiotherapy.* Acta Oncol, 1999. **38 Suppl 13**: p. 75-83.
76. Chatal, J.F. and C.A. Hoefnagel, *Radionuclide therapy.* Lancet, 1999. **354**(9182): p. 931-5.
77. Ezziddin, S., et al., *Predictors of long-term outcome in patients with well-differentiated gastroenteropancreatic neuroendocrine tumors after peptide receptor radionuclide therapy with 177Lu-octreotate.* J Nucl Med, 2014. **55**(2): p. 183-90.
78. Ezziddin, S., et al., *Impact of the Ki-67 proliferation index on response to peptide receptor radionuclide therapy.* Eur J Nucl Med Mol Imaging, 2011. **38**(3): p. 459-66.

79. Gudkov, S.V., et al., *Targeted Radionuclide Therapy of Human Tumors.* Int J Mol Sci, 2015. **17**(1).
80. Waser, B., et al., *Highly efficient in vivo agonist-induced internalization of sst2 receptors in somatostatin target tissues.* J Nucl Med, 2009. **50**(6): p. 936-41.
81. Cescato, R., et al., *Internalization of sst2, sst3, and sst5 receptors: effects of somatostatin agonists and antagonists.* J Nucl Med, 2006. **47**(3): p. 502-11.
82. Cescato, R., et al., *Evaluation of 177Lu-DOTA-sst2 antagonist versus 177Lu-DOTA-sst2 agonist binding in human cancers in vitro.* J Nucl Med, 2011. **52**(12): p. 1886-90.
83. Ginj, M., et al., *Radiolabeled somatostatin receptor antagonists are preferable to agonists for in vivo peptide receptor targeting of tumors.* Proc Natl Acad Sci U S A, 2006. **103**(44): p. 16436-41.
84. Cescato, R., et al., *Bombesin receptor antagonists may be preferable to agonists for tumor targeting.* J Nucl Med, 2008. **49**(2): p. 318-26.
85. Gotthardt, M., et al., *Indication for different mechanisms of kidney uptake of radiolabeled peptides.* J Nucl Med, 2007. **48**(4): p. 596-601.
86. Huizing, D.M.V., et al., *Dosimetry methods and clinical applications in peptide receptor radionuclide therapy for neuroendocrine tumours: a literature review.* EJNMMI Res, 2018. **8**(1): p. 89.
87. Damle, N.A., et al., *Discordance in 68Ga-DOTANOC and 177Lu-DOTATATE uptake in diagnostic and post-therapy scans in patients with medullary thyroid cancer-likely reasons.* J Cancer Res Ther, 2013. **9**(4): p. 754-5.
88. Basu, S., et al., *'Reverse discordance' between 68Ga-DOTA-NOC PET/CT and 177Lu-DOTA-TATE posttherapy scan: the plausible explanations and its implications for high-dose therapy with radiolabeled somatostatin receptor analogs.* Nucl Med Commun, 2011. **32**(7): p. 654-8.
89. Wild, D., et al., *Comparison of 68Ga-DOTANOC and 68Ga-DOTATATE PET/CT within patients with gastroenteropancreatic neuroendocrine tumors.* J Nucl Med, 2013. **54**(3): p. 364-72.
90. Kaemmerer, D., et al., *Molecular imaging with (6)(8)Ga-SSTR PET/CT and correlation to immunohistochemistry of somatostatin receptors in neuroendocrine tumours.* Eur J Nucl Med Mol Imaging, 2011. **38**(9): p. 1659-68.
91. Price, E.W. and C. Orvig, *Matching chelators to radiometals for radiopharmaceuticals.* Chem Soc Rev, 2014. **43**(1): p. 260-90.
92. Raghu, G., et al., *An official ATS/ERS/JRS/ALAT statement: idiopathic pulmonary fibrosis: evidence-based guidelines for diagnosis and management.* Am J Respir Crit Care Med, 2011. **183**(6): p. 788-824.
93. American Thoracic, S. and S. European Respiratory, *American Thoracic Society/European Respiratory Society International Multidisciplinary Consensus Classification of the Idiopathic Interstitial Pneumonias. This joint statement of the American Thoracic Society (ATS), and the European Respiratory Society (ERS) was adopted by the ATS board of directors, June 2001 and by the ERS Executive Committee, June 2001.* Am J Respir Crit Care Med, 2002. **165**(2): p. 277-304.
94. Navaratnam, V., et al., *The rising incidence of idiopathic pulmonary fibrosis in the U.K.* Thorax, 2011. **66**(6): p. 462-7.
95. Flaherty, K.R., et al., *Idiopathic interstitial pneumonia: do community and academic physicians agree on diagnosis?* Am J Respir Crit Care Med, 2007. **175**(10): p. 1054-60.
96. Meltzer, E.B. and P.W. Noble, *Idiopathic pulmonary fibrosis.* Orphanet J Rare Dis, 2008. **3**: p. 8.

97. Devaraj, A., *Imaging: how to recognise idiopathic pulmonary fibrosis.* Eur Respir Rev, 2014. **23**(132): p. 215-9.
98. Lamas, D.J., et al., *Delayed access and survival in idiopathic pulmonary fibrosis: a cohort study.* Am J Respir Crit Care Med, 2011. **184**(7): p. 842-7.
99. Wuyts, W.A., et al., *Differential diagnosis of usual interstitial pneumonia: when is it truly idiopathic?* Eur Respir Rev, 2014. **23**(133): p. 308-19.
100. Hansell, D.M., et al., *Fleischner Society: glossary of terms for thoracic imaging.* Radiology, 2008. **246**(3): p. 697-722.
101. Arakawa, H. and K. Honma, *Honeycomb lung: history and current concepts.* AJR Am J Roentgenol, 2011. **196**(4): p. 773-82.
102. Lee, H.Y., et al., *High-resolution CT findings in fibrotic idiopathic interstitial pneumonias with little honeycombing: serial changes and prognostic implications.* AJR Am J Roentgenol, 2012. **199**(5): p. 982-9.
103. Bartholmai, B.J., et al., *Quantitative computed tomography imaging of interstitial lung diseases.* J Thorac Imaging, 2013. **28**(5): p. 298-307.
104. John, A.E., et al., *Preclinical SPECT/CT imaging of alphavbeta6 integrins for molecular stratification of idiopathic pulmonary fibrosis.* J Nucl Med, 2013. **54**(12): p. 2146-52.
105. Desogere, P., et al., *Type I collagen-targeted PET probe for pulmonary fibrosis detection and staging in preclinical models.* Sci Transl Med, 2017. **9**(384).
106. Desogere, P., et al., *Optimization of a Collagen-Targeted PET Probe for Molecular Imaging of Pulmonary Fibrosis.* J Nucl Med, 2017. **58**(12): p. 1991-1996.
107. Hunninghake, G.W., et al., *Utility of a lung biopsy for the diagnosis of idiopathic pulmonary fibrosis.* Am J Respir Crit Care Med, 2001. **164**(2): p. 193-6.
108. Flaherty, K.R., et al., *Idiopathic interstitial pneumonia: what is the effect of a multidisciplinary approach to diagnosis?* Am J Respir Crit Care Med, 2004. **170**(8): p. 904-10.
109. Hutchinson, J., et al., *Global incidence and mortality of idiopathic pulmonary fibrosis: a systematic review.* Eur Respir J, 2015. **46**(3): p. 795-806.
110. Kaarteenaho, R. and V.L. Kinnula, *Diffuse alveolar damage: a common phenomenon in progressive interstitial lung disorders.* Pulm Med, 2011. **2011**: p. 531302.
111. Park, J.H., et al., *Mortality and risk factors for surgical lung biopsy in patients with idiopathic interstitial pneumonia.* Eur J Cardiothorac Surg, 2007. **31**(6): p. 1115-9.
112. Nicholson, A.G., et al., *The relationship between individual histologic features and disease progression in idiopathic pulmonary fibrosis.* Am J Respir Crit Care Med, 2002. **166**(2): p. 173-7.
113. Enomoto, N., et al., *Quantitative analysis of fibroblastic foci in usual interstitial pneumonia.* Chest, 2006. **130**(1): p. 22-9.
114. King, T.E., Jr., et al., *Idiopathic pulmonary fibrosis: relationship between histopathologic features and mortality.* Am J Respir Crit Care Med, 2001. **164**(6): p. 1025-32.
115. Lee, S.H., et al., *Prognostic factors for idiopathic pulmonary fibrosis: clinical, physiologic, pathologic, and molecular aspects.* Sarcoidosis Vasc Diffuse Lung Dis, 2011. **28**(2): p. 102-12.
116. Hanak, V., et al., *Profusion of fibroblast foci in patients with idiopathic pulmonary fibrosis does not predict outcome.* Respir Med, 2008. **102**(6): p. 852-6.

117. Baumgartner, K.B., et al., *Occupational and environmental risk factors for idiopathic pulmonary fibrosis: a multicenter case-control study. Collaborating Centers.* Am J Epidemiol, 2000. **152**(4): p. 307-15.
118. Steele, M.P., et al., *Clinical and pathologic features of familial interstitial pneumonia.* Am J Respir Crit Care Med, 2005. **172**(9): p. 1146-52.
119. Renzoni, E., V. Srihari, and P. Sestini, *Pathogenesis of idiopathic pulmonary fibrosis: review of recent findings.* F1000Prime Rep, 2014. **6**: p. 69.
120. Brown, A.W., H. Kaya, and S.D. Nathan, *Lung transplantation in IIP: A review.* Respirology, 2016. **21**(7): p. 1173-84.
121. Weill, D., et al., *A consensus document for the selection of lung transplant candidates: 2014--an update from the Pulmonary Transplantation Council of the International Society for Heart and Lung Transplantation.* J Heart Lung Transplant, 2015. **34**(1): p. 1-15.
122. Barberis, M., et al., *Recurrence of primary disease in a single lung transplant recipient.* Transplant Proc, 1992. **24**(6): p. 2660-2.
123. Idiopathic Pulmonary Fibrosis Clinical Research, N., et al., *Randomized trial of acetylcysteine in idiopathic pulmonary fibrosis.* N Engl J Med, 2014. **370**(22): p. 2093-101.
124. Raghu, G., et al., *Prednisone, azathioprine, and N-acetylcysteine for pulmonary fibrosis.* N Engl J Med, 2012. **366**(21): p. 1968-77.
125. King, T.E., Jr., et al., *A phase 3 trial of pirfenidone in patients with idiopathic pulmonary fibrosis.* N Engl J Med, 2014. **370**(22): p. 2083-92.
126. Hirano, A., et al., *Pirfenidone modulates airway responsiveness, inflammation, and remodeling after repeated challenge.* Am J Respir Cell Mol Biol, 2006. **35**(3): p. 366-77.
127. Iyer, S.N., G. Gurujeyalakshmi, and S.N. Giri, *Effects of pirfenidone on transforming growth factor-beta gene expression at the transcriptional level in bleomycin hamster model of lung fibrosis.* J Pharmacol Exp Ther, 1999. **291**(1): p. 367-73.
128. Nakazato, H., et al., *A novel anti-fibrotic agent pirfenidone suppresses tumor necrosis factor-alpha at the translational level.* Eur J Pharmacol, 2002. **446**(1-3): p. 177-85.
129. Oku, H., et al., *Antifibrotic action of pirfenidone and prednisolone: different effects on pulmonary cytokines and growth factors in bleomycin-induced murine pulmonary fibrosis.* Eur J Pharmacol, 2008. **590**(1-3): p. 400-8.
130. Iyer, S.N., G. Gurujeyalakshmi, and S.N. Giri, *Effects of pirfenidone on procollagen gene expression at the transcriptional level in bleomycin hamster model of lung fibrosis.* J Pharmacol Exp Ther, 1999. **289**(1): p. 211-8.
131. Noble, P.W., et al., *Pirfenidone in patients with idiopathic pulmonary fibrosis (CAPACITY): two randomised trials.* Lancet, 2011. **377**(9779): p. 1760-9.
132. Raghu, G., et al., *An Official ATS/ERS/JRS/ALAT Clinical Practice Guideline: Treatment of Idiopathic Pulmonary Fibrosis. An Update of the 2011 Clinical Practice Guideline.* Am J Respir Crit Care Med, 2015. **192**(2): p. e3-19.
133. Wollin, L., et al., *Mode of action of nintedanib in the treatment of idiopathic pulmonary fibrosis.* Eur Respir J, 2015. **45**(5): p. 1434-45.
134. Hostettler, K.E., et al., *Anti-fibrotic effects of nintedanib in lung fibroblasts derived from patients with idiopathic pulmonary fibrosis.* Respir Res, 2014. **15**: p. 157.

135. Wollin, L., et al., *Antifibrotic and anti-inflammatory activity of the tyrosine kinase inhibitor nintedanib in experimental models of lung fibrosis.* J Pharmacol Exp Ther, 2014. **349**(2): p. 209-20.
136. Collard, H.R., et al., *Acute exacerbations of idiopathic pulmonary fibrosis.* Am J Respir Crit Care Med, 2007. **176**(7): p. 636-43.
137. Collard, H.R., et al., *Acute exacerbations in the INPULSIS trials of nintedanib in idiopathic pulmonary fibrosis.* Eur Respir J, 2017. **49**(5).
138. Ley, B., H.R. Collard, and T.E. King, Jr., *Clinical course and prediction of survival in idiopathic pulmonary fibrosis.* Am J Respir Crit Care Med, 2011. **183**(4): p. 431-40.
139. Jenkins, R.G., et al., *Longitudinal change in collagen degradation biomarkers in idiopathic pulmonary fibrosis: an analysis from the prospective, multicentre PROFILE study.* Lancet Respir Med, 2015. **3**(6): p. 462-72.
140. Gross, T.J. and G.W. Hunninghake, *Idiopathic pulmonary fibrosis.* N Engl J Med, 2001. **345**(7): p. 517-25.
141. Raghu, G., et al., *Incidence and prevalence of idiopathic pulmonary fibrosis.* Am J Respir Crit Care Med, 2006. **174**(7): p. 810-6.
142. Meissner, H.H., et al., *Idiopathic pulmonary fibrosis: evaluation with positron emission tomography.* Respiration, 2006. **73**(2): p. 197-202.
143. Ambrosini, V., et al., *68Ga-DOTANOC PET/CT allows somatostatin receptor imaging in idiopathic pulmonary fibrosis: preliminary results.* J Nucl Med, 2010. **51**(12): p. 1950-5.
144. Win, T., et al., *Novel positron emission tomography/computed tomography of diffuse parenchymal lung disease combining a labeled somatostatin receptor analogue and 2-deoxy-2[18F]fluoro-D-glucose.* Mol Imaging, 2012. **11**(2): p. 91-8.
145. Flaherty, K.R., et al., *Clinical significance of histological classification of idiopathic interstitial pneumonia.* Eur Respir J, 2002. **19**(2): p. 275-83.
146. Katzenstein, A.L. and J.L. Myers, *Idiopathic pulmonary fibrosis: clinical relevance of pathologic classification.* Am J Respir Crit Care Med, 1998. **157**(4 Pt 1): p. 1301-15.
147. Goodman, S.L. and M. Picard, *Integrins as therapeutic targets.* Trends Pharmacol Sci, 2012. **33**(7): p. 405-12.
148. Goodwin, A. and G. Jenkins, *Role of integrin-mediated TGFbeta activation in the pathogenesis of pulmonary fibrosis.* Biochem Soc Trans, 2009. **37**(Pt 4): p. 849-54.
149. Xu, M.Y., et al., *Lysophosphatidic acid induces alphavbeta6 integrin-mediated TGF-beta activation via the LPA2 receptor and the small G protein G alpha(q).* Am J Pathol, 2009. **174**(4): p. 1264-79.
150. Shu, H.K., et al., *Inhibition of the CXCL12/CXCR4-axis as preventive therapy for radiation-induced pulmonary fibrosis.* PLoS One, 2013. **8**(11): p. e79768.
151. Song, J.S., et al., *Inhibitory effect of CXC chemokine receptor 4 antagonist AMD3100 on bleomycin induced murine pulmonary fibrosis.* Exp Mol Med, 2010. **42**(6): p. 465-72.
152. Prasse, A., et al., *Molecular Imaging of CXCR4 by Gallium-68-Pentixafor PET in Patients with Idiopathic Pulmonary Fibrosis Treated with Pirfenidone.* Am J Respir Crit Care Med, 2017. **195**: p. A7678.
153. Reimann, C., et al., *Contrast-Enhanced Magnetic Resonance Angiography Using a Novel Elastin-Specific Molecular Probe in an Experimental Animal Model.* Contrast Media Mol Imaging, 2018. **2018**: p. 9217456.

154. Upagupta, C., et al., *Matrix abnormalities in pulmonary fibrosis.* Eur Respir Rev, 2018. **27**(148).
155. Lever, S.Z., K.H. Fan, and J.R. Lever, *Tactics for preclinical validation of receptor-binding radiotracers.* Nucl Med Biol, 2017. **44**: p. 4-30.
156. Sharma, R. and E. Aboagye, *Development of radiotracers for oncology--the interface with pharmacology.* Br J Pharmacol, 2011. **163**(8): p. 1565-85.
157. Rankovic, Z., *CNS drug design: balancing physicochemical properties for optimal brain exposure.* J Med Chem, 2015. **58**(6): p. 2584-608.
158. Waterhouse, R.N., *Determination of lipophilicity and its use as a predictor of blood-brain barrier penetration of molecular imaging agents.* Mol Imaging Biol, 2003. **5**(6): p. 376-89.
159. Pajouhesh, H. and G.R. Lenz, *Medicinal chemical properties of successful central nervous system drugs.* NeuroRx, 2005. **2**(4): p. 541-53.
160. Coenen, H.H., et al., *Consensus nomenclature rules for radiopharmaceutical chemistry - Setting the record straight.* Nucl Med Biol, 2017. **55**: p. v-xi.
161. Grady, E.F., et al., *Direct observation of endocytosis of gastrin releasing peptide and its receptor.* J Biol Chem, 1995. **270**(9): p. 4603-11.
162. Simaan, M., et al., *Dissociation of beta-arrestin from internalized bradykinin B2 receptor is necessary for receptor recycling and resensitization.* Cell Signal, 2005. **17**(9): p. 1074-83.
163. Vines, C.M., et al., *N-formyl peptide receptors internalize but do not recycle in the absence of arrestins.* J Biol Chem, 2003. **278**(43): p. 41581-4.
164. De Silva, R.A., et al., *Imaging CXCR4 expression in human cancer xenografts: evaluation of monocyclam 64Cu-AMD3465.* J Nucl Med, 2011. **52**(6): p. 986-93.
165. Gandomkar, M., et al., *Preclinical evaluation of [99mTc/EDDA/tricine/HYNIC0, 1-Nal3, Thr8]-octreotide as a new analogue in the detection of somatostatin-receptor-positive tumors.* Nucl Med Biol, 2007. **34**(6): p. 651-7.
166. Eckelman, W.C., et al., *Receptor-binding radiotracers: a class of potential radiopharmaceuticals.* J Nucl Med, 1979. **20**(4): p. 350-7.
167. Maguire, J.J., R.E. Kuc, and A.P. Davenport, *Radioligand binding assays and their analysis.* Methods Mol Biol, 2012. **897**: p. 31-77.
168. Motulsky, H.J. and R.R. Neubig, *Analyzing binding data.* Curr Protoc Neurosci, 2010. **Chapter 7**: p. Unit 7 5.
169. Hulme, E.C. and M.A. Trevethick, *Ligand binding assays at equilibrium: validation and interpretation.* Br J Pharmacol, 2010. **161**(6): p. 1219-37.
170. Bylund, D.B. and M.L. Toews, *Radioligand binding methods: practical guide and tips.* Am J Physiol, 1993. **265**(5 Pt 1): p. L421-9.
171. Baldessarini, R.J., et al., *Prolonged D2 antidopaminergic activity of alkylating and nonalkylating derivatives of spiperone in rat brain.* Mol Pharmacol, 1992. **42**(5): p. 856-63.
172. Lyon, R.A., et al., *3H-3-N-methylspiperone labels D2 dopamine receptors in basal ganglia and S2 serotonin receptors in cerebral cortex.* J Neurosci, 1986. **6**(10): p. 2941-9.
173. Doot, R.K., et al., *Selectivity of probes for PET imaging of dopamine D3 receptors.* Neurosci Lett, 2018.
174. Luedtke, R.R., et al., *Bitropic D3 Dopamine Receptor Selective Compounds as Potential Antipsychotics.* Curr Pharm Des, 2015. **21**(26): p. 3700-24.
175. Luedtkea, R.R. and R.H. Mach, *Progress in developing D3 dopamine receptor ligands as potential therapeutic agents for neurological and neuropsychiatric disorders.* Curr Pharm Des, 2003. **9**(8): p. 643-71.

176. Laruelle, M., M. Slifstein, and Y. Huang, *Relationships between radiotracer properties and image quality in molecular imaging of the brain with positron emission tomography.* Mol Imaging Biol, 2003. **5**(6): p. 363-75.
177. Slifstein, M., et al., *In vivo affinity of [18F]fallypride for striatal and extrastriatal dopamine D2 receptors in nonhuman primates.* Psychopharmacology (Berl), 2004. **175**(3): p. 274-86.
178. Kopp, J., et al., *Temperature dependence of [3H]Ro 15-1788 binding to benzodiazepine receptors in human postmortem brain homogenates.* J Neurochem, 1990. **55**(4): p. 1310-5.
179. Zoghbi, S.S., et al., *PET imaging of the dopamine transporter with 18F-FECNT: a polar radiometabolite confounds brain radioligand measurements.* J Nucl Med, 2006. **47**(3): p. 520-7.
180. Welman, A., et al., *Increases in c-Src expression level and activity do not promote the growth of human colorectal carcinoma cells in vitro and in vivo.* Neoplasia, 2006. **8**(11): p. 905-16.
181. Maetzig, T., et al., *All-in-One inducible lentiviral vector systems based on drug controlled FLP recombinase.* Biomaterials, 2014. **35**(14): p. 4345-56.
182. Leurquin-Sterk, G., et al., *What We Observe In Vivo Is Not Always What We See In Vitro: Development and Validation of 11C-JNJ-42491293, A Novel Radioligand for mGluR2.* J Nucl Med, 2017. **58**(1): p. 110-116.
183. Goertzen, A.L., et al., *NEMA NU 4-2008 comparison of preclinical PET imaging systems.* J Nucl Med, 2012. **53**(8): p. 1300-9.
184. Hume, S.P., R.N. Gunn, and T. Jones, *Pharmacological constraints associated with positron emission tomographic scanning of small laboratory animals.* Eur J Nucl Med, 1998. **25**(2): p. 173-6.
185. Liu, H., et al., *Molecular imaging of integrin alphavbeta6 expression in living subjects.* Am J Nucl Med Mol Imaging, 2014. **4**(4): p. 333-45.
186. Hynes, R.O., *Integrins: bidirectional, allosteric signaling machines.* Cell, 2002. **110**(6): p. 673-87.
187. Takada, Y., X. Ye, and S. Simon, *The integrins.* Genome Biol, 2007. **8**(5): p. 215.
188. Hall, E.R., L.I. Bibby, and R.J. Slack, *Characterisation of a novel, high affinity and selective alphavbeta6 integrin RGD-mimetic radioligand.* Biochem Pharmacol, 2016. **117**: p. 88-96.
189. Alam, I.S., et al., *Radiolabeled RGD tracer kinetics annotates differential alphavbeta 3 integrin expression linked to cell intrinsic and vessel expression.* Mol Imaging Biol, 2014. **16**(4): p. 558-66.
190. Kraft, S., et al., *Definition of an unexpected ligand recognition motif for alphav beta6 integrin.* J Biol Chem, 1999. **274**(4): p. 1979-85.
191. Maltsev, O.V., et al., *Stable Peptides Instead of Stapled Peptides: Highly Potent alphavbeta6-Selective Integrin Ligands.* Angew Chem Int Ed Engl, 2016. **55**(4): p. 1535-9.
192. Brakebusch, C., et al., *Integrins in invasive growth.* J Clin Invest, 2002. **109**(8): p. 999-1006.
193. Guo, W. and F.G. Giancotti, *Integrin signalling during tumour progression.* Nat Rev Mol Cell Biol, 2004. **5**(10): p. 816-26.
194. Ramos, D.M., et al., *Expression of integrin beta 6 enhances invasive behavior in oral squamous cell carcinoma.* Matrix Biol, 2002. **21**(3): p. 297-307.
195. Arihiro, K., et al., *Significance of alpha 9 beta 1 and alpha v beta 6 integrin expression in breast carcinoma.* Breast Cancer, 2000. **7**(1): p. 19-26.

196. Zhang, Z.Y., et al., *Integrin alphanvbeta6 acts as a prognostic indicator in gastric carcinoma.* Clin Oncol (R Coll Radiol), 2008. **20**(1): p. 61-6.
197. Kawashima, A., et al., *Expression of alphav integrin family in gastric carcinomas: increased alphavbeta6 is associated with lymph node metastasis.* Pathol Res Pract, 2003. **199**(2): p. 57-64.
198. Sipos, B., et al., *Immunohistochemical screening for beta6-integrin subunit expression in adenocarcinomas using a novel monoclonal antibody reveals strong up-regulation in pancreatic ductal adenocarcinomas in vivo and in vitro.* Histopathology, 2004. **45**(3): p. 226-36.
199. Bates, R.C., et al., *Transcriptional activation of integrin beta6 during the epithelial-mesenchymal transition defines a novel prognostic indicator of aggressive colon carcinoma.* J Clin Invest, 2005. **115**(2): p. 339-47.
200. Elayadi, A.N., et al., *A peptide selected by biopanning identifies the integrin alphavbeta6 as a prognostic biomarker for nonsmall cell lung cancer.* Cancer Res, 2007. **67**(12): p. 5889-95.
201. Thomas, G.J., M.L. Nystrom, and J.F. Marshall, *Alphavbeta6 integrin in wound healing and cancer of the oral cavity.* J Oral Pathol Med, 2006. **35**(1): p. 1-10.
202. Regezi, J.A., et al., *Tenascin and beta 6 integrin are overexpressed in floor of mouth in situ carcinomas and invasive squamous cell carcinomas.* Oral Oncol, 2002. **38**(4): p. 332-6.
203. Sheppard, D., *Integrin-mediated activation of latent transforming growth factor beta.* Cancer Metastasis Rev, 2005. **24**(3): p. 395-402.
204. Ramos, D.M., D. Dang, and S. Sadler, *The role of the integrin alpha v beta6 in regulating the epithelial to mesenchymal transition in oral cancer.* Anticancer Res, 2009. **29**(1): p. 125-30.
205. Van Aarsen, L.A., et al., *Antibody-mediated blockade of integrin alpha v beta 6 inhibits tumor progression in vivo by a transforming growth factor-beta-regulated mechanism.* Cancer Res, 2008. **68**(2): p. 561-70.
206. Ramsay, A.G., et al., *HS1-associated protein X-1 regulates carcinoma cell migration and invasion via clathrin-mediated endocytosis of integrin alphavbeta6.* Cancer Res, 2007. **67**(11): p. 5275-84.
207. Lanzetti, L. and P.P. Di Fiore, *Endocytosis and cancer: an 'insider' network with dangerous liaisons.* Traffic, 2008. **9**(12): p. 2011-21.
208. Mignogna, M.D., S. Fedele, and L. Lo Russo, *The World Cancer Report and the burden of oral cancer.* Eur J Cancer Prev, 2004. **13**(2): p. 139-42.
209. Neville, B.W. and T.A. Day, *Oral cancer and precancerous lesions.* CA Cancer J Clin, 2002. **52**(4): p. 195-215.
210. Westernoff, T.H., et al., *Beta-6 Integrin, tenascin-C, and MMP-1 expression in salivary gland neoplasms.* Oral Oncol, 2005. **41**(2): p. 170-4.
211. Hamidi, S., et al., *Expression of alpha(v)beta6 integrin in oral leukoplakia.* Br J Cancer, 2000. **82**(8): p. 1433-40.
212. Hsiao, J.R., et al., *Cyclic alphavbeta6-targeting peptide selected from biopanning with clinical potential for head and neck squamous cell carcinoma.* Head Neck, 2010. **32**(2): p. 160-72.
213. Mateu, M.G., et al., *Systematic replacement of amino acid residues within an Arg-Gly-Asp-containing loop of foot-and-mouth disease virus and effect on cell recognition.* J Biol Chem, 1996. **271**(22): p. 12814-9.
214. O'Donnell, V., et al., *Analysis of foot-and-mouth disease virus internalization events in cultured cells.* J Virol, 2005. **79**(13): p. 8506-18.

215. Duque, H. and B. Baxt, *Foot-and-mouth disease virus receptors: comparison of bovine alpha(V) integrin utilization by type A and O viruses.* J Virol, 2003. **77**(4): p. 2500-11.
216. Jackson, T., et al., *The epithelial integrin alphavbeta6 is a receptor for foot-and-mouth disease virus.* J Virol, 2000. **74**(11): p. 4949-56.
217. van der Pluijm, G., et al., *Bone sialoprotein peptides are potent inhibitors of breast cancer cell adhesion to bone.* Cancer Res, 1996. **56**(8): p. 1948-55.
218. Humphrey, J.M. and A.R. Chamberlin, *Chemical Synthesis of Natural Product Peptides: Coupling Methods for the Incorporation of Noncoded Amino Acids into Peptides.* Chem Rev, 1997. **97**(6): p. 2243-2266.
219. Metcalfe, K., et al., *Family history of cancer and cancer risks in women with BRCA1 or BRCA2 mutations.* J Natl Cancer Inst, 2010. **102**(24): p. 1874-8.
220. Prat, A., et al., *Phenotypic and molecular characterization of the claudin-low intrinsic subtype of breast cancer.* Breast Cancer Res, 2010. **12**(5): p. R68.
221. Perou, C.M., et al., *Molecular portraits of human breast tumours.* Nature, 2000. **406**(6797): p. 747-52.
222. Ronnov-Jessen, L., O.W. Petersen, and M.J. Bissell, *Cellular changes involved in conversion of normal to malignant breast: importance of the stromal reaction.* Physiol Rev, 1996. **76**(1): p. 69-125.
223. Cervino, A.R., et al., *Molecular pathways and molecular imaging in breast cancer: an update.* Nucl Med Biol, 2013. **40**(5): p. 581-91.
224. Slamon, D.J., et al., *Studies of the HER-2/neu proto-oncogene in human breast and ovarian cancer.* Science, 1989. **244**(4905): p. 707-12.
225. Slamon, D.J., et al., *Human breast cancer: correlation of relapse and survival with amplification of the HER-2/neu oncogene.* Science, 1987. **235**(4785): p. 177-82.
226. Romond, E.H., et al., *Trastuzumab plus adjuvant chemotherapy for operable HER2-positive breast cancer.* N Engl J Med, 2005. **353**(16): p. 1673-84.
227. Piccart-Gebhart, M.J., et al., *Trastuzumab after adjuvant chemotherapy in HER2-positive breast cancer.* N Engl J Med, 2005. **353**(16): p. 1659-72.
228. Arribas, J., et al., *p95HER2 and breast cancer.* Cancer Res, 2011. **71**(5): p. 1515-9.
229. Muraoka, R.S., et al., *Increased malignancy of Neu-induced mammary tumors overexpressing active transforming growth factor beta1.* Mol Cell Biol, 2003. **23**(23): p. 8691-703.
230. Wang, S.E., et al., *HER2/Neu (ErbB2) signaling to Rac1-Pak1 is temporally and spatially modulated by transforming growth factor beta.* Cancer Res, 2006. **66**(19): p. 9591-600.
231. Ueda, Y., et al., *Overexpression of HER2 (erbB2) in human breast epithelial cells unmasks transforming growth factor beta-induced cell motility.* J Biol Chem, 2004. **279**(23): p. 24505-13.
232. Munger, J.S., et al., *The integrin alpha v beta 6 binds and activates latent TGF beta 1: a mechanism for regulating pulmonary inflammation and fibrosis.* Cell, 1999. **96**(3): p. 319-28.
233. Allen, M.D., et al., *Altered microenvironment promotes progression of preinvasive breast cancer: myoepithelial expression of alphavbeta6 integrin in DCIS identifies high-risk patients and predicts recurrence.* Clin Cancer Res, 2014. **20**(2): p. 344-57.
234. Moore, K.M., et al., *Therapeutic targeting of integrin alphavbeta6 in breast cancer.* J Natl Cancer Inst, 2014. **106**(8).

235. Hazelbag, S., et al., *Overexpression of the alpha v beta 6 integrin in cervical squamous cell carcinoma is a prognostic factor for decreased survival.* J Pathol, 2007. **212**(3): p. 316-24.
236. Puthawala, K., et al., *Inhibition of integrin alpha(v)beta6, an activator of latent transforming growth factor-beta, prevents radiation-induced lung fibrosis.* Am J Respir Crit Care Med, 2008. **177**(1): p. 82-90.
237. Huang, X., et al., *Expression of the human integrin beta6 subunit in alveolar type II cells and bronchiolar epithelial cells reverses lung inflammation in beta6 knockout mice.* Am J Respir Cell Mol Biol, 1998. **19**(4): p. 636-42.
238. Ramesh, S., G.M. Wildey, and P.H. Howe, *Transforming growth factor beta (TGFbeta)-induced apoptosis: the rise & fall of Bim.* Cell Cycle, 2009. **8**(1): p. 11-7.
239. Prud'homme, G.J., *Pathobiology of transforming growth factor beta in cancer, fibrosis and immunologic disease, and therapeutic considerations.* Lab Invest, 2007. **87**(11): p. 1077-91.
240. Tatler, A.L. and G. Jenkins, *TGF-beta activation and lung fibrosis.* Proc Am Thorac Soc, 2012. **9**(3): p. 130-6.
241. Yang, Z., et al., *Absence of integrin-mediated TGFbeta1 activation in vivo recapitulates the phenotype of TGFbeta1-null mice.* J Cell Biol, 2007. **176**(6): p. 787-93.
242. Jenkins, R.G., et al., *Ligation of protease-activated receptor 1 enhances alpha(v)beta6 integrin-dependent TGF-beta activation and promotes acute lung injury.* J Clin Invest, 2006. **116**(6): p. 1606-14.
243. Zlotnik, A., O. Yoshie, and H. Nomiyama, *The chemokine and chemokine receptor superfamilies and their molecular evolution.* Genome Biol, 2006. **7**(12): p. 243.
244. Balabanian, K., et al., *The chemokine SDF-1/CXCL12 binds to and signals through the orphan receptor RDC1 in T lymphocytes.* J Biol Chem, 2005. **280**(42): p. 35760-6.
245. Wright, L.M., et al., *Stromal cell-derived factor-1 binding to its chemokine receptor CXCR4 on precursor cells promotes the chemotactic recruitment, development and survival of human osteoclasts.* Bone, 2005. **36**(5): p. 840-53.
246. Petit, I., et al., *Atypical PKC-zeta regulates SDF-1-mediated migration and development of human CD34+ progenitor cells.* J Clin Invest, 2005. **115**(1): p. 168-76.
247. Narducci, M.G., et al., *Skin homing of Sezary cells involves SDF-1-CXCR4 signaling and down-regulation of CD26/dipeptidylpeptidase IV.* Blood, 2006. **107**(3): p. 1108-15.
248. Vianello, F., et al., *A CXCR4-dependent chemorepellent signal contributes to the emigration of mature single-positive CD4 cells from the fetal thymus.* J Immunol, 2005. **175**(8): p. 5115-25.
249. Dar, A., et al., *Chemokine receptor CXCR4-dependent internalization and resecretion of functional chemokine SDF-1 by bone marrow endothelial and stromal cells.* Nat Immunol, 2005. **6**(10): p. 1038-46.
250. Teicher, B.A. and S.P. Fricker, *CXCL12 (SDF-1)/CXCR4 pathway in cancer.* Clin Cancer Res, 2010. **16**(11): p. 2927-31.
251. Zou, Y.R., et al., *Function of the chemokine receptor CXCR4 in haematopoiesis and in cerebellar development.* Nature, 1998. **393**(6685): p. 595-9.
252. Ma, Q., et al., *Impaired B-lymphopoiesis, myelopoiesis, and derailed cerebellar neuron migration in CXCR4- and SDF-1-deficient mice.* Proc Natl Acad Sci U S A, 1998. **95**(16): p. 9448-53.

253. Redjal, N., et al., *CXCR4 inhibition synergizes with cytotoxic chemotherapy in gliomas.* Clin Cancer Res, 2006. **12**(22): p. 6765-71.
254. Balkwill, F., *The significance of cancer cell expression of the chemokine receptor CXCR4.* Semin Cancer Biol, 2004. **14**(3): p. 171-9.
255. Yoon, Y., et al., *CXC chemokine receptor-4 antagonist blocks both growth of primary tumor and metastasis of head and neck cancer in xenograft mouse models.* Cancer Res, 2007. **67**(15): p. 7518-24.
256. Taichman, R.S., et al., *Use of the stromal cell-derived factor-1/CXCR4 pathway in prostate cancer metastasis to bone.* Cancer Res, 2002. **62**(6): p. 1832-7.
257. Burger, J.A. and T.J. Kipps, *CXCR4: a key receptor in the crosstalk between tumor cells and their microenvironment.* Blood, 2006. **107**(5): p. 1761-7.
258. Horuk, R. and A.E. Proudfoot, *Drug discovery targeting the chemokine system--where are we?* Front Biosci (Elite Ed), 2009. **1**: p. 209-19.
259. Singh, B., et al., *Evaluation of a CXCR4 antagonist in a xenograft mouse model of inflammatory breast cancer.* Clin Exp Metastasis, 2010. **27**(4): p. 233-40.
260. Porvasnik, S., et al., *Effects of CXCR4 antagonist CTCE-9908 on prostate tumor growth.* Prostate, 2009. **69**(13): p. 1460-9.
261. Azab, A.K., et al., *CXCR4 inhibitor AMD3100 disrupts the interaction of multiple myeloma cells with the bone marrow microenvironment and enhances their sensitivity to therapy.* Blood, 2009. **113**(18): p. 4341-51.
262. Marechal, R., et al., *High expression of CXCR4 may predict poor survival in resected pancreatic adenocarcinoma.* Br J Cancer, 2009. **100**(9): p. 1444-51.
263. Akashi, T., et al., *Chemokine receptor CXCR4 expression and prognosis in patients with metastatic prostate cancer.* Cancer Sci, 2008. **99**(3): p. 539-42.
264. Lee, H.J., et al., *Chemokine receptor CXCR4 expression, function, and clinical implications in gastric cancer.* Int J Oncol, 2009. **34**(2): p. 473-80.
265. Otsuka, S., et al., *CXCR4 overexpression is associated with poor outcome in females diagnosed with stage IV non-small cell lung cancer.* J Thorac Oncol, 2011. **6**(7): p. 1169-78.
266. Holm, N.T., et al., *Elevated levels of chemokine receptor CXCR4 in HER-2 negative breast cancer specimens predict recurrence.* J Surg Res, 2007. **141**(1): p. 53-9.
267. Liu, Y., et al., *Correlation effect of EGFR and CXCR4 and CCR7 chemokine receptors in predicting breast cancer metastasis and prognosis.* J Exp Clin Cancer Res, 2010. **29**: p. 16.
268. Yang-Hartwich, Y., et al., *Ovulation and extra-ovarian origin of ovarian cancer.* Sci Rep, 2014. **4**: p. 6116.
269. Duda, D.G., et al., *CXCL12 (SDF1alpha)-CXCR4/CXCR7 pathway inhibition: an emerging sensitizer for anticancer therapies?* Clin Cancer Res, 2011. **17**(8): p. 2074-80.
270. Thomas, R.M., et al., *The chemokine receptor CXCR4 is expressed in pancreatic intraepithelial neoplasia.* Gut, 2008. **57**(11): p. 1555-60.
271. Porcile, C., et al., *CXCR4 activation induces epidermal growth factor receptor transactivation in an ovarian cancer cell line.* Ann N Y Acad Sci, 2004. **1030**: p. 162-9.
272. Porcile, C., et al., *Stromal cell-derived factor-1alpha (SDF-1alpha/CXCL12) stimulates ovarian cancer cell growth through the EGF receptor transactivation.* Exp Cell Res, 2005. **308**(2): p. 241-53.
273. Heinrich, E.L., et al., *Chemokine CXCL12 activates dual CXCR4 and CXCR7-mediated signaling pathways in pancreatic cancer cells.* J Transl Med, 2012. **10**: p. 68.

274. Guo, Q., et al., *[Relationship between chemokine axis CXCL12-CXCR4 and epithelial ovarian cancer].* Zhonghua Yi Xue Za Zhi, 2013. **93**(21): p. 1677-80.
275. Righi, E., et al., *CXCL12/CXCR4 blockade induces multimodal antitumor effects that prolong survival in an immunocompetent mouse model of ovarian cancer.* Cancer Res, 2011. **71**(16): p. 5522-5534.
276. Ray, P., et al., *Noninvasive imaging reveals inhibition of ovarian cancer by targeting CXCL12-CXCR4.* Neoplasia, 2011. **13**(12): p. 1152-61.
277. Kajiyama, H., et al., *Involvement of SDF-1alpha/CXCR4 axis in the enhanced peritoneal metastasis of epithelial ovarian carcinoma.* Int J Cancer, 2008. **122**(1): p. 91-9.
278. Zeng, Z., et al., *Targeting the leukemia microenvironment by CXCR4 inhibition overcomes resistance to kinase inhibitors and chemotherapy in AML.* Blood, 2009. **113**(24): p. 6215-24.
279. Smith, M.C., et al., *CXCR4 regulates growth of both primary and metastatic breast cancer.* Cancer Res, 2004. **64**(23): p. 8604-12.
280. Kwong, J., et al., *An antagonist of the chemokine receptor CXCR4 induces mitotic catastrophe in ovarian cancer cells.* Mol Cancer Ther, 2009. **8**(7): p. 1893-905.
281. Xu, L., et al., *Direct evidence that bevacizumab, an anti-VEGF antibody, up-regulates SDF1alpha, CXCR4, CXCL6, and neuropilin 1 in tumors from patients with rectal cancer.* Cancer Res, 2009. **69**(20): p. 7905-10.
282. Shaked, Y., et al., *Rapid chemotherapy-induced acute endothelial progenitor cell mobilization: implications for antiangiogenic drugs as chemosensitizing agents.* Cancer Cell, 2008. **14**(3): p. 263-73.
283. Welschinger, R., et al., *Plerixafor (AMD3100) induces prolonged mobilization of acute lymphoblastic leukemia cells and increases the proportion of cycling cells in the blood in mice.* Exp Hematol, 2013. **41**(3): p. 293-302 e1.
284. Salomonnson, E., et al., *Imaging CXCL12-CXCR4 signaling in ovarian cancer therapy.* PLoS One, 2013. **8**(1): p. e51500.
285. Ratajczak, M.Z., et al., *Induction of a tumor-metastasis-receptive microenvironment as an unwanted and underestimated side effect of treatment by chemotherapy or radiotherapy.* J Ovarian Res, 2013. **6**(1): p. 95.
286. Hernandez, L., et al., *Opposing roles of CXCR4 and CXCR7 in breast cancer metastasis.* Breast Cancer Res, 2011. **13**(6): p. R128.
287. Cappellari, R., et al., *Plerixafor improves the endothelial health balance. The effect of diabetes analysed by polychromatic flow cytometry.* Atherosclerosis, 2016. **251**: p. 373-380.
288. Scala, S., et al., *Expression of CXCR4 predicts poor prognosis in patients with malignant melanoma.* Clin Cancer Res, 2005. **11**(5): p. 1835-41.
289. Herhaus, P., et al., *Targeted positron emission tomography imaging of CXCR4 expression in patients with acute myeloid leukemia.* Haematologica, 2016. **101**(8): p. 932-40.
290. Rubin, J.B., et al., *A small-molecule antagonist of CXCR4 inhibits intracranial growth of primary brain tumors.* Proc Natl Acad Sci U S A, 2003. **100**(23): p. 13513-8.
291. Scotton, C.J., et al., *Multiple actions of the chemokine CXCL12 on epithelial tumor cells in human ovarian cancer.* Cancer Res, 2002. **62**(20): p. 5930-8.
292. Berning, P., et al., *The CXCR4 antagonist plerixafor (AMD3100) promotes proliferation of Ewing sarcoma cell lines in vitro and activates receptor tyrosine kinase signaling.* Cell Commun Signal, 2018. **16**(1): p. 21.

293. Morimoto, M., et al., *Enhancement of the CXCL12/CXCR4 axis due to acquisition of gemcitabine resistance in pancreatic cancer: effect of CXCR4 antagonists.* BMC Cancer, 2016. **16**: p. 305.
294. Wang, Y., et al., *Chinese medicine Ginseng and Astragalus granules ameliorate autoimmune diabetes by upregulating both CD4+FoxP3+ and CD8+CD122+PD1+ regulatory T cells.* Oncotarget, 2017. **8**(36): p. 60201-60209.
295. Nagasawa, T., et al., *Defects of B-cell lymphopoiesis and bone-marrow myelopoiesis in mice lacking the CXC chemokine PBSF/SDF-1.* Nature, 1996. **382**(6592): p. 635-8.
296. Guo, Y., et al., *SDF-1/CXCL12 enhances survival and chemotaxis of murine embryonic stem cells and production of primitive and definitive hematopoietic progenitor cells.* Stem Cells, 2005. **23**(9): p. 1324-32.
297. Hashimoto, N., et al., *Bone marrow-derived progenitor cells in pulmonary fibrosis.* J Clin Invest, 2004. **113**(2): p. 243-52.
298. Phillips, R.J., et al., *Circulating fibrocytes traffic to the lungs in response to CXCL12 and mediate fibrosis.* J Clin Invest, 2004. **114**(3): p. 438-46.
299. Bucala, R., et al., *Circulating fibrocytes define a new leukocyte subpopulation that mediates tissue repair.* Mol Med, 1994. **1**(1): p. 71-81.
300. Strieter, R.M., B.N. Gomperts, and M.P. Keane, *The role of CXC chemokines in pulmonary fibrosis.* J Clin Invest, 2007. **117**(3): p. 549-56.
301. Madala, S.K., et al., *Bone marrow-derived stromal cells are invasive and hyperproliferative and alter transforming growth factor-alpha-induced pulmonary fibrosis.* Am J Respir Cell Mol Biol, 2014. **50**(4): p. 777-86.
302. Andersson-Sjoland, A., et al., *Fibrocytes are a potential source of lung fibroblasts in idiopathic pulmonary fibrosis.* Int J Biochem Cell Biol, 2008. **40**(10): p. 2129-40.
303. Chesney, J., et al., *Regulated production of type I collagen and inflammatory cytokines by peripheral blood fibrocytes.* J Immunol, 1998. **160**(1): p. 419-25.
304. Wang, J.F., et al., *Fibrocytes from burn patients regulate the activities of fibroblasts.* Wound Repair Regen, 2007. **15**(1): p. 113-21.
305. Moore, B.B., et al., *CCR2-mediated recruitment of fibrocytes to the alveolar space after fibrotic injury.* Am J Pathol, 2005. **166**(3): p. 675-84.
306. Lama, V.N. and S.H. Phan, *The extrapulmonary origin of fibroblasts: stem/progenitor cells and beyond.* Proc Am Thorac Soc, 2006. **3**(4): p. 373-6.
307. Moeller, A., et al., *Circulating fibrocytes are an indicator of poor prognosis in idiopathic pulmonary fibrosis.* Am J Respir Crit Care Med, 2009. **179**(7): p. 588-94.
308. Fujiwara, A., et al., *Correlation between circulating fibrocytes, and activity and progression of interstitial lung diseases.* Respirology, 2012. **17**(4): p. 693-8.
309. Liang, Z., et al., *Development of a unique small molecule modulator of CXCR4.* PLoS One, 2012. **7**(4): p. e34038.
310. Makino, H., et al., *Antifibrotic effects of CXCR4 antagonist in bleomycin-induced pulmonary fibrosis in mice.* J Med Invest, 2013. **60**(1-2): p. 127-37.
311. Xu, J., et al., *Role of the SDF-1/CXCR4 axis in the pathogenesis of lung injury and fibrosis.* Am J Respir Cell Mol Biol, 2007. **37**(3): p. 291-9.
312. Altmann, A., et al., *Identification of a Novel ITGalphavbeta6-Binding Peptide Using Protein Separation and Phage Display.* Clin Cancer Res, 2017. **23**(15): p. 4170-4180.
313. Herraiz, J.L., et al., *FIRST: Fast Iterative Reconstruction Software for (PET) tomography.* Phys Med Biol, 2006. **51**(18): p. 4547-65.

314. Loening, A.M. and S.S. Gambhir, *AMIDE: a free software tool for multimodality medical image analysis.* Mol Imaging, 2003. **2**(3): p. 131-7.
315. Weinreb, P.H., et al., *Function-blocking integrin alphavbeta6 monoclonal antibodies: distinct ligand-mimetic and nonligand-mimetic classes.* J Biol Chem, 2004. **279**(17): p. 17875-87.
316. Hausner, S.H., et al., *Use of a peptide derived from foot-and-mouth disease virus for the noninvasive imaging of human cancer: generation and evaluation of 4-[18F]fluorobenzoyl A20FMDV2 for in vivo imaging of integrin alphavbeta6 expression with positron emission tomography.* Cancer Res, 2007. **67**(16): p. 7833-40.
317. Hausner, S.H., et al., *Targeted in vivo imaging of integrin alphavbeta6 with an improved radiotracer and its relevance in a pancreatic tumor model.* Cancer Res, 2009. **69**(14): p. 5843-50.
318. Hausner, S.H., et al., *Evaluation of [64Cu]Cu-DOTA and [64Cu]Cu-CB-TE2A chelates for targeted positron emission tomography with an alphavbeta6-specific peptide.* Mol Imaging, 2009. **8**(2): p. 111-21.
319. Hu, L.Y., et al., *Characterization and evaluation of (64)Cu-labeled A20FMDV2 conjugates for imaging the integrin alphavbeta 6.* Mol Imaging Biol, 2014. **16**(4): p. 567-77.
320. Hausner, S.H., et al., *In vivo positron emission tomography (PET) imaging with an alphavbeta6 specific peptide radiolabeled using 18F-"click" chemistry: evaluation and comparison with the corresponding 4-[18F]fluorobenzoyl- and 2-[18F]fluoropropionyl-peptides.* J Med Chem, 2008. **51**(19): p. 5901-4.
321. Kimura, R.H., et al., *Pharmacokinetically stabilized cystine knot peptides that bind alpha-v-beta-6 integrin with single-digit nanomolar affinities for detection of pancreatic cancer.* Clin Cancer Res, 2012. **18**(3): p. 839-49.
322. Hackel, B.J., et al., *18F-fluorobenzoate-labeled cystine knot peptides for PET imaging of integrin alphavbeta6.* J Nucl Med, 2013. **54**(7): p. 1101-5.
323. Singh, A.N., et al., *Dimerization of a phage-display selected peptide for imaging of alphavbeta6- integrin: two approaches to the multivalent effect.* Theranostics, 2014. **4**(7): p. 745-60.
324. Notni, J., et al., *In Vivo PET Imaging of the Cancer Integrin alphavbeta6 Using (68)Ga-Labeled Cyclic RGD Nonapeptides.* J Nucl Med, 2017. **58**(4): p. 671-677.
325. Saha, A., et al., *High-resolution in vivo imaging of breast cancer by targeting the pro-invasive integrin alphavbeta6.* J Pathol, 2010. **222**(1): p. 52-63.
326. Zhu, X., et al., *99mTc-labeled cystine knot peptide targeting integrin alphavbeta6 for tumor SPECT imaging.* Mol Pharm, 2014. **11**(4): p. 1208-17.
327. Liu, Z., et al., *Integrin alphavbeta(6)-Targeted SPECT Imaging for Pancreatic Cancer Detection.* J Nucl Med, 2014. **55**(6): p. 989-94.
328. Wangler, C., et al., *Multimerization of cRGD peptides by click chemistry: synthetic strategies, chemical limitations, and influence on biological properties.* Chembiochem, 2010. **11**(15): p. 2168-81.
329. Dijkgraaf, I., et al., *Improved targeting of the alpha(v)beta (3) integrin by multimerisation of RGD peptides.* Eur J Nucl Med Mol Imaging, 2007. **34**(2): p. 267-73.
330. Poethko, T., et al., *Two-step methodology for high-yield routine radiohalogenation of peptides: (18)F-labeled RGD and octreotide analogs.* J Nucl Med, 2004. **45**(5): p. 892-902.

331. Thumshirn, G., et al., *Multimeric cyclic RGD peptides as potential tools for tumor targeting: solid-phase peptide synthesis and chemoselective oxime ligation.* Chemistry, 2003. **9**(12): p. 2717-25.
332. Simecek, J., et al., *A cyclen-based tetraphosphinate chelator for the preparation of radiolabeled tetrameric bioconjugates.* Chemistry, 2013. **19**(24): p. 7748-57.
333. Nothelfer, E.M., et al., *Identification and characterization of a peptide with affinity to head and neck cancer.* J Nucl Med, 2009. **50**(3): p. 426-34.
334. Keat, N., et al., *A First Time in Human, Microdose, Positron Emission Tomography Study of the Safety, Immunogenicity, Biodistribution and Radiation Dosimetry of [(18)F]FB-A20FMDV2 for Imaging the Integrin alphavbeta6.* J Nucl Med Technol, 2018.
335. Hays, M.T., et al., *MIRD dose estimate report no. 19: radiation absorbed dose estimates from (18)F-FDG.* J Nucl Med, 2002. **43**(2): p. 210-4.
336. Adair, B.D., et al., *Three-dimensional EM structure of the ectodomain of integrin {alpha}V{beta}3 in a complex with fibronectin.* J Cell Biol, 2005. **168**(7): p. 1109-18.
337. Bruning, A. and I.B. Runnebaum, *CAR is a cell-cell adhesion protein in human cancer cells and is expressionally modulated by dexamethasone, TNFalpha, and TGFbeta.* Gene Ther, 2003. **10**(3): p. 198-205.
338. Cawthorne, C., et al., *Biodistribution, pharmacokinetics and metabolism of interleukin-1 receptor antagonist (IL-1RA) using [(1)(8)F]-IL1RA and PET imaging in rats.* Br J Pharmacol, 2011. **162**(3): p. 659-72.
339. Kimura, R.H., et al., *Engineered knottin peptides: a new class of agents for imaging integrin expression in living subjects.* Cancer Res, 2009. **69**(6): p. 2435-42.
340. Kimura, R.H., et al., *Engineered cystine knot peptides that bind alphavbeta3, alphavbeta5, and alpha5beta1 integrins with low-nanomolar affinity.* Proteins, 2009. **77**(2): p. 359-69.
341. Otte, A., et al., *Yttrium-90 DOTATOC: first clinical results.* Eur J Nucl Med, 1999. **26**(11): p. 1439-47.
342. Kwekkeboom, D.J., et al., *Radiolabeled somatostatin analog [177Lu-DOTA0,Tyr3]octreotate in patients with endocrine gastroenteropancreatic tumors.* J Clin Oncol, 2005. **23**(12): p. 2754-62.
343. Eder, M., et al., *68Ga-complex lipophilicity and the targeting property of a urea-based PSMA inhibitor for PET imaging.* Bioconjug Chem, 2012. **23**(4): p. 688-97.
344. Gourni, E., et al., *PET of CXCR4 expression by a (68)Ga-labeled highly specific targeted contrast agent.* J Nucl Med, 2011. **52**(11): p. 1803-10.
345. Hausner, S.H., et al., *The Effect of Bi-Terminal PEGylation of an Integrin alphavbeta(6)-Targeted (1)(8)F Peptide on Pharmacokinetics and Tumor Uptake.* J Nucl Med, 2015. **56**(5): p. 784-90.
346. Xiong, C., et al., *In vivo small-animal PET/CT of EphB4 receptors using 64Cu-labeled peptide.* J Nucl Med, 2011. **52**(2): p. 241-8.
347. Schottelius, M., et al., *Twins in spirit - episode I: comparative preclinical evaluation of [(68)Ga]DOTATATE and [(68)Ga]HA-DOTATATE.* EJNMMI Res, 2015. **5**: p. 22.
348. Mould, R., et al., *Binding kinetics differentiates functional antagonism of orexin-2 receptor ligands.* Br J Pharmacol, 2014. **171**(2): p. 351-63.
349. Nederpelt, I., et al., *From receptor binding kinetics to signal transduction; a missing link in predicting in vivo drug-action.* Sci Rep, 2017. **7**(1): p. 14169.

350. Fleck, B.A., et al., *Binding kinetics redefine the antagonist pharmacology of the corticotropin-releasing factor type 1 receptor.* J Pharmacol Exp Ther, 2012. **341**(2): p. 518-31.
351. Benedetto, S., et al., *Quantification of the expression level of integrin receptor alpha(v)beta3 in cell lines and MR imaging with antibody-coated iron oxide particles.* Magn Reson Med, 2006. **56**(4): p. 711-6.
352. Beer, A.J. and M. Schwaiger, *PET of alphavbeta3-integrin and alphavbeta5-integrin expression with 18F-fluciclatide for assessment of response to targeted therapy: ready for prime time?* J Nucl Med, 2011. **52**(3): p. 335-7.
353. Battle, M.R., et al., *Monitoring tumor response to antiangiogenic sunitinib therapy with 18F-fluciclatide, an 18F-labeled alphaVbeta3-integrin and alphaV beta5-integrin imaging agent.* J Nucl Med, 2011. **52**(3): p. 424-30.
354. Schottelius, M., et al., *Modulation of pharmacokinetics of radioiodinated sugar-conjugated somatostatin analogues by variation of peptide net charge and carbohydration chemistry.* Bioconjug Chem, 2005. **16**(2): p. 429-37.
355. Kratochwil, N.A., et al., *Predicting plasma protein binding of drugs--revisited.* Curr Opin Drug Discov Devel, 2004. **7**(4): p. 507-12.
356. Tabata, T., et al., *Induction of an epithelial integrin alphavbeta6 in human cytomegalovirus-infected endothelial cells leads to activation of transforming growth factor-beta1 and increased collagen production.* Am J Pathol, 2008. **172**(4): p. 1127-40.
357. Burke, B.P., et al., *Chelator free gallium-68 radiolabelling of silica coated iron oxide nanorods via surface interactions.* Nanoscale, 2015. **7**(36): p. 14889-96.
358. McDermott, D.H., et al., *AMD3100 is a potent antagonist at CXCR4(R334X) , a hyperfunctional mutant chemokine receptor and cause of WHIM syndrome.* J Cell Mol Med, 2011. **15**(10): p. 2071-81.
359. Rosenkilde, M.M., et al., *Molecular mechanism of AMD3100 antagonism in the CXCR4 receptor: transfer of binding site to the CXCR3 receptor.* J Biol Chem, 2004. **279**(4): p. 3033-41.
360. De Clercq, E., *The AMD3100 story: the path to the discovery of a stem cell mobilizer (Mozobil).* Biochem Pharmacol, 2009. **77**(11): p. 1655-64.
361. Schols, D., et al., *Inhibition of T-tropic HIV strains by selective antagonization of the chemokine receptor CXCR4.* J Exp Med, 1997. **186**(8): p. 1383-8.
362. Flomenberg, N., J. DiPersio, and G. Calandra, *Role of CXCR4 chemokine receptor blockade using AMD3100 for mobilization of autologous hematopoietic progenitor cells.* Acta Haematol, 2005. **114**(4): p. 198-205.
363. Poty, S., et al., *New AMD3100 derivatives for CXCR4 chemokine receptor targeted molecular imaging studies: synthesis, anti-HIV-1 evaluation and binding affinities.* Dalton Trans, 2015. **44**(11): p. 5004-16.
364. Bridger, G.J., et al., *Synthesis and structure-activity relationships of azamacrocyclic C-X-C chemokine receptor 4 antagonists: analogues containing a single azamacrocyclic ring are potent inhibitors of T-cell tropic (X4) HIV-1 replication.* J Med Chem, 2010. **53**(3): p. 1250-60.
365. Wong, R.S., et al., *Comparison of the potential multiple binding modes of bicyclam, monocylam, and noncyclam small-molecule CXC chemokine receptor 4 inhibitors.* Mol Pharmacol, 2008. **74**(6): p. 1485-95.
366. Gerlach, L.O., et al., *Molecular interactions of cyclam and bicyclam non-peptide antagonists with the CXCR4 chemokine receptor.* J Biol Chem, 2001. **276**(17): p. 14153-60.

367. Bai, R., et al., *Symmetrical bis-tertiary amines as novel CXCR4 inhibitors.* Eur J Med Chem, 2016. **118**: p. 340-50.
368. Gerlach, L.O., et al., *Metal ion enhanced binding of AMD3100 to Asp262 in the CXCR4 receptor.* Biochemistry, 2003. **42**(3): p. 710-7.
369. Jacobson, O., et al., *64Cu-AMD3100--a novel imaging agent for targeting chemokine receptor CXCR4.* Bioorg Med Chem, 2009. **17**(4): p. 1486-93.
370. Nimmagadda, S., et al., *Molecular imaging of CXCR4 receptor expression in human cancer xenografts with [64Cu]AMD3100 positron emission tomography.* Cancer Res, 2010. **70**(10): p. 3935-44.
371. Boswell, C.A., et al., *Comparative in vivo stability of copper-64-labeled cross-bridged and conventional tetraazamacrocyclic complexes.* J Med Chem, 2004. **47**(6): p. 1465-74.
372. Wadas, T.J., et al., *Copper chelation chemistry and its role in copper radiopharmaceuticals.* Curr Pharm Des, 2007. **13**(1): p. 3-16.
373. Smith-Jones, P.M., et al., *Antibody labeling with copper-67 using the bifunctional macrocycle 4-[(1,4,8,11-tetraazacyclotetradec-1-yl)methyl]benzoic acid.* Bioconjug Chem, 1991. **2**(6): p. 415-21.
374. Navratilova, I., M. Dioszegi, and D.G. Myszka, *Analyzing ligand and small molecule binding activity of solubilized GPCRs using biosensor technology.* Anal Biochem, 2006. **355**(1): p. 132-9.
375. Navratilova, I., J. Sodroski, and D.G. Myszka, *Solubilization, stabilization, and purification of chemokine receptors using biosensor technology.* Anal Biochem, 2005. **339**(2): p. 271-81.
376. Stenlund, P., et al., *Capture and reconstitution of G protein-coupled receptors on a biosensor surface.* Anal Biochem, 2003. **316**(2): p. 243-50.
377. Navratilova, I., J. Besnard, and A.L. Hopkins, *Screening for GPCR Ligands Using Surface Plasmon Resonance.* ACS Med Chem Lett, 2011. **2**(7): p. 549-554.
378. Navratilova, I. and A.L. Hopkins, *Fragment screening by surface plasmon resonance.* ACS Med Chem Lett, 2010. **1**(1): p. 44-8.
379. Vega, B., et al., *Real-time detection of the chemokine CXCL12 in urine samples by surface plasmon resonance.* Talanta, 2013. **109**: p. 209-15.
380. Costa, S., et al., *Fusion tags for protein solubility, purification and immunogenicity in Escherichia coli: the novel Fh8 system.* Front Microbiol, 2014. **5**: p. 63.
381. Khan, A., et al., *Binding optimization through coordination chemistry: CXCR4 chemokine receptor antagonists from ultrarigid metal complexes.* J Am Chem Soc, 2009. **131**(10): p. 3416-7.
382. Philipp-Abbrederis, K., et al., *In vivo molecular imaging of chemokine receptor CXCR4 expression in patients with advanced multiple myeloma.* EMBO Mol Med, 2015. **7**(4): p. 477-87.
383. Silversides, J.D., C.C. Allan, and S.J. Archibald, *Copper(II) cyclam-based complexes for radiopharmaceutical applications: synthesis and structural analysis.* Dalton Trans, 2007(9): p. 971-8.
384. Silversides, J.D., R. Smith, and S.J. Archibald, *Challenges in chelating positron emitting copper isotopes: tailored synthesis of unsymmetric chelators to form ultra stable complexes.* Dalton Trans, 2011. **40**(23): p. 6289-97.
385. Sun, X., et al., *Radiolabeling and in vivo behavior of copper-64-labeled cross-bridged cyclam ligands.* J Med Chem, 2002. **45**(2): p. 469-77.

386. Maples, R.D., et al., *Aspartate-Based CXCR4 Chemokine Receptor Binding of Cross-Bridged Tetraazamacrocyclic Copper(II) and Zinc(II) Complexes.* Chemistry, 2016. **22**(36): p. 12916-30.
387. Liang, X., et al., *Structure and dynamics of metallomacrocycles: recognition of zinc xylyl-bicyclam by an HIV coreceptor.* J Am Chem Soc, 2002. **124**(31): p. 9105-12.
388. Schuck, P., *Use of surface plasmon resonance to probe the equilibrium and dynamic aspects of interactions between biological macromolecules.* Annu Rev Biophys Biomol Struct, 1997. **26**: p. 541-66.
389. Schuck, P. and H. Zhao, *The role of mass transport limitation and surface heterogeneity in the biophysical characterization of macromolecular binding processes by SPR biosensing.* Methods Mol Biol, 2010. **627**: p. 15-54.
390. Miranda, C.S., *Evaluation of new PET tracers for receptor tumour imaging*, in *School of Life Sciences*. 2018, University of Hull. p. 207.
391. Kenny, L.M. and E.O. Aboagye, *Clinical translation of molecular imaging agents used in PET studies of cancer.* Adv Cancer Res, 2014. **124**: p. 329-74.
392. Stabin, M.G., R.B. Sparks, and E. Crowe, *OLINDA/EXM: the second-generation personal computer software for internal dose assessment in nuclear medicine.* J Nucl Med, 2005. **46**(6): p. 1023-7.
393. Stabin, M.G. and J.A. Siegel, *RADAR Dose Estimate Report: A Compendium of Radiopharmaceutical Dose Estimates Based on OLINDA/EXM Version 2.0.* J Nucl Med, 2018. **59**(1): p. 154-160.

# 7 Appendix

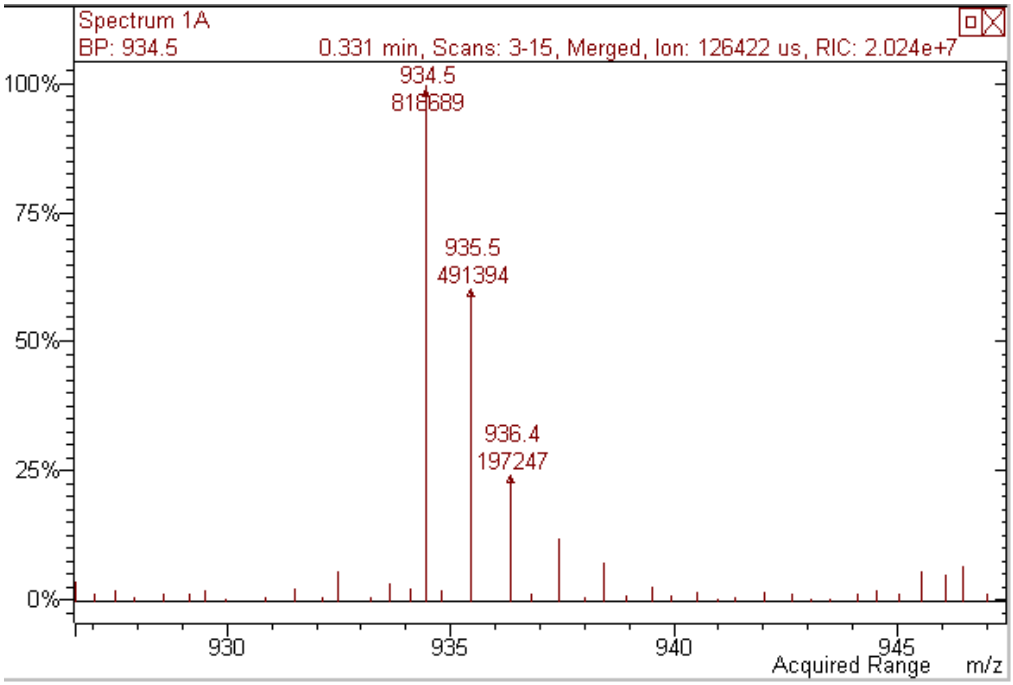


**Appendix Figure 1. Mass spectrometry chromatogram of RGD1 peptide**

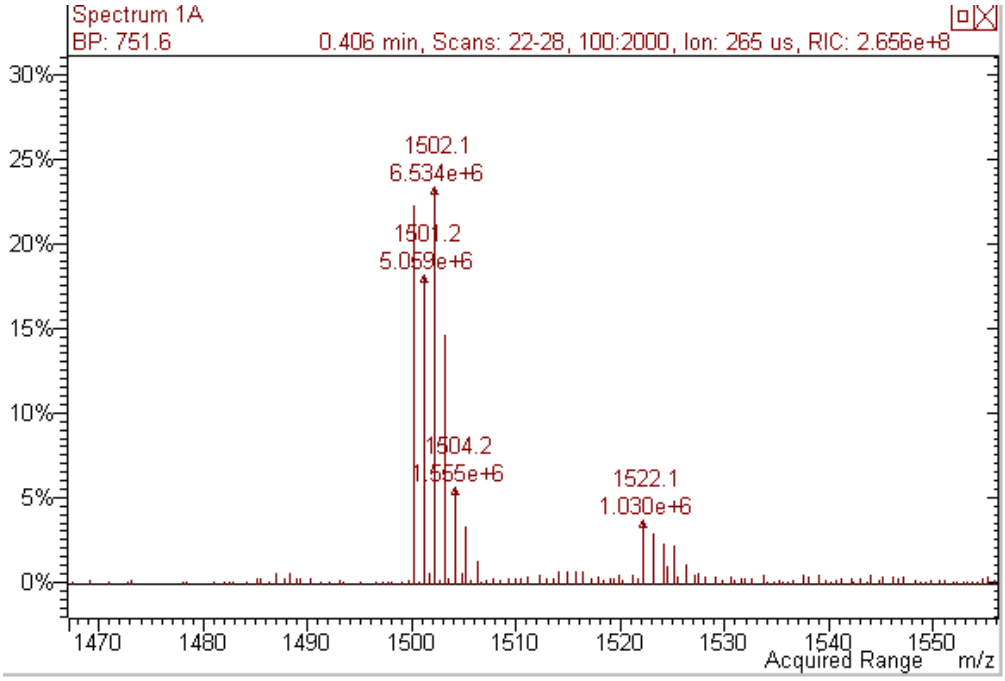


**Appendix Figure 2. Mass spectrometry chromatogram of [$^{nat}$Ga]Ga-DO3A-JD1-RGD1 peptide**

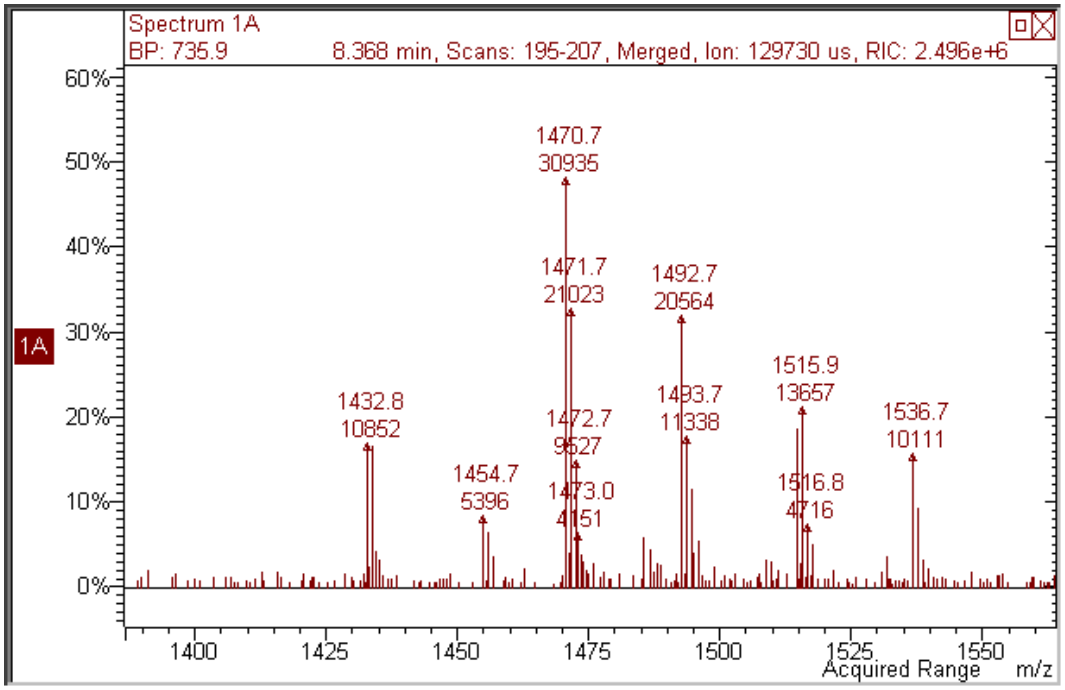


**Appendix Figure 3. Mass spectrometry chromatogram of [$^{nat}$Ga]Ga-DO3A-JD2-RGD1**

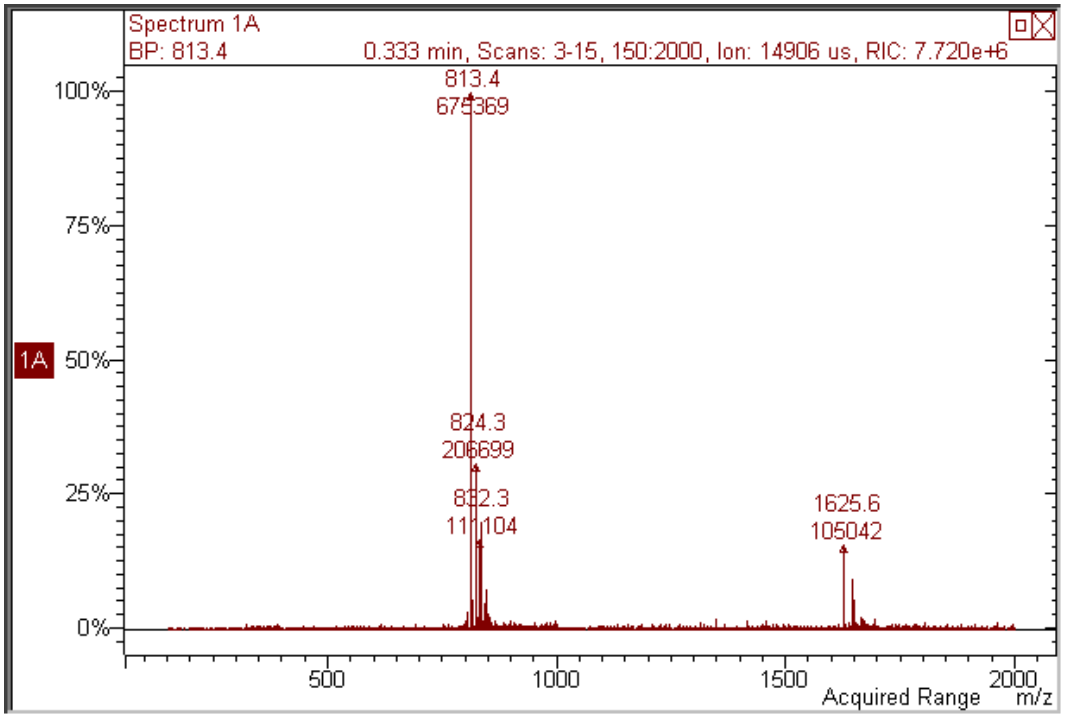


**Appendix Figure 4. Mass spectrometry chromatogram of [$^{na}$Lu]Lu-DO3A-JD2-RGD1**

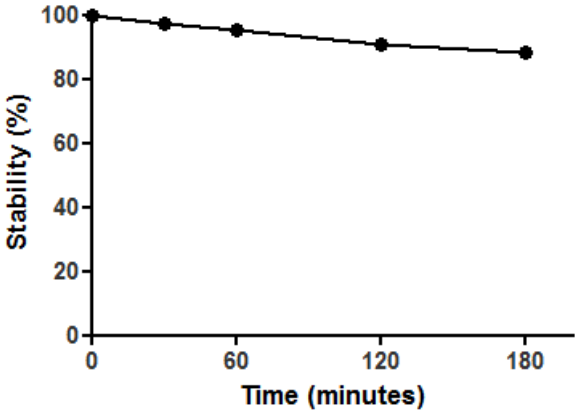


**Appendix Figure 5. Serum stability time course of [$^{68}$Ga]Ga-DO3A-RGD3 over 3 hours**

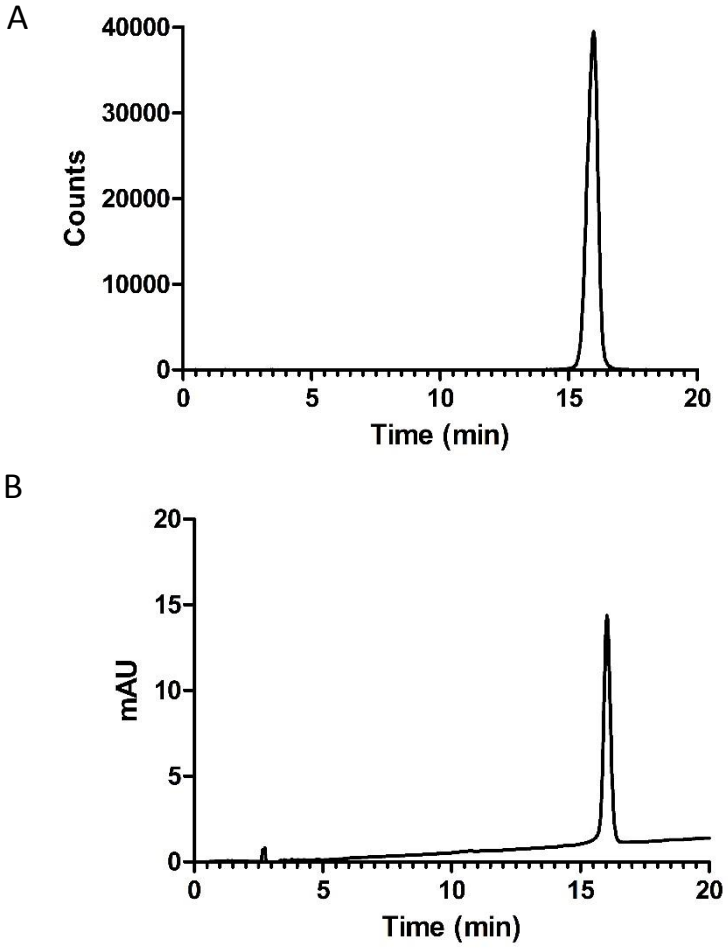


**Appendix Figure 6. (A) Radio-HPLC chromatogram of [68Ga]Ga-DO3A-JD2-RGD1. (B) UV chromatogram of [68Ga]Ga-DO3A-JD2-RGD1. Radiolabeled peptide eluted at approximately 16 minutes.**

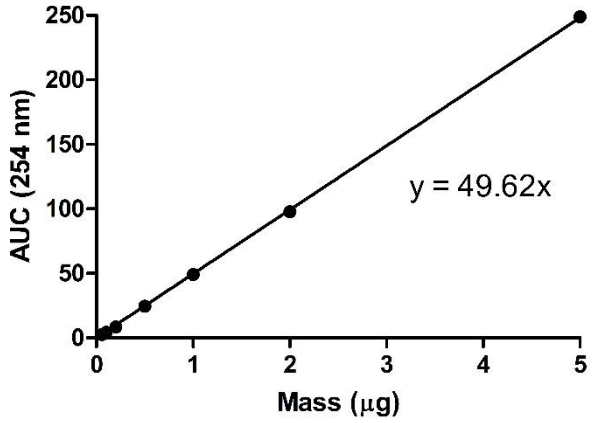


**Appendix Figure 7. Specific activity calibration curve. The area under the curve of [$^{68}$Ga]Ga-DO3A-JD2-RGD1, detected under UV, were plotted against the mass of peptide injected. The line-of-best-fit equation was used to calculate the specific activity of [$^{68}$Ga]Ga-DO3A-JD2-RGD1.**

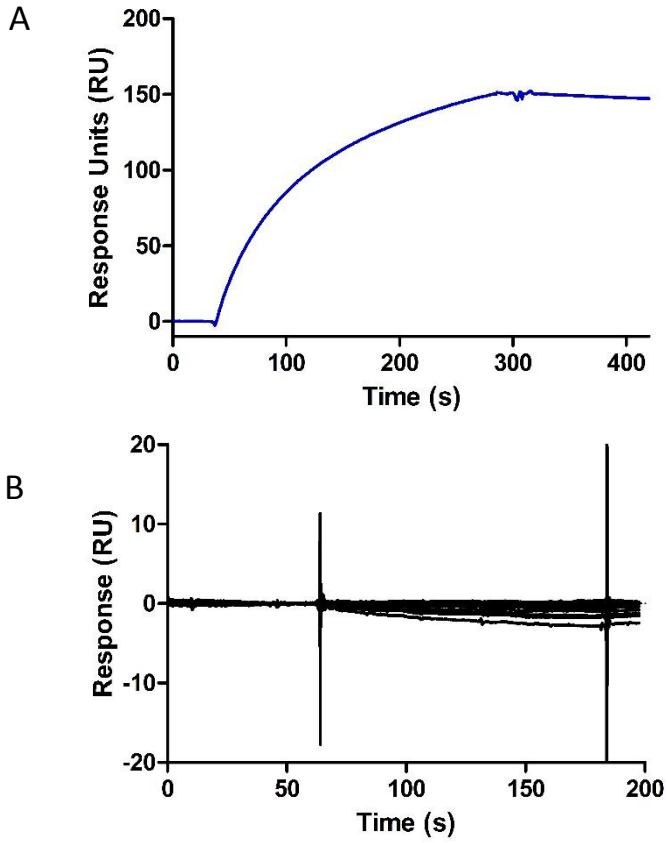


**Appendix Figure 8. (A) Sensorgram of anti-αvβ6 mAb injection following immobilisation of recombinant αvβ6 on a series S CM5 sensor chip. (B) Multi-cycle kinetics sensorgram of [$^{nat}$Ga]Ga-DO3A-JD2-RGD1. The maximum response observed following antibody injection is approximately 150 RU, therefore the $R_{max}$ for [$^{nat}$Ga]Ga-DO3A-JD2-RGD1 is approximately 150-fold less, based on relative molecular weights of the analytes.**

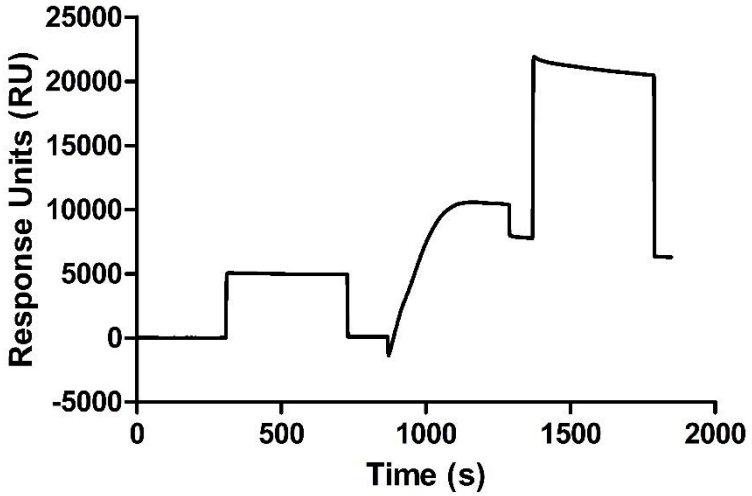


**Appendix Figure 9. Immobilisation of anti-GST pAb on a Series S CM4 sensor surface chip by standard amine coupling.**

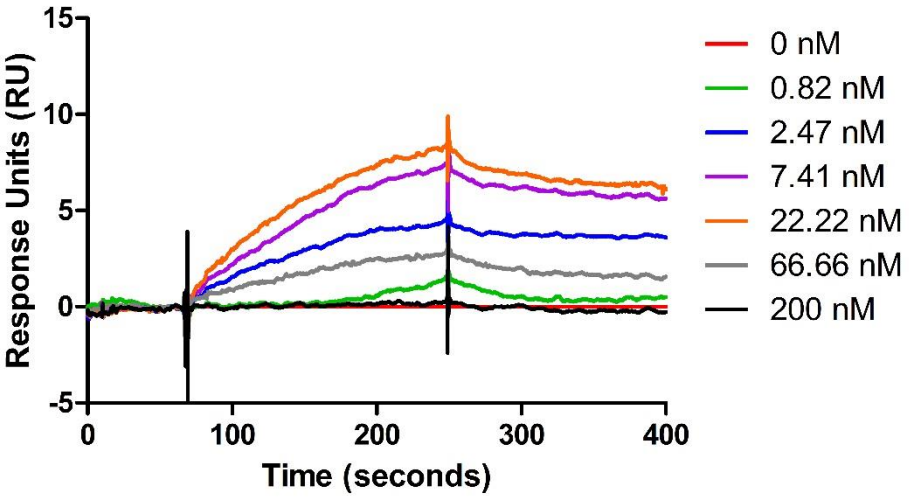


**Appendix Figure 10. Multi-cycle kinetics sensorgram of [$^{nat}$Cu]Cu-CB-Bicyclam. Analyte was injected at the concentrations indicated by the legend (right)**

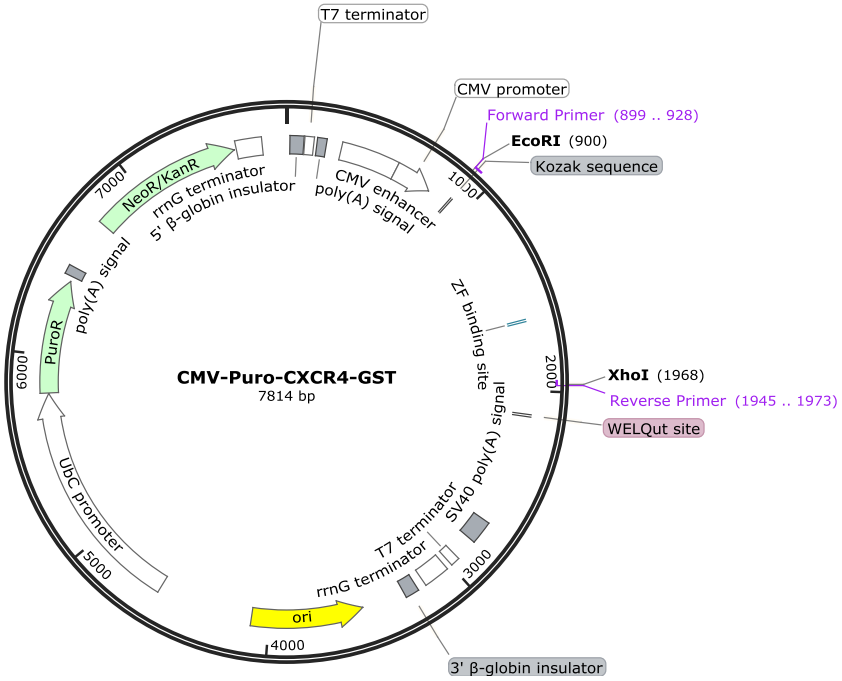


**Appendix Figure 11. Vector map for GST-tagged CXCR4 sequence**